FACULTÉ DES LETTRES ET SCIENCES HUMAINES
DÉPARTEMENT DE GÉOMATIQUE APPLIQUÉE

UNIVERSITÉ DE SHERBROOKE

# Analyse de la modélisation de l'émission multi-fréquences micro-onde des sols et de la neige, incluant les croutes de glace à l'aide du modèle Microwave Emission Model of Layered Snowpacks (MEMLS).

Benoit MONTPETIT

Thèse présentée pour l'obtention du grade de Philosophiae Doctor (Ph. D.) en télédétection,
Cheminement en physique de la télédétection

Mai 2015

©Benoit Montpetit, 2015

Directeur de recherche : Prof. Alain Royer
Membres du Jury Interne : Prof. Kalifa Goïta et Prof. Robert Lecomte
Membres du Jury Externe : Prof. Micheal Durand (Ohio State University)
Membres du Jury Expert Supplémentaire : Prof. Alexandre Langlois (Université de Sherbrooke)

**Résumé**

L'étude du couvert nival est essentielle afin de mieux comprendre les processus climatiques et hydrologiques. De plus, avec les changements climatiques observés dans l'hémisphère nord, des événements de dégel-regel ou de pluie hivernale sont de plus en plus courants et produisent des croutes de glace dans le couvert nival affectant les mœurs des communautés arctiques en plus de menacer la survie de la faune arctique. La télédétection micro-ondes passives (MOP) démontre un grand potentiel de caractérisation du couvert nival. Toutefois, afin de bien comprendre les mesures satellitaires, une modélisation adéquate du signal est nécessaire.

L'objectif principal de cette thèse est d'analyser le transfert radiatif (TR) MOP des sols, de la neige et de la glace afin de mieux caractériser les propriétés géophysiques du couvert nival par télédétection. Il a été démontré que le ratio de polarisation (PR) est très affecté par la présence de croutes de glace dans le couvert de neige et une étude de sensibilité du PR aux différents paramètres des croutes de glace a été réalisée et validée. Il a été démontré qu'il est possible de détecter les croutes de glace par télédétection MOP satellitaire à partir d'une approche par seuillage. Pour ce faire, le modèle Microwave Emission Model of Layered Snowpacks (MEMLS) a été étudié et calibré afin de minimiser les erreurs des températures de brillance simulées en présences de croutes de glace.

La première amélioration faite à la modélisation du TR MOP de la neige a été la caractérisation de la taille des grains de neige. Deux nouveaux instruments, utilisant la réflectance dans le proche infrarouge, ont été développés afin de mesurer la surface spécifique de la neige (SSA). Il a été démontré que la SSA est un paramètre plus précis et plus objectif pour caractériser la taille des grains de neige. Les deux instruments ont démontré une incertitude de 10% sur la mesure de la SSA. De plus, la SSA a été calibré pour la modélisation MOP afin de minimiser l'erreur sur la modélisation de la température de brillance. Il a été démontré qu'un facteur multiplicatif $\phi = 1.3$ appliqué au paramètre de taille des grains de neige dans MEMLS, paramètre dérivé de la SSA, est nécessaire afin de minimiser l'erreur des simulations.

La deuxième amélioration apportée à la modélisation du TR MOP a été l'estimation de l'émission du sol. Des mesures radiométriques MOP in-situ ainsi que des profils de températures de sols organiques arctiques gelés ont été acquis et caractérisés afin de simuler l'émission MOP de ces sols. Des constantes diélectriques effectives à 10.7, 19 et 37 GHz ainsi qu'une rugosité de surface

effective des sols ont été déterminés pour simuler l'émission des sols. Une erreur quadratique moyenne (RMSE) de 4.65 K entre les simulations et les mesures MOP a été obtenue.

Suite à la calibration du TR MOP du sol et de la neige, un module de TR de la glace a été implémenté dans MEMLS. Avec ce nouveau module, il a été possible de démontré que l'approximation de Born améliorée, déjà implémenté dans MEMLS, pouvait être utilisé pour simuler des croutes de glace pure à condition que la couche de glace soit caractérisée par une densité de 917 kg $m^{-3}$ et une taille des grains de neige de 0 mm. Il a aussi été démontré que, pour des sites caractérisés par des croutes de glace, les températures de brillances simulées des couverts de neige avec des croutes de glace ayant les propriétés mesurées in-situ (RMSE=11.3 K), avaient une erreur similaire aux températures de brillances simulées des couverts de neige pour des sites n'ayant pas de croutes de glace (RMSE=11.5 K).

Avec le modèle MEMLS validé pour la simulation du TR MOP du sol, de la neige et de la glace, un indice de détection des croutes de glace par télédétection MOP a été développé. Il a été démontré que le ratio de polarisation (PR) était très affecté par la présence de croutes de glace dans le couvert de neige. Avec des simulations des PR à 10.7, 19 et 37 GHz sur des sites mesurés à Churchill (Manitoba, Canada), il a été possible de déterminer des seuils entre la moyenne hivernale des PR et les valeurs des PR mesurés indiquant la présence de croutes de glace. Ces seuils ont été appliqués sur une série temporelle de PR de 33 hivers d'un pixel du Nunavik (Québec, Canada) où les conditions de sols étaient similaires à ceux observés à Churchill. Plusieurs croutes de glace ont été détectées depuis 1995 et les mêmes événements entre 2002 et 2009 que (Roy, 2014) ont été détectés. Avec une validation in-situ, il serait possible de confirmer ces événements de croutes de glace mais (Roy, 2014) a démontré que ces événements ne pouvaient être expliqués que par la présence de croutes de glace dans le couvert de neige. Ces mêmes seuils sur les PR ont été appliqués sur un pixel de l'Île Banks (Territoires du Nord-Ouest, Canada). L'événement répertorié par (Grenfell et Putkonen, 2008) a été détecté. Plusieurs autres événements de croutes de glace ont été détectés dans les années 1990 et 2000 avec ces seuils. Tous ces événements ont suivi une période où les températures de l'air étaient près ou supérieures au point de congélation et sont rapidement retombées sous le point de congélation. Les températures de l'air peuvent être utilisées pour confirmer la possibilité de présence de croutes de glace mais seul la validation in-situ peut définitivement confirmer la présence de ces croutes.

**Mots clés :** Arctique, sub-arctique, neige, sol, glace, micro-ondes passives, température de brillance, télédétection, croutes de glace, modélisation, transfert radiatif, MEMLS.

**Extended Abstract**

Snow cover studies are essential to better understand climatic and hydrologic processes. With recent climate change observed in the northern hemisphere, more frequent rain-on-snow and melt-refreeze events have been reported, which affect the habits of the northern comunities and the survival of arctique wildlife. Passive microwave remote sensing has proven to be a great tool to characterize the state of snow cover. Nonetheless, proper modeling of the microwave signal is needed in order to understand how the parameters of the snowpack affect the measured signal.

The main objective of this study is to analyze the soil, snow and ice radiative transfer in order to better characterize snow cover properties and develop an ice lens detection index with satellite passive microwave brightness temperatures. To do so, the passive microwave radiative transfer modeling of the Microwave Emission Model of Layered Snowpacks (MEMLS) was improved in order to minimize the errors on the brightness temperature simulations in the presence of ice lenses.

The first improvement to passive microwave radiative transfer modeling of snow made was the snow grain size parameterization. Two new instruments, based on short wave infrared reflectance to measure the snow specific surface area (SSA) were developed. This parameter was shown to be a more accurate and objective to characterize snow grain size. The instruments showed an uncertainty of 10% to measure the SSA of snow. Also, the SSA of snow was calibrated for passive microwave modeling in order to reduce the errors on the simulated brightness temperatures. It was showed that a correction factor of $\phi = 1.3$ needed to be applied to the grain size parameter of MEMLS, obtain through the SSA measurements, to minimize the simulation error.

The second improvement to passive microwave radiative transfer modeling was the estimation of passive microwave soil emission. In-situ microwave measurements and physical temperature profiles of frozen organic arctic soils were acquired and characterized to improve the modeling of the soil emission. Effective permittivities at 10.7, 19 and 37 GHz and effective surface roughness were determined for this type of soil and the soil brightness temperature simulations were obtain with a minimal root mean square error (RMSE) of 4.65K.

With the snow grain size and soil contributions to the emitted brightness temperature optimized, it was then possible to implement a passive microwave radiative transfer module of ice into MEMLS. With this module, it was possible to demonstrate that the improved Born approximation already implemented in MEMLS was equivalent to simulating a pure ice lens when the density of the layer was set to 917 kg $m^{-3}$ and the grain size to 0 mm. This study also showed that by simulating

ice lenses within the snow with there measured properties, the RMSE of the simulations (RMSE= 11.3 K) was similar to the RMSE for simulations of snowpacks where no ice lenses were measured (only snow, RMSE= 11.5 K).

With the validated MEMLS model for snowpacks with ice lenses, an ice index was created. It is shown here that the polarization ratio (PR) was strongly affected by the presence of ice lenses within the snowpack. With simulations of the PR at 10.7, 19 and 37 GHz from measured snowpack properties in Chucrhill (Manitoba, Canada), thresholds between the measured PR and the mean winter PR were determined to detect the presence of ice within the snowpack. These thresholds were applied to a timeseries of nearly 34 years for a pixel in Nunavik (Quebec, Canada) where the soil surface is similar to that of the Churchill site. Many ice lenses are detected since 1995 with these thresholds and the same events as Roy (2014) were detected. With in-situ validation, it would be possible to confirm the precision of these thresholds but Roy (2014) showed that these events can not be explained by anything else than the presence of an ice layer within the snowpack. The same thresholds were applied to a pixel on Banks island (North-West Territories, Canada). The 2003 event that was reported by Grenfell et Putkonen (2008) was detected by the thresholds. Other events in the years 1990 and 2000's were detected with these thresholds. These events all follow periods where the air temperature were warm and were followed by a quick drop in air temperature which could be used to validate the presence of ice layer within the snowpack. Nonetheless, without in-situ validation, these events can not be confirmed.

**Keywords :** Arctic, sub-arctic, snow, soil, ice, passive microwaves, brightness temperatures, remote sensing, ice lenses, modeling, radiative transfer, MEMLS.

## Avant-Propos

Ce document se veut être une thèse par articles. Ceci signifie que certains des résultats présentés dans cette thèse ont fait l'objet d'articles publiés dans des revues scientifiques, d'autres font l'objet d'articles soumis et en révision et certains résultats n'ont pas été soumis au moment de la rédaction de la thèse. Cette thèse comporte donc deux articles publiés dans des revues scientifiques ainsi qu'un article en révision. Chacune de ces publications fait l'objet d'un ou plusieurs chapitre(s) de résultats de cette thèse. Afin de ne pas dénaturer ces documents, ils sont inclus tels qu'ils sont présentés dans les revues scientifiques (si publiés) où tels que présentés aux comités de révision de revues scientifiques respectifs. Ces articles sont présentés dans la langue de publication, soit en anglais. Toutefois, chacune de ces publications est précédée par une brève introduction en français décrivant l'objectif et les résultats de l'étude publiée. Chaque article a été inséré dans cette thèse une seule fois et lorsqu'un deuxième chapitre de résultats fait référence à un article déjà inséré dans cette thèse, cet article est indiqué dans l'introduction du chapitre de résultats. Afin de faciliter la révision du document en français et en anglais, les légendes des figures de la thèse sont présentées dans les deux langues.

Ce manuscrit est donc composé de 7 chapitres. Le premier est une introduction générale expliquant la problématique, les buts et hypothèses liés à cette thèse. La deuxième section décrit les sites d'étude ainsi que les mesures acquises pour atteindre les objectifs décrits dans le chapitre précédent. Les chapitres 3 à 6 sont des chapitres de résultats. Chacun de ces chapitres débute par une courte introduction en français. Le chapitre 3 présente les deux articles publiés dans des revues scientifiques (Montpetit *et al.*, 2012, 2013). Le chapitre 4 présente l'article qui fait l'objet de révisions (Montpetit *et al.*, En Revision). Le chapitre 5 réfère à des résultats présentés dans une autre section du deuxième article du chapitre 3 (Montpetit *et al.*, 2013). Le chapitre 6 présente des résultats de cette étude qui n'ont pas fait l'objet d'une publication scientifique. Finalement, le chapitre 7 présente une conclusion ainsi que des travaux futurs liés à cette thèse. En annexe sont présentés les résultats d'une étude effectuée dans le cadre de cette thèse qui sont indirectement liés à l'objectif général. Afin de faciliter la lecture de ce document, cette partie du travail publiée dans le journal *Remote Sensing of Environment* (Montpetit *et al.*, 2015) est présentée en annexe.

B. Montpetit, A. Royer, A. Langlois, P. Cliche, A. Roy, N. Champollion, G. Picard, F. Domine et R. Obbard : New shortwave infrared albedo measurements for snow specific surface area retrieval. *Journal of Glaciology*, 58(211) :941-952, 2012. ISSN 00221430.

B. Montpetit, A. Royer, A. Roy et A. Langlois : In-situ passive microwave parameterization of subarctic frozen organic soils. *Geoscience and Remote Sensing Letters*, xxx :xxx, En Revision.

B. Montpetit, A. Royer, A. Roy, A. Langlois et C. Derksen : Snow microwave emission modeling of ice lenses within a snowpack using the microwave emission model for layered snowpacks. *IEEE Transactions on Geoscience and Remote Sensing*, 51(9) :4705-4717, 2013. ISSN 0196-2892.

B. Montpetit, A. Royer, J.-P. Wigneron, A. Chanzy et A. Mialon : Evaluation of multi-frequencybare soil passive microwave reflectivity models. *Remote Sensing of Environment*, 162 :186-195, 2015.

# Table des matières

# Liste des figures

# Liste des tableaux

**Liste d'abréviations**

**3D :** *Trois dimensions*

**ASC :** Agence Spatiale Canadienne

**AMSR-E :** Advanced Microwave Scanning Radiometer - EOS

**CARTEL :** Centre d'Applications et de Recherches en Télédétection

**CLASS :** *Canadian LAnd Surface Scheme*

**CoReH2O :** *Cold Regions Hydrology High-Resolution Observatory* (programme de l'ESA et ASC)

**DMRT-ML :** Dense Media Radiative Transfer - Multi Layer

**DUFISSS :** *DUal-Frequenices Integrating Sphere for Snow Specific Surface Area*

**EASE-Grid :** *Equal-Area Scalable Earth Grid*

**ESA :** Agence Spatiale Européenne (*European Space Agency*)

**ÉEN :** Équivalent en Eau de la Neige

**GHz :** Giga Hertz

**GR :** Ratio de gradient fréquentiel

**H-Pol :** Polarisation horizontale

**HUT :** Helsinki University of Technology

**API :** Année Polaire Internationale

**IR :** Infrarouge

**INRA :** *Institut National Recherche Agronomique*

**INRS :** *Institut National de Recherche Scientifiques*

**IRIS :** *InfraRed Intergrating Sphere*

**LGGE :** *Laboratoire de Glaciologie et de Géophysique de l'Environnement*

**MEMLS :** Microwave Emission Model of Layered Snowpacks

**MOP :** Micro-ondes passives

**NARR :** North American Regional Reanalysis

**NSIDC :** National Snow and Ice Data Center

**PR :** Ratio de polarisation

**RMSE :** Erreur quadratique moyenne (*Root Mean Square Error*)

**SIRENE :** Site Interdisciplinaire de Recherche en ENvironnement Extérieur

**SMAP :** Soil Moisture Active and Passive mission (NASA, lancement prévu en Janvier 2015)

**SMMR :** Special Multichannel Microwave Radiometer

**SSA :** Surface spécifique de la neige (*Specific Surface Area*)

**SSM/I :** Special Sensor Microwave/Imager

**SWIRcam :** *ShortWave Infrared Camera*

**TR :** Transfer radiatif

**V-Pol :** Polarisation verticale

**Liste de symboles**

$D_{max}$ **:** Diamètre maximale du grain de neige

$D_o$ **:** Diamètre optique du grain de neige

$e(f, p)$ **:** Émissivité d'une cible à une fréquence $f$ et polarisation $p$

$f$ **:** Fréquence

$k$ **:** Nombre d'onde $(2\pi/\lambda)$

$p$ **:** Polarisation

$p_c$ **:** Longueur de corrélation des grains de neige

$T_B(f, p)$ **:** Température de brillance à la fréquence $f$ et polarisation $p$

$T_{B\downarrow}$ **:** Température de brillance atmosphérique descendante

$T_{B\uparrow}$ **:** Température de brillance atmosphérique ascendante

$T_{neige}$ **:** Température physique de la neige

$T_{max}$ **:** Température physique maximale de l'air

$T_{min}$ **:** Température physique minimale de l'air

$\epsilon$ **:** Constante diélectrique complexe (permittivité)

$\epsilon'$ **:** Partie réelle de la constante diélectrique (perte diélectrique)

$\epsilon''$ **:** Partie imaginaire de la constante diélectrique

$\epsilon'_{air}$ **:** Partie réelle de la constante diélectrique de l'air ($\epsilon'_{air} = 1$)

$\epsilon'_{glace}$ **:** Partie réelle de la constante diélectrique de la glace ($\epsilon'_{glace} = 3.2$)

$\epsilon'_{neige}$ **:** Partie réelle de la constante diélectrique de la neige

$\Gamma(f,p)$ **:** Coefficient de réflectivité d'une surface à une fréquence $f$ et polarisation $p$

$\Gamma_{fresnel}(f,p)$ **:** Coefficient de réflectivité de Fresnel d'une surface à une fréquence $f$ et polarisation $p$

$\phi$ **:** Facteur de correction de la taille des grains de neige dans le modèle MEMLS

$\kappa$ **:** Indice de Cohen

$\rho_{neige}$ **:** Densité de la neige

$\rho_{sol}$ **:** Densité du sol

$\rho_{glace}$ **:** Densité de la glace (917 kg m$^{-3}$)

$\sigma_{sol}$ **ou** $\sigma$ **:** Rugosité de surface du sol

$\tau_{atm}$ **:** Transmissivité de l'atmosphère

$\theta$ **:** Angle d'incidence

**Remerciements**

J'aimerais personnellement remercier mon directeur, le professeur Alain Royer. Je lui suis grandement reconnaissant de la grande liberté et la confiance qu'il m'a fait preuve tout au long de ce cheminement. Il a su me laisser aller et me donner carte blanche aux bons moments ainsi que de me donner tous les outils nécessaires pour accomplir mes travaux de recherche. De plus, ces conseils, sa disponibilités et ses idées, autant les idées les plus logiques que les plus farfelues, m'ont permis d'avancer et d'accomplir les travaux désirés et d'obtenir les résultats originaux présentés ici. Il a été très intéressant et stimulant de côtoyer quelqu'un d'aussi passionné par le monde de la géophysique. Nos échanges Skype lorsque j'étais à l'extérieur de Sherbrooke ont toujours été inspirants et une bougie d'allumage pour augmenter mon niveau de production.

Cette recherche a été financée par le Conseil de recherche en sciences naturelles et génie du Canada ainsi que le Ministère de l'Environnement (Environnement Canada) pour l'aide financière aux campagnes de terrain à Churchill (Manitoba) et à Inuvik (Territoires du Nord-Ouest). De plus, des contributions du Global Environmental and Climate Change Center (GEC3), La Commission permanente de coopération franco-québecoise (CPCFQ) et de la faculté des Lettres et Sciences Humaines de l'Université de Sherbrooke m'ont permis de participer à différentes conférences internationales. Aussi, les résultats de l'annexe A de cette thèse ont été acquis lors de la campagne PORTOS-93 qui a été financée par l'Institut National de Recherche Agronomique d'Avignon (France).

Je tiens aussi à remercier tous ceux qui ont contribué aux différents travaux de cette thèse. Je tiens à remercier particulièrement Alexandre Roy (Bobby) et Alexandre Langlois pour leurs nombreux échanges scientifiques et les superbes campagnes terrains. Je garderai un souvenir permanent de nos campagnes terrain (pinky). Un merci particulier à tous les membres du département de géomatique appliquée à l'environnement ainsi que le CARTEL qui m'ont toujours fourni le support demandé. Je remercie tous les étudiants et professeurs du CARTEL pour leur support durant ces dernières années surtout lorsque j'étais à l'extérieur de Sherbrooke ! Un merci particulier à Bruno Courtemanche qui m'a toujours offert un endroit où rester lors de mes courts séjours à Sherbrooke ces dernières années. Merci aussi à ma famille qui m'a offert tout le support possible.

Je remercie et dédie se travail à Mylène Lanthier qui m'a aidé dans la révision de ce manuscrit et qui m'a toujours supporté lors des différents succès et épreuves ces dernières années.

# 1 Introduction générale

## 1.1 L'étude du couvert nival dans un contexte de changements climatiques

Dans le contexte actuel des changements climatiques, le manteau neigeux joue un rôle primordial dans l'étude des processus climatiques et hydrologiques terrestres. De plus, le couvert nival est un excellent indicateur de changements climatiques. En effet, de fortes rétroactions climatiques (e.g. des changements de l'étendue du couvert nival et de la température de l'air) peuvent être observées suite aux changements des propriétés géophysiques de la neige (e.g. Fletcher *et al.*, 2009; Qu et Hall, 2007; Armstrong et Brun, 2008). Par exemple, l'albédo (i.e. la fraction d'énergie solaire incidente réfléchie par une cible) de la neige étant initialement très élevée, cette neige réfléchit davantage de rayonnement solaire vers l'atmosphère que la neige vieillie, limitant donc l'énergie pouvant atteindre les surfaces terrestres, limitant ainsi son réchauffement. De plus, la neige, ayant une très faible conductivité thermique, agit comme un excellent isolant entre les températures de l'air hivernales froides et certains systèmes racinaires leur permettant de survivre aux hivers. Les changements climatiques liés au couvert nival sont principalement dus à la modification des paramètres optiques de la neige suite au métamorphisme, au changement de couverture spatiale et d'épaisseur de la neige (Negi et Kokhanovsky, 2011; Klingaman *et al.*, 2008; Vavrus, 2007). C'est paramètres de la neige jouent un rôle sur le bilan énergétique terrestre en modifiant l'albédo de surface. Quant au bilan hydrique, l'eau retenue sous forme solide et liquide dans la neige modifie significativement les débits et les événements de crues (Jones et Perkins, 2010; Turcotte *et al.*, 2007). De plus, le couvert nival joue un rôle important dans les mœurs des communautés nordiques tels que la chasse, la pêche et les transports, et affecte aussi les comportements et la survie de la faune arctique (Miller *et al.*, 1975; Putkonen et Roe, 2003). L'étude du couvert nival a donc un impact sur le plan économique (transports en milieux arctiques), environnemental (faune, flore, changements climatiques) et social (mœurs des communautés nordiques). C'est pourquoi il est essentiel de développer et d'améliorer les outils et les connaissances utiles au suivi et à l'étude du couvert nival.

## 1.2 Problématique de l'étude

### 1.2.1 Étude du couvert nival dans les régions nordiques

L'étendue du couvert nival peut atteindre jusqu'à 50% de la superficie de l'Amérique du Nord. Par exemple, l'hiver 2012-2013 a été un des hivers les plus chauds enregistrés en Amérique du Nord et l'étendue du couvert nival a atteint plus de 5.08 millions de km$^2$ (NOAA, 2013). Toutefois, une importante superficie de cette étendue de neige se trouve au-delà du 50$^e$ parallèle. La figure 1.1(a) présente une carte des stations météorologiques du Canada. Les provinces de l'ouest canadien entre le 50$^e$ et 55$^e$ parallèle ont une densité de station météorologique relativement importante mais les provinces de l'est ainsi que les territoires canadiens ont une très faible densité de stations météorologiques.

Les figures 1.1(b) et 1.1(c) présentent la différence de densité de stations météorologiques entre le sud et le nord du Québec. Comme les régions nordiques présentent des conditions climatiques et météorologiques souvent hostiles, il est difficile d'obtenir des informations sur le couvert nival par les méthodes conventionnelles. C'est pourquoi la télédétection micro-ondes passives (MOP) devient un outil indispensable au suivi et à l'étude du couvert nival. Comme le montrent de nombreuses études depuis les trois dernières décennies, la télédétection MOP a un grand potentiel de caractérisation du couvert nival notamment pour l'estimation de l'équivalent en eau de la neige (ÉEN) (e.g. Chang *et al.*, 1982; Walker et Goodison, 1993; Tait, 1998; Pulliainen et Hallikainen, 2001; Kelly *et al.*, 2003; Derksen, 2008; Vachon *et al.*, 2010; Langlois *et al.*, 2012).

### 1.2.2 Étude du couvert nival par télédétection MOP dans le contexte de changements climatiques

Bien que la télédétection MOP soit un outil privilégié pour l'étude du couvert nival, les changements climatiques observés en Amérique du Nord engendrent de nouveaux défis pour l'utilisation de la température de brillance ($T_B$ ) MOP satellitaire. La figure 1.2 présente les températures mesurées à la station météorologique d'Environnement Canada à Sachs Harbour sur l'île Banks de l'archipel canadien (Territoires du Nord-Ouest) pour les années 2003 et 2004.

En octobre 2003, l'île Banks a connu une courte période de redoux où les températures ont dépassé le point de congélation ($> 0^o$C) et simultanément, un événement de pluie (figure 1.2). Les températures sont rapidement redescendues sous le point de congélation créant une épaisse couche de glace dans le couvert nival. Cet événement et son impact ont été étudiés par Grenfell et Putkonen

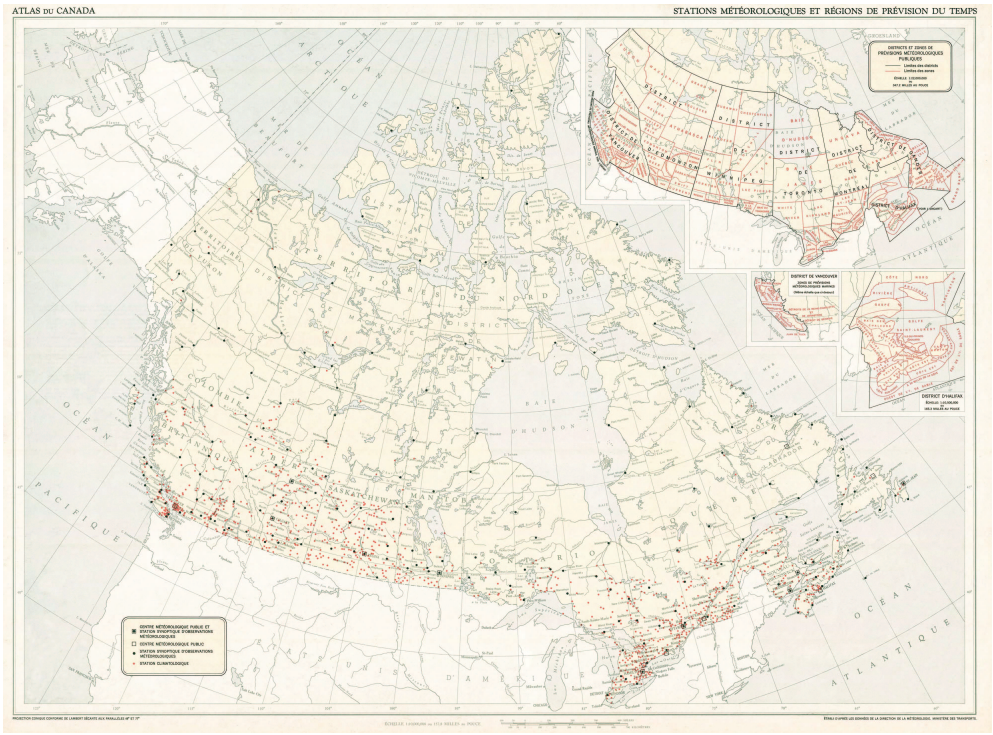


(a)

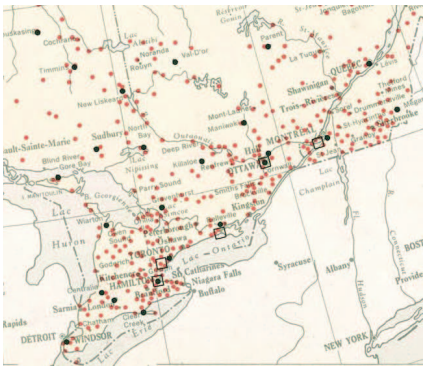


(b)


(c)

Figure 1.1 – Densité des stations météorologiques (points rouges) du Canada (a), du sud du Québec (b) et du nord du Québec (c). Cartes extraites de l'Atlas du Canada (http ://atlas.gc.ca/site/francais/index.html) — Weather station density (red dots) in Canada (a), for southern Quebec (b) and northern Quebec (c). This map was selected from the Atlas of Canada (http ://atlas.gc.ca/site/francais/index.html)

(2008) qui a démontré un nombre de mortalités important de plusieurs espèces animales ongulées. Avec le réchauffement que connaissent plusieurs régions de l'hémisphère nord (Serreze et Barry,

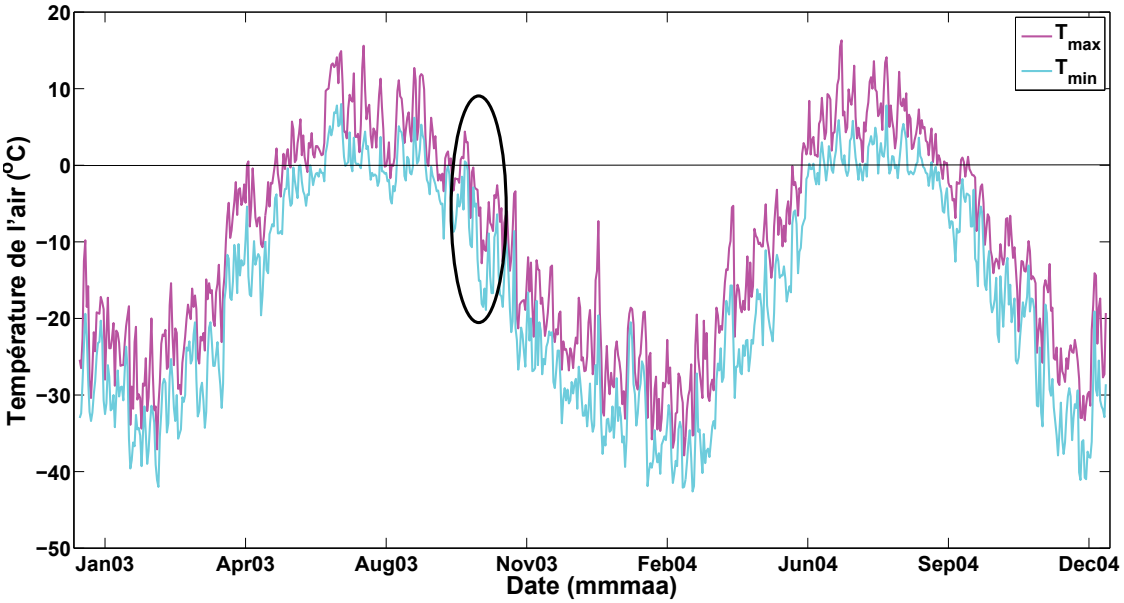


Figure 1.2 – Températures mesurées à la station météorologique d'Environnement Canada de Sachs Harbour (Territoires du Nord-Ouest), Canada (http ://climat.meteo.gc.ca/). L'ellipse noire présente la période durant le mois d'Octobre 2003 où les températures étaient supérieures au point de congélation et ont été suivies d'une chute importante sous le point de congélation créant une croute de glace dans le couvert nival. — Measured temperatures at the Environment Canada weather station in Sachs Harbour (North-West Territories), Canada (http ://climat.meteo.gc.ca/). The black ellipse shows the period where the temperatures were above freezing point and quickly drop below the freezing point which created an ice lens within the snowpack.

2011), ces événements de pluie hivernale ou de périodes de dégel-regel pourraient être de plus en plus fréquents comme le démontrent Liston et Hiemstra (2011).

Les formations de croutes de glace dans le couvert neigeux ont aussi un impact sur le signal MOP satellitaire. Rees *et al.* (2010) ont étudié, au niveau in-situ, un événement de formation de croutes de glace près du lac Daring (Territoires du Nord-Ouest, Canada) survenu en 2007. Ils ont montré que l'introduction d'une croute de glace dans le couvert nival pouvait modifier la $T_B$ de 40 K en H-Pol sans modifier significativement l'épaisseur et l'ÉEN du couvert nival. Ceci introduit donc des biais majeurs dans les modèles et algorithmes de suivi des propriétés du couvert nival utilisant les MOP. C'est pourquoi il est important d'approfondir nos connaissances sur les propriétés géophysiques du couvert nival qui affectent le signal MOP.

### 1.2.3 Étude de la modélisation du TR MOP

Plusieurs modèles de TR MOP existent à ce jour (Armstrong et Brun, 2008). Chaque modèle a ses particularités, défauts et limitations. L'étude approfondie et la modification de ces modèles suite à l'identification de leurs limitations est donc nécessaire. Il a été démontré que le paramètre le plus sensible des différents modèles de TR MOP de la neige est la taille des grains de neige (figure 1.3, Durand *et al.*, 2008; Langlois *et al.*, 2010b; Brucker *et al.*, 2011). Dominé *et al.* (2008) ont démontré que la définition de la taille des grains de neige est très complexe et qu'il est important de développer des instruments de mesure pouvant mesurer un paramètre de taille des grains de neige décrivant avec précision les effets physiques de ce dernier.

Le diamètre maximal ($D_{max}$) du grain de neige a longtemps été utilisé pour définir la taille des grains de neige (Fierz *et al.*, 2009). Étant donné la grande diversité de taille et de forme des grains de neige (dendrites, agrégats, sphères, etc., Fierz *et al.* (2009)) et leur pertinence aux modèles de TR, cette définition est très ambiguë (Aoki *et al.*, 2000; Mätzler, 2002; Taillandier *et al.*, 2007). De plus, les frontières entre les grains de neige sont souvent très difficiles à déterminer (Dominé *et al.*, 2008). Mätzler (2002) a démontré que les paramètres les plus pertinents pour le TR sont le diamètre optique ($D_o$, qui correspond au diamètre d'une sphère de glace ayant des propriétés physiques identiques) et la longueur de corrélation ($p_c$). La longueur de corrélation décrit la taille des particules (la glace) par rapport à leur positionnement dans un milieu (l'air). La longueur de corrélation dépend du positionnement des particules dans le milieu qui est décrit par une fonction d'auto-corrélation. Dans le cas où cette fonction d'auto-corrélation est décrite par une exponentielle, la longueur de corrélation est connue sous la longueur de corrélation exponentielle ($p_{ex}$).

Mätzler (2002) a aussi démontré dans cette même étude que ces deux paramètres sont étroitement liés à la surface spécifique de la neige (SSA) qui est déterminée par le ratio de la surface de glace sur la quantité de masse de la glace. La figure 1.3 illustre la sensibilité des modèles *Microwave Emission Model of Layered Snowpacks* (MEMLS, Wiesmann et Mätzler, 1999), *Dense Media Radiative Transfer - Multi-Layer* (DMRT-ML, Picard *et al.*, 2013) et *Helsinki University of Technology* (HUT, Pulliainen *et al.*, 1999) à la surface spécifique de la neige (SSA), paramètre pouvant être lié à longueur de corrélation utilisé dans le modèle MEMLS ($p_c$), le rayon optique utilisé dans DMRT-ML ($R_o$) et au diamètre optique ($D_o$) utilisé dans le modèle HUT par les équations suivantes :

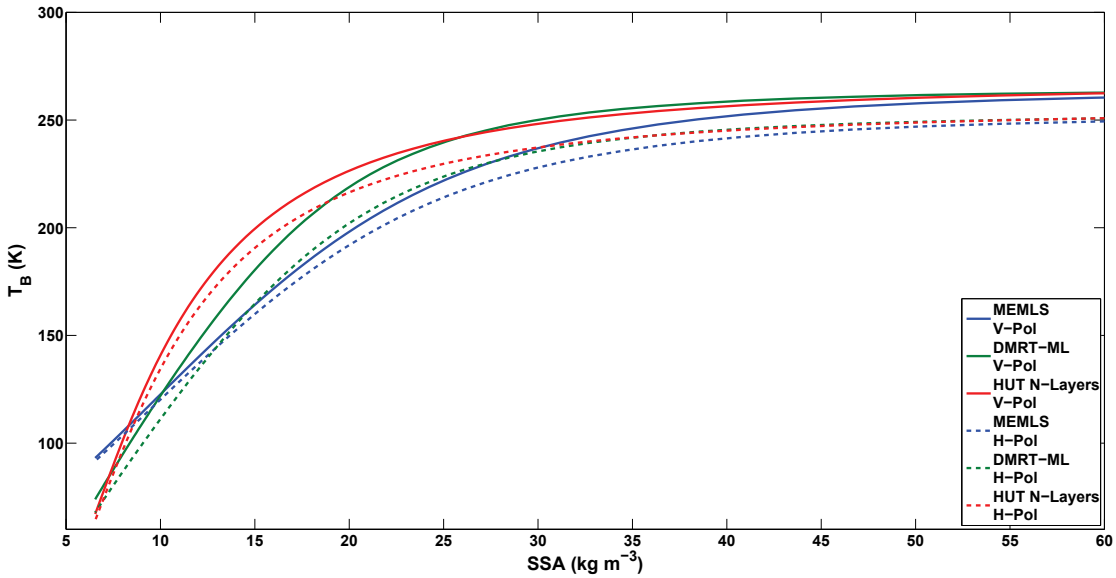


Figure 1.3 – Sensibilité des modèles MEMLS, DMRT-ML et HUT à la SSA. Les paramètres de neige pour ces simulations sont : 1 couche, épaisseur = 100 cm, $\rho_{neige} = 250$ kg m$^{-3}$, $T_{neige} = 260K$. C'est simulations ont été faites avec les paramètres de sol du l'article Montpetit *et al.* (En Revision) et des paramètres d'optimisation de la neige des articles Roy *et al.* (2013) (HUT et DMRT-ML) et Montpetit *et al.* (2013) (MEMLS) — Sensitivity of the models MEMLS, DMRT-ML and HUT to SSA. The snow parameters used for these simulations are : snow depth = 100 cm, $\rho_{snow} = 250$ kg m$^{-3}$, $T_{snow} = 260K$. These simulations were done with the soil parameters described by Montpetit *et al.* (En Revision) and the snow optimsations parameters of Roy *et al.* (2013) (HUT et DMRT-ML) and Montpetit *et al.* (2013) (MEMLS).

$$p_c = \frac{4}{3}\frac{(1-\nu)}{\rho_{ice} SSA} \tag{1.2.1}$$

$$D_o = 2R_o = \frac{6}{\rho_{ice} SSA} \tag{1.2.2}$$

où $\rho_{ice}$ est la densité de la glace pure (917 kg m$^{-3}$) et $\nu$ est la fraction de glace définie par : $\nu = \rho_{snow}/\rho_{ice}$ Il existe différentes méthodes afin de mesurer la SSA telles la stéréologie (Matzl et Schneebeli, 2010), la mesure d'adsorption du méthane (Dominé *et al.*, 2001), la micro-tomographie par rayons X (Chen et Baker, 2010) et des méthodes optiques (Matzl et Schneebeli, 2006; Painter *et al.*, 2007; Gallet *et al.*, 2009; Langlois *et al.*, 2010a; Arnaud *et al.*, 2011). Malgré le fait que les méthodes optiques soient légèrement moins précises que les autres méthodes, elles ont l'avantage de permettre l'acquisition rapide de données directement sur le terrain.

Les modèles MEMLS, DMRT-ML et HUT sont des modèles multicouches qui simulent la température de brillance ($T_B$ ) MOP du couvert nival à partir de données géophysiques de la neige telles que l'épaisseur, la température, la densité, la teneur en eau et la taille des grains de neige. Le modèle HUT est un modèle semi-empirique qui simule l'absorption et la réflexion aux interfaces de la neige par les équations physiques du TR MOP et qui simule la diffusion de la $T_B$ par la neige par des équations empiriques. Les modèles DMRT-ML et MEMLS sont des modèles physiques qui simulent tous les paramètres du TR MOP par des équations et des approximations des équations physiques. DMRT-ML utilise un schéma du TR MOP à multiples flux (64 flux) dans un plan bidimensionnel (2D) et MEMLS utilise un schéma à 6 flux dans un espace tridimensionnel (3D).

Un phénomène qui affecte significativement la modélisation du TR MOP du couvert nival est la présence de croutes de glace (Grody, 2008).Grody (2008) a démontré l'effet des croutes de glace en surface du couvert nival sur le TR du signal MOP en modélisant le signal de la neige à l'aide du modèle DMRT et ensuite en modélisant ce signal à travers une croute de glace. Malgré le fait que la modélisation soit entièrement physique, cette approche est limitée à des croutes de glace en surface du couvert nival. Comme il est fréquent d'observer des croutes de glace sous la surface du couvert nival et même à la surface du sol (Putkonen et Roe, 2003), il est important de développer un modèle qui peut tenir compte du positionnement à l'intérieur du couvert nival.

Lemmetyinen *et al.* (2010a) ont utilisé le modèle TR HUT afin d'estimer l'effet et les biais des croutes de glace sur la modélisation du signal MOP. De plus, Rees *et al.* (2010) et Lemmetyinen *et al.* (2010b) ont utilisé les modèles HUT et MEMLS afin de simuler les effets des croutes de glace sur le signal MOP du couvert nival et ont comparé les performances de ces deux modèles à l'aide de mesures acquises sur le terrain. Ils ont démontré que les deux modèles pouvaient reproduire l'effet relatif qu'avaient les croutes de glace avec une certaine précision (5 K < RMSE < 20 K dépendamment de la fréquence et polarisation). Toutefois, pour simuler les croutes de glace à l'aide de MEMLS, ils ont dû considérer les couches de glace comme étant des couches de neige très dense. Or, la théorie des MOP suggère qu'une couche de neige diffuse le signal MOP tandis qu'une croute de glace pure absorbe et réfléchit le signal MOP. L'équation 1.2.3 présente le calcul de la diffusion par l'approximation de Born améliorée (IBA, Mätzler, 1998) utilisée dans MEMLS dans le cas simplifié où les grains de neige sont considérés sphériques seulement.

$$\gamma_s = \frac{3p_c^3k^4}{32}\nu(1-\nu)\left|\frac{(\epsilon_2-\epsilon_1)(2\epsilon_{eff}+\epsilon_1)}{2\epsilon_{eff}+\epsilon_2}\right|^2 \tag{1.2.3}$$

où $\gamma_s$ est le coefficient de diffusion, $p_c$ est la longueur de corrélation, $k$ est le nombre d'onde, $\nu$ la fraction de glace, $\epsilon_1$ est la constante diélectrique du milieux hôte (l'air), $\epsilon_2$ est la constante diélectrique des particules du milieux (sphères de glace) et $\epsilon_{eff}$ est la constante diélectrique effective du milieux (la neige) calculée par l'IBA. Avec l'équation 1.2.3, l'on remarque que le seul moyen d'obtenir les conditions de diffusion de la glace, i.e. une diffusion nulle, il est nécessaire de simuler une couche ayant la densité de la glace pure (917 kg m$^{-3}$, i.e. $\nu = 1$) et/ou une longueur de corrélation nulle. Ainsi, les simulations de Rees *et al.* (2010) et Lemmetyinen *et al.* (2010b) ne sont pas physiquement adéquate pour la glace pure.

La figure 1.4 présente la sensibilité de la $T_B$ à 10.7, 19 et 37 GHz du modèle MEMLS à l'épaisseur d'une croute de glace placée en surface du couvert de neige. La croute de glace a été obtenue en simulant une couche de neige d'une densité de 917 kg m$^{-3}$, d'une température de 260 K et d'une longueur de corrélation de 0 mm. La figure 1.4 montre que lorsque l'épaisseur des croutes de glace est inférieure au quart de la longueur d'onde ($\lambda/4$), le modèle MEMLS simule des effets de cohérences qui sont dus à des réflexions multiples du rayonnement MOP à l'intérieur des croutes de glace qui causent des interférences constructives et destructives. On remarque aussi que pour ce type de neige, le signal peut être atténué de plus de 90 K à 37 GHz en H-Pol. Contrairement au modèle MEMLS, les modèles HUT et DMRT-ML ne modélisent pas ces effets de cohérences. Il est donc important de développer un modèle de TR radiatif des MOP capable de modéliser une croute de glace à l'intérieur du couvert nival avec la physique adéquate.

Une autre incertitude du TR du signal MOP du couvert nival est la contribution du sol. Prigent *et al.* (2000) et Wigneron *et al.* (2011) ont fait des études afin de modéliser l'émissivité MOP du sol pour les basses fréquences mais la modélisation du sol aux fréquences plus élevées ($\geq$ 10 GHz) demeure peu documentée. Wegmüller et Mätzler (1999) ont tout de même développé un modèle d'émissivité MOP du sol pour une gamme de fréquences allant de 1 à 100 GHz. Ce modèle est implémenté dans le modèle de TR des MOP HUT. Toutefois, ce modèle demeure empirique et adapté aux mesures in-situ utilisées lors de cette étude. Il est donc nécessaire de développer un modèle d'émissivité du sol pour les fréquences plus élevées adapté à différentes conditions de mesures et mieux adapté aux fréquences utilisées pour l'étude de la neige. La figure 1.5 présente le schéma multicouche utilisé dans le cadre de cette thèse.

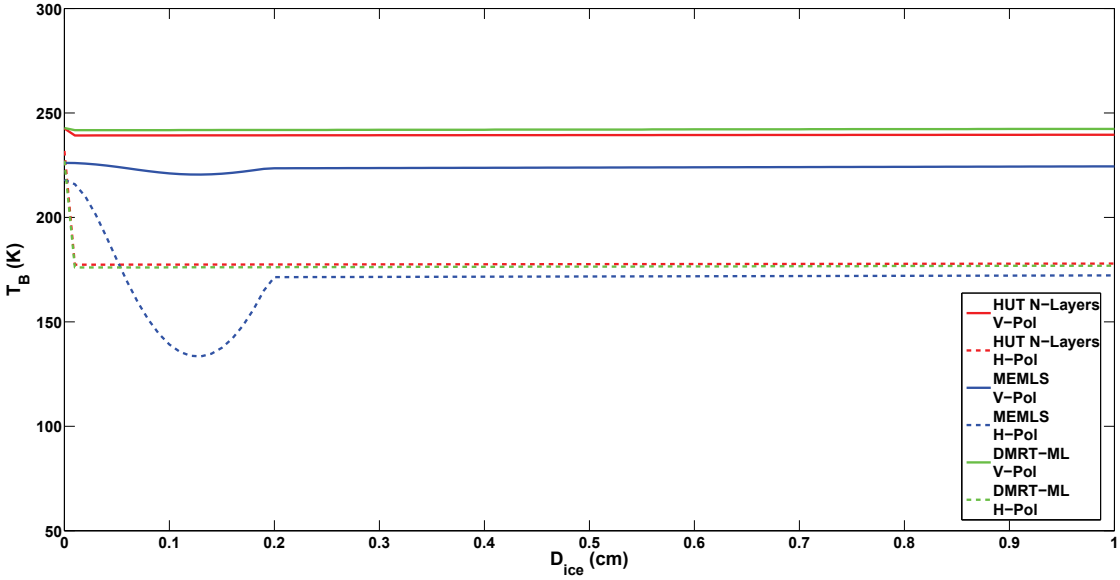


Figure 1.4 – Sensibilité des modèles MEMLS, DMRT-ML et HUT à 37 GHz à l'épaisseur des croutes de glaces placées en surface d'un couvert nival monocouche d'une densité de 250 kg $m^{-3}$, une température de 260 K, une épaisseur de 100 cm et une SSA de 26.2 $m^2$ $kg^{-1}$. — Sensitivity of the MEMLS, DMRT-ML and HUT models at 37 GHz to the ice lens thickness present at the surface of a one layer snowpack of density = 250 kg $m^{-3}$, temperature = 260 K, snow depth = 100 cm and SSA = 26.2 $m^2$ $kg^{-1}$.

## 1.3 Objectifs et hypothèses

L'objectif général de cette thèse est de développer une meilleure compréhension de la modélisation du TR MOP des neiges saisonnières de l'Amérique du Nord (régions sub-arctiques et arctiques). Cette étude a pour but de mieux comprendre et caractériser les effets sur l'émission MOP de la stratigraphie du couvert nival, en particulier, détecter des croutes de glace par télédétection MOP. Avec une amélioration de la modélisation MOP, il sera aussi possible d'améliorer les modèles et algorithmes utilisant les MOP pour détecter l'ÉEN et l'épaisseur de neige dans des conditions plus diversifiées (ex. : présence de croutes de glace).

Ainsi, l'amélioration de la modélisation du TR MOP de la neige comporte donc trois objectifs spécifiques :

a) Développer des instruments de mesure de la taille des grains de neige précis et valider ces mesures dans un modèle MOP.

b) Implémenter et valider un module de TR des MOP des croutes de glace dans le couvert nival

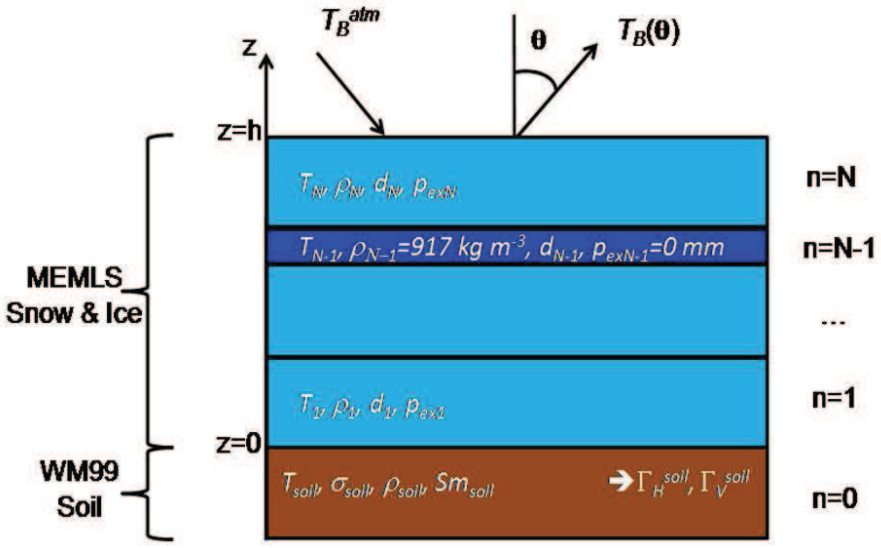


Figure 1.5 – Schéma de la modélisation multicouche du sol, de la neige et de la glace utilisé dans cette étude. — The multi-layer modeling scheme used in this study.

pour en déduire un indice de détection des croutes de glace par satellite.

c) Implémenter, calibrer et valider un modèle d'émissivité du sol pour les hautes fréquences (> 10 GHz) afin d'améliorer l'estimation de la contribution du sol au TR du couvert nival.

Ces objectifs spécifiques reposent sur les hypothèses suivantes :

a) Mätzler (2002) mentionne que les paramètres adéquats pour simuler la $T_B$ MOP est le diamètre optique ($D_o$) et la longueur de corrélation ($p_c$) qui sont tous deux liés à la SSA. La SSA serait donc un paramètre pertinent pour améliorer la précision des simulations des $T_B$ MOP.

b) Rees *et al.* (2010), Lemmetyinen *et al.* (2010a) et Grody (2008) ont démontré que de considérer certains effets des croutes de glace dans les simulations des $T_B$ sans utiliser la physique du TR MOP adéquat ou les bonnes propriétés géophysiques de la glace, améliore la précision des simulations. L'utilisation de la physique appropriée et des paramètres géophysiques mesurés des croutes de glace pourra améliorer davantage les résultats des simulations des $T_B$ pour des couverts de neige ayant des croutes de glace.

c) Wegmüller et Mätzler (1999) ont démontré qu'il est possible de calibrer un modèle d'émission MOP du sol pour différents types de sol. Toutefois, il a été démontré par Roy *et al.* (2013) que le modèle calibré par Wegmüller et Mätzler (1999) nécessite des ajustements pour les sites de l'Arctique canadien. En calibrant un tel modèle sur des sites de l'Arctique canadien pour mieux estimer la contribution provenant du sol à la $T_B$ du couvert nival, il sera possible d'améliorer les résultats de la modélisation des $T_B$ MOP.

d) Grenfell et Putkonen (2008) ont démontré que les événements sévères de pluies hivernales formant d'épaisses croutes de glace ont un impact sur le signal MOP en particulier, le rapport de polarisation (PR). En étudiant la sensibilité du PR aux différents paramètres des croutes de glace, il sera donc possible de développer un indice de détection des croutes de glace pas télédétection MOP.

## 1.4 Méthodologie et organisation du manuscrit

La figure 1.6 présente l'organigramme méthodologique du travail de cette thèse. Le travail se divise donc sous quatre grands thèmes. Ces thèmes correspondent aussi aux différents chapitres de cette thèse. Avant de traiter de ces thèmes, le chapitre 2 présentera les différents jeux de données in-situ, satellitaires et de modèles de réanalyses atmosphériques utiles au travail de recherche de cette thèse. Par la suite, le premier grand thème étudié sera le TR MOP de la neige. Dans ce chapitre, les différents instruments de mesures de la SSA développés lors de cette étude ainsi que leur validation seront présentés. De plus, dans ce chapitre, les résultats de l'analyse de l'utilisation de la SSA pour la modélisation de la $T_B$ MOP seront présentés. Le deuxième thème présenté du travail sera l'étude du TR MOP du sol. Cette section présentera les modèles, données, théories, analyses et résultats reliés à l'amélioration de la modélisation de l'émissivité du sol. Dans cette section la modélisation de l'émissivité du sol gelé retrouvé surtout dans les zones sub-arctiques et arctiques du Canada sera traitée. Le troisième thème étudié sera le TR MOP de la glace. Les résultats de l'implémentation d'un module TR MOP de la glace pure dans MEMLS seront présentés dans ce chapitre. Le dernier thème étudié dans cette thèse sera le développement d'un indice de détection des croutes de glace par télédétection MOP satellitaire. Dans ce chapitre, la théorie et les travaux menant au développement d'un indice de détection des croutes de glace seront présentés. Dans chacune de ces sections, les contributions scientifiques (articles et présentations dans des conférences) seront mises en évidence. Les contributions directes liées à cette thèse ainsi que celles des co-auteurs à ces différents travaux seront aussi précisées. De plus, en annexe seront présentés différents travaux scientifiques, effectués durant les études de cette thèse, qui se rapprochent des différents thèmes de

cette thèse mais qui ne sont pas directement liés aux travaux de la thèse. Les contributions faites à ces travaux dans le cadre de cette thèse seront précisées.

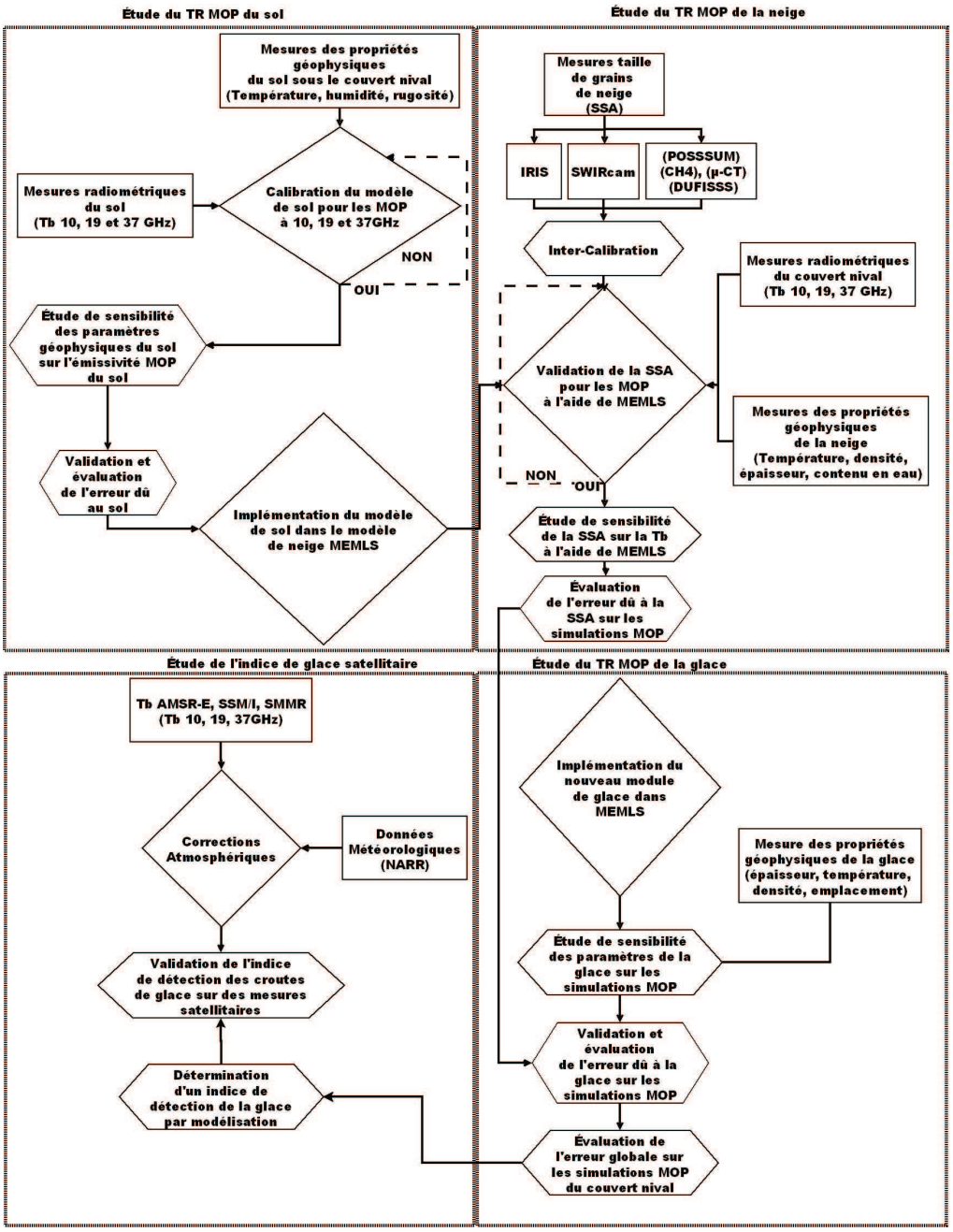


Figure 1.6 – Organigramme méthodologique de l'étude de la thèse. — Methodological flowchart of this thesis.

Comme la partie la plus originale de la thèse est l'inclusion et l'étude des croutes de glace dans la modélisation du TR MOP du couvert nival, le choix du modèle est très importante. Afin de faciliter l'analyse des effets des croutes de glace sur la $T_B$ , un modèle physique est plus adéquat étant donné qu'il est davantage possible d'expliquer les erreurs provenant des paramètres de la neige. De plus, comme les croutes de glace observées ont souvent une épaisseur inférieure au quart de la longueur d'onde utilisé pour l'étude du couvert nival, les effets de cohérences sont présents et un phénomène important à considérer. C'est pourquoi le modèle MEMLS a été sélectionné puisqu'il satisfait ces critères.

Un aspect original des travaux de cette thèse a été l'utilisation d'une grande gamme de mesures géophysiques et radiométriques in-situ précises et objectives (voir section 2) pour valider le modèle MEMLS. Le développement de la caméra mesurant la réflectance dans le proche infrarouge (1.3 $\mu$m) n'a jamais été réalisé auparavant. Ceci a permis d'obtenir de l'information plus précise sur la taille des grains de neige que les photographies infrarouges traditionnelles. Très peu d'études du TR MOP possèdent une telle base de données. De plus, pour la première fois, le TR MOP des croutes de glace à l'intérieur du couvert nival a été validé avec la physique adéquate ainsi que leurs propriétés géophysiques mesurées in-situ à partir d'expériences originales d'excavation (mesures radiométriques avec et sans croutes de glace). La création de croutes de glace artificielles afin de mieux contrôler l'environnement de mesures et acquérir une plus grande base de données de croutes de glace est aussi une originalité du travail. Une nouvelle étude de sensibilité du PR aux croutes de glace (configuration multiples des croutes dans différents couvert de neige) a été réalisée grâce à cette modélisation validée des effets des croutes de glace. Ce travail, intégrant l'étude du sol, de la neige et de la glace dans la neige apporte ainsi une contribution originale à l'étude du TP MOP du couvert nival.

# 2 Sites d'étude et données expérimentales

Les travaux de cette thèse incluent de multiples sources de données provenant de différents capteurs satellitaires, modèles et mesures de campagnes de terrain. La Figure 2.1 présente les sites de mesures ainsi que les pixels satellitaires choisis pour les régions canadiennes.

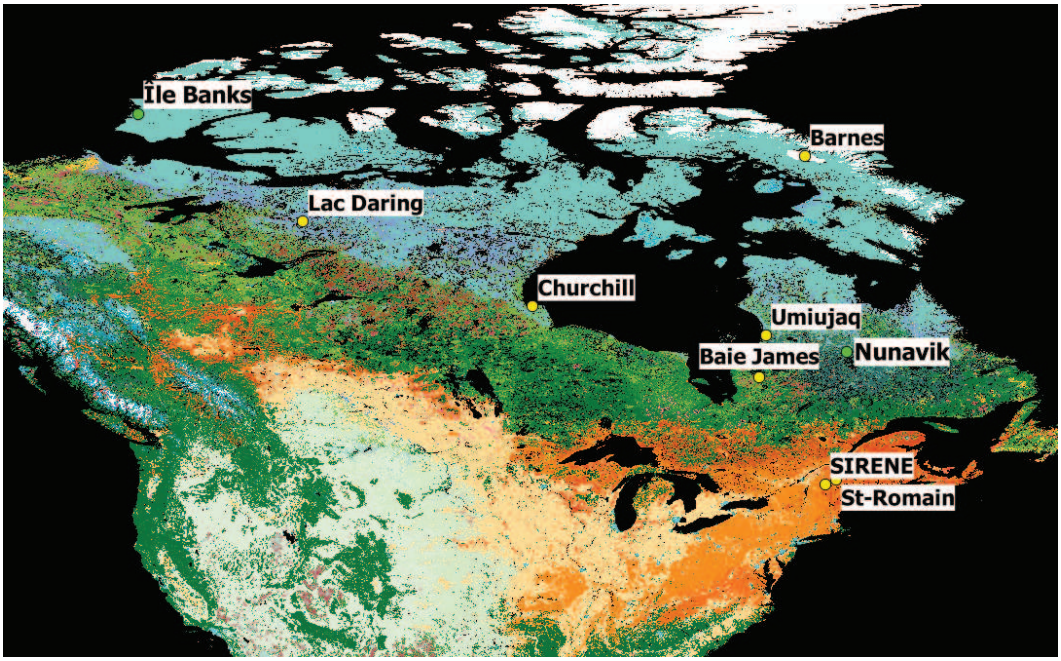


Figure 2.1 – Carte des sites d'acquisition de données in-situ (jaune) et des sites de validation satellitaire (vert) pour les régions canadiennes.

## 2.1 Mesures géophysiques in-situ du sol gelé, de la neige et de la glace

Les données géophysiques et radiométriques du sol gelé ont été acquises lors de deux campagnes de terrain par l'équipe neige du Centre d'Applications et de Recherches en Télédétection (CARTEL) de l'Université de Sherbrooke, des collaborateurs de l'Institut National de Recherche Scientifique (INRS) à Québec (Canada) et du Laboratoire de Glaciologie et de Géophysique de l'Environnement (LGGE) à Grenoble (France). La première campagne terrain a eu lieu dans la région de la Baie James (Québec, Canada) lors de l'hiver 2012-2013 (point Baie James, Figure 2.1). La deuxième campagne a eu lieu à Umiujuaq (Québec, Canada) lors de l'hiver 2013-2014 (point Umiujuaq, Figure 2.1). Les mesures radiométriques comprennent des mesures de $T_B$ à 10.7, 19 et 37 GHz en V-Pol et H-Pol du sol découvert. De plus, les mêmes données radiométriques ont été acquises pour la neige couvrant ces sols. Aussi, lors de ces deux campagnes, des mesures de températures de sol à différentes profondeurs ont été acquises ainsi que des données géophysiques de la neige à différentes profondeur du couvert soit : l'épaisseur de la couche de neige (en cm), la température (en K), la densité (en kg $m^{-3}$) et la taille des grains de neige (section 3.1). Les mesures de sol gelé seront davantage détaillées dans la section 4 tandis que les mesures de neige seront détaillées dans la section 6.3.

Lors de multiples campagnes de terrain de l'équipe neige du CARTEL, des données géophysiques et radiométriques de la neige ont été acquises. En mars 2011, l'équipe du CARTEL composée des professeurs Alexandre Langlois et Alain Royer, ainsi que de Partick Cliche et Miroslav Chum de l'Université de Sherbrooke, acompagnés par les docteurs Ghislain Picard et Florent Dupont du LGGE ont acquis des mesures de neige sur la calotte glacière Barnes (île de Baffin, Nunavut, Canada ; point Barnes, Figure 2.1). Les mesures de taille de grains de neige (SSA) acquises à l'aide des instruments IRIS et SWIRcam (section 3.1) ont été traitées dans le cadre de cette thèse afin de calibrer ces deux instruments pour la mesure précise d'un paramètre de taille des grains de neige. Ces données sont détaillées dans la section 3.1.

De plus, lors de l'hiver 2010-2011, une campagne terrain près de la municipalité de St-Romain (Québec, Canada ; point St-Romain, Figure 2.1) a été entreprise par l'équipe neige du CARTEL composée des professeurs Alain Royer et Alexandre Langlois, de Patrick Cliche, d'Alexandre Roy et moi-même. Des mesures radiométriques du couvert de neige ont été acquises à 10.7, 19 et 37 GHz en V-Pol et H-Pol ainsi que des mesures géophysiques de la neige. De plus, des croutes de glace ont été observées à la fin du mois de janvier suite à un court épisode de dégel-regel. Des mesures d'épaisseur et de position de ces croutes de glace ont été acquises. Ces données ont été traitées dans le cadre de cette thèse et sont détaillées dans la section 5.

Durant les hivers 2010 à 2013, des mesures géophysiques et radiométriques de la neige ont été acquises à la station SIRENE du CARTEL sur le campus principal de l'Université de Sherbrooke (point SIRENE, Figure 2.1). Durant l'hiver 2010-2011, afin d'obtenir des mesures de couvert nival avec croutes de glace, des croutes de glace artificielles ont été créées sur une partie du couvert de neige à la station SIRENE. Cette expérience et les mesures acquises dans le cadre de cette thèse sont décrites en détail dans la section 5.

Durant l'hiver 2009-2010, dans le cadre du programme *Cold Regions Hydrology High-Resolution Observatory* (CoReH2O) des Agences Spatiales Européenne (ESA) et Canadienne (ASC), une campagne terrain intensive dirigée par Environnement Canada et composée d'une équipe de chercheurs provenant des plusieurs pays différents a été réalisée à Churchill, au Manitoba, Canada (point Churchill, Figure 2.1). Comme dans la section précédente, des données géophysiques et radiométriques de la neige ont été acquises par l'équipe du CARTEL et d'Environnement Canada pendant quatre périodes intensives entre janvier et avril 2010. Les données géophysiques ont été traitées dans le cadre de cette thèse par l'équipe neige du CARTEL. Les données radiométriques utilisées dans ce travail ont été traitées et fournies par Environnement Canada. Des croutes de glace ont été observées dans le couvert de neige de certains de ces sites. Ces données sont détaillées dans

l'article de Derksen *et al.* (2012) et dans la section 5 de ce travail.

Lors de l'hiver 2007, une équipe d'Environnement Canada a acquis des mesures radiométriques et géophysiques de la neige au Lac Daring, Territoires du Nord-Ouest, Canada (point Lac Daring, Figure 2.1). Les mesures géophysiques de la neige sont identiques aux mesures acquises lors des campagnes de terrains décrites dans les sections précédentes, à l'exception de la taille des grains de neige. Ce dernier paramètre a été mesuré par évaluation visuelle où le plus grand diamètre des grains visible au microscope sur une plaque millimétrique a été associé à la taille des grains de neige des différentes couches. Lors de cette campagne, l'équipe d'Environnement Canada a été témoin d'un événement de pluie hivernale qui a laissé une mince couche de glace à la surface du couvert nival. Ces mesures ainsi que la campagne sont décrites dans l'article de Rees *et al.* (2010) ainsi que dans la section 5 de ce travail.

Le tableau 2.1 présente les différentes mesures utilisées pour chacune des campagnes de mesures dans le cadre de cette thèse.

## 2.2 Données satellitaires

Les données satellitaires utilisées dans cette thèse sont des données MOP disponibles depuis 1978. Le tableau 2.2 présente les caractéristiques des différents capteurs et canaux utilisés pour ce travail.

Les données ont été acquises du *National Snow and Ice Data Center* (NSIDC et Center, 2014). Elles ont aussi été ré-échantillonnées sur le EASE-Grid du NISDC. Ce ré-échantillonnage a permis d'étudier une même région pour la période de 1978 à 2011 sans se soucier des différences géographiques des empreintes mesurées au sol quotidiennement. Le premier site choisi se trouve au Nunavik (Québec, Canada ; point Nunavik, Figure 2.1). Ce site a été choisi particulièrement parce qu'il présentait un faible indice foliaire (Roy, 2014) et que l'occupation du sol est similaire au site où le plus grand nombre de profils de neige a été mesuré dans le cadre de cette thèse (Churchill, Figure 2.1). Le deuxième pixel choisi se situe sur l'île Banks, dans les Territoires du Nord-Ouest. Ces données satellitaires sont présentées et analysées dans la section 6.4.

Tableau 2.1 – Données géophysiques et radiométriques du sol, de la neige et de la glace utilisées dans le cadre de cette thèse. — Soil, snow and ice geophysical data used in this thesis.

| Site | Date | $f$ (GHz) | Données sol | Données neige | Données glace |
|---|---|---|---|---|---|
| Lac Daring | Avr 2007 | 19, 37 | $T_{sol}$ | $T_B$ , $T_{neige}$, $\rho_{neige}$, $h_{neige}$, $d_{neige}$, $D_{max}$ | $T_B$ , $d_{glace}$, $h_{glace}$ |
| Churchill | Jan, Feb, Mar, Avr 2010 | 19, 37 | $T_{sol}$ | $T_B$ , $T_{neige}$, $\rho_{neige}$, $h_{neige}$, $d_{neige}$, $SSA$ | $T_B$ , $d_{glace}$, $h_{glace}$ |
| Barnes | Mar 2011 | | | $SSA$ | |
| St-Romain | Jan, Feb, Mar 2011 | 19, 37 | $T_{sol}$ | $T_B$ , $T_{neige}$, $\rho_{neige}$, $h_{neige}$, $d_{neige}$, $SSA$ | $T_B$ , $d_{glace}$, $h_{glace}$ |
| SIRENE | Hivers 2011-2013 | 19, 37 | $T_{sol}$ | $T_B$ , $T_{neige}$, $\rho_{neige}$, $h_{neige}$, $d_{neige}$, $SSA$ | $T_B$ , $d_{glace}$, $h_{glace}$ |
| Baie James | Jan, Feb, Mar 2013 | 19, 37 | $T_B$ , $T_{sol}$ | $T_B$ , $T_{neige}$, $\rho_{neige}$, $h_{neige}$, $d_{neige}$, $SSA$ | $T_B$ , $d_{glace}$, $h_{glace}$ |
| Umiujaq | Jan 2014 | 19, 37 | $T_B$ , $T_{sol}$ | $T_B$ , $T_{neige}$, $\rho_{neige}$, $h_{neige}$, $d_{neige}$, $SSA$ | $T_B$ , $d_{glace}$, $h_{glace}$ |

Tableau 2.2 – Capteurs et canaux des données satellitaires utilisées dans le cadre de cette thèse. Toutes les données satellitaires ont été acquises en V-Pol et H-Pol. La résolution spatiale est celle de la EASE-Grid du NSIDC (NSIDC et Center, 2014). — Sensors and channels of the satellite data used in this thesis. All the data was acquired in V-Pol and H-Pol. The spatial resolution corresponds to the resolution of the EASE-Grid of the NSIDC (NSIDC et Center, 2014)

| Capteur | Fréquences (GHz) | Angle d'incidence | Résolution spatiale (km) | Années |
|---|---|---|---|---|
| SMMR | 10.69 ; 18.0 ; 37.0 | 51 $^o$ | 25 | 1978-1987 |
| SSM/I | 19.35 ; 37.0 | 53 $^o$ | 25 | 1987-2002 |
| AMSR-E | 10.65 ; 18.7 ; 36.5 | 55 $^o$ | 25 | 2002-2011 |

## 2.3 Données de réanalyses atmosphériques

Afin de comparer les mesures radiométriques satellitaires aux signaux simulés à la surface du couvert nival, des corrections atmosphériques ont dû être apportées aux signaux satellitaires. Les don-

nées atmosphériques ont été acquises des données de réanalyses atmosphériques du modèle *North American Regional Analysis* (NARR, NOAA (2014)). Elles consistent en mesures d'eau précipitable de 29 couches atmosphériques. Par la suite, à l'aide de régressions linéaires développées par Roy (2014) il a été possible de calculer la transmissivité de l'atmosphère ($\tau_{atm}$) et la $T_B$ descendante de l'atmosphère ($T_{B\downarrow}$). Ces données ainsi que les corrections atmosphériques apportées aux signaux satellitaires sont présentées dans la section 6.4.

# 3 Résultats : Étude de la paramétrisation de la neige

## 3.1 Instruments de mesures de la SSA

Afin d'améliorer la compréhension du TR à travers le couvert neigeux, de nouveaux instruments de mesure de la taille des grains de neige ont dû être développés afin d'améliorer la précision de cette mesure. Plusieurs études (Durand *et al.*, 2008; Brucker *et al.*, 2011) ont démontré que ce paramètre est le plus sensible dans la modélisation du signal MOP du couvert nival. De plus, d'autres études ont démontré qu'il était difficile de bien caractériser la taille des grains de neige par les méthodes conventionnelles (Fierz *et al.*, 2009; Dominé *et al.*, 2008). Des études récentes (Gallet *et al.*, 2009; Matzl et Schneebeli, 2006) ont démontré qu'il était possible d'obtenir la SSA de la neige, un paramètre objectif et plus précis pour la caractérisation de la taille des grains de neige, à partir de mesures de réflectométrie IR. C'est pourquoi un des objectifs secondaires de la thèse est de développer des instruments précis qui permettent d'utiliser la réflectance IR afin d'extraire la SSA de la neige. Ce travail a été publié dans la revue *Journal of Glaciology* (Montpetit *et al.*, 2012) et a aussi été présenté lors de la conférence *Eastern Snow Conference 2011* à Montréal (Québec), Canada. Cette étude a permis le développement des instruments *InfraRed Integrating Sphere* (IRIS) et de la toute nouvelle *Short Wave InfraRed Camera* (SWIRcam) qui permettent d'extraire la SSA de la neige avec précision (précision de 10 % sur la SSA). L'IRIS a été monté par l'équipe du CARTEL à partir du concept de l'instrument DUal Frenquency Integrating Sphere for Snow SSA (DUFISSS) et de différentes pièces manufacturées par des entreprises spécialisées (Montpetit *et al.*, 2012). Par la suite, dans le cadre des travaux de cette thèse, l'étalonnage et la validation à été effectuée afin d'obtenir des mesures précises de la SSA par l'auteur principal avec l'aide des co-auteurs de l'article Montpetit *et al.* (2012). Dans le cas de la SWIRcam, elle a été acquise et adaptée par l'équipe du CARTEL afin de faciliter la prise de mesures sur le terrain. Le protocole de mesures ainsi que l'étalonnage et la validation ont été complété par l'auteur principal avec l'aide des co-

auteurs de l'article Montpetit *et al.* (2012). De plus, pour la première fois, des photographies de réflectance IR acquises à l'aide de la SWIRcam ont pu être reliées par modélisation physique à la SSA de la neige, ce qui n'avait pas été réussi auparavant par Langlois *et al.* (2010b) et Matzl et Schneebeli (2006).

### 3.1.1 Article : New shortwave infrared albedo measurements for snow specific surface area retrieval

La caractérisation de la taille des grains de neige, son évolution verticale et temporelle est très importante pour l'amélioration et la validation de modèles de TR (optique et micro-ondes). Dans cet article, deux méthode sont décrites, une active et une passive, utilisant la réflectance dans le proche infrarouge ($\approx$ 1.3 $\mu$m) afin de mesurer la surface spécifique de la neige (SSA) in-situ. Une nouvelle approche utilisant une caméra dans le proche infrarouge est présentée. Cette méthode est comparée et validée avec la méthode de réflectométrie utilisant une sphère intégrante (InfraRed Integrating Sphere, IRIS). Une précision de 10% et une bonne reproductibilité dans la mesure de la SSA a été obtenu avec l'IRIS sur des échantillons de neige ayant une densité supérieure à 200 kg m$^{-3}$. Les mesures avec l'IRIS ont été validées avec des mesures du DUal Frequency Integrating Sphere for Snow SSA (DUFISSS) et de la micro-tomographie à rayon-X. La nouvelle caméra infrarouge démontre une plus grande sensibilité à la SSA lorsque comparée aux caméras infrarouge utilisant des longueurs d'ondes plus courtes. Le tableau 3.1 présente les principales statistiques de cette étude.

Tableau 3.1 – RMSE, coefficient de corrélation et précision des instruments IRIS et SWIRcam. — RMSE, correlation coefficients and SSA accuracy of IRIS and the SWIRcam.

| Instrument | RMSE (m$^2$ kg$^{-1}$) | R$^2$ | Précision |
|---|---|---|---|
| IRIS | 3.83 | 0.99 | 10% |
| SWIRcam | 3.45 | 0.82 | 10% |

# Instruments and Methods

# New shortwave infrared albedo measurements for snow specific surface area retrieval

B. MONTPETIT,[1] A. ROYER,[1] A. LANGLOIS,[1] P. CLICHE,[1] A. ROY,[1]
N. CHAMPOLLION,[2] G. PICARD,[2] F. DOMINE,[2] R. OBBARD[3]

[1]*Centre d'Applications et de Recherche en Télédétection (CARTEL), Université de Sherbrooke, Sherbrooke, Québec, Canada*
*E-mail: benoit.montpetit2@usherbrooke.ca*
[2]*Laboratoire de Glaciologie et Géophysique de l'Environnement, CNRS/Université Joseph Fourier – Grenoble I, Grenoble, France*
[3]*Thayer School of Engineering, Dartmouth College, Hanover, NH, USA*

**ABSTRACT. Snow grain-size characterization, its vertical and temporal evolution is a key parameter for the improvement and validation of snow and radiative transfer models (optical and microwave) as well as for remote-sensing retrieval methods. We describe two optical methods, one active and one passive shortwave infrared, for field determination of the specific surface area (SSA) of snow grains. We present a new shortwave infrared (SWIR) camera approach. This new method is compared with a SWIR laser-based system measuring snow albedo with an integrating sphere (InfraRed Integrating Sphere (IRIS)). Good accuracy (10%) and reproducibility in SSA measurements are obtained using the IRIS system on snow samples having densities greater than 200 kg m$^{-3}$, validated against X-ray microtomography measurements. The SWIRcam approach shows improved sensitivity to snow SSA when compared to a near-infrared camera, giving a better contrast of the snow stratigraphy in a snow pit.**

## INTRODUCTION

Snowpack state variables such as depth, density, wetness, temperature and snow grain morphology are important for many climate and hydrological applications such as surface energy balance, avalanche predictions and water resources management (e.g. Hall, 2004; Armstrong and Brun, 2008; Brown, 2010; Foster and others, 2011). Characterizing the seasonal and vertical snow grain size is key for snow grain-size retrieval from visible and near-infrared (NIR) satellite data (Jin and others, 2008; Fernandes and others, 2009; Lyapustin and others, 2009), for snow water equivalent (SWE) retrieval from passive microwave satellite data (e.g. Chang and others, 1982; Mätzler, 2006; Pulliainen, 2006; Durand and others, 2008; Derksen and others, 2010; Langlois and others, 2010a; Takala and others, 2011) and for studies of atmospheric/snow chemical interactions (Grannas and others, 2007; Domine and others, 2008). Grain size has also been shown to be the most sensitive parameter of all the snow physical properties in microwave radiative transfer models such as the Microwave Emission Model of Layered Snowpacks (MEMLS; Durand and others, 2008; Langlois and others, 2010a; Brucker and others, 2011), the Helsinki University of Technology model (HUT; Butt and Kelly, 2008; Kontu and Pulliainen, 2010) and the dense-media radiative transfer model (DMRT; Tedesco and Kim, 2006; Grody, 2008; Brucker and others, 2010). Previous studies used different methods to measure snow grain size to validate the MEMLS model, as discussed below (Mätzler and Wiesmann, 1999; Wiesmann and Mätzler, 1999; Toure and others, 2008). Nonetheless, these analytical models still need to be further validated with more reliable and accurate ground-based snow grain measurements to improve their modeling accuracy.

The greatest diameter, $D_{max}$, of a snow grain has long been used as a classical parameter for characterizing grain size (Fierz and others, 2009). Given the variety of grain shapes and its relevance to radiative transfer models, the definition of grain size remains ambiguous (Aoki and others 2000; Mätzler, 2002; Taillandier and others, 2007). Moreover, demarcation of individual snow grains is ambiguous as the boundaries between grains are not always clearly identifiable (Domine and others, 2008). This reduces the repeatability of such snow grain measurements, due to the subjectivity of the observer. There are several methods for characterizing the physical properties of snow grain size, including stereology (e.g. Matzl and Schneebeli, 2010), methane adsorption measurements (Domine and others, 2001), X-ray computed microtomography (μ-CT; Flin and others, 2005; Chen and Baker, 2010) and optical methods (Matzl and Schneebeli, 2006; Painter and others, 2007; Gallet and others, 2009; Langlois and others, 2010b; Arnaud and others, 2011). Here we focus on optical approaches allowing in-field or in situ measurements. As the spectral reflectance (or its hemispherical component: spectral albedo, hereafter referred to as albedo) of snow is very sensitive to grain size (e.g. Wiscombe and Warren, 1980; Nolin and Dozier, 2000; Kokhanovsky and Zege, 2004; Domine and others, 2006; Xie and others, 2006) and shape (e.g. Jin and others, 2008; Picard and others, 2009), albedo can be used to derive snow grain size and, more precisely, the specific surface area (SSA), a fundamental geometrical characteristic of porous materials. Here SSA quantifies the ice surface-to-volume ratio of a snow grain. Several studies have illustrated the usefulness of SSA measurements, and different methods have been developed for measuring it (Domine and others, 2001; Matzl and Schneebeli, 2006;

Painter and others, 2007; Gallet and others, 2009; Langlois and others, 2010b; Arnaud and others, 2011).

Matzl and Schneebeli (2006) suggested a method based on the use of a commercial camera modified to measure the NIR albedo near 900 nm. The advantage of this method is that it yields vertical SSA profiles rapidly from photos of the snow-pit wall. However, despite its robustness, the method is limited to the NIR spectrum due to the charge-coupled device's (CCD) sensitivity spectrum that abruptly drops above 1000 nm, which reduces the sensitivity to SSA measurement when compared to SWIR albedo measurements (Gallet and others, 2009). This limited sensitivity renders this method difficult to accurately calibrate, and results are hard to reproduce, particularly under variable illumination conditions in deep snow pits, even with a modified protocol as discussed by Langlois and others (2010b). Painter and others (2007) suggested a system based on directional spectral reflectance measurements of snow using a spectroradiometer in the range 950–1050 nm under controlled illumination. However, the resolution of this measurement (2 cm) is rather coarse and is inadequate to properly characterize thinner snow layers (<1 cm) within the snowpack. Also, these wavelengths are more sensitive to absorbing impurities which affect the snow reflectance (Warren and Wiscombe, 1980; Flanner and others, 2007). In addition, Grenfell and Warren (1999) suggest that to reach higher effective grain-size accuracy, hemispherical reflectance is better than biconical reflectance measured by Painter and others (2007). Nonetheless, this method is less destructive and avoids possible snow grain alteration from sampling. Gallet and others (2009) developed a shortwave infrared (SWIR) albedo measurement system using an integrating sphere and laser diodes at 1310 and 1550 nm as illumination sources. This system, DUal-Frequency Integrating Sphere for Snow SSA (DUFISSS), requires extraction of a snow sample, which can be difficult in weakly cohesive snow hoar layers and in the presence of ice lenses. The vertical resolution is also less detailed than with photographs since these measurements are punctual. However, using such a device in a fixed position (in more controllable measurement conditions) improves the accuracy and reproducibility of such measurements. Arnaud and others (2011) modified the method using a profiler, Profiler Of Snow Specific Surface area Using SWIR reflectance Measurement (POSSSUM), to measure a normalized SWIR reflectance within a drilled hole up to 20 m deep. POSSSUM retrieves SSA profiles with an effective vertical resolution of 10–20 mm, but the drilling approach is not applicable in non-cohesive seasonal snow. To limit the issues due to the destructiveness of drilling a hole in seasonal snow, the Laboratoire de Glaciologie et Géophysique de l'Environnement (LGGE) developed the Alpine Snow Specific Surface Area Profiler (ASSSAP) which measures the reflectance profile within a cylindrical dug hole using the same principles as POSSSUM. This instrument is still in development by the LGGE.

Here we present a new approach based on a SWIRcam (hereafter referred to as SWIRcam), at wavelengths comparable to the SWIR integrating sphere system used in this study (InfraRed Integrating Sphere (IRIS)) developed at Université de Sherbrooke, southeastern Québec, Canada, and based on the DUFISSS design (Gallet and others, 2009). Compared to IRIS and DUFISSS, this new camera gives high-resolution SSA profiles. Hence, the main objective of this paper is to analyze and compare the two optically based field retrieval methods of snow grain size (SWIRcam and IRIS) and to discuss their accuracy and reproducibility with various measurements taken in arctic, subarctic and southern regions of Canada.

The next section briefly recalls the theory behind the snow spectral albedo. The different systems used are then described: the new SWIRcam and IRIS. Finally, the advantages and drawbacks of each approach are discussed.

## BACKGROUND

In radiative transfer studies, the 'optical' diameter of particles, $D_o$, is commonly used to characterize particle sizes using the volume ($V$) to surface area ($A$) ratio where $D_o = 6(V/A)$ (e.g. Grenfell and Warren, 1999). The optical diameter of a particle is defined as the diameter of a sphere having optical properties identical to those of the measured particle regardless of its shape. For a single size distribution of spheres, $D_o$ corresponds to their diameter. The optical diameter can also be related to the SSA of particles. For snow, SSA can be defined either by its surface-area-of-ice ($A$) to volume-of-ice ($V$) ratio ($\mathrm{SSA}_V = A/V$) ($\mathrm{m}^{-1}$) or its surface area of ice per unit of mass of ice ($M$) ($\mathrm{SSA} = \frac{A}{M} = \frac{A}{\rho_{\mathrm{ice}} V}$) ($\mathrm{m}^2\,\mathrm{kg}^{-1}$), where $\rho_{\mathrm{ice}}$ is the density of pure ice (917 $\mathrm{kg\,m}^{-3}$ at 0°C). The latter definition of SSA can be related to gas adsorption measurements as described by Domine and others (2001). The relationship between the optical diameter and the SSA is then

$$D_o = \frac{6}{\mathrm{SSA}_V} = \frac{6}{\rho_{\mathrm{ice}} \mathrm{SSA}} \tag{1}$$

The SSA of snow can be related to its albedo using a simple optical equation model suggested by Kokhanovsky and Zege (2004), hereafter referred to as KZ04:

$$\begin{aligned} R_{a,\lambda}(\xi) &= \exp\left(-K_0(\xi) b \sqrt{\gamma_\lambda \left(\frac{6}{\rho_{\mathrm{ice}} \mathrm{SSA}}\right)}\right) \\ &= \exp\left(-K_0(\xi) b \sqrt{\gamma_\lambda D_o}\right) \end{aligned} \tag{2}$$

where $R_{a,\lambda}(\xi)$ is the spectral albedo at the wavelength $\lambda$ and illumination angle $\xi$, $\gamma_\lambda$ is the absorption coefficient of ice which depends on the imaginary part of the refraction index of ice (W.J. Wiscombe, ftp://climate1.gsfc.nasa.gov/wiscombe/), the constant $b$ represents the shape factor of snow grains ($b$ ranges from 4.53 for spheres to 3.62 for tetrahedral grains; Picard and others, 2009), $D_o$ is the optical diameter of the snow grain and $K_0$ is the escape function which determines the angular distribution of light escaping the medium and depends mainly on the incident lighting conditions (9/7 for normal incidence albedo and 1 for spherical albedo). Figure 1 shows the spectral spherical albedo ($K_0 = 1$) of snow simulated with the KZ04 model for different grain sizes, $D_o$, and a shape factor, $b$, of 4.3. Figure 1 shows the higher sensitivity of snow albedo to $D_o$ in the SWIR region (>1.2 μm) compared to the NIR region (<1.0 μm). For a fixed value of $b = 4.3$, a variation of $\Delta D_o = 0.8$ mm (SSA of 8.2 $\mathrm{m}^2\,\mathrm{kg}^{-1}$), for instance, gives a variation of $\Delta R_a = 0.275$ at 1.3 μm, while this variation is only $\Delta R_a = 0.172$ at 0.9 μm. In other words, a given error in measured albedo translates into a larger error on $D_o$ at 0.9 μm than at 1.3 μm.

Simulations with the KZ04 model using different values of $b$ were compared to computed spectral spherical albedo

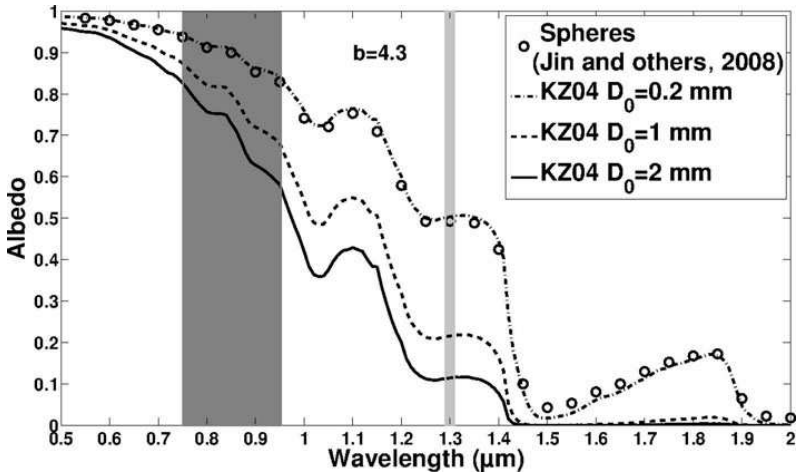


**Fig. 1.** Spectral albedo of snow for different grain sizes, $D_o$, simulated with the KZ04 model (Eqn (2)) for spherical albedo ($K_0 = 1$). A shape factor, *b*, of 4.3 fitted best for spheres in the data presented by Jin and others (2008). The spectral responses of the NIR (dark gray rectangle) and SWIR (light gray rectangle) cameras are displayed. The wavelength of the IRIS and that of the DUFISSS laser system are included in the SWIRcam spectral response.

using the improved geometric–optics method (IGOM) developed by Yang and Liou (1996) (derived from the data of Jin and others, 2008; Z. Jin and others, personal communication, 2011). Using an iterative approach to optimize the correlation between the KZ04 and Jin and others (2008) models, we sought the value of *b* that provides the best fit. Results show that $b = 4.3$ for spheres gives the best correlation (rmse = 0.01; Fig. 1). The spectral albedo variations (Fig. 1) computed for monodispersed sizes of idealized particle shapes suggest (not shown) that the shape of snow grains could be important in the retrieval procedure, as also outlined by Jin and others (2008) and Picard and others (2009). In practice, however, snow samples include different sizes and shapes giving a polydispersed particle distribution and theoretically affect the shape factor *b* (Picard and others, 2009). The shape and size variability within a snow sample can clearly be seen in microtomography measurements (e.g. Chen and Baker, 2010; Matzl and Schneebeli, 2010). However, Gallet and others (2009) and Arnaud and others (2011), based on simultaneous measurements of SSA using $CH_4$ adsorption and IR reflectance of natural snow samples, could not detect any effect of grain shape and fitted their data using the *b* value adequate for spheres. This indicates that shape effects may cancel out in natural snow, which then behaves as a collection of disconnected spheres.

## DATA AND METHODS

### Study sites

Intercomparison field campaigns include snow-pit measurements from: (1) the Centre d'Applications et de Recherche en Télédétection (CARTEL) experimental site SIRENE at Université de Sherbrooke throughout several winters since 2008, and (2) Barnes Ice Cap, Baffin Island, Nunavut, Canada, in March 2011 (Dupont and others, 2012).

The first site is an open mid-latitude area where different types of snow grains from fresh snow, rounded grains to depth hoar are found. The second site is an arctic ice cap where the observed snow grains were mostly dense rounded grains, wind crusts and depth hoar. No firn was observed between the ice layers and the seasonal snow. Further details are provided by Dupont and others (2012).

Two other datasets were collected for calibration purposes (12 samples overall) in cold rooms at Dartmouth College, Hanover, New Hampshire, USA, and Québec City, Canada. The grains measured were mainly rounded grains and depth hoar. One fresh snow sample was observed at the time of the measurements in Québec City (Table 1).

## LASER ALBEDO MEASUREMENTS

### Instrument description

The first system used to measure snow albedo was the Shortwave InfraRed Integrating Sphere (IRIS) system, similar to that developed by Gallet and others (2009), using an integrating sphere (Labsphere®; 10 cm diameter) with three ports. The main difference between the IRIS and the DUFISSS systems is the sphere geometries. DUFISSS has a larger inner diameter (15 cm) and wider ports. The first port of the IRIS system is for illumination by a 1.33 μm laser (1.31 μm for the DUFISSS system) with a 1 cm beam expander. The second port, in front of the laser, is placed in front of the target (snow sample), and the third one, in the perpendicular plane, is for an indium gallium arsenide (InGaAs) photodiode detector. A diaphragm is placed in front of the laser beam in order to measure the dark current and possible stray light entering the sphere. A first measurement with, and a second without, the diaphragm is done. Subtracting the first measurement (dark current and stray light) from the second (signal of the sample) determines the exact signal of the laser reflected on the snow sample. This lightweight and simple system is used in a fixed mode where a snow sample is extracted (Fig. 2) and placed under the integrating sphere, rather than a mobile mode where the integrating sphere is placed against the snow wall. It should be noted that the surface of the snow sample is slightly lower than the sphere's inner surface, giving an effective solid

**Fig. 2.** The IRIS sampler before extraction of the snow sample within the snow cover (left) and after the sample extraction with the cut surface (right).

angle of the reflected radiation lower than $2\pi$ steradians. The sample cup is an aluminum cylinder (10 cm in diameter and 6 cm high) with a metallic plate that slides at the bottom portion of the cylinder (Fig. 2). The sampler was built sufficiently large and deep to limit errors due to possible internal reflections within the sampler (Gallet and others, 2009, p. 171–172).

### Calibration and measurements

To provide accurate albedo measurements, the IRIS system is calibrated to albedo for each snow pit using reference Lambertian Spectralon reflectance targets (0.01, 0.07, 0.12, 0.27, 0.47, 0.64, 0.86 and 0.99 at 1330 nm) taking into account any possible shift in the laser intensity between every measurement session. Two calibrations, before and after snow measurements, are done to check the stability of the laser measurements. Figure 3 shows an example of a calibration curve. The nonlinear response is due to a reillumination effect of the reference panels by reflected light (the higher the albedo, the stronger is the reillumination; Gallet and others 2009). A fit is computed using a third-degree polynomial (rmse of 0.008 albedo and $R^2 = 0.999$). The mean measured variability before and after snow-pit measurements (15–30 min) is of the order of 1.3% which is comparable to the variability of the DUFISSS system (1%) (Gallet and others, 2009). This variability is mainly due to the temperature dependency of the laser (Park and others, 1999). Note that the calibration curve does not pass through zero; such an offset is due to photons diffracted by the beam expender and directly reflected by the inner sphere surface toward the InGaAs detector, thus giving a signal even if the albedo sample is zero. This offset is taken into account by the calibration curve (Fig. 3).

To extract an undisturbed snow sample, the sampler is slid inside the snow pit from the surface at desired depth with a 3 cm vertical resolution (the top portion of the sampler corresponds to the measurement height). The sample is then placed under the integrating sphere, three measurements are made to ensure measurement stability and the mean value is taken. To ensure no external light penetrates the integrating sphere, the system is placed inside an enclosed box and the sample is placed directly under the sphere, leaving no space between the sphere port and the sample.

## SWIR PHOTOGRAPHS ALBEDO MEASUREMENTS

### Instrument description

The other instrument used in this study is a camera sensitive to the NIR and SWIR (0.9–1.7 μm) based on a cooled InGaAs array (320 × 256 pixels) (© Xenics Xeva-320). A filter centered at 1.295 ± 0.012 μm (Edmund NT62-863) is placed in front of the lens to narrow the range. This wavelength was

**Table 1.** Study sites for the intercomparison field campaigns (SIRENE and Barnes) and the instrument calibration (Québec City and Dartmouth College)

| Site | Lat. | Long. | Altitude m | Date | SSA instruments |
|---|---|---|---|---|---|
| SIRENE, Sherbrooke, Qué., Canada | 45°22′ N | 71°56′ W | 300 | Winters 2008–11 | IRIS, NIR and SWIRcams |
| Barnes Ice Cap, Baffin Island, Nunavut, Canada | 70° N | 73° W | 1124 | Mar 2011 | IRIS, NIR and SWIRcams |
| *IRIS calibration sites* | | | | | |
| Dartmouth College, Hanover, NH, USA | 43°42′ N | 72°17′ W | 161 | Feb 2011 | IRIS and μ-CT |
| Québec City, Qué., Canada | 46°48′ N | 71°12′ W | 15 | Apr 2012 | IRIS and DUFISSS |

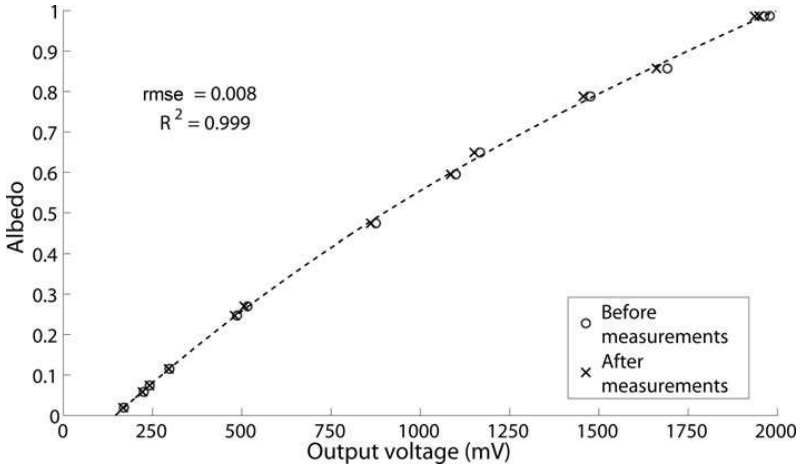


**Fig. 3.** Example of an IRIS calibration curve. The relationship is $R = (3.23 \times 10^{-11})V^3 - (2.11 \times 10^{-7})V^2 + (8.53 \times 10^{-4})V - 0.12$. The nonlinear response is due to a reillumination effect of the reference panels by reflected light inside the integrating sphere.

chosen for the best compromise between sensitivity of the spectrum albedo to SSA and signal intensity (Fig. 1). The advantage of such an instrument compared to a commercial camera (Matzl and Schneebeli, 2006; Langlois and others, 2010b) is the possibility of directly deriving (after calibration) SSA from the KZ04 model with greater precision as shown in the previous section (Eqn (2)).

### Measurement and calibration

The SWIRcam measurement protocol was based on that suggested by Langlois and others (2010b) for snow NIR photographs. Some modifications were made to the protocol concerning control of the ambient lighting conditions and transmission of light through the top layers of the snow pit, in order to improve the accuracy and reproducibility of the measurements. After the snow pit is dug and a clean snow profile has been prepared with a sharp spatula, the camera is placed perpendicularly in front of the snow wall. All measurements were made under diffuse lighting conditions using a white translucent cover, avoiding direct solar illumination. Also, to avoid measurement artifacts due to direct light transmission penetrating the snow cover from the surface to the top portion of the snow profile, a large Styrofoam panel is placed on top of the snow profile (at the snow-cover surface). For calibration from grayscale values to albedo, five reference targets (Lambertian Spectralon targets: 0.06, 0.25, 0.59, 0.79 and 0.99 at 1300 nm) and a rigid ruler are placed along the snow profile (Fig. 4). A first picture is taken with a Styrofoam panel placed in front of the snow wall and the reference targets. This picture is used for image normalization to correct illumination variations over the image. Prior to the snow measurements, the mean albedo ($R_{a,\lambda} = 0.97$) and standard deviation (0.00) of this reference panel (80 cm × 80 cm) was measured under controlled illumination (using a 600 W halogen lamp, Q60-SGL). A picture of the snow profile without the Styrofoam panel is then taken. Both photos (snow and reference panel) are taken with a minimum time lag (seconds). The diffuse solar conditions are assumed constant between the two photographs (Fig. 4).

Before calibrating the photographs from grayscale to albedo, the photograph is normalized by dividing, pixel by pixel, the grayscale values of the snow wall picture with the grayscale values of the Styrofoam panel picture (Fig. 4). This corrects illumination variations along the snow profile as seen in Figure 4 where the bottom part of the profile is less dark on the normalized picture (right picture, Fig. 4) than the original snow picture (left picture, Fig. 4). After normalization, a calibration is done between the measured normalized grayscale pixels of the reference target and their albedo values given by the manufacturer (Fig. 5). Figure 5 shows the expected linearity of the calibration (rmse = 0.01; $R^2 = 0.99$). Such linear relationships are computed for each snow pit taking into account relative lighting and geometric conditions specific to each snow pit. No geometric deformation within the pictures was detected. The pixel to cm conversion is thus vertically constant. To produce an albedo profile, a section of the snow wall (~5–10 cm wide) is extracted in the SWIR picture and the mean horizontal albedo value is then associated with its height. In this study, the mean SWIR photograph resolution was 2 mm pixel$^{-1}$ since no thin layer (<2 mm) was observed. Nonetheless, if there were thin snow or ice layers within the snowpack, multiple pictures of the snow wall (taken at different depth) could be taken, with a minimal time lag, closer to the snow wall to increase the image resolution.

## RESULTS AND DISCUSSION

In this section, various albedo and SSA measurements from both SWIR instruments (IRIS and SWIRcam) acquired during several field campaigns in mountainous, northern temperate, subarctic and arctic regions are compared. To limit any possible artifacts due to the sample holder of the IRIS system (Gallet and others, 2009), measurements from snow layers having a density lower than 200 kg m$^{-3}$ have been rejected. These layers were all fresh snow layers and comprised 6% of the overall data given in the following subsections.

### IRIS albedo measurement validation for SSA

Figure 6 shows the relationship between albedo measurements taken with the IRIS system and SSA values obtained from two different methods: (1) SWIR albedo measurements with DUFISSS (Gallet and others, 2009) and (2) X-ray computed microtomography (μ-CT) (Chen and Baker, 2010).

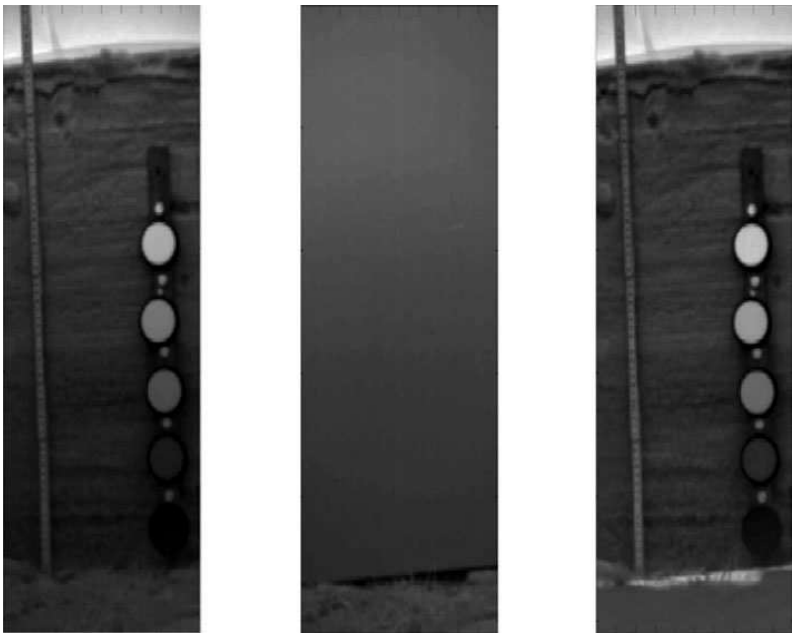

**Fig. 4.** Example of a snow profile picture (left), a reference Styrofoam panel picture (middle) and a normalized picture (right) taken at the SIRENE study site on 16 February 2011. The normalized picture is the product of the snow profile picture divided by the reference panel picture.

The DUFISSS dataset was fitted to the KZ04 model (Eqn (2)) to validate both the IRIS measurement and the KZ04 simulations.

Albedo measurements from both instruments (IRIS and DUFISSS) were taken from the same snow samples. In fact, the samples were taken with the same sampler and placed under both systems with a minimal time lag (a few minutes) in order to limit any changes in the physical properties. The SSA was then derived from the DUFISSS measurements with the Gallet and others (2009) relationship and compared to the IRIS albedo measurements. Since there are differences in the geometries of both spheres (sphere inner diameter and port geometry and inner diameters) and in the wavelengths used in both systems (1310 nm for DUFISSS and 1330 nm for IRIS), directly comparing the albedo measurements is not adequate. As discussed by Gallet and others (2009) and Arnaud and others (2011), these IR albedo integrating sphere systems do not directly measure directional-hemispherical albedo but rather a combination of directional-hemispherical and diffuse-hemispherical albedos that are highly dependent on the sphere's geometry (Gallet and others, 2009, equation 6).

Nine samples ranging from 6.0 to 57.4 $m^2\,kg^{-1}$ were measured in a cold room in Québec City. Results show good

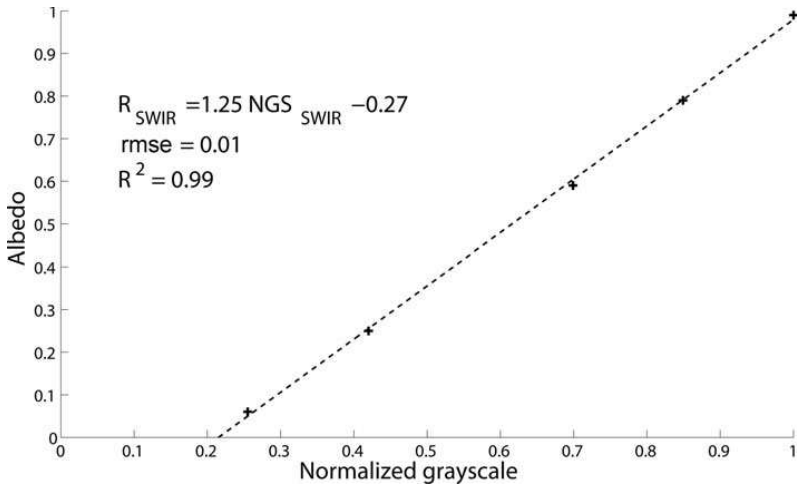


**Fig. 5.** Example of a calibration curve between the normalized grayscale values and the manufactured albedo values for the SWIRcam.

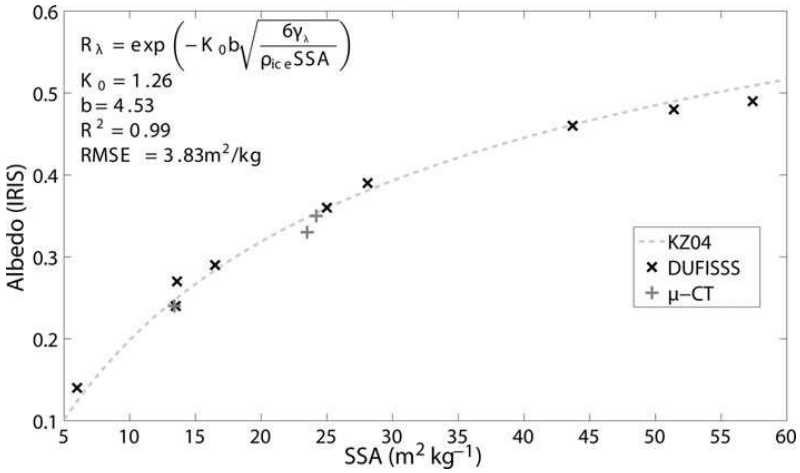


**Fig. 6.** Relationship between the IRIS-derived albedo and SSA measurements from the DUFISSS system (×) and μ-CT measurements (+). Dashed line corresponds to the KZ04 albedo model (Eqn (2)).

agreement with the KZ04 model using a shape factor $b$ of 4.53 (snow grain shape corresponding to spheres according to Picard and others, 2009) and an escape function $K_0$ of 1.26 ($R^2 = 0.99$; rmse = 2.33 $m^2\,kg^{-1}$), meaning that the snow grain shape does not scatter the points in these conditions. This calibration is, however, valid over a limited range of SSA (SSA < 57.4 $m^2\,kg^{-1}$) and may differ for SSA values higher than 57.4 $m^2\,kg^{-1}$. Arnaud and others (2011) showed that directional-hemispherical albedo SSA measurements tend to give a shape factor corresponding to spheres ($b = 4.53$; Picard and others, 2009) with $K_0 = 9/7$ as used for the SSA retrieval using the SWIRcam. The difference with the escape function given in Figure 6 ($K_0 = 1.26$) is explained by the combination of directional/diffuse-hemispherical albedo measured with IRIS compared to the SWIRcam measurements.

Another independent dataset was used to validate this relationship. The albedo measurements were acquired on the same samples with the IRIS system and the SSA measurements obtained from the μ-CT at Thayer School of Engineering, Hanover. The rmse from the model is 1.33 $m^2\,kg^{-1}$. The overall accuracy of the IRIS system using the KZ04 model for retrieving the SSA in comparison to these two SSA datasets is 1.89 $m^2\,kg^{-1}$, i.e. of the order of 7%.

## SWIRcam comparison

Figure 7 shows an example of a normalized image acquired with the NIR (left) and SWIR (right) cameras with their respective albedo profiles. The NIR image was taken with the same measurement protocol as the SWIRcam; details of the apparatus are provided by Langlois and others (2010b). One should note that the differences in the albedo profiles (0.8–0.9 for the NIR picture and 0.25–0.3 for the SWIR picture) are simply due to a difference in wavelengths (~850 nm for the NIR image and 1300 nm for the SWIR image). The NIR image shows a better vertical resolution (1.3 mm $pixel^{-1}$), but the SWIR image (2.0 mm $pixel^{-1}$) shows a much more detailed snow-pit stratigraphy (i.e. more sensitive to changes in SSA). This is shown by the albedo profiles beside the pictures. There is much more variability, especially in the top portion of the profile where the albedo

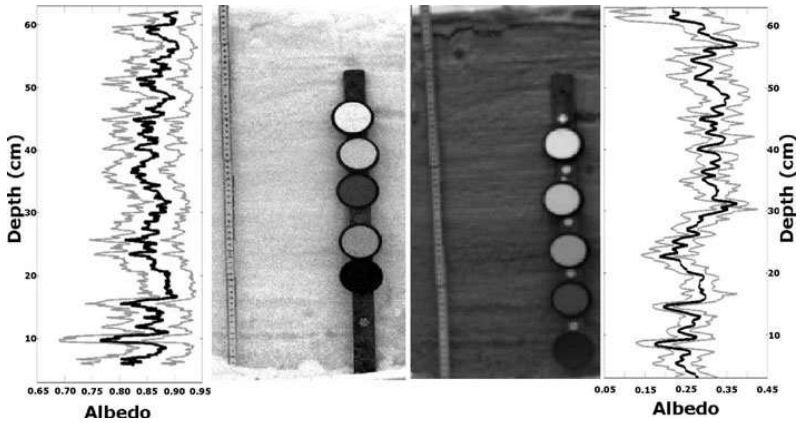


**Fig. 7.** Albedo profile taken with NIR (left) and SWIR (right) pictures with their mean horizontal (black), minimum and maximum (gray) profiles.

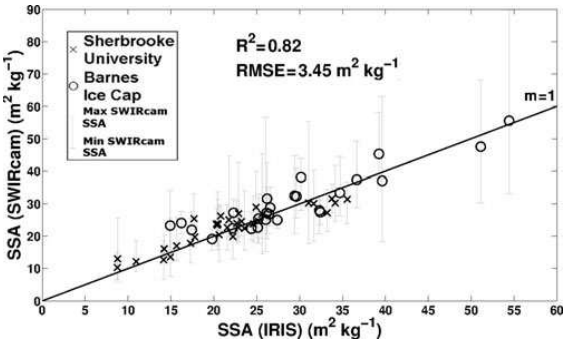


**Fig. 8.** Compared SSA measurements of the IRIS system and the SWIRcam taken at the experimental site SIRENE (×) and Barnes Ice Cap (○) during the 2011 winter. The error bars give the minimum and maximum horizontal SWIRcam albedo variation at their respective heights.

range is ~0.1 for the NIR picture and ~0.2 for the SWIR picture. This variability is mainly due to the presence of an ice lens near the surface which is not clearly visible in the NIR picture because of its high sensitivity to lighting conditions. This shows the advantage of using instruments in the SWIR spectrum rather than the NIR spectrum since the SWIRcam is less sensitive to lighting conditions.

To validate the albedo measurements taken with the SWIRcam, five profiles were taken during the 2011 winter and compared with point measurements taken with the IRIS system along those profiles. Figure 8 shows the comparison between the SSA data derived from the SWIRcam and IRIS measurements taken at SIRENE (three profiles) and on Barnes Ice Cap (two profiles). The error bars correspond to the minimum and maximum SWIRcam SSA horizontal values of the snow wall section. The SSA measurements derived from the SWIRcam were calculated using equation 6 of Arnaud and others (2011) since the SWIRcam albedo measurements are hemispherical-directional ($K_0 = 9/7$). The SSAs measured with both SWIRcam and IRIS systems are in good agreement, with little variability ($R^2 = 0.82$; rmse = 3.45 $m^2\,kg^{-1}$). There is some variability in the SWIRcam measurements because the values extracted from the profiles are averaged over 5–10 cm horizontally. The averaged horizontal length depends on the length available within the picture and can vary from one site to another. This averaging does not eliminate the possibility of extracting two-dimensional SSA information within a SWIR picture. It is done mainly to extract the overall vertical variability due to the layering of snowpack stratigraphy. The mean standard deviation over the averaged values is of the order of 2.0 $m^2\,kg^{-1}$, which is comparable to the rmse. This explains most of the variability in the comparison between the two instruments.

The SWIRcam also provides more information than the IRIS system, by allowing characterization of the stratigraphy within the snow pit. Figures 9–11 show examples of SWIR photographs (right side) taken with the camera and the derived SSA profile (left side) taken at the SIRENE experimental site (Figs 9 and 11) and on Barnes Ice Cap (Fig. 10). SSA measurements taken with the IRIS system along the same profiles are also shown.

As mentioned by Langlois and others (2010b), the use of a passive-based camera to measure snow albedo is complex because numerous variables (lighting conditions, camera angle, lighting normalization) affect the measure-

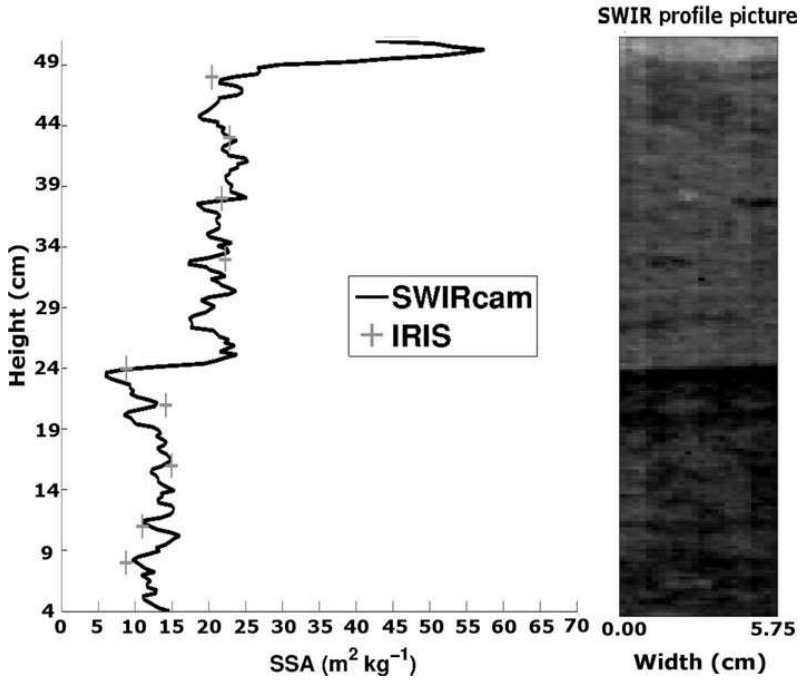


**Fig. 9.** SSA profile derived from the IRIS system and the SWIRcam taken at SIRENE during the 2011 winter. The picture on the right shows the portion of the snow pit (5.75 cm width) from which the mean SWIR albedo was computed.

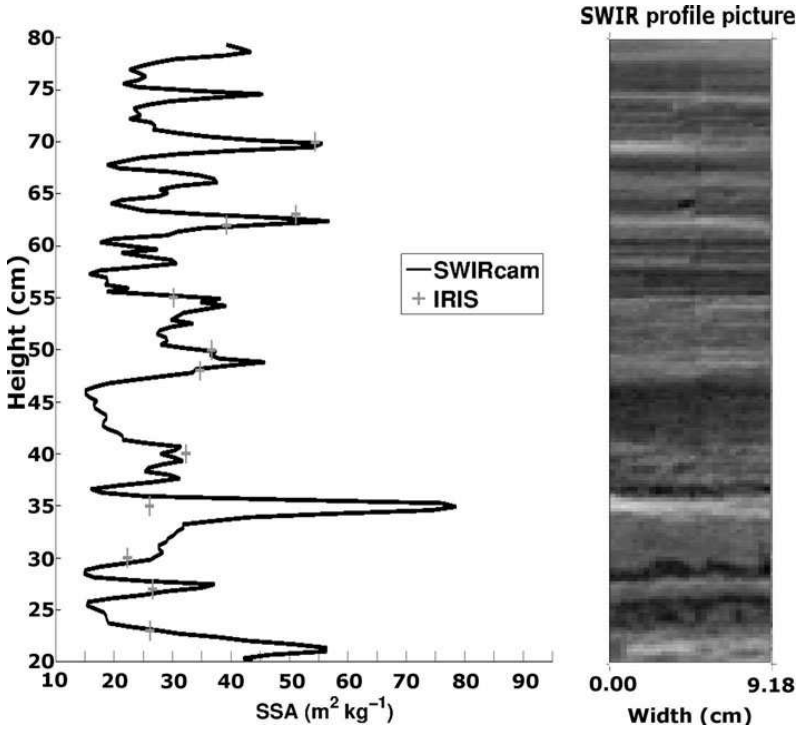


**Fig. 10.** SSA profile derived from the IRIS system and the SWIRcam taken on Barnes Ice Cap in March 2011. The picture on the right shows the portion of the snow pit (9.18 cm width) from which the mean SWIR albedo was computed.

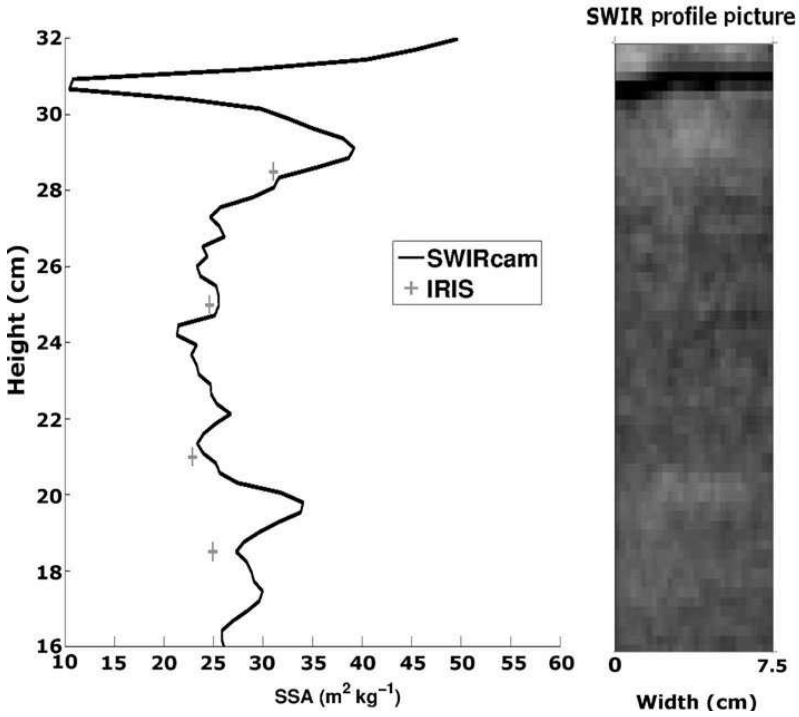


**Fig. 11.** SSA profile derived from the IRIS system and the SWIRcam taken at SIRENE during the 2011 winter. The picture on the right shows the portion of the snow pit (7.5 cm width) from which the mean SWIR albedo was computed. The ice lens (height ~31 cm) can clearly be distinguished by its dark region at the top of the snow pit.

ments. This reduces the accuracy and reproducibility of the measurements compared to those made with IRIS. The Figure 9 profile was measured twice with a 5 min interval, the set-up was dismantled between measurements, and the mean albedo variation between the two measurements along the entire profile was 5%, with an rmse of 0.02. Another interesting feature of these measurements (Figs 9–11) is the albedo variability provided at 2 mm vertical resolution. At this resolution, one can distinguish from the SSA profile a fresh snow layer (49–50 cm; $39\,m^2\,kg^{-1} < SSA < 55\,m^2\,kg^{-1}$, mean SSA = $47.4\,m^2\,kg^{-1}$), a dense rounded snow grain slab (25–49 cm; $17.0\,m^2\,kg^{-1} < SSA < 27.0\,m^2\,kg^{-1}$, mean SSA = $21.6\,m^2\,kg^{-1}$) a hard snow crust (21–24 cm; $5.0\,m^2\,kg^{-1} < SSA < 13.0\,m^2\,kg^{-1}$, mean SSA = $9.0\,m^2\,kg^{-1}$) and a coarse depth-hoar layer (4–21 cm; $8.0\,m^2\,kg^{-1} < SSA < 16.0\,m^2\,kg^{-1}$, mean SSA = $12.8\,m^2\,kg^{-1}$).

The SWIR image (Fig. 10, right) from which the SSA profile was extracted also reveals the fine vertical variability of SSA well. Figure 10 is a good example of the vertical information that the SWIRcam provides. Compared to Figure 9, Figure 10 shows much more vertical SSA variability on Barnes Ice Cap, which could be omitted by IRIS measurements. In fact, thin (~2 cm) high-SSA (>$50\,m^2\,kg^{-1}$) layers could be missed with IRIS since the sampler is 6 cm high. This shows the importance of high-resolution SSA profiles. This high resolution can even distinguish a 4 mm thick ice lens within the snow pit as shown in Figure 11. The dark region with a minimal SSA of $4.6\,m^2\,kg^{-1}$ at 31 cm was visually associated with a clear ice lens. The value shown of $10.5\,m^2\,kg^{-1}$ at 31 cm on the SSA profile (Fig. 11) is caused by the slight inclination of the ice lens. Thus, the horizontal mix of snow with ice raises the averaged SSA value at that height.

Since ice lenses affect the snow microwave signature considerably (Grody, 2008; Rees and others, 2010), it is essential that they be detected and characterized. With the SWIRcam it is possible to characterize fairly precisely the position of the lens and its thickness along a certain horizontal width. This is another excellent application of this new SWIRcam.

## CONCLUSION

The main objective of this paper was to test the robustness of the determination of snow SSA from SWIR albedo measurements using two methods that differ in their sampling technique, lighting conditions and detector type. The two instruments presented in this paper, which are based on passive optical solar measurements (SWIRcam) or active laser-based devices (IRIS), have been compared. The IRIS measurements were validated with an independent method (μ-CT) and have proven to be accurate for SSA measurements within 10%. For both instruments, we used the Kokhanovsky and Zege (2004) model to derive the snow grain SSA, showing the usefulness of this equation with a fixed shape factor ($b$) value for the different shapes measured (fresh snow, rounded grains, depth hoar) and an escape function, $K_0$, adapted to the type of albedo measured (directional and/or hemispherical).

Among the optical methods tested here, the most accurate and precise instrument for determining snow SSA is the IRIS system (relative variations of 3–5% on SSA measurements). Similar to the DUFISSS instrument (Gallet and others, 2009), the mean accuracy of the IRIS device is on the order of 10% compared to the methane adsorption method (considered as reference measurement). The downside of such a system is the need to extract snow samples for measurements, which can be difficult depending on snow conditions and stratigraphy (ice lenses, non-cohesive layers) and which lengthens the acquisition time to complete a full snow profile (15–30 min). Also, the vertical resolution of this system is lower than NIR and SWIRcams or with POSSSUM.

The lower sensitivity to illumination conditions (Fig. 7) and the lower sensitivity to absorbing snow impurities make the SWIRcam a more accurate instrument for snow grain-size retrieval than the 850 nm NIR camera used by Langlois and others (2010b). Also, the vertical resolution for albedo measurements using the SWIRcam (~2 mm) gives more detailed stratigraphic information than the IRIS system (Fig. 10) and can detect thin ice lenses within the snowpack (Fig. 11). Another version of the SWIRcam used in this study was developed by © Xenics with a better spatial resolution, meaning the SWIR image could have a better resolution without having to take multiple pictures closer to the snow wall to increase the resolution.

In addition to other types of profile measurements for density, thermal conductivity (Morin and others, 2010) or liquid water content using capacitance plates (e.g. Denoth, 1989) or snow forks (e.g. Sihvola and Tiuri, 1986), the precise determination of vertical profiles of snow grain SSA and stratigraphy (layering) using a lightweight optical system is essential for improving snow and radiative transfer models. A thorough comparison between existing methods for SSA determination – optical, stereology, methane adsorption and X-ray microtomography – is needed to further define the accuracy and limitations of each approach.

## ACKNOWLEDGEMENTS

We thank Ian Baker who allowed us to acquire the μ-CT grain-size measurements. The research at Dartmouth College was supported by US National Science Foundation (NSF) grant OPP-0821056. The views and conclusions contained herein are those of the authors and should not be interpreted as necessarily representing official policies, either expressed or implied, of the NSF or the US Government. We thank Jean-Charles Gallet who processed and provided the methane adsorption measurements, and Z. Jin who provided albedo calculations for different grain shapes (Fig. 1). All of our colleagues who helped us during the field campaigns in France and Canada are also gratefully acknowledged. This work was supported by the Natural Sciences and Engineering Research Council of Canada, the Canadian Polar Continental Shelf Program (Barnes Ice Cap field campaign), Environment Canada (principal investigator Anne Walker), Centre National de la Recherche Scientifique (CNRS), France, Institut Paul-Émile Victor (IPEV; French Polar Institute), the Programme International de Collaboration Scientifique (PICS) of CNRS, and the Ministère des Relations Internationales du Québec and Ministère des Affaires Étrangères et Européennes de la République Française (Consulat Général de France à Québec) in the framework of the 63e Session de la Commission Permanente de Coopération Franco-Québécoise.

## REFERENCES

Aoki T, Aoki T, Fukabori M, Hachikubo A, Tachibana Y and Nishio F (2000) Effects of snow physical parameters on spectral albedo

and bi-directional reflectance of snow surface. *J. Geophys. Res.,* **105**(D8), 10 219–10 236 (doi: 10.1029/1999JD901122)

Armstrong RL and Brun E eds. (2008) *Snow and climate: physical processes, surface energy exchange and modelling.* Cambridge University Press, Cambridge

Arnaud L and 7 others (2011) Measurement of vertical profiles of snow specific surface area with a 1 cm resolution using infrared reflectance: instrument description and validation. *J. Glaciol.,* **57**(201), 17–29 (doi: 10.3189/002214311795306664)

Brown RD (2010) Analysis of snow cover variability and change in Québec, 1948–2005. *Hydrol. Process.,* **24**(14), 1929–1954 (doi: 10.1002/hyp.7565)

Brucker L, Picard G and Fily M (2010) Snow grain-size profiles deduced from microwave snow emissivities in Antarctica. *J. Glaciol.,* **56**(197), 514–526

Brucker L and 7 others (2011) Modeling time series of microwave brightness temperature at Dome C, Antarctica, using vertically resolved snow temperature and microstructure measurements. *J. Glaciol.,* **57**(201), 171–182 (doi: 10.3189/002214311795306736)

Butt MJ and Kelly REJ (2008) Estimation of snow depth in the UK using the HUT snow emission model. *Int. J. Remote Sens.,* **29**(14), 4249–4267 (doi: 10.1080/01431160801891754)

Chang ATC, Foster JL, Hall DK, Rango A and Hartline BK (1982) Snow water equivalent estimation by microwave radiometry. *Cold Reg. Sci. Technol.,* **5**(3), 259–267 (doi: 10.1016/0165-232X(82)90019-2)

Chen S and Baker I (2010) Evolution of individual snowflakes during metamorphism. *J. Geophys. Res.,* **115**(D21), D21114 (doi: 10.1029/2010JD014132)

Denoth A (1989) Snow dielectric measurements. *Adv. Space Res.,* **9**(1), 233–243

Derksen C and 6 others (2010) Development of a tundra-specific snow water equivalent retrieval algorithm for satellite passive microwave data. *Remote Sens. Environ.,* **114**(8), 1699–1709 (doi: 10.1016/j.rse.2010.02.019)

Domine F, Cabanes A, Taillandier AS and Legagneux L (2001) Specific surface area of snow samples determined by $CH_4$ adsorption at 77 K and estimated by optical microscopy and scanning electron microscopy. *Environ. Sci. Technol.,* **35**(4), 771–780 (doi: 10.1021/es001168n)

Domine F, Salvatori R, Legagneux L, Salzano R, Fily M and Casacchia R (2006) Correlation between the specific surface area and the short wave infrared (SWIR) reflectance of snow. *Cold Reg. Sci. Technol.,* **46**(1), 60–68 (doi: 10.1016/j.coldregions.2006.06.002 )

Domine F and 7 others (2008) Snow physics as relevant to snow photochemistry. *Atmos. Chem. Phys.,* **8**(2), 171–208 (doi: 10.5194/acp-8-171-2008)

Dupont F and 7 others (2012) Monitoring the melt season length of the Barnes Ice Cap over the 1979–2010 period using active and passive microwave remote sensing data. *Hydrol. Process.* (doi: 10.1002/hyp.9382)

Durand M, Kim EJ and Margulis SA (2008) Quantifying uncertainty in modeling snow microwave radiance for a mountain snowpack at the point-scale, including stratigraphic effects. *IEEE Trans. Geosci. Remote Sens.,* **46**(6), 1753–1767 (doi: 10.1109/TGRS.2008.916221)

Fernandes R, Zhao H, Wang X, Key J, Qu X and Hall A (2009) Controls on Northern Hemisphere snow albedo feedback quantified using satellite Earth observations. *Geophys. Res. Lett.,* **36**(21), L21702 (doi: 10.1029/2009GL040057)

Fierz C and 8 others. (2009) *The international classification for seasonal snow on the ground.* UNESCO–International Hydrological Programme, Paris (IHP Technical Documents in Hydrology 83)

Flanner MG, Zender CS, Randerson JT and Rasch PJ (2007) Present-day climate forcing and response from black carbon in snow. *J. Geophys. Res.,* **112**(D11), D11202 (doi: 10.1029/2006JD008003)

Flin F and 9 others (2005) Adaptive estimation of normals and surface area for discrete 3-D objects: application to snow binary data from x-ray tomography. *IEEE Trans. Image Process.,* **14**(5), 585–596 (doi: 10.1109/TIP.2005.846021)

Foster JL and 10 others (2011) A blended global snow product using visible, passive microwave and scatterometer satellite data. *Int. J. Remote Sens.,* **32**(5), 1371–1395 (doi: 10.1080/01431160903548013)

Gallet J-C, Domine F, Zender CS and Picard G (2009) Measurement of the specific surface area of snow using infrared reflectance in an integrating sphere at 1310 and 1550 nm. *Cryosphere,* **3**(2), 167–182 (doi: 10.5194/tc-3-167-2009)

Grannas AM and 34 others (2007) An overview of snow photochemistry: evidence, mechanisms and impacts. *Atmos. Chem. Phys.,* **7**(16), 4329–4373 (doi: 10.5194/acp-7-4329-2007)

Grenfell TC and Warren SG (1999) Representation of a non-spherical ice particle by a collection of independent spheres for scattering and absorption of radiation. *J. Geophys. Res.,* **104**(D24), 31 697–31 709 (doi: 10.1029/2005JD005811)

Grody N (2008) Relationship between snow parameters and microwave satellite measurements: theory compared with Advanced Microwave Sounding Unit observations from 23 to 150 GHz. *J. Geophys. Res.,* **113**(D22), D22108 (doi: 10.1029/2007JD009685)

Hall A (2004) The role of surface albedo feedback in climate. *J. Climate,* **17**(7), 1550–1568 (doi: 10.1175/1520-0442(2004)017<1550:TROSAF>2.0.CO;2)

Jin Z, Charlock TP, Yang P, Xie Y and Miller W (2008) Snow optical properties for different particle shapes with application to snow grain size retrieval and MODIS/CERES radiance comparison over Antarctica. *Remote Sens. Environ.,* **112**(9), 3563–3581 (doi: 10.1016/j.rse.2008.04.011)

Kokhanovsky AA and Zege EP (2004) Scattering optics of snow. *Appl. Opt.,* **43**(7), 1589–1602 (doi: 10.1364/AO.43.001589)

Kontu A and Pulliainen J (2010) Simulation of spaceborne microwave radiometer measurements of snow cover using in situ data and brightness temperature modeling. *IEEE Trans. Geosci. Remote Sens.,* **48**(3), 1031–1044 (doi: 10.1109/TGRS.2009.2030499)

Langlois A, Royer A and Goïta K (2010a) Analysis of simulated and spaceborne passive microwave brightness temperatures using in situ measurements of snow and vegetation properties. *Can. J. Remote Sens.,* **36**(S1), S135–S148 (doi: 10.5589/m10-016)

Langlois A and 8 others (2010b) On the relationship between snow grain morphology and *in-situ* near infrared calibrated reflectance photographs. *Cold Reg. Sci. Technol.,* **61**(1), 34–42 (doi: 10.1016/j.coldregions.2010.01.004)

Lyapustin A, Tedesco M, Wang Y, Aoki T, Hori M and Kokhanovsky A (2009) Retrieval of snow grain size over Greenland from MODIS. *Remote Sens. Environ.,* **113**(9), 1976–1987 (doi: 10.1016/j.rse.2009.05.008)

Matzl M and Schneebeli M (2006) Measuring specific surface area of snow by near-infrared photography. *J. Glaciol.,* **52**(179), 558–564 (doi: 10.3189/172756506781828412)

Matzl M and Schneebeli M (2010) Stereological measurement of the specific surface area of seasonal snow types: comparison to other methods, and implications for mm-scale vertical profiling. *Cold Reg. Sci. Technol.,* **64**(1), 1–8 (doi: 10.1016/j.coldregions.2010.06.006)

Mätzler C (2002) Relation between grain-size and correlation length of snow. *J. Glaciol.,* **48**(162), 461–466 (doi: 10.3189/172756502781831287)

Mätzler C (2006) *Thermal microwave radiation: applications for remote sensing.* Institution of Engineering and Technology, London (IET Electronic Waves Series 52)

Mätzler C and Wiesmann A (1999) Extension of the microwave emission model of layered snowpacks to coarse-grained snow. *Remote Sens. Environ.,* **70**(3), 317–325 (doi: 10.1016/S0034-4257(99)00047-4)

Morin S, Domine F, Arnaud L and Picard G (2010) In-situ monitoring of the time evolution of the effective thermal

conductivity of snow. *Cold Reg. Sci. Technol.,* **64**(2), 73–80 (doi: 10.1016/j.coldregions.2010.02.008)

Nolin AW and Dozier J (2000) A hyperspectral method for remotely sensing the grain size of snow. *Remote Sens. Environ.,* **74**(2), 207–216 (doi: 10.1016/S0034-4257(00)00111-5)

Painter TH, Molotch NP, Cassidy M, Flanner M and Steffen K (2007) Contact spectroscopy for determination of stratigraphy of snow optical grain size. *J. Glaciol.,* **53**(180), 121–127 (doi: 10.3189/172756507781833947)

Park G, Huffaker DL, Zou Z, Shchekin OB and Deppe DG (1999) Temperature dependence of lasing characteristics for long-wavelength (1.3-$\mu$m) GaAs-based quantum-dot lasers. *Photon. Technol. Let.,* **11**(3), 301–303

Picard G, Arnaud L, Domine F and Fily M (2009) Determining snow specific surface area from near-infrared reflectance measurements: numerical study of the influence of grain shape. *Cold Reg. Sci. Technol.,* **56**(1), 10–17 (doi: 10.1016/j.coldregions.2008.10.001)

Pulliainen J (2006) Mapping of snow water equivalent and snow depth in boreal and sub-arctic zones by assimilating space-borne microwave radiometer data and ground-based observations. *Remote Sens. Environ.,* **101**(2), 257–269 (doi: 10.1016/j.rse.2006.01.002)

Rees A, Lemmetyinen J, Derksen C, Pulliainen J and English M (2010) Observed and modelled effects of ice lens formation on passive microwave brightness temperatures over snow covered tundra. *Remote Sens. Environ.,* **114**(1), 116–126 (doi: 10.1016/j.rse.2009.08.013)

Sihvola A and Tiuri M (1986) Snow fork for field determination of the density and wetness profiles of a snow pack. *IEEE Trans. Geosci. Remote Sens.,* **24**(5), 717–721 (doi: 10.1109/TGRS.1986.289619)

Taillandier A-S, Domine F, Simpson WR, Sturm M and Douglas TA (2007) Rate of decrease of the specific surface area of dry snow: isothermal and temperature gradient conditions. *J. Geophys. Res.,* **112**(F3), F03003 (doi: 10.1029/2006JF000514)

Takala M and 7 others (2011) Estimating northern hemisphere snow water equivalent for climate research through assimilation of space-borne radiometer data and ground-based measurements. *Remote Sens. Environ.,* **115**(12), 3517–3529 (doi: 10.1016/j.rse.2011.08.014)

Tedesco M and Kim EJ (2006) Retrieval of dry-snow parameters from microwave radiometric data using a dense-medium model and genetic algorithms. *IEEE Trans. Geosci. Remote Sens.,* **44**(8), 2143–2151 (doi: 10.1109/TGRS.2006.872087)

Toure AM, Goïta K, Royer A, Mätzler C and Schneebeli M (2008) Near-infrared digital photography to estimate snow correlation length for microwave emission modeling. *Appl. Opt.,* **47**(36), 6723–6733 (doi: 10.1364/AO.47.006723)

Warren SG and Wiscombe WJ (1980) A model for the spectral albedo of snow. II. Snow containing atmospheric aerosols. *J. Atmos. Sci.,* **37**(12), 2734–2745 (doi: 10.1175/1520-0469(1980)037<2734:AMFTSA>2.0.CO;2)

Wiesmann A and Mätzler C (1999) Microwave emission model of layered snowpacks. *Remote Sens. Environ.,* **70**(3), 307–316 (doi: 10.1016/S0034-4257(99)00046-2)

Wiscombe WJ and Warren SG (1980) A model for the spectral albedo of snow. I. Pure snow. *J. Atmos. Sci.,* **37**(12), 2712–2733 (doi: 10.1175/1520–0469(1980)037<2712:AMFTSA>2.0.CO;2)

Xie Y, Yang P, Gao B, Kattawar G and Mishchenko M (2006) Effect of ice crystal shape and effective size on snow bidirectional reflectance. *J. Quant. Spectrosc. Radiat. Transfer,* **100**(1–3), 457–469 (doi: 10.1016/j.jqsrt.2005.11.056)

Yang P and Liou KN (1996) Geometric-optics–integral-equation method for light scattering by nonspherical ice crystals. *Appl. Opt.,* **35**(33), 6568–6584 (doi: 10.1364/AO.35.006568)

*MS received 30 November 2011 and accepted in revised form 25 May 2012*

## 3.2 Paramétrisation de la SSA dans MEMLS

Malgré la précision des nouvelles mesures de SSA de la neige, ce dernier paramètre n'a pas été validé pour la modélisation du TR MOP du couvert nival. Suite au développement des instruments IRIS et SWIRcam, un deuxième objectif secondaire de la thèse est de valider et calibrer la SSA de la neige comme paramètre de taille de grains de neige pour la modélisation du signal MOP du couvert nival. Des études récentes (Langlois *et al.*, 2010a; Brucker *et al.*, 2011) ont démontré qu'il est possible de minimiser l'erreur de la modélisation du signal MOP provenant de la paramétrisation de la taille des grains de neige en optimisant un facteur multiplicatif à la SSA. Ce travail s'inscrit donc dans le cadre de cette thèse et a été publié dans la revue *IEEE Transaction on Geoscience and Remote Sensing* (Montpetit *et al.*, 2013) et a aussi fait l'objet d'une présentation à la conférence *Eastern Snow Conference 2012* à Frost Valley (NY), États-Unis. Ce travail a permis de démontrer qu'il est possible de réduire l'erreur de la modélisation de la $T_B$ à 11.6 K en appliquant un facteur multiplicatif de 1.3 sur le paramètre de taille de grains de neige du modèle *Microwave Emission Model of Layered Snowpacks* (MEMLS) issu de la SSA mesurée à l'aide des instruments IRIS et SWIRcam. L'avantage de ce résultat comparativement aux études antérieures est que les mesures de la SSA avec l'IRIS et la SWIRcam sont plus précis et reproductibles et donc les résultats des simulations avec MEMLS sont eux aussi plus reproductibles et précis. Ces résultats sont présentés dans la section *III.A* de l'article Montpetit *et al.* (2013) présentée en section 5.0.2 de cette thèse. L'acquisition, le traitement, l'analyse de données, la production des résultats ainsi que la rédaction et la révision de l'article (Montpetit *et al.*, 2013) ont été réalisé dans le cadre de cette thèse avec l'aide des co-auteurs de l'article.

# 4 Résultats : Modélisation de l'émission MOP du sol gelé

Une grande incertitude de la modélisation de la $T_B$ du couvert nival est la contribution provenant du sol. Très peu d'études récentes se sont concentrées sur la modélisation du signal MOP du sol gelé dans les régions arctiques. Il a été démontré par Roy *et al.* (2013) que le sol peut avoir un impact sur le signal MOP même pour des fréquences plus élevées (jusqu'à 37 GHz) pour des couverts de neige moins dense et épais. Wegmüller et Mätzler (1999) ont démontré qu'il est possible de modéliser l'émissivité du sol à ces fréquences mais Roy *et al.* (2013) ont démontré que ce modèle nécessitait des modifications afin que la modélisation du TR MOP du manteau neigeux soit optimale. Le travail présenté dans l'article Montpetit *et al.* (2013) de la section 5.0.2 démontre aussi que le

modèle de Wegmüller et Mätzler (1999) nécessite des modifications pour son utilisation dans le modèle MEMLS. Toutefois, ce travail était incomplet dû au manque de données géophysiques et radiométriques précises du sol. Dans l'optique d'améliorer la modélisation du TR MOP du couvert nival, l'amélioration de la modélisation de l'émissivité MOP du sol gelé s'inscrit donc dans le cadre de cette thèse. Les données utilisées pour cette section du travail ont été acquises par l'équipe neige du CARTEL et des collaborateurs dans la région de la Baie James et Umiujaq (Québec), Canada, durant les hivers 2012-2013 et 2013-2014. Les mesures de la campagne Baie James 2012-2013 ont fait l'objet d'une présentation par affiche à la conférence *Eastern Snow Conference 2013* à Huntsville (Ontario), Canada. Les résultats de l'analyse de la modélisation de l'émissivité du signal MOP du sol gelé sont aussi présentés dans un article présentement en révision dans le journal *Geoscience and Remote Sensing Letters* (Montpetit *et al.*, En Revision). Ce travail démontre qu'il est possible calibrer le modèle de Wegmüller et Mätzler (1999) afin de minimiser l'erreur entre la $T_B$ mesurée et simulée à 4.65 K pour des fréquences de 10.7, 19 et 37 GHz en H-Pol et V-Pol. L'acquisition, le traitement et l'analyse des mesures ainsi que la production des résultats, la rédaction et la révision (en cours) de l'article ont été fait dans le cadre de cette thèse avec l'aide des co-auteurs de l'article.

### 4.0.1 Article : In-situ passive microwave parameterization of sub-arctic frozen organic soils

Plusieurs applications MOP telles que l'estimation de l'émissivité de surface ou l'analyse du couvert nival, nécessitent l'estimation de l'émission provenant du sol. De grandes incertitudes persistent dans la modélisation de l'émissivité du sol lorsqu'il est gelé. Dans cet article, une méthode empirique pour estimer l'émission de sols organiques de l'Arctique canadien à 10.7, 19 et 37 GHz est présentée. Cette méthode a été calibrée et validée à l'aide de mesures radiométriques in-situ à des angles d'incidences de $0^o$ à $60^o$ de sols du nord-est de l'Arctique canadien. Les valeurs de permittivités effectives retrouvées donnent une RMSE entre les $T_B$ mesurées et simulées de 4.8 K considérant toutes les fréquences. Cette méthode présente un très grand potentiel dans l'amélioration de l'estimation de la contribution du sol gelé à la $T_B$ du couvert nival. L'originalité de ce travail provient du fait que très peu d'études ont acquis le type de mesures radiométriques ($T_B$ multi-angles et multifréquences) pour évaluer l'émission de sols organiques en milieu Arctique. Les tableaux 4.1 et 4.2 montre les résultats principaux de ce travail.

Tableau 4.1 – Permittivité effective ($\epsilon'_{eff}$), rugosité de surface effective($\sigma_{eff}$) ainsi que le paramètre de dépolarisation ($\beta$) retrouvés pour des sols organiques de l'Arctique canadien. — Effective permittivity ($\epsilon_{eff}$), effective soil surface roughness ($\sigma_{eff}$) and depolarisation coefficient ($\beta$) retrieved for organic soils of the canadian Arctic.

| $f$ (GHz) | $\epsilon'_{eff}$ | $\sigma_{eff}$ | $\beta$ |
|---|---|---|---|
| 10.7 | 3.20 | | 1.08 |
| 19 | 3.45 | 0.19 | 0.72 |
| 37 | 4.53 | | 0.42 |

Tableau 4.2 – Biais et RMSE entre les $T_B$ mesurées et simulées pour six canaux pour des sites de sols organiques de l'Arctique canadien. — Bias and RMSE between modeled and measured $T_B$ for six channels for organic soil sites of the canadian Arctic.

| Canal | Biais (K) | RMSE (K) |
|---|---|---|
| 11V | -1.3 | 1.6 |
| 11H | -0.5 | 4.0 |
| 19V | -2.2 | 4.4 |
| 19H | -1.5 | 3.9 |
| 37V | 0.6 | 5.8 |
| 37H | 2.2 | 6.0 |
| Tous | -0.5 | 4.8 |

# In-situ passive microwave parameterization of sub-arctic frozen organic soils

Benoit Montpetit*, Alain Royer*, Alexandre Roy* and Alexandre Langlois* *Centre d'Application et de Recherche en Télédétection, Université de Sherbrooke, Sherbrooke, Québec, Canada

**Abstract**

Many applications such as passive microwave emissivity estimates or snow cover analysis need to take into account the soil contribution to the overall signal emission. Soil emission modeling presents large uncertainties when the soil is frozen. In this paper, an empirical retrieval method is presented, specifically for rough frozen soil permittivity estimates at 10.7, 19 and 37 GHz. The method was tested and validated using in-situ passive microwave measurements at incidence angles from 0 to $60^o$ of sub-arctic frozen organic soils in Northeastern Canada. The retrieved permittivity values give an overall RMSE between the measured and simulated brightness temperatures of 4.57 K for all frequencies combined. The method shows great potential to improve the estimation of the frozen soil contribution to the measured passive microwave brightness temperature.

**Index Terms**

Passive Microwave, frozen soil, rough soil, dielectric soil properties, soil reflectivity modeling.

## I. Introduction

FOR many years, scientists have studied bare soil reflectivity modeling ( [1]; [2]; [3]; [4]; [5]), partly motivated by the ability to retrieve soil moisture from satellite data; such as the Soil Moisture and Ocean Salinity (SMOS) mission [6]. The future Soil Moisture Active and Passive (SMAP) mission [7] will also study soil moisture from satellite-based data, but will also study the soil state (frozen/thawed) in northern regions [8]. The majority of these studies mainly focus on L-band rather than higher frequencies ( [9]; [10]; [5]; [11]; [12]), given the ability of such wavelengths to penetrate vegetation and snow. For cryosphere studies frequencies up to 37 GHz are commonly used [13]. Some studies have shown that, even at these high frequencies, the soil contribution to the emitted signal at the surface of the snowpack has to be estimated ( [14]; [15]). A major issue with the estimation of the soil contribution to the emitted signal at the surface is the estimation of frozen soil permittivity where the real part drastically changes when the soil freezes and the very low imaginary part controls the penetration depth [16]. Different models exist but still need soil in-situ measurements (soil bulk density, volumetric moisture, temperature, etc.) that are complex to extract in remote arctic soils.

In this paper, we present a simple method to retrieve passive microwave soil properties from brightness temperature measurements using the semi-empirical model developed by Wegmüller & Mätzler [3] (hereafter referred to as WM99) and validate these properties using an independent dataset taken at the calibration site and another site in northern Québec (see Section II). We first describe the study sites and the geophysical and radiometric measurements. Then, the models and the optimization method will be detailed. Finally, the optimization and validation results will be presented and discussed.

## II. Study sites and measurements

The soil and radiometric data for this study were first collected in the James Bay area, Québec ($53^o$26'N, $76^o$46'W, 186 m a.s.l.) during three intensive measurement periods (IMP) in January ($8^{th}$ to $12^{th}$, IMP1),

Manuscript received July X, 2014; revised July X, 2014. Corresponding author: B. Montpetit (benoit.montpetit2@usherbrooke.ca).

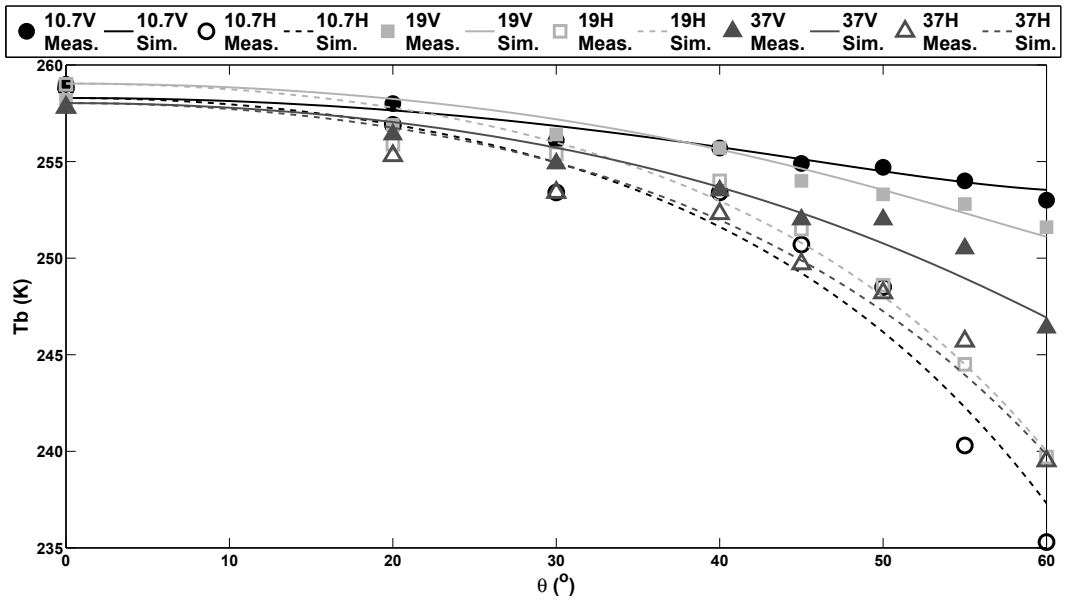


Fig. 1. Typical angular $Tb$ measurements (points) acquired at the BJCal site and the resulting simulations (lines) using the WM99 model with the optimized parameters of Table I at 10.7 (black circles and lines), 19 (light gray squares and lines) and 37 (dark gray triangles and lines) GHz at V-Pol (filled shapes and full lines) and H-Pol (empty shapes and dotted lines). $T_{soil}^{eff} = -5 \pm 2.5^{o}$C.

February ($12^{th}$ to $17^{th}$, IMP2) and March ($19^{th}$ to $23^{rd}$, IMP3) of 2013. More data was also acquired near Umiujaq, Québec ($56^{o}$33'N, $76^{o}$30'W, 74 m a.s.l.) during one intensive period in January ($21^{st}$ to $28^{th}$ of 2014). The bare soil measurements were done in clearings with minimal influence from the environment (topography, vegetation, etc.) to the measured microwave brightness temperature ($Tb$). A total of 8 sites were selected in this study where the soil composition mainly consisted of organic matter.

The soil $Tb$ measurements were acquired using surface-based radiometers on a mobile sled at 10.7, 19 and 37 GHz in both horizontal (H-Pol) and vertical (V-Pol) polarizations. Calibrations were done on a regular basis throughout the winter season using a warm and cold target as described by Asmus and Grant [17]. The downwelling $Tb_{sky}$ were estimated with an atmospheric absorption microwave model [18] implemented in the Helsinki University of Technology (HUT, [19]) model, using the 29 atmospheric layers above surface of the North American Regional Reanalysis (NARR) data. The measured Tb at frequency $f$ and polarization $p$ can then be described by:

$$Tb_{soil}(f,p) = (1 - \Gamma_{f,p})T_{soil}^{eff} + \Gamma_{f,p}Tb_{sky}^{eff}(f,p) \quad (1)$$

where $\Gamma_{f,p}$ is the rough soil reflectivity at polarization $p$ and $T_{soil}^{eff}$ is the effective soil physical temperature. Temperature profiles were taken using a Traceable 2000 digital temperature probe with an accuracy of 0.1 $^{o}$C for depths of 0 to 10 cm with an interval of 2 cm. Since the soil is considered a homogeneous medium for this study, the effective soil temperature was estimated to be the averaged temperature over the first 5 cm.

Among the 8 sites analyzed, a James Bay site, measured on February $13^{th}$ 2013, was considered for model calibration purposes (hereafter referred to as the BJcal site) since it was the only site where a wide range of incidence angle ($0^{o}$ to $60^{o}$) was measured with the surface-based radiometer. The site consisted of a bare soil area where the snow was removed (20 m long by 5 m wide) to eliminate any possible contribution coming from the snow walls around the bare soil surface. Measurements over the 20 m long transects were taken in order to establish the variability of the soil $Tb$ measurements. The averaged soil temperature over the first 5 cm was -5 $\pm$ 2.5 $^{o}$C. The same site was revisited during the winter IMPs and

other sites were measured during the 2013 winter campaign for validation purposes (hereafter referred to as BJval sites). The BJval sites were also clearings and soil temperatures varied from -13$^o$C to -5$^o$C. Three other validation sites were measured during the 2014 winter campaign in Umiujaq (hereafter referred to as UMIval sites). The UMIval sites were clearings and soil temperatures varied from -17$^o$ C to -10$^o$C.

## III. Method

The WM99 model describes the rough soil reflectivity at a frequency $f$ and polarization $p$ ($\Gamma_{f,p}$) by its smooth Fresnel reflectivity in H-Pol ($\Gamma_{f,p}^{Fresnel}$) which depends on the incidence angle ($\theta$) and the real part of the soil permittivity ($\epsilon'$), weighted by an attenuation factor that depends on the standard deviation in height of the surface (soil roughness, $\sigma$), the measured wavenumber ($k$) and a polarization ratio dependency factor. As shown in [14], a modification to this model was applied for this study using a $\beta$ factor to take into account the frequency dependency of the polarization reflectivity ratio. The WM99 model for incidence angle lower than 60$^o$ is therefore described by:

$$\Gamma_{f,H}(\theta, \epsilon'_f, \sigma) = \Gamma_{f,H}^{Fresnel}(\theta, \epsilon'_f) \exp(-(k\sigma)^{\sqrt{-0.1\cos\theta}}) \quad (2)$$

$$\Gamma_{f,V}(\theta, \epsilon'_f, \sigma) = \Gamma_{f,H}(\theta, \epsilon'_f, \sigma) \cos^{\beta_f}\theta \quad (3)$$

The first part of the optimization process consisted in obtaining the soil permittivity ($\epsilon'_f$) for each frequency and surface roughness ( $\sigma$) that minimized the error between simulated and measured $Tb$ in H-pol using Eq. 2 for all the incidence angles between 0$^o$ and 60$^o$. The optimization algorithm used is the least squared error minimization algorithm of Levenberg-Marquardt ( [20], hereafter referred to as LM63). Afterwards, using the soil properties of the first step, the $\beta_f$ factor was determined with Eq. 3 using the LM63 algorithm to minimize the error between the V-pol $Tb$ measurements and the simulations.

Once the optimized parameters were obtained, these retrieved parameters were inserted in the WM99 and the soil $Tb$ were modeled and compared to the measured $Tb$ of the BJval sites. Finally, these parameters were validated against $Tb$ measurements acquired at another northern sites (UMIval sites).

## IV. Results

Table I shows the optimization results using the LM63 algorithm at H-Pol and V-Pol. The final RMSE obtained for each optimization is given. Since the soil roughness is considered as a geophysical parameter specific to the soil, it can be considered frequency independent ( [3]; [21]) and a different soil permittivity per frequency was obtained with the LM63 optimization on H-Pol measurements. It should be noted that since no soil surface roughness measurements were acquired, the surface roughness value ($\sigma$) obtained in Table I is an effective parameter retrieved through model inversion and should not be considered as a true geophysical parameter. An optimization per frequency was done for the $\beta_f$ factor in V-Pol to determine if the $\beta_f$ factor was frequency dependent. Given the different values of $\beta_f$ obtained, it can be concluded that the $\beta_f$ factor is frequency dependent as mentioned by [14].

TABLE I

TABLE 1: FROZEN SOIL PERMITTIVITY AND ROUGHNESS (EQ. 2) AND THE $\beta_f$ FACTOR (EQ. 3) RETRIEVED THROUGH THE LM63 OPTIMIZATION PROCESS USING THE H-POL $Tb$ AND V-POL $Tb$ RESPECTIVELY, AT 10.7, 19 AND 37 GHZ IN THE WM99. THE RESULTING RMSE OF THE OPTIMIZATION PROCESS IS ALSO GIVEN.

| Frequency (GHz) | Soil Permittivity | Soil Rougness (cm) | RMSE $Tb$(H-Pol) (K) | $\beta_f$ | RMSE $Tb$(V-Pol) (K) |
|---|---|---|---|---|---|
| 10.7 | 3.20 | | | 1.08 | 0.93 |
| 19 | 3.45 | 0.19 | 1.23 | 0.72 | 0.75 |
| 37 | 4.53 | | | 0.42 | 0.43 |

Figure 1 presents the typical angular $Tb$ measurements acquired at the James Bay site (BJcal). The results of the modeling using the WM99 model and the parameters of Table I are also given in Figure

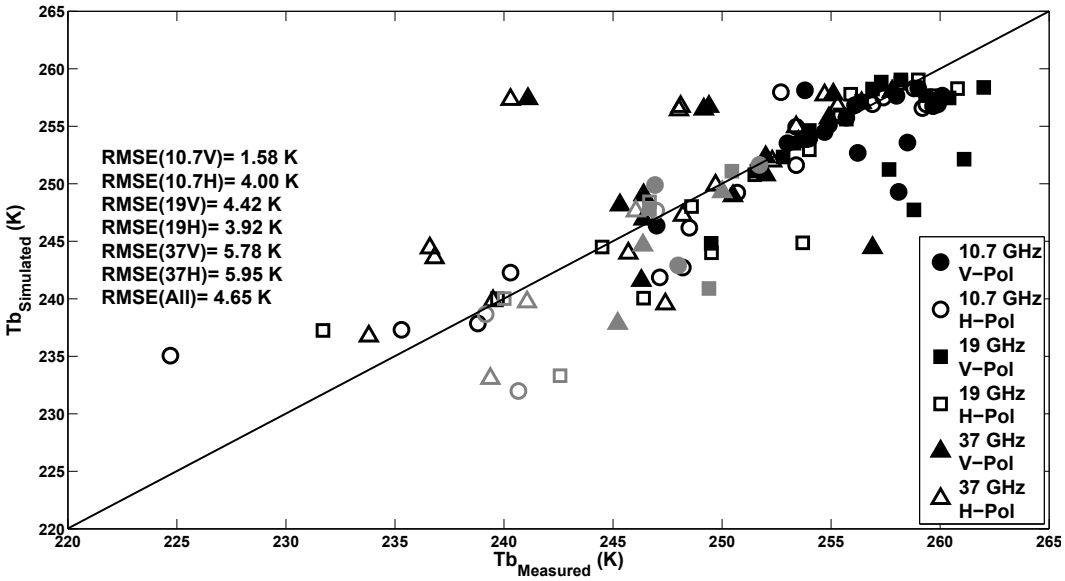


Fig. 2. Validation results between modeled and measured $Tb$ for a frozen bare soil using the WM99 model and the parameters of Table I at 10.7, 19 and 37 GHz at both H-Pol and V-Pol for the James Bay sites (BJcal and BJval) (black) and the Umiujaq sites (UMIval) (gray). The RMSE of the different channels are given. The solid black line corresponds to the 1:1 line.

1. Figure 1 shows the decrease in $Tb$ with increasing incidence angle. This means that the reflectivity increases with incidence angle (Eq. 1). This result is similar to what was previously obtained by [3]. It also shows that the decrease is stronger in H-Pol compared to V-Pol. This can be explained by a stronger increase of the surface reflectivity with incidence angle in H-Pol compared to V-Pol.

Figure 2 shows the results of comparison between the simulations using the WM99 model optimized with the parameters of Table I against the measured $Tb$ of the James Bay sites (BJcal and BJval sites) acquired throughout the 2013 winter, and the Umiujaq sites (UMIval). The measured and simulated $Tb$ are, in general, in agreement with a RMSE ranging from 1.6 to 6.0 K (overall RMSE = 4.65 K). There is some scatter especially at 19 and 37 GHz (overall $R^2$=0.64) which could be explained by the roughness variability (see discussion below) and the uncertainty in the downwelling $Tb$ where the surrounding environment can be slightly more important than the estimated $Tb_{sky}$.

The RMSE obtained at James Bay (4.58 K) is similar to the one of the Umiujaq sites (4.49 K) which suggests that the optimization process could be applied to other sites characterized by similar northern organic frozen soil composition. Table II summarizes the errors obtained between the simulations and the measurements for both the James Bay and Umiujaq campaigns and two campaigns combined. The mean bias appears relatively small at -0.45 K. The overall RMSE is comparable to the measured $Tb$ variability over a 20 m transect which was of 5.18 K, 4.41 K and 6.79 K at 37, 19 and 10.7 GHz respectively. This variability can be explained by the surface roughness variability. As a matter of fact, over this transect, keeping the same permittivity as obtained above (Table I) and fitting an optimized roughness value for each site, over a range of 0 to 2 cm, reduces the RMSE from 6.07 K to 0.37 K. The range of surface roughness obtained in this optimization process was $0.01 \leq \sigma \leq 2$ cm, $0.36 \leq \sigma \leq 2$ cm and $0.01 \leq \sigma \leq 0.23$ cm at 10.7, 19 and 37 GHz respectively.

It is difficult to compare the real part of the permittivity values ($\epsilon'_f$) obtained in this study to previous studies because of all the factors and conditions (soil types, soil ice fraction, soil temperatures, frequencies, etc.) that influence these values. This information is not always available. As reference, from 1 to 100 GHz and at a temperature of 0 $^o$C, $\epsilon'_f$ of pure ice is constant at $\approx 3.2$ (with a weak temperature dependence), where $\epsilon'_f$ of free water decreases following a power function from 90 to 6 [16] (according to [22], we get $\epsilon'_f$ of pure water at 0 $^o$C of 85.9, 38.3, 20.5 and 10.2 at 1.4, 11, 19 and 37 GHz respectively).

TABLE II
MEAN BIASES AND RMSE BETWEEN SIMULATED AND MEASURED $Tb$ AT 10.7, 19 AND 37 GHZ AT BOTH H-POL AND V-POL FOR THE JAMES BAY AND UMIUJAQ MEASUREMENT CAMPAIGNS. THE OVERALL MEAN BIAS AND RMSE ARE ALSO GIVEN.

| Channel | James Bay | | Umiujaq | | All | |
|---|---|---|---|---|---|---|
| | Bias (K) | RMSE (K) | Bias (K) | RMSE (K) | Bias (K) | RMSE (K) |
| 10.7V | -1.36 | 3.15 | -0.73 | 3.40 | -1.26 | 1.58 |
| 10.7H | -0.10 | 3.77 | -2.83 | 5.03 | -0.53 | 4.00 |
| 19V | -2.19 | 4.31 | -2.24 | 4.97 | -2.20 | 4.42 |
| 19H | -1.34 | 3.57 | -2.50 | 5.44 | -1.52 | 3.92 |
| 37V | 1.36 | 6.01 | -3.26 | 4.38 | 0.63 | 5.78 |
| 37H | 2.97 | 6.27 | -2.02 | 3.83 | 2.18 | 5.95 |
| 10.7 | -0.73 | 3.47 | -1.78 | 4.29 | -0.89 | 3.62 |
| 19 | -1.76 | 3.95 | -2.37 | 5.21 | -1.86 | 4.18 |
| 37 | 2.17 | 6.14 | -2.64 | 4.12 | 1.41 | 5.87 |
| All | -0.11 | 4.67 | -2.26 | 4.56 | -0.45 | 4.65 |

Rautiainen et al. [23] showed that at L-band the soil permittivity varied from 3.3 to 3.8 in frozen soils having temperature ranging between -6 $^o$C to -3.7 $^o$C but measured in-situ permittivity values of 6.3 to 7.1 for a frozen wetland site in Northern Finland [24]. Schwank et al. [25] showed that for L-band, the frozen soil permittivity varies from 3.5 to 4.5, while Hallikainen et al. [26] showed that it varies from 5 up to 8 in the 10 to 18 GHz frequency range. Puilliainen et al. [27] used a fixed value of 6 to simulate the frozen soil $Tb$ at 19 and 37 GHz. Finally, Mironov et al. [28] developed a temperature dependent permittivity model and showed that the permittivity could vary from 3 to 4.5 in the 10 to 16 GHz range for a frozen soil at -25$^o$C. Here, we obtained values of 3.20 at 10.7 GHz, 3.45 at 19 GHz and 4.53 at 37 GHz for soils between -13$^o$C to -5$^o$C (the first 5 cm). This is in agreement with these different studies where for lower frequencies, we have a lower soil permittivity. The retrieved values of this study might have been different if another rough bare soil reflectivity model was used (e.g. [2], [21]) but such models had too many parameters to inverse in the optimization process to be an efficient method of retrieving effective soil parameters.

As mentioned above, one of the main difficulties in the retrieval process is the combined effect of permittivity and the surface roughness. Figure 3 shows the sensitivity of the mean measured-simulated $Tb$ (V & H) RMSE on the soil permittivity and the surface roughness. The simulations conditions are those of the BJcal site.

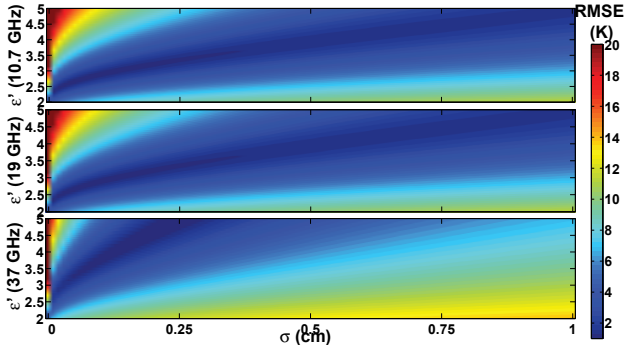


Fig. 3. Sensitivity test of the $Tb$ RMSE (in K, color scale) on the soil permittivity ($\epsilon'$) and the surface roughness ($\sigma$) on the BJcal site measurements (Figure 1), and for 3 frequencies.

Figure 3 shows that the sensitivity to the surface roughness is weaker than for the permittivity. Note that the pattern for $1 \leq \sigma \leq 2$ cm (not shown) can be extrapolated from the one around $\sigma$=1 cm, and that for $\sigma$=0 cm, a discontinuity results from the abrupt change from the Fresnel reflectivity to the rough surface reflectivity (Eq. 2). For $\sigma < 1$ cm, it appears that it exist an ensemble of $(\epsilon', \sigma)$ couples that

provides an ensemble of solutions with low RMSE (dark blue in Fig. 3). However, when combining the three frequencies showing different behaviour for the lowest RMSE values, the range where the minimum RMSE combining all three frequencies occurs for a limited range of $\sigma$, $0.1 < \sigma < 0.23$ cm. The optimized $(\epsilon', \sigma)$ couples are found for $\sigma$=0.19 cm (Table I). The results from Figure 3 and assuming variability in $Tb$ of the order of 5 K, suggest that the retrieved soil permittivity values can be defined with an accuracy of $\pm$ 1.00 and the retrieved surface roughness with an accuracy of $\pm$ 0.12 cm.

## V. Conclusion

In this study, we show that the simple rough soil emission model proposed by [3] can be optimized for frozen soils using a least squared minimization function on the soil permittivity from in-situ brightness temperature measurements at several angles. This approach has been applied to retrieve the soil permittivity at 10.7, 19 and 37 GHz for one sub-arctic site in Northern Québec, and validated over different independent sites in the same region and at different dates during the winter covering a range of soil temperatures (-13$^o$C to -5$^o$C). The retrieved permittivity values of 3.20, 3.45 and 4.53, respectively at 10.7, 19 and 37 GHz, give an overall RMSE = 4.57 K between measured and simulated brightness temperatures. This error is comparable to the standard deviation (local variability of $\pm$ 6.79 K) of the measured $Tb$ over a 20 m transect analysed. These retrieved soil permittivity values are in the range of previous frozen soil studies. It was also show that the retrieved permittivity is within an accuracy of $\pm$ 1 in permittivity value.

## Acknowledgment

The authors would like to thank Patrick Cliche, Serge Langlois, Nathalie Thériault, Nicolas Marchand, Caroline Dolant and Bruno-Charles Busseau from Université de Sherbrooke, Éric Lefebvre, Bernard Lesaffre and Ghislain Picard for the Laboratoire de glaciologie et géophysique de lenvironnement de Grenoble and and Florent Dominé and Mathieu Barrere from Takuvik, CNRS, Université de Laval, Québec for their contributions to the field work achieved to retrieve these measurements. This work was funded by NSERC, CFI, ENVIRO-Nord and NSTP from Canada and by IPEV from France.

## References

[1] J.R.Wang and B.J. Choudhury Remote sensing of soil moisture content over bare field at 1.4 GHz frequency. *Journal of Geophysical Research*, 86(C6):5277–5282, 1981.

[2] B.J. Choudhury, T.J. Schmugge, A. Chang and R.W. Newton Effect of surface roughness on the microwave emission from soils. *Journal of Geophysical Research*, 89(C9):5699–5706, 1979.

[3] U. Wegmüller and C. Mätzler Rough bare soil reflectivity model *IEEE Transactions on Geoscience and Remote Sensing*, 37(3):1391–1395, 1999.

[4] M. Schwank, J.-P. Wigneron, E. López-Baeza, I. Völksch, C. Mätzler and Y.H. Kerr L-band radiative properties of vine vegetation at the MELBEX III SMOS cal/val site *IEEE Transactions on Geoscience and Remote Sensing*, 50(5):1587–1601, 2010.

[5] J.-P. Wigneron, A. Chanzy, Y.H. Kerr, H. Lawrence, J. Shi, M.J. Escorihuela, V. and Mironov, A. Mialon, F. Demontoux, P. De Rosnay and K. Saleh-Contell Evaluating an improved parameterization of the soil emission in L-MEB *IEEE Transactions on Geoscience and Remote Sensing*, 49(4):1177-1189, 2011.

[6] Y.H. Kerr, P. Waldteufel, J.-P. Wigneron, J.-M. Martinuzzi, J. Font and M. Berger Soil moisture retrieval from space: The Soil Moisture and Ocean Salinity (SMOS) mission *IEEE Transactions on Geoscience and Remote Sensing*, 39(8):1729–1735, 2001.

[7] M.E. Brown, V. Escobar, S. Moran, D. Entekhabi, P.E. O'Neill, E.G. Njoku, B. Doorn and J.K. Entin NASA's soil moisture active passive (SMAP) mission and opportunities for applications users *Bulletin of the American Meteorological Society*, 94(8):1125–1128, 2013.

[8] M. Spencer, S. Dunbar and C. Chen The Soil Moisture Active Passive (SMAP) radar: Measurements at high latitudes and of surface freeze/thaw state *IEEE National Radar Conference - Proceedings*, Ottawa, ON, Canada, 2013.

[9] Y.H. Kerr, P. Waldteufel, P. Richaume, J.-P. Wigneron, P. Ferrazzoli, A. Mahmoodi, A. Al Bitar, F. Cabot, C. Gruhier, S.E. Juglea, D. Leroux, A. Mialon and S. Delwart The SMOS soil moisture retrieval algorithm *IEEE Transactions on Geoscience and Remote Sensing*, 50(5):1384-1403, 2012.

[10] A. Mialon, J.-P. Wigneron, P. De Rosnay, M.J. Escorihuela and Y.H. Kerr Evaluating the L-MEB model from long-term Microwave measurements over a rough field, SMOSREX 2006 *IEEE Transactions on Geoscience and Remote Sensing*, 50(5):1458–1467, 2012.

[11] H. Lawrence, J.-P. Wigneron, F. Demontoux, A. Mialon and Y.H. Kerr Evaluating the Semiempirical HQ Model used to Calculate the L-Band Emissivity of a Rough Bare Soil *IEEE Transaction on Geoscience and Remote Sensing*, 51(7):4075-4084, 2013.

[12] J. Shi, K.S. Chen, Q. Li, T.J. Jackson, P.E. O'Neill and L. Tsang A parameterized surface reflectivity model and estimation of bare-surface soil moisture with L-band radiometer *IEEE Transactions on Geoscience and Remote Sensing*, 40(12):2674–2686, 2002.

[13] A.J. Dietz, C. Kuenzer, U. Gessner and S. Dech Remote sensing of snow - a review of available methods *International Journal of Remote Sensing*, 33(13):4094–4134, 2012.
[14] B. Montpetit, A. Royer, A. Roy, A. Langlois and C. Derksen Snow Microwave Emission Modeling of Ice Lenses Within a Snowpack Using the Microwave Emission Model for Layered Snowpacks *IEEE Transactions on Geoscience and Remote Sensing*, 51(9):4705–4717, 2013.
[15] A. Roy, G. Picard, A. Royer, B. Montpetit, F. Dupont, A. Langlois, C. Derksen and Nicolas Champollion Brightness Temperature Simulations of the Canadian Seasonal Snowpack Driven by Measurements of the Snow Specific Surface Area *IEEE Transactions on Geoscience and Remote Sensing*, 51(9):4692–4704, 2013.
[16] C. Mätzler, W. Ellison, B. Thomas, A. Sihvola and M. Schwanck Dielectric properties of natural media *In C. Mätzler (Ed.), Thermal microwave radiation: Applications for remote sensing*, 427–539, 2006.
[17] K.W. Asmus and C.Grant. Surface based radiometer (sbr) data acquisition system. *International Journal of Remote Sensing*, 20(15-16):3125–3129,1999.
[18] H.J. Liebe MPM-An atmospheric millimeter-wave propagation model *International Journal of Infrared and Millimeter Waves*, 10:631-650.
[19] J.T. Pulliainen, J. Grandell and M.T. Hallikainen HUT Snow Emission Model and its Applicability to Snow Water Equivalent Retrieval *IEEE Transactions on Geoscience and Remote Sensing*, 37:1378-1390, 1999.
[20] D. Marquardt An Algorithm for Least-Squares Estimation of Nonlinear Parameters *SIAM Journal of Applied Mathematics*, 11:431–441, 1963.
[21] B. Montpetit, A. Royer, J.-P. Wigneron, A. Chanzy and A. Mialon Evaluation of multi-frequency bare soil reflectivity models *Submitted to Remote Sensing of Environment*, July 2014.
[22] T.Meissner and F. J. Wentz The complex dielectric constant of pure and sea water from microwave satellite observations. *IEEETransactions on Geoscience and Remote Sensing*, 42(9):1836–1849, 2004.
[23] K. Rautiainen, J. Lemmetyinen, J. Pulliainen, J. Vehvilainen, M. Drusch, A. Kontu, J. Kainulainen and J. Seppänen L-band radiometer observations of soil processes in boreal and subarctic environments *IEEE Transactions on Geoscience and Remote Sensing*, 50:1483-1497, 2012.
[24] K. Rautiainen, J. Lemmetyinen, M. Schwank, A. Kontu, C. B. Ménard, C. Mätzler, M. Drusch, A. Wiesmann, J. Ikonen and J. Pulliainen Detection of soil freezing from L-band passive microwave observations *Remote Sensing of Environment*, 147(5):206–218, 2014.
[25] M. Schwank, M. Stähli, H. Wydler, J. Leuenberger, C. Mätzler and H. Flühler Microwave L-band emission of freezing soil *IEEE Transactions on Geoscience and Remote Sensing*, 42:1252-1261, 2004.
[26] M.T. Hallikainen, F.T Ulaby, M.C. Dobson, M.A. El-Rayes and L.-K. Wu Microwave dielectric behavior of wet soil - part I: empirical models and experimental observations *IEEE Transactions on Geoscience and Remote Sensing*, GE-23:25-34, 1985.
[27] J. Pulliainen Mapping of snow water equivalent and snow depth in boreal and sub-arctic zones by assimilating space-borne microwave radiometer data and ground-based observations *Remote Sensing of Environment*, 101:257-269, 2006.
[28] V.L. Mironov, R.D. De Roo and I.V. Savin Temperature-dependable microwave dielectric model for an arctic soil *IEEE Transactions on Geoscience and Remote Sensing*, 48(6):2544–2556, 2010.

# 5 Résultats : Modélisation du TR MOP des croutes de glace à l'intérieur du couvert neigeux

Dans le contexte des changements climatiques, des événements extrêmes surviennent durant la saison hivernale, comme des périodes de dégel-regel ou des épisodes de pluie, ce qui provoque la formation de croutes de glace à la surface ou à l'intérieur, par percolation de l'eau, du couvert nival (Putkonen *et al.*, 2011; Rennert *et al.*, 2009). Ces croutes de glace modifient fortement le signal MOP du couvert nival (Rees *et al.*, 2010; Grody, 2008). Il est donc important de modéliser adéquatement les effets des croutes de glace sur le TR MOP du couvert neigeux. Cet objectif s'inscrit donc dans le cadre de l'objectif général de cette thèse qui est d'améliorer la modélisation du TR MOP du couvert nival. Il a été démontré qu'il était possible de diminuer l'erreur entre les $T_B$ mesurées et simulées en simulant une glace pure en surface du couvert nival (Grody, 2008) ou en simulant une couche de neige très dense (Lemmetyinen *et al.*, 2010b) lorsqu'il y a présence de croutes de glace dans le couvert neigeux. Cette partie de l'étude a été présentée dans les sections III.C et IV de l'article présenté à la section 5.0.2 (Montpetit *et al.*, 2013). Ce travail a permis de démontrer qu'en simulant une couche de glace pure, là où la croute de glace a été observée dans le couvert neigeux, il est possible de retrouver une erreur entre les $T_B$ mesurées et simulées de 14.0 K. Cette erreur est similaire à celle observée sur les simulations de couverts de neige où il n'y a pas de croutes de glace.

### 5.0.2 Article : Snow microwave emission modeling of ice lenses within a snowpack using the Microwave Emission Model for Layered Snowpacks

La formation de croutes de glace suivant des événements de pluies hivernales ou de dégel-regel risque de devenir de plus en plus fréquente avec l'augmentation de la température dans les hautes latitudes. Ces croutes de glace affectent significativement les propriétés micro-ondes du couvert nival, notamment la $T_B$ qui est grandement utilisée pour assurer le suivit du couvert nival par télédétection satellitaire. Afin de mieux comprendre leur impact, une modélisation adéquate des effets des croutes de glace est nécessaire. Cet article montre les effets des croutes de glace sur la $T_B$ utilisant le modèle Microwave Emission Model of Layered Snowpacks (MEMLS) couplé à un modèle d'émission MOP du sol à 19 et 37 GHz en polarisation verticale et horizontale. Les résultats montrent une amélioration de 20.5 K sur la RMSE entre les $T_B$ simulées et mesurées. La $T_B$ montre une très grande sensibilité à la position verticale de la croute de glace dans le couvert

nival. Le tableau 5.1 montre les principaux résultats de l'article pour les sites de références sans glace mesurée (référence), pour les simulations omettant les croutes de glace (sans glace), simulant une croute en surface (glace surface) et en simulant une croute à l'endroit mesurée dans le couvert nival (glace). Il est a noté que la légende du Tableau V de l'article Montpetit *et al.* (2013) devrait être « Estimated downwelling Tb and measured snow surface Tb (in K) at 19 and 37 GHz and in V and H polarizations for the sites having ice lenses in Table 3. No measurements at 19 GHz were taken for the SIR2 site because the radiometer was not available. ».

Tableau 5.1 – RMSE entre les $T_B$ mesurées et simulées pour quatre canaux pour des sites présentant des croutes de glace comparés à des sites de références n'ayant pas de croutes de glace. — RMSE between modeled and measured $T_B$ for four channels for sites with ice lenses compared with referenced sites without ice lenses.

| | RMSE (K) | | | |
|---|---|---|---|---|
| Canal | Référence | Sans Glace | Glace surface | Glace |
| 19V | 9.4 | 10.8 | 10.4 | 12.9 |
| 19H | 12.1 | 47.7 | 25.3 | 6.9 |
| 37V | 12.1 | 21.0 | 19.2 | 18.8 |
| 37H | 12.4 | 43.9 | 26.3 | 13.6 |
| Tous | 11.6 | 34.5 | 21.4 | 14.0 |

This article has been accepted for inclusion in a future issue of this journal. Content is final as presented, with the exception of pagination.



# Snow Microwave Emission Modeling of Ice Lenses Within a Snowpack Using the Microwave Emission Model for Layered Snowpacks

Benoit Montpetit, Alain Royer, Alexandre Roy, Alexandre Langlois, and Chris Derksen

***Abstract*— Ice lens formation, which follows rain on snow events or melt-refreeze cycles in winter and spring, is likely to become more frequent as a result of increasing mean winter temperatures at high latitudes. These ice lenses significantly affect the microwave scattering and emission properties, and hence snow brightness temperatures that are widely used to monitor snow cover properties from space. To understand and interpret the spaceborne microwave signal, the modeling of these phenomena needs improvement. This paper shows the effects and sensitivity of ice lenses on simulated brightness temperatures using the microwave emission model of layered snowpacks coupled to a soil emission model at 19 and 37 GHz in both horizontal and vertical polarizations. Results when considering pure ice lenses show an improvement of 20.5 K of the root mean square error between the simulated and measured brightness temperature (Tb) using several *in situ* data sets acquired during field campaigns across Canada. The modeled Tbs are found to be highly sensitive to the vertical location of ice lenses within the snowpack.**

***Index Terms*— Canada, ice lens, *in situ* measurements, microwave emission model of layered snowpacks (MEMLS), microwave snow emission model, snow specific surface area.**

## I. Introduction

BASED on the increasing mean winter temperatures in many regions of the northern hemisphere [43], [54], there are observations of midwinter melt-refreeze cycles [3], [45] and more frequent winter rain on snow events [38], [40]. These events create ice lenses at the surface or within the snowpack through drainage [39]. It is known that ice lens formation increases the mean soil temperature by releasing latent heat during the freezing process, and ice lenses create impermeable ice barrier layers. Ice lenses also reduce the midwinter vegetation respiration and modify the physical properties of snow [16] because of weak thermal diffusivity of ice. It is also reported that the formation of ice lenses within the snowpack affects the feeding habits of ungulate species in northern regions [18], [33], [40], [43]. Identifying the formation of ice lenses at the regional scale and monitoring their spatial extent requires further study.

Manuscript received June 14, 2012; revised October 18, 2012 and February 7, 2013; accepted February 12, 2013. This work was supported in part by the NSERC, the Canadian Space Agency (Canadian CoReH2O Field Campaign), and Environment Canada (Climate Research Division).

B. Montpetit, A. Royer, A. Roy, and A. Langlois are with the Centre d'Application et de Recherches en Télédétection, Université de Sherbrooke, Sherbrooke, QC J1K 2R1, Canada (e-mail: benoit.montpetit2@usherbrooke.ca).

C. Derksen is with the Climate Research Division, Environment Canada, Toronto, ON M3H 5T4, Canada.

Digital Object Identifier 10.1109/TGRS.2013.2250509

Microwave remote sensing (both passive and active) has proven useful in the detection of ice lenses [3], [24], [39]. However, the coarse spatial resolution of the microwave signal is not only affected by ice lenses, but also by other contributions such as the snow properties, bare ground, vegetation, lake ice, as well as topographic and atmospheric effects [32]. Microwave radiative transfer models are important tools for improving our understanding of the effects of the different environmental parameters on the measured signal [17], [21], [37], [52]. There are five main factors that can significantly affect microwave emission of dry snow: 1) snow grain size; 2) snow density; 3) layering; 4) the soil under the snowpack; and 5) ice lenses within the snowpack. In this paper, we focus on analyzing ice lenses, but acknowledge that large uncertainties remain, however because of the parameterization of the snow grain size [13], [20], [41]. Much of the literature has shown that the snow grain size is the most sensitive parameter in many radiative transfer models, such as the microwave emission model of layered snowpacks (MEMLS) [5], [13], [22], [52], Helsinki University of Technology model (HUT) [6], [8], [19], [37], as well as dense media radiative transfer theory (DMRT) [4], [17], [47], [49]. A further complication is the uncertainty in the measurements of the snow grain size that are taken in the field (e.g., [10]). Nonetheless, recent studies demonstrated a link between the specific surface area of snow and different measurements, such as near infrared photography [23], [26], [48], shortwave infrared photography [34], and infrared laser reflectance [1], [10], [15], [34], [35]. Even with these improved snow grain measurements, the grain size parameterization within microwave radiative transfer models typically requires optimization [20].

Another uncertainty in these radiative transfer models is the soil contribution. Several studies were conducted to model soil emissivity at lower frequencies [36], [53], but it is poorly documented for frequencies above 19 GHz. Wegmüller and Mätzler [50] developed a soil emissivity model that is implemented in the HUT radiative transfer model based on 19- and 37-GHz measurements [37]. As this soil model is derived from *in situ* measurements of bare soil, it has to be tested on different types of surfaces. Grody [17] demonstrated the effects of an ice lens at the surface of a snowpack on modeled passive microwave brightness temperatures (Tb) using the DMRT model [49]. Lemmetyinen *et al.* [24] used a multilayer adaptation of the HUT [37] microwave snow emission model to estimate the effects and observed biases

0196-2892/$31.00 © 2013 IEEE

This article has been accepted for inclusion in a future issue of this journal. Content is final as presented, with the exception of pagination.



TABLE I
AVERAGE SNOWPIT VALUES AND THEIR STANDARD DEVIATIONS (IN PARENTHESIS) FOR SITES WITHOUT ICE LENSES. $H_{\text{snow}}$ IS SNOW DEPTH; $T_{\text{snow}}$ IS MEAN SNOWPACK TEMPERATURE; $\rho_{\text{snow}}$ IS MEAN SNOWPACK DENSITY; $p_c$ IS MEAN CORRELATION LENGTH; AND $T_{\text{soil}}$ IS SOIL TEMPERATURE AT SNOW/SOIL INTERFACE

| # | Site | Date | $H_{\text{snow}}$ (cm) | $T_{\text{snow}}$ (K) | $\rho_{\text{snow}}$ ($\text{kg} \cdot \text{m}^{-3}$) | $p_c$ (mm) | $T_{\text{soil}}$ (K) |
|---|---|---|---|---|---|---|---|
| 1 | SIR | 17-01-2011 | 21 | 266.57 (4.23) | 248.68 (110.53) | 0.1258 (0.0498) | 272.25 |
| 2 | SIR | 27-01-2011 | 33 | 271.52 (0.69) | 245.96 (61.85) | 0.1540 (0.0343) | 272.95 |
| 3 | CH | 09-02-2010 | 37 | 258.74 (5.98) | 238.13 (54.39) | 0.2498 (0.0593) | 267.85 |
| 4 | CH | 10-02-2010 | 69 | 258.18 (5.48) | 320.12 (52.52) | 0.1982 (0.0460) | 270.25 |
| 5 | CH | 18-03-2010 | 118 | 269.79 (2.55) | 373.57 (47.06) | 0.1862 (0.0690) | 272.65 |
| 6 | CH | 20-03-2010 | 82 | 265.44 (4.15) | 284.51 (65.18) | 0.2047 (0.1151) | 271.75 |
| 7 | CH | 20-03-2010 | 91 | 268.21 (3.65) | 309.31 (80.45) | 0.2497 (0.1298) | 272.45 |
| 8 | CH | 20-03-2010 | 83 | 267.65 (5.72) | 291.08 (58.26) | 0.2194 (0.1242) | 272.85 |
| 9 | CH | 22-03-2010 | 174 | 268.29 (4.81) | 388.02 (72.64) | 0.1571 (0.0820) | 272.75 |
| 10 | CH | 22-03-2010 | 180 | 268.80 (5.08) | 386.62 (82.79) | 0.1570 (0.0582) | 272.85 |
| 11 | CH | 22-03-2010 | 150 | 267.51 (5.07) | 381.94 (92.62) | 0.1669 (0.0787) | 272.65 |
| 12 | CH | 22-03-2010 | 119 | 266.89 (4.38) | 353.64 (89.18) | 0.1691 (0.1021) | 272.45 |
| 13 | CH | 24-03-2010 | 48 | 255.67 (7.06) | 260.43 (27.19) | 0.3456 (0.0310) | 269.55 |
| 14 | CH | 24-03-2010 | 45 | 258.69 (7.81) | 229.76 (28.59) | 0.3815 (0.1151) | 270.25 |
| 15 | CH | 26-03-2010 | 44 | 252.31 (8.69) | 285.89 (49.44) | 0.2707 (0.0539) | 269.75 |
| 16 | StR | 08-12-2010 | 47 | 269.72 (3.26) | 182.58 (43.31) | 0.0936 (0.0168) | 273.45 |
| 17 | CH | 13-02-2010 | 51 | 258.70 (5.55) | 307.69 (83.07) | 0.2074 (0.0896) | 269.65 |
| 18 | CH | 13-02-2010 | 34 | 259.07 (4.91) | 262.36 (48.52) | 0.2249 (0.0663) | 267.15 |
| 19 | CH | 23-03-2010 | 57 | 261.18 (7.16) | 309.03 (71.63) | 0.2702 (0.0911) | 270.05 |
| 20 | CH | 23-03-2010 | 19 | 258.61 (2.56) | 266.66 (43.61) | 0.3562 (0.0477) | 264.55 |

between the measured and modeled Tb when an ice layer is added at the surface of the snowpack. Rees *et al.* [39] and Lemmetyinen *et al.* [25] used the multilayer HUT version and MEMLS [52] to simulate and describe the effects of ice lenses on emitted Tb, and they compared the simulations to field measurements to determine the performance of each model. However, to optimize the simulated Tb with ice lenses using MEMLS, Lemmetyinen *et al.* [25] and Rees *et al.* [39] added dense snow layers as a proxy for ice lenses. Microwave theory, however, suggests that even a very dense snow layer acts as a microwave scatterer whereas pure ice lenses absorb and reflect incoming microwave radiation without scattering. In addition, attention focused on ice lenses at the surface (i.e., [17]) whereas Rees *et al.* [16], [39] clearly demonstrated that ice lenses can be found deeper in the snowpack.

The main objective of this paper is to simulate Tb using MEMLS for snowpacks with ice lenses using measured *in situ* properties of the ice lenses (depth, thickness, and temperature) assuming pure ice lenses and determine the sensitivity of the ice lens parameters on the modeled Tb. Specifically, we want to: 1) optimize the characterization of the snow grain size and the soil roughness for snowpacks without ice lenses; 2) validate the simulations with *in situ* Tb measurements acquired with ground-based radiometers during winter field campaigns across Canada to evaluate the performance of this modeling; and 3) conduct tests to determine the sensitivity of the microwave signal to the ice lens parameters.

## II. DATA AND METHODS

### A. Study Sites

Measurements from three field campaigns across Canada in Arctic, subarctic, and midlatitude regions are used in this paper: 1) Daring Lake, Northwest Territories; 2) Churchill, Manitoba; and 3) southeastern Québec. The first campaign was in April 2007 near Daring Lake (64°50' N, 111°38' W), Northwest Territories, Canada. Tb using a sled-based passive microwave radiometer system (6.9, 19, 37, and 89 GHz) were measured at eight undisturbed sites. Measurements were also made after removing a surface ice lens created by a rain-on-snow event in late winter. A complete description of the measurements is found in [41].

At the second site, Tb (using the same sled-based radiometer system) and detailed snowpit physical properties were taken in forest clearings near Churchill (58°46' N, 94°11' W), Manitoba (labeled Churchill (CH) sites), at regular intervals during the 2009–2010 winter season as in [8]. During measurement periods in March and April, ice lenses that are the result of melt-refreeze events were observed and measured in the snowpack.

During the winter of 2011, similar Tb and snowpit measurements were taken at two different sites in southeastern Québec, Canada. The first site is an open grassy area located in the town of St-Romain (StR) (labeled StR sites, 45°47' N, 71°1' W) where thick ice lenses (1 to 2 cm) were observed within the snowpack after a prolonged melt-refreeze event

This article has been accepted for inclusion in a future issue of this journal. Content is final as presented, with the exception of pagination.



TABLE II
AVERAGE SNOWPIT VALUES AND STANDARD DEVIATION (IN PARENTHESIS) FOR DARING LAKE TUNDRA SITES WITH SURFACE ICE LENSES. SITE NUMBERS (#) CORRESPOND TO SITE NUMBERS OF [39]

| # | Date | $H_{\text{snow}}$ (cm) | $T_{\text{snow}}$ (K) | $\rho_{\text{snow}}$ (kg · m$^{-3}$) | $p_c$ (mm) | $T_{\text{soil}}$ (K) |
|---|---|---|---|---|---|---|
| 1 | 10-04-2007 | 8 | 263.7 (0.0) | 344.00 (0.00) | 0.1800 (0.0000) | 263.7 |
| 2 | 14-04-2007 | 18 | 262.7 (0.6) | 290.00 (0.00) | 0.1600 (0.0346) | 262.1 |
| 3 | 15-04-2007 | 35 | 261.0 (0.1) | 326.25 (72.96) | 0.2275 (0.1069) | 261.1 |
| 4 | 15-04-2007 | 44 | 263.9 (1.3) | 398.75 (62.50) | 0.1650 (0.0574) | 262.7 |
| 5 | 10-04-2007 | 48 | 264.8 (0.4) | 335.00 (120.21) | 0.2700 (0.1273) | 265.0 |
| 6 | 11-04-2007 | 50 | 264.2 (0.8) | 358.33 (45.37) | 0.1933 (0.0643) | 263.5 |
| 7 | 11-04-2007 | 68 | 263.4 (0.0) | 310.00 (69.76) | 0.2700 (0.0383) | 263.4 |
| 8 | 15-04-2007 | 82 | 263.6 (0.4) | 343.75 (57.93) | 0.1650 (0.0574) | 263.1 |

TABLE III
AVERAGE SNOWPIT VALUES AND STANDARD DEVIATION (IN PARENTHESIS) FOR SITES WITH ICE LENSES. TYPE OF SITE: [1] OPEN MIDLATITUDE GRASSY SITE AND [2] SUBARCTIC FOREST SITE

| Site | Type of Site | Date | $H_{\text{snow}}$ (cm) | $T_{\text{snow}}$ (K) | $\rho_{\text{snow}}$ (kg · m$^{-3}$) | $p_c$ (mm) | $T_{\text{soil}}$ (K) |
|---|---|---|---|---|---|---|---|
| SIR1 | 1 | 27-01-2011 | 33 | 270.22 (1.51) | 255.14 (66.06) | 0.0487 (0.0233) | 272.90 |
| SIR2 | 1 | 09-02-2011 | 64 | 271.44 (1.30) | 251.35 (42.47) | 0.0450 (0.0270) | 272.70 |
| StR1 | 1 | 20-01-2011 | 55 | 269.43 (2.79) | 231.85 (65.96) | 0.1507 (0.0654) | 272.90 |
| Str2 | 1 | 01-02-2011 | 53 | 268.91 (2.92) | 271.36 (67.91) | 0.1566 (0.0413) | 272.90 |
| CH1 | 2 | 19-03-2010 | 52 | 266.37 (4.00) | 276.05 (29.55) | 0.3309 (0.0902) | 270.50 |
| CH2 | 2 | 25-03-2010 | 55 | 260.45 (5.28) | 261.75 (44.86) | 0.2988 (0.1020) | 268.40 |

in February 2011. The second site is located at the Site Interdisciplinaire de Recherche en Environnement Extérieur [SIRENE (SIR)], a research station (labeled SIR sites) of the Centre d'Applications et de Recherches en TELédétection (CARTEL), on the Université de Sherbrooke main campus (45°22′ N, 71°55′ W). This site is also an open grassy area, but the ice lenses were created artificially by gently spraying water on top of the snowpack on cold days ($< -15$ °C). This created a thin ice lens at the surface of the snowpack because the water froze immediately on contact with snow. The gentle spray created a smooth ice surface. When the first artificial lens was buried by subsequent snowfall, a second surface ice lens was created by spraying the area once more.

### *B. In situ Data*

*1) Snow and Ice Data:* To properly optimize the snow grain size parameter and the soil roughness parameter for the microwave radiative transfer model MEMLS, sites without ice lenses were chosen (Table I). Afterward, to test the ice lens treatment with a modified version of MEMLS (see below), sites with ice lenses within the snowpack were chosen (Tables II and III). The average snow geophysical properties of the snowpacks are shown in Tables I to IV.

Table I shows the physical properties of the measured snowpacks without ice lenses from the 2010 and 2011 campaigns. The snow grain size is parameterized by the correlation length as in Section II-C.1.

For the Daring Lake campaign in 2007, Table II shows the mean values and the standard deviations for the snow temperature ($T_{\text{snow}}$), density ($\rho_{\text{snow}}$), and grain size characterized by the correlation length ($p_c$, [31]). For this field campaign, the grain size measurements were made manually using a gridded reference card and a field microscope ($D_{\max}$). The $p_c$ were then derived from these measurements using the nonlinear method of [11] (Section II-C.1). The total snow depth ($H_{\text{snow}}$) and soil temperature ($T_{\text{soil}}$) are also shown in Table II. The measurements were taken in a tundra environment. The data in Table II are described in more detail in [39].

Table III shows the mean values and the standard deviations for the remaining measurement sites with ice lenses. Measurements were taken in two environments: 1) open midlatitude grassy areas (SIR and StR sites in Table III) and 2) subarctic forest clearings (CH sites in Table III).

Table IV shows values for the different parameters (i.e., profile height, ice thickness, and temperature), which characterize each ice lens within the snowpack for the 2009–2010 and 2010–2011 winter sites shown in Table III. Two ice lenses were observed at the SIR2, CH1, and CH2 sites.

*2) Tb Data:* Tb measurements were acquired using surface-based radiometers on mobile sleds at an incidence angle of 55°. Calibrations were conducted on a regular basis using warm (ambient temperature microwave absorber) and cold (liquid nitrogen) targets as described by Asmus and Grant [2] and Solheim [44]. Uncertainty in the measurement of the calibration target temperature is estimated at $\pm$ 2 K. The 19- and 37-GHz radiometers are calibrated simultaneously therefore, the same target temperature uncertainties for a given calibration applied to both frequencies. Radiometer stability depended on the frequency and varied somewhat from campaign to campaign, but the overall precision is estimated at $\pm 2$ K at 19 GHz, and $< 1$ K at 37 GHz, based on a 3-db width of the main beam.

The measured Tb correspond to the Tb of the target ($\text{Tb}_{\text{target}}$) and a contribution from the downwelling radiation

This article has been accepted for inclusion in a future issue of this journal. Content is final as presented, with the exception of pagination.



TABLE IV
MEASURED ICE LENS PROPERTIES (HEIGHT, THICKNESS, AND TEMPERATURE) FOR SITES SHOWN IN TABLE III. TWO ICE LENSES ARE OBSERVED AT SITES SIR2, CH1, AND CH2

| Site | Height (cm) | | Thickness (cm) | | Temperature (K) | |
|---|---|---|---|---|---|---|
| SIR1 | 32.7 | | 0.3 | | 269.0 | |
| SIR2 | 23.7 | 63.7 | 0.3 | 0.3 | 271.8 | 272.5 |
| StR1 | 19 | | 1.0 | | 272.0 | |
| Str2 | 19 | | 2.0 | | 270.2 | |
| CH1 | 30.0 | 51.7 | 0.5 | 0.3 | 266.9 | 260.7 |
| CH2 | 40.0 | 50.5 | 0.5 | 0.3 | 255.7 | 253.5 |

TABLE V
MEASURED ICE LENS PROPERTIES (HEIGHT, THICKNESS, AND TEMPERATURE) FOR SITES SHOWN IN TABLE III. TWO ICE LENSES ARE OBSERVED AT SITES SIR2, CH1, AND CH2

| | 19 GHz | | | | 37 GHz | | | |
|---|---|---|---|---|---|---|---|---|
| Site | Downwelling | | Surface | | Downwelling | | Surface | |
| | V-Pol | H-Pol | V-Pol | H-Pol | V-Pol | H-Pol | V-Pol | H-Pol |
| SIR1 | 8.0 | 8.4 | 248.7 | 169.1 | 16.6 | 16.7 | 240.2 | 186.2 |
| SIR2 | — | — | — | — | 15.0 | 15.3 | 233.9 | 176.6 |
| StR1 | 15.3 | 15.3 | 257.1 | 218.6 | 18.9 | 18.2 | 241.6 | 215.1 |
| Str2 | 10.8 | 10.8 | 255.0 | 218.3 | 18.2 | 17.6 | 237.2 | 207.9 |
| CH1 | 52.3 | 51.6 | 231.5 | 182.1 | 64.0 | 63.6 | 170.2 | 140.9 |
| CH2 | 50.7 | 50.2 | 232.8 | 168.2 | 61.5 | 61.3 | 180.4 | 162.3 |

($\mathrm{Tb}_{\downarrow}$) reflected by the surface as follows:

$$\mathrm{Tb} = \mathrm{Tb}_{\mathrm{target}} + (1-e)\mathrm{Tb}_{\downarrow} \tag{1}$$

where $e$ is the surface emissivity estimated by MEMLS.

When the sites do not correspond to large open areas, the downwelling $\mathrm{Tb}_{\downarrow}$ includes a contribution from the tree emission around the target in addition to the sky contribution ($\mathrm{Tb}_{\mathrm{sky}}$)

$$\mathrm{Tb}_{\downarrow} = aTb_{\mathrm{sky}} + bTb_{\mathrm{veg}} \tag{2}$$

where $a$ and $b$ are weight functions (Appendix A) and $\mathrm{Tb}_{\mathrm{veg}}$ is the Tb of the vegetation (trees).

The downwelling $\mathrm{Tb}_{\mathrm{sky}}$ for the SIR and StR sites are derived from measured nadir downwelling sky Tbs ($\mathrm{Tb}_{\mathrm{sky}}^{\mathrm{nadir}}$) taken in open areas to avoid any contributions from the surrounding vegetation. The sky Tb is estimated using the equations of Mätzler and Rosenkranz [28] as follows:

$$\mathrm{Tb}_{\mathrm{sky}} = \mathrm{Tb}_{\mathrm{sky}}^{\mathrm{nadir}} \frac{\left(1-\gamma_{\mathrm{atm}}^{\mathrm{eff}}\right)}{\left(1-\gamma_{\mathrm{atm}}^{\mathrm{nadir}}\right)} \tag{3}$$

where $\gamma_{\mathrm{atm}}^{\mathrm{eff}}$ and $\gamma_{\mathrm{atm}}^{\mathrm{nadir}}$ are the atmospheric transmissivity for an effective angle $\theta_{\mathrm{eff}}$ and at nadir, respectively. These parameters are modeled using the atmospheric model implemented in the HUT snow model [37] driven by the air temperature and moisture profiles of the atmospheric layers above the surface from the 29 North American Regional Reanalysis (NARR) atmospheric layers.

For the CH sites, no $\mathrm{Tb}_{\mathrm{sky}}^{\mathrm{nadir}}$ were measured. The values were modeled using the same atmospheric model used in HUT as for the atmospheric transmissivity. The NARR data were also used as input for these modeled values. In addition, as the CH sites are located in small forest clearings, the downwelling vegetation Tb ($\mathrm{Tb}_{\mathrm{veg}}$) was estimated using the vegetation temperature as follows:

$$\mathrm{Tb}_{\mathrm{veg}} = \omega(1-\gamma)\mathrm{Tb}_{\mathrm{surface}} + (1-\omega)(1-\gamma)T_{\mathrm{veg}} \tag{4}$$

where $\mathrm{Tb}_{\mathrm{surface}}$ is the modeled Tb emitted by the surface of the snowpack without any contribution from the sky or the vegetation, $T_{\mathrm{veg}}$ is the vegetation temperature ($\approx$ air temperature, $T_{\mathrm{air}}$), $\omega$ is the single scattering albedo, and $\gamma$ is the transmissivity of the vegetation. The first term in (4) represents the contribution from the snowpacks emitted signal scattered and absorbed by the vegetation, and the second term represents the direct contribution of the vegetation to the overall downwelling vegetation Tb ($\mathrm{Tb}_{\mathrm{veg}}$). The values of $\omega$ and $\gamma$ at 19 GHz (respectively 0.065 and 0.710) and at 37 GHz (respectively 0.062 and 0.677) are determined by a linear fit to the data in [42] for values of stem volume (SV) $< 200\ \mathrm{m}^3 \cdot \mathrm{ha}^{-1}$. The measured SV for the CH sites is $53\ \mathrm{m}^3 \cdot \mathrm{ha}^{-1}$. This linear fit is chosen instead of the exponential fit shown in [42] because of the limited range of values of SV.

Table V shows the estimated downwelling and measured surface Tb at 19 and 37 GHz in both polarizations for the 2009–2010 and 2010–2011 winter sites. The estimated downwelling Tb [(2), (3) and (4)] are then added [(1)] to the simulated snowpack Tb corresponding to open areas (next section) to consider the contribution of the surrounding environment in the comparison analysis with Tb measurements. For details on the measured Tb for the sites shown in Table I, see [41].

Tb measurements were also conducted for different snow depths at the SIR sites by gradually removing layers of snow and ice (excavation experiment). Measurements were taken at the ice lens surface and at the snow surface beneath the ice lens (after careful removal of the ice lens). The results of these profile-like Tb are shown and described in Section III-B.

### C. Models

The passive microwave snow radiative transfer model used in this paper is the MEMLS [52]. This model is used because of its multilayer design that enabled discrete ice lens treatment for pure ice layers within the snowpack. In addition, we added a soil model [50] to improve the estimation of the soil contribution under the snow.

*1) Snow Emission Model:* The MEMLS snow emission model describes the snow cover as a stack of horizontal layers characterized by the snow's temperature, density, thickness, liquid water content, salinity, and grain size. The radiative transfer parameters (reflection and refraction at layer interfaces and layer reflection and absorption) are based on physical equations integrated in a six-flux stream parameterization. A combination of coherent and incoherent superposition is used to calculate the signal transmission between every layer interface (see [29] and [52] for a complete description of the model). In this paper, the scattering coefficient of each snow layer is determined by the improved born approximation (IBA) [27]. The six-flux radiative transfer scheme in MEMLS also describes multiple-volume scattering and

This article has been accepted for inclusion in a future issue of this journal. Content is final as presented, with the exception of pagination.



absorption, including trapped radiation because of internal reflection (see [29] and [52]).

Durand *et al.* [12] showed that the most sensitive parameter in MEMLS is the snow grain size. The snow grain size parameter used in MEMLS is the correlation length ($\mathrm{p}_c$). According to Debye *et al.* [7] and Mätzler [31], this parameter is related to the snow grain optical diameter ($\mathrm{D}_o$) by the following relationship:

$$\mathrm{p}_c = \frac{2}{3} D_o (1 - \nu) \tag{5}$$

where $\nu$ is the ice fraction ($\rho_{\mathrm{snow}}/\rho_{\mathrm{ice}}$). $D_o$ is derived from measurements of the specific surface area of snow grains (specific surface area (SSA); [9]): $D_o = 6/\rho_{\mathrm{ice}} SSA$. The SSA parameter can be accurately measured in the field by shortwave infrared reflectometry (e.g., [34]). Another way to define $p_c$ is to use the longest diameter of the snow grain ($D_{\max}$) [14]. Durand *et al.* [11] derived the following relationship between $p_c$ and $D_{\max}$:

$$p_c = \begin{cases} (0.18 + 0.09 \ln D_{\max}) \pm 0.03 & \text{for } \rho_{\mathrm{snow}}/\rho_{\mathrm{ice}} > 0.2 \\ & \text{and } D_{\max} > 0.125 \text{ mm} \\ 0.05 \pm 0.015 & \text{otherwise.} \end{cases} \tag{6}$$

However, recent research [5], [41] show that the SSA needs to be calibrated for microwave radiative transfer models as discussed by Mätzler [31] and Wiesmann *et al.* [51]. These researches, however, used different snow emission models or did not use SSA measurements for the snow grain size parameterization. Hence, it is necessary to validate the need for this correction factor. A method similar to Brucker *et al.* [5] and Roy *et al.* [41] is used in this paper to estimate the correction factor. The correlation length is adjusted with a multiplying factor $\phi$ to minimize the root mean square error (RMSE) between the measured and simulated Tb using MEMLS at 37 GHz

$$p_c' = \phi p_c. \tag{7}$$

Among the sites shown in Table I, only those for which the soil did not affect the Tb at 37 GHz (11 sites) are chosen (the selection is made by a sensitivity study using the measured snowpack characteristics, [41]). This ensured that the correction factor $\phi$ addressed the errors due to the snow grain size parameterization and not errors in the soil modeling. In addition, as the penetration depth of the microwave signal at 37 GHz is lower than at 19 GHz, this channel makes it less sensitive to the soil emission. In addition, the snow geophysical properties for the selected sites are similar to the sites shown in Table III.

*2) Ice Lens Modeling:* In this paper, ice lenses are characterized by their temperature, vertical position in the snowpack, and thickness. To simulate an ice lens with no scattering using IBA of MEMLS the density of the ice lenses is considered constant in this paper (density of pure ice $= 917 \text{ kg} \cdot \text{m}^{-3}$). This renders the scattering coefficient null, given by (25) of [27]. The ice lens model of [17] is also implemented in MEMLS. Based on this model, the ice lenses are associated with a nonscattering type (scattering coefficient is null) with attenuation described below. The dielectric constant of the ice layers is calculated using the equations of Mätzler [30] for pure ice. The layer interface reflectivity values are calculated using the Fresnel equations. The ice lens model is defined by the absorption coefficient ($\alpha_{\mathrm{ice}}$) and the ice transmissivity ($\tau_{\mathrm{ice}}$), and are calculated using the equations of Grody [17] as follows:

$$\alpha_{\mathrm{ice}} = \frac{2\pi}{\lambda} \frac{\epsilon''}{\sqrt{\epsilon'}} \tag{8}$$

$$\tau_{\mathrm{ice}} = \exp(-\alpha_{\mathrm{ice}} d_{\mathrm{ice}} \sec\theta) \tag{9}$$

where $\epsilon'$ and $\epsilon''$ are respectively, the real and imaginary parts of the pure ice dielectric constant, $\mathrm{d}_{\mathrm{ice}}$ is the ice lens thickness (cm), and $\theta$ is the propagation angle within the ice lens. Finally, the upward Tb contribution of the ice lens is calculated as follows:

$$\mathrm{Tb}_{\mathrm{ice}} = (1 - \tau_{\mathrm{ice}}) T_{\mathrm{ice}} \tag{10}$$

where $\mathrm{T}_{\mathrm{ice}}$ is the ice physical temperature (K). The upward contribution (10) of the ice lens is attenuated by the interface reflectivities within the MEMLS formulation.

*3) Soil Modeling:* The soil reflectivity model proposed by Wegmüller and Mätzler [50] determines the soil interface reflectivity, at a given frequency, in horizontal polarization ($\Gamma_{\mathrm{H}}$) and vertical polarization ($\Gamma_{\mathrm{V}}$) with the following equations for an incidence angle lower than 60°:

$$\Gamma_H = \Gamma_H^{\mathrm{Fresnel}} \exp(-(k\sigma)^{\sqrt{-0.1\cos\theta}}) \tag{11}$$

$$\Gamma_V = \Gamma_H \cos\theta^{\beta} \tag{12}$$

where $k$ is the wave number, $\sigma$ is the soil roughness parameter, $\theta$ is the incidence angle, and $\beta$ is a factor that is set to 0.655 by Wegmüller and Mätzler [50]. We consider $\sigma$ and $\beta$ as two unknowns to be determined.

In this paper, $\beta$ and $\sigma$ are determined by minimizing the biases between the modeled and measured Tb using MEMLS at 19 GHz V-Pol (19 V) and H-Pol (19 H) and different values of soil reflectivity for both polarizations. Only sites where snow had a minimal impact are chosen (nine sites). Based on this derived optimal reflectivity and the known incidence angle, $\beta$ is determined from (12) as follows:

$$\beta = \frac{\log\left(\frac{\Gamma_V}{\Gamma_H}\right)}{\log(\cos\theta)}. \tag{13}$$

Having obtained this factor, the roughness parameter ($\sigma$) for both frequencies is determined by minimizing the RMSE between the optimal and modeled reflectivity at 19 GHz using MEMLS with (11).

## III. Ice Lens Modeling Validation

Prior to the ice lens modeling analysis, the snow and soil parameterizations are optimized for snowpits without ice lenses and snowpits where ice lenses are removed (Table I). This allowed us to minimize the snow model uncertainties, assuming that the snow properties remained similar for the corresponding snowpits with ice lenses. Afterward, an analysis and validation of the ice lens treatment is conducted on two independent data sets. Finally, a sensitivity test of the different ice lens properties is presented in next section (Section IV) to determine the importance of accurately measure ice lenses.

This article has been accepted for inclusion in a future issue of this journal. Content is final as presented, with the exception of pagination.



### A. Snow and Soil Optimizations

Based on the method in Section II-C.1, Tb simulations are performed at 37 GHz using MEMLS with values of factor $\phi$ ranging from 0 to 3 with an increment of 0.1 (7) for 11 selected sites where the contribution of the soil is deemed to be negligible (sites 5, 6, 7, 8, 9, 10, 11, 12, 13, 14, and 19 in Table I) as discussed in [41]. Those sites, without ice lenses, where selected because the Tb only depended upon the snowpack characteristics (mainly grain size), ensuring that $\phi$ is not biased by hypotheses concerning the soil conditions. Those sites showed a weak variation lower than 5 K for the modeled Tb for soil reflectivity ranging from 0 to 0.5 (range measured by [50]). The $\mathrm{RMSE}_\phi$ (subscript $\phi$ is to differentiate the RMSE of the grain size optimization from the other RMSE) is then calculated with the measured Tb as follows:

$$\mathrm{RMSE}_\phi = \sqrt{\frac{\sum_{i=1}^{N}\left[\left(\mathrm{Tb}_{\mathrm{sim};i}^{37\ V}-\mathrm{Tb}_{\mathrm{mes};i}^{37\ V}\right)^2+\left(\mathrm{Tb}_{\mathrm{sim};i}^{37H}-\mathrm{Tb}_{\mathrm{mes};i}^{37H}\right)^2\right]}{2N}} \tag{14}$$

where $\mathrm{Tb}_{\mathrm{sim};i}$ and $\mathrm{Tb}_{\mathrm{mes};i}$ are respectively, the simulated and measured Tbs for the sites $i$ and $N$ is the total number of sites used for the snow grain size optimization. Fig. 1 shows the relationship between the calculated $\mathrm{RMSE}_\phi$ and the correction factor $\phi$ applied to the snow grain size for each simulation. The range of correction factor shown in Fig. 1 is chosen to make sure the minimum $\mathrm{RMSE}_\phi$ found is not only a local minimum. This shows strong sensitivity to the snow grain size over the range of $\phi$ values; the $\mathrm{RMSE}_\phi$ is 17.6 K for no correction ($\phi = 1$) and 13.7 K for the best fit obtained with $\phi = 1.3$ (Fig. 1). Although there is a need to evaluate this factor in future studies using larger data sets and the known uncertainties of the snow grain size measurements, this factor is applied to all the simulations in this paper. The next step in optimizing the simulations is to determine the best $\beta$ factor (soil contribution) in (12) using the method in Section II-C.3. Using the correction factor $\phi = 1.3$ (Fig. 1) in the Tb simulations, the optimal reflectivity values are determined by minimizing the biases between the simulated and measured Tb for both polarizations (V and H) at 19 GHz. Table VI shows the results of these optimizations and the reflectivity ratios ($\Gamma_V/\Gamma_H$) for the polarizations and for the 20 sites in Table I. There are important variations in the derived ratio values. This is possibly due to the residual error introduced by the snow grain size variations between the sites remained important. Considering only the sites where the snow grain size have little influence on the modeled Tb (i.e., for the nine sites: 1, 2, 3, 4, 15, 16, 17, 18, and 20), the mean ratio is $0.40 \pm 0.23$, leading to the best factor $\beta = 1.72$ (12).

Using (11) and (12) and the $\phi$ factor calculated previously, the soil reflectivity is calculated by iterations on the soil roughness parameter. Two types of sites are distinguished: 1) midlatitude grassy sites (referred to as grass; sites 1, 2, and 16 of Table VI) and 2) tundra sites (tundra; sites 3, 15, 17, 18, and 20 of Table VI). The optimal soil roughness parameters

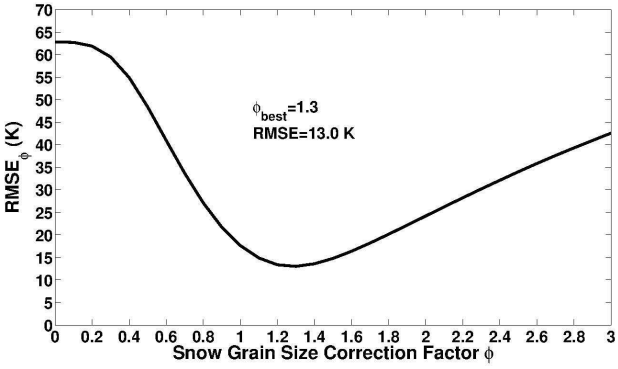


Fig. 1. Snow grain size optimization at 37 GHz using MEMLS (RMSE between measured and simulated Tb) for selected sites without ice lenses or soil contribution.

TABLE VI
OPTIMAL SOIL REFLECTIVITIES OBTAINED USING MEMLS AT 19 GHZ FOR 20 SITES DESCRIBED IN TABLE I

| Site | $\Gamma_V$ | $\Delta\mathrm{Tb}_V$ (K) | $\Gamma_H$ | $\Delta\mathrm{Tb}_H$ (K) | $\Gamma_V/\Gamma_H$ |
|---|---|---|---|---|---|
| 1 | 0.03 | −0.7 | 0.08 | −0.7 | 0.38 |
| 2 | 0.02 | 0.9 | 0.09 | 1.0 | 0.22 |
| 3 | 0.02 | −0.7 | 0.09 | 0.8 | 0.22 |
| 4 | 0.00 | −2.2 | 0.05 | 0.2 | 0.00 |
| 5 | 0.02 | −0.3 | 0.13 | −0.2 | 0.15 |
| 6 | 0.02 | −0.4 | 0.03 | 0.3 | 0.67 |
| 7 | 0.00 | 0.4 | 0.05 | 0.4 | 0.00 |
| 8 | 0.00 | −7.1 | 0.17 | 0.5 | 0.00 |
| 9 | 0.03 | −0.5 | 0.08 | −0.1 | 0.38 |
| 10 | 0.15 | 0.1 | 0.45 | 0.4 | 0.33 |
| 11 | 0.08 | −0.3 | 0.26 | −0.3 | 0.31 |
| 12 | 0.02 | 0.2 | 0.13 | −0.4 | 0.15 |
| 13 | 0.00 | −9.7 | 0.02 | −0.6 | 0.00 |
| 14 | 0.00 | −16.7 | 0.00 | −5.7 | 0.00 |
| 15 | 0.09 | 0.7 | 0.12 | 0.5 | 0.75 |
| 16 | 0.06 | −0.4 | 0.09 | 0.6 | 0.67 |
| 17 | 0.06 | 0.0 | 0.15 | −0.7 | 0.40 |
| 18 | 0.05 | −0.1 | 0.11 | −0.6 | 0.45 |
| 19 | 0.12 | −0.3 | 0.23 | 0.6 | 0.52 |
| 20 | 0.11 | −0.7 | 0.22 | 0.8 | 0.50 |

for these two types of sites are determined by minimizing the RMSE [$\mathrm{RMSE}_\sigma$, (15)] between the optimal soil reflectivity ($\Gamma_V$ and $\Gamma_H$ of Table VI) and the modeled reflectivity ($\Gamma'_V$ and $\Gamma'_H$) as follows:

$$\mathrm{RMSE}_\sigma = \sqrt{\frac{\sum_{i=1}^{N}[(\Gamma'_V-\Gamma_V)^2+(\Gamma'_H-\Gamma_H)^2]}{2N}}. \tag{15}$$

Fig. 2 shows the relationship between the $\mathrm{RMSE}_\sigma$ and the soil roughness parameters. The optimal parameters are found to be $\sigma_{\mathrm{grass}} = 1.1$ cm ($\mathrm{RMSE}_\sigma = 0.04$) for the grass sites and $\sigma_{\mathrm{tundra}} = 0.4$ cm ($\mathrm{RMSE}_\sigma = 0.07$) for the tundra sites.

The results for the snow simulations at 19 and 37 GHz and V and H polarizations are then determined using $\phi = 1.3$, $\beta = 1.72$, $\sigma_{\mathrm{grass}}$, or $\sigma_{\mathrm{tundra}}$ for all the sites in Table I, including the sites not considered in the optimization process (Fig. 3). Fig. 3 shows the comparison between the measured and modeled Tb (top left), the comparison between the H and V polarizations at 19 GHz (top right), the comparison

This article has been accepted for inclusion in a future issue of this journal. Content is final as presented, with the exception of pagination.



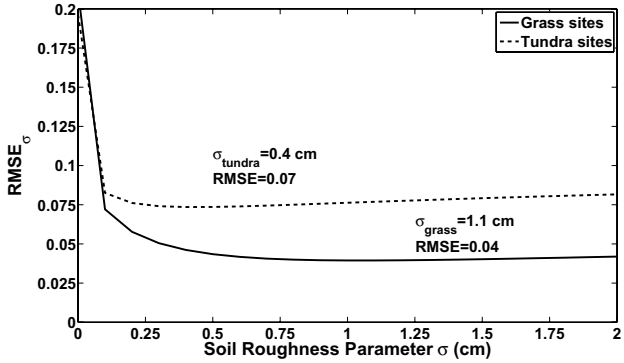


Fig. 2. Optimization of soil roughness parameter using soil model of Wegmüller and Mätzler [50] at 19 GHz for grass sites (solid line) and tundra sites (dashed line) shown in Table I.

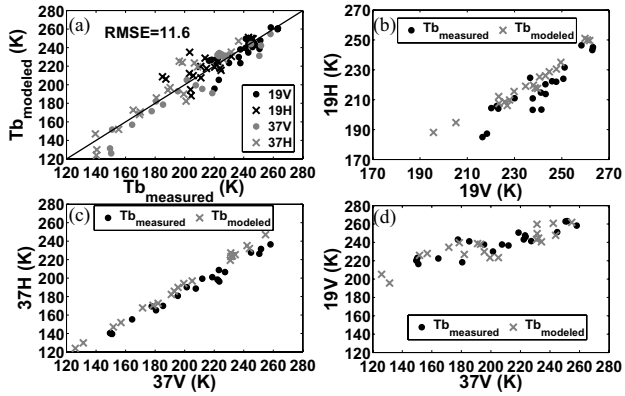


Fig. 3. MEMLS simulations with $\phi = 1.3$ and optimized $\sigma$ for all 20 snowpits without ice lenses (Table I) for 19 and 37 GHz and two polarizations H and V. (a) Modeled Tb compared with measured Tb, overall RMSE. (b) Tb at 19 H versus Tb at 19 V. (c) Tb at 37 H versus Tb at 37 V. (d) Tb at 19 V versus Tb at 37 V.

between the H and V polarizations at 37 GHz (bottom left), and the comparison between the 19 and 37 GHz frequencies in V polarization (bottom right).

The cross-polarization figures show that the soil contribution is adequately considered in the modeled Tb as the modeled and measured Tb are significantly correlated. The scatter in Fig. 3(b) at 19 GHz comes from variability in the soil reflectivity (Table VI). The correlation at 37 GHz [$r = 0.99$, Fig. 3(c)], where the soil contribution is less important, is better than at 19 GHz [$r = 0.91$, Fig. 3(b)]. The modeled spectral dependency [19 V versus 37 V, Fig. 3(d)] is also well-correlated with the measured spectral dependency. This shows that using the same correction factor for the snow grain size for both frequencies is adequate. The overall RMSE between the modeled and measured Tb [Fig. 3(a)] is 11.6 K, which is comparable with similar published results [4], [24], [25], [41]. Table VII shows the RMSE for the four different channels (19 V, 19 H, 37 V, and 37 H) shown in Fig. 3. The higher errors in H-Pol could be explained by the increased sensitivity to stratigraphic variability (i.e., density). The lower errors at 19 GHz can be explained by the lower sensitivity to the snow grain size.

As the snowpack conditions at the sites without ice lenses (Table I) are similar to those with ice lenses (Table III), the optimal parameters ($\phi = 1.3$, $\beta = 1.72$, $\sigma_{\text{grass}}$, or $\sigma_{\text{tundra}}$) previously derived are also applied to those sites. The next section analyzes the MEMLS simulations, including the ice lens model.

### *B. Analysis of the Snow and Ice Emission Model*

Fig. 4 shows the measured Tb profiles for the sites in Table III where the effect of the ice lenses is clearly apparent (excavation experiment). In agreement with [39], relatively small effects of the ice lenses are seen in V-Pol at both frequencies (mean attenuation of 5.7 K) whereas pronounced effects occur in H-Pol in both frequencies (mean attenuation of 32.8 K). Fig. 4 also shows that the signal attenuation in H-Pol by the ice lens is stronger, usually, at 19 GHz than at 37 GHz. The stronger ice lens effects observed at 19 GHz compared with 37 GHz are due to the weaker downwelling Tb at 19 GHz. The higher downwelling Tb at 37 GHz (Table V) tend to minimize the effects of the ice lens. The observed differences between sites having similar ice lenses is the result of the differences in the snow densities of the layers below and above the ice lenses, which leads to different dielectric contrasts.

To evaluate the performance of the ice lens treatment in Section II-C.2, a preliminary simulation for all six sites in Table III is performed without a specific treatment for the ice lenses. Fig. 5(a) shows the comparison between the measured Tb and the modeled Tb without the ice lens treatment at 19 and 37 GHz and V and H polarizations. The overall RMSE between the modeled and measured Tb is 34.5 K, mainly because of the Tb values at H polarization. As expected, the RMSE is significantly higher than is determined for snowpacks without ice lenses (RMSE = 11.6 K, Fig. 4), meaning that the error is attributable to the presence of an ice lens.

Grody [17], Lemmetyinen *et al.* [25], and Rees *et al.* [39] modeled the effects of ice lenses on top of a snowpack. Fig. 5(b) shows a comparison of the measured and modeled Tb when the ice lens is arbitrarily simulated at the top of the snowpack. The overall RMSE (21.4 K) shows an improvement of 13.1 K (38%) when compared with the simulations without the ice lens treatment [Fig. 5(b) compared with Fig. 5(a)]. However, the RMSE in Fig. 5(b) still remains higher than the mean level of error for snowpacks without an ice lens [Fig. 3]. This shows that the vertical position of the ice lenses within the snowpack must be considered.

Fig. 5(c) shows the results with the ice lenses modeled at their measured depth within the snowpack. Again, an improvement of 7.4 K (35%) in the RMSE (14.0 K) is observed relative to the results of Fig. 5(b), and an improvement of 20.5 K (59%) is achieved compared with the results of Fig. 5(a). This shows the importance of modeling ice lenses at their exact depths within the snowpack. In addition, the RMSE of Fig. 5(c) is comparable with the RMSE shown in Fig. 3 (11.6 K) for snowpacks where no ice lenses are present. This indicates that the error in Fig. 5(c) most likely comes from the snow modeling rather than the ice lens treatment. Table VII

This article has been accepted for inclusion in a future issue of this journal. Content is final as presented, with the exception of pagination.



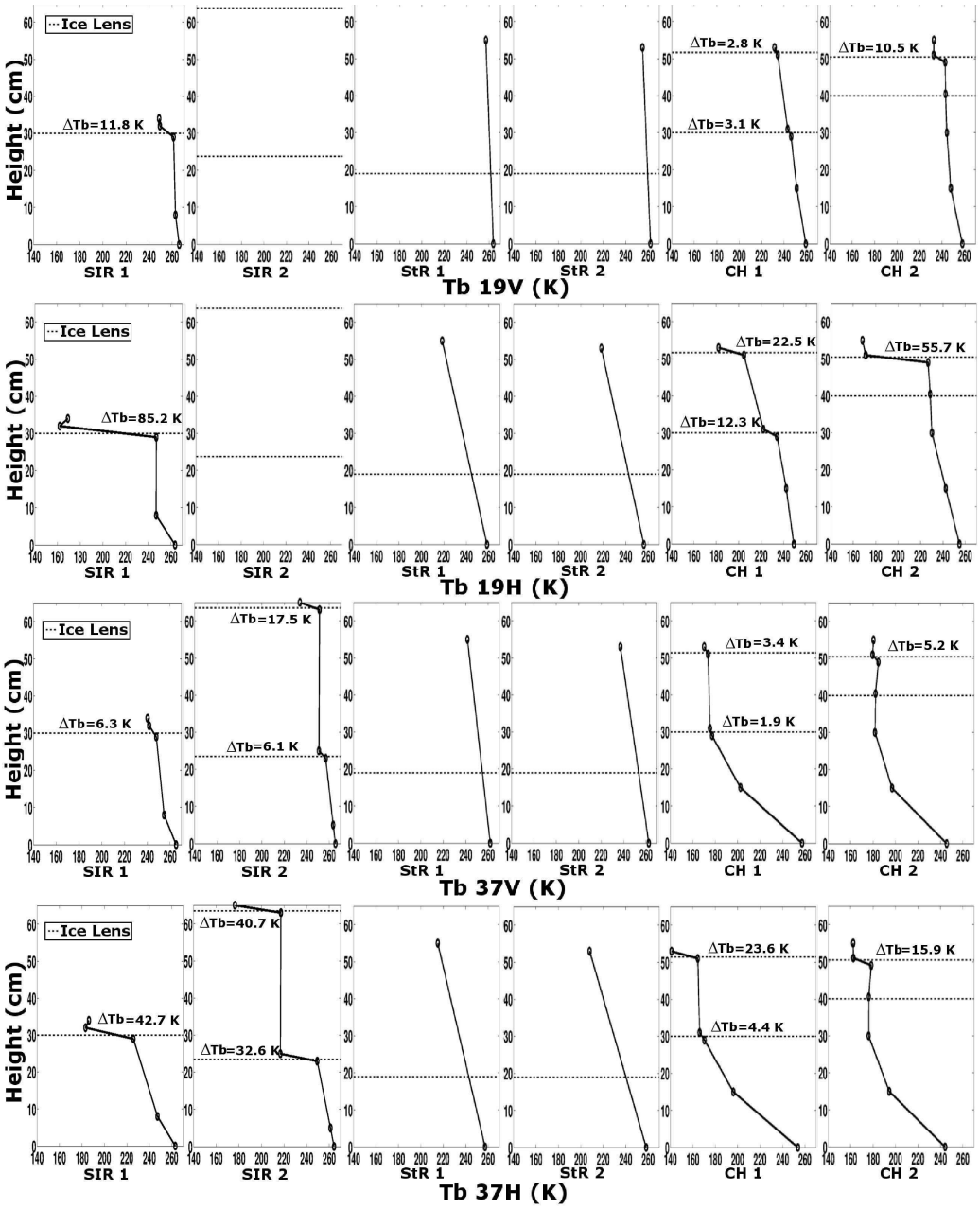


Fig. 4. Measured Tb profiles derived from excavation experiment (i.e., by successively removing upper layers of snow and ice lens) for sites shown in Table III. Dotted lines: vertical position of ice lenses. Respectively, from top to bottom: 19 GHz in polarizations V and H; 37 GHz in polarizations V and H. Measured Tb attenuation ($\Delta$Tb) by ice lenses, where Tb measurements are taken exactly above and below ice lenses are shown. 19-GHz data were not available for SIR2 site.

summarizes the RMSE between the modeled and measured Tb for all four channels shown in Figs. 3 and 5.

The ice lenses do not seem to affect the Tb in V-Pol at either frequency (standard deviation of 1.5 K at 19 V and 3.9 K at 37 V between the results of Figs. 3 and 5). The greatest impact of the ice lenses can be seen in H-Pol. It is known that H-Pol is more sensitive to snowpack stratigraphy [39]. This explains the major improvement in H-Pol at both frequencies that is achieved by the addition of a proper ice lens parameterization in MEMLS. Table VII also shows the results of the ice lens modeling using the equations of Grody [17] in Section II-C.2. The differences between both parameterizations are mainly given by the absorption coefficient calculation that slightly differ [17], [27]. Nonetheless, it is fair to say that the IBA theory is valid with a difference of 0.3 K in the overall RMSE.

### *C. Ice Lens Modeling at Daring Lake*

To further validate the ice lens model presented in this paper, the same analysis is conducted on another independent

This article has been accepted for inclusion in a future issue of this journal. Content is final as presented, with the exception of pagination.



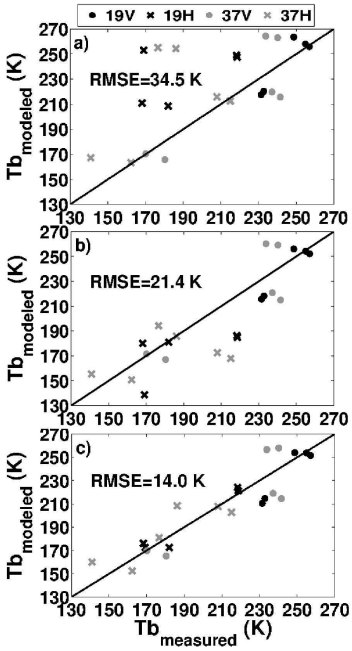


Fig. 5. MEMLS was used to model Tb (a) without an ice lens, (b) with an ice lens at the surface of the snowpack, (c) and with ice lenses at their measured depths within the snowpack with $\phi = 1.3$ and optimized $\sigma$ compared to measured Tb for all six sites having ice lenses (see Table III) for 19 and 37 GHz and two polarizations H and V. Overall RMSE are shown for each case.

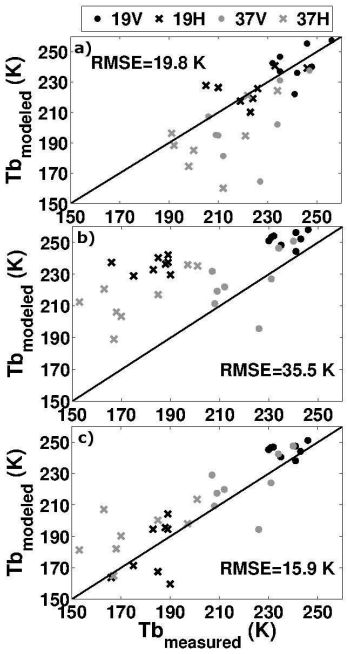


Fig. 6. MEMLS was used to model Tb (a) without an ice lens, (b) with an ice lens at the surface of the snowpack, (c) and with ice lenses at their measured depths within the snowpack, with $\phi = 1.0$ and optimized $\sigma = 0.0$ cm compared to measured Tb for all eight sites taken at Daring Lake with ice lenses [39] for 19 and 37 GHz and two polarizations H and V. Overall RMSE are shown.

TABLE VII
RMSE BETWEEN MODELED AND MEASURED TB FOR FOUR CHANNELS FOR SITES WITH ICE LENSES (TABLE III) COMPARED WITH REFERENCE SITES WITHOUT ICE LENS (TABLE I)

| Channel | RMSE (K) | | | | |
|---|---|---|---|---|---|
| | No Ice | Without Ice Lens | Ice Lens On Top | Ice Lens Within | Ice Lens Within |
| | Fig. 3(a) | Fig. 5(a) | Fig. 5(b) | Fig. 5(c) | Grody [17] Eqns. |
| 19V | 9.4 | 10.8 | 10.4 | 12.9 | 12.4 |
| 19H | 12.1 | 47.7 | 25.3 | 6.9 | 13.0 |
| 37V | 12.1 | 21.0 | 19.2 | 18.8 | 18.0 |
| 37H | 12.4 | 43.9 | 26.3 | 13.6 | 12.5 |
| All | 11.6 | 34.5 | 21.4 | 14.0 | 14.3 |

data set provided by Rees *et al.* [39]. However, the major difference between the analysis of this data set and the one in Section II-C.1 is the snow grain size measurements. Rees *et al.* [39] considered the geometrical diameter ($D_{\max}$) whereas we used the optical diameter [derived from the SSA measurements, (5)], the physical meaning of these parameters is not the same [31]. It is thus necessary to determine another correction factor $\phi$ to optimize the simulations.

The same optimization process is conducted to minimize the errors because of the snow grain size and soil roughness. To do so, three sites (sites 5, 6, and 7 of Rees *et al.* [39]) are selected. These sites are selected because the snowpack under the ice lens is sufficiently thick to minimize any soil effects at 37 GHz. The results of the snow grain size optimization at 37 GHz showed no need for correction ($\phi = 1$) meaning that the parameter $D_{\max}$ without correction gives the minimum $\text{RMSE}_\phi = 19.3$ K. The soil roughness parameter at 19 GHz for all the sites (the sites are all measured in the same region) is found to be $\sigma = 0.0$ cm (minimum $\text{RMSE}_\sigma = 0.097$). The soil roughness parameter is null suggests that the soil roughness had a minimal effect on reflectivity at 19 GHz. In addition, the best parameter derived for the soil reflectivity ratio is $\beta = 2.50$ (13).

Fig. 6 shows comparisons between the modeled and measured Tb at 19 and 37 GHz and V and H polarizations for Fig. 6(a) the layers of snow under the ice lenses (i.e., without ice lenses), Fig. 6(b) simulations without ice lenses, and Fig. 6(c) with the ice lenses modeled at their measured depths. The simulations in Fig. 6(a) are conducted to determine the errors coming from the snow simulation (RMSE = 19.8 K). This RMSE (19.8 K) is comparable with the RMSE of the simulations with the ice lenses at their exact depths (15.9 K). This is a good indicator that the residual error in Fig. 6(c) is more likely because of the snow modeling rather than the ice lens modeling. In addition, the RMSE shows an improvement of 19.6 K with the ice lenses compared with simulations without ice lenses [Fig. 6(b)]. In addition, the 19 H and 37 H channels lead to greater overestimates compared with the 19 V and 37 V channels may indicate that the snow grain size parameter did not adequately simulate snow scattering.

The results for the sites at Daring Lake, characterized by the geometrical diameter ($D_{\max}$), appear to be less accurate than the previous sites (Tables I and III), characterized by the optical diameter ($D_o$). The accuracy of the $D_o$ measurements is estimated to be of the order of 10% [15], [34], which is better than the visual estimate of $D_{\max}$ [22].

This article has been accepted for inclusion in a future issue of this journal. Content is final as presented, with the exception of pagination.



## IV. Ice Lens Modeling Sensitivity

The radiometric impacts of ice lenses are shown in Figs. 7 and 8 for two sensitivity tests, respectively. The first test used one homogeneous snow layer underneath an ice lens of 1 or 10 mm-thickness. Fig. 7 shows the modeled emissivity of snow ($\mathrm{Tb}_{\mathrm{snow}}/T_{\mathrm{snow}}$) for different snow depths without an ice lens at the surface [Fig. 7(a) and (b)] and with an ice lens over the snowpack [Fig. 7(c) and (d)]. It is clear that the snow emissivity is less sensitive to ice thickness at 19 GHz (mean difference of 0.01 in emissivity) than at 37 GHz (mean difference of 0.05 in emissivity). The slight drop in emissivity at 19 GHz is due to the coherence effects [Fig. 8(b) below]. For a 1-mm ice lens, the simulated Tb is slightly higher than a 10-mm ice lens. At 37 GHz, for a 1-mm ice lens, the simulated Tb is lower than for a 10-mm ice lens. The difference in emissivity between the simulations with an ice lens and without an ice lens is mainly because of the coherence effects by adding a thin ice layer. The snow emissivity also drops with a thicker snowpack as the emitted signal is more attenuated by scattering. These results are in agreement with those of Grody [17].

A second sensitivity test is conducted using the observed *in situ* conditions of site StR2 (Table III), and we thus studied the simulated Tb variation for this analysis instead of the emissivity of an idealized homogeneous snowpack. Fig. 8 shows the effects of the ice lens temperature, thickness, and position on the modeled Tb at 19 and 37 GHz in V and H polarizations. It is shown that the temperature has a minimal effect on the modeled Tb. This is explained by the weak modeled emissivity of pure ice at these frequencies ranging between 0.00 ($d_{\mathrm{ice}} = 1$ mm) to 0.01 ($d_{\mathrm{ice}} = 10$ mm) and 0.00 ($d_{\mathrm{ice}} = 1$ mm) to 0.02 ($d_{\mathrm{ice}} = 10$ mm) for 19 and 37 GHz, respectively. In addition, the major difference in the sensitivity of the modeled Tb to the ice lens' thickness is observed for ice lens thicknesses between 0 (no ice lens) and 0.2 cm at 19 GHz and between 0 and 0.4 at 37 GHz. These variations are due to the coherence effects. For ice lenses thicker than 0.4 cm, the effect on the modeled Tb seems minimal. This is due to the weak transmittance for thick ice lenses [17]. The modeled Tb is very sensitive to the vertical position of the ice lens within the snowpack [Fig. 8(c)]. This is explained by the strong variations of the interface reflectivity given by the Fresnel equations. At the top of the snowpit, the dielectric constant contrast between the air-ice and ice-low density snow ($\rho_{\mathrm{snow}} \leq 200\ \mathrm{kg \cdot m^{-3}}$) interfaces increases the reflectivity leading to an increase of the attenuation of the modeled Tb. On the contrary, the low dielectric contrast between the ice-ground and ice-high density snow ($\rho_{\mathrm{snow}} > 350\ \mathrm{kg \cdot m^{-3}}$) interface lowers the reflectivity and decreases the attenuation of the modeled Tb. This abrupt change in Tb at 19 GHz for a change of 0 to 5 cm of the ice lens height is due to this dielectric contrast. At 37 GHz, this change is less significant because of the lower penetration depth of the signal. As the signal at the surface is less affected by the changes at the bottom of the snowpack, the difference between an ice lens at 0 or 5 cm is less important. This result highlights two facts: 1) the most sensitive phenomenon is the reflectivity between the layers; and 2) the measurement of the snow density of the underlying and overlying layers needs to be accurate as they determine the reflectivity of the layer.

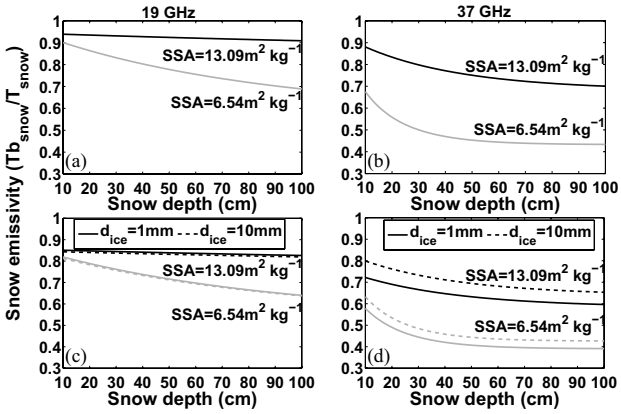


Fig. 7. Modeled snow emissivity ($\mathrm{Tb}_{\mathrm{snow}}/T_{\mathrm{snow}}$) without (a) and (b) and with (c) and (d) ice lens at surface of snowpack at 19 GHz (a) and (c) and 37 GHz (b) and (d) for two snow grain sizes defined by SSA and two ice lens thicknesses ($\mathrm{d}_{\mathrm{ice}}$). Modeled snow layer parameters are: $T_{\mathrm{snow}} = 268$ K and $\rho_{\mathrm{snow}} = 250\ \mathrm{kg \cdot m^{-3}}$ for nadir incidence angle. Black and gray lines: V and H polarizations, respectively.

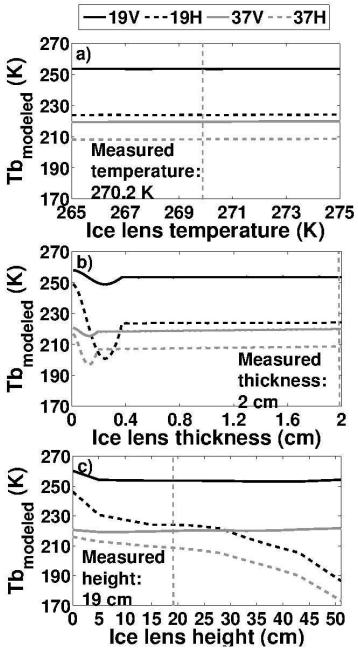


Fig. 8. Modeled Tb at 19 and 37 GHz and at V and H polarizations using MEMLS for different ice lens temperature. (a) Thickness. (b) Position within snowpack. (c) Simulations are done using StR2 site conditions. Ice lens height set to 0 cm in (c) describes lens at bottom of snowpack, i.e., at soil–snow interface.

## V. Conclusion

The main objective of this paper was to improve the Tb simulations of a snowpack having ice lenses within it and determine the sensitivity of the signal to the different properties of ice lenses. The MEMLS was used and an optimization process was proposed to minimize the errors because of the snow grain size measurements and to the soil reflectivity

This article has been accepted for inclusion in a future issue of this journal. Content is final as presented, with the exception of pagination.



parameterization. The use of a unique and detailed data set for the physical properties of snow allowed us to minimize the uncertainties because of snow (without ice lenses) and soil and to accurately estimate the effects of ice lenses.

The sensitivity analysis of the ice lens model showed that the thickness of the ice lens was important for a thickness less than 0.2 or 0.4 cm depending on the frequency, but there was little variation for thicker ice lenses. The vertical location of the ice lens within the snowpack was, however, a key parameter that had to be precisely determined. This finding has important implications for operational applications of snow emission models, for instance in snow water equivalent retrieval schemes as in Takala *et al.* [46]. These hemispheric scale emission model implementations currently use only a single snowpack layer. To properly account for ice lenses, it would be necessary to use up to three layers: one for the lens plus an underlying snow layer and one layer above the lens if necessary. Given the lack of *in situ* stratigraphic snow observations at the hemispheric scale, the vertical location of ice lenses in the snowpack needs to be inferred or estimated from a physical snow model. Given the challenges in deriving multilayer inputs for snow emission models at the hemispheric scale, stratigraphic properties such as ice lenses will likely continue to be a source of uncertainty in operational applications of snow emission models.

A multiplicative correction factor ($\phi$) was applied to the snow grain size parameter derived from optical diameter measurements and the soil parameters were fitted to improve simulations of the snow Tbs at 19 and 37 GHz. The optimal factor was determined to be $\phi = 1.3$ for the SSA measurements and $\phi = 1.0$ for snow grains defined by the longest diameter (i.e., geometrical diameter, $D_{max}$) measured manually. In addition, a soil reflectivity ratio parameter $\beta = 1.72$ and soil roughness parameters for two types of sites ($\sigma_{\text{grass}} = 1.1$ cm and $\sigma_{\text{tundra}} = 0.4$ cm) were determined.

Based on these optimal parameters, comparisons between modeled and measured Tbs were performed without the ice lens treatment [Fig. 5(a)], with an ice lens modeled on top of the snowpack [Fig. 5(b)], and with an ice lens modeled at its measured depth within the snowpack [Fig. 5(c)]. An improvement of 13.1 K for the RMSE was observed by modeling an ice lens on top of the snowpack and an improvement of 20.5 K when modeling the ice lenses at their measured depths within the snowpacks. The simulations presented gave an RMSE of the same order of magnitude (8–20 K) for snow without ice lenses as for snow with ice lenses.

Another comparison was conducted using an independent data set [39] to further validate the ice lens treatment. Again, a significant improvement of 19.6 K of the RMSE was observed by modeling the ice lenses at their measured depths compared with simulations without ice lenses. The higher RMSE compared with the first data set was explained by the snow grain size characterization that was a subjective estimate of the geometrical diameter as opposed to an objective measurement of SSA.

The next step in testing the ice lens model is to measure the ice lens density to verify if there are air bubbles within the lenses and to determine if there is any effect on the microwave signal. In addition, a validation with satellite data would be useful. When validated at this scale, this model could be extremely useful in developing an algorithm to remotely detect ice lenses from satellite measurements.

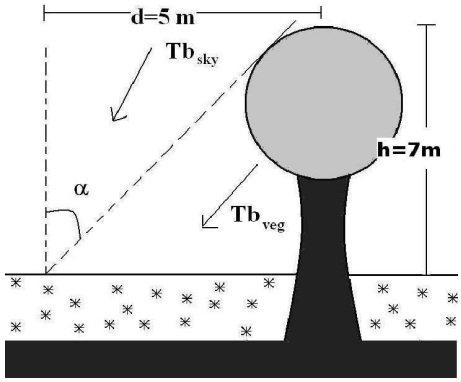


Fig. 9. Representation of different measured downwelling Tb for forest site.

## APPENDIX A

Appendix A demonstrates how the downwelling radiation is estimated when the environment of the target is not open sky (i.e., when the sky view is obscured by trees at temperature $T_{\text{veg}}$). We consider a target in the middle of a circular clearing surrounded by trees.

Fig. 9 shows the Tb measurement conditions for the two CH sites (Table V).

The contribution from the downwelling Tb can be expressed by

$$\text{Tb}_{\downarrow} = \frac{1}{\pi}\left(\iint_{\Omega_{\text{sky}}} \text{Tb}_{\text{sky}} \cos\theta d\theta d\phi + \iint_{\Omega_{\text{veg}}} \text{Tb}_{\text{veg}} \cos\theta d\theta d\phi\right). \quad \text{(A1)}$$

If the vegetation is uniformly distributed and an isotropic $\text{Tb}_{\text{sky}}$ around the measuring site, we obtain the following:

$$\begin{aligned}\text{Tb}_{\downarrow} &= 2\text{Tb}_{\text{sky}} \int_0^{\alpha} \cos\theta \text{d}\theta + 2\text{Tb}_{\text{veg}} \int_{\alpha}^{90} \cos\theta \text{d}\theta \\ &= 2\text{Tb}_{\text{sky}} \left[\frac{1}{2}\sin^2\theta\right]_0^{\alpha} + 2\text{Tb}_{\text{veg}} \left[\frac{1}{2}\sin^2\theta\right]_{\alpha}^{90} \\ &= \text{Tb}_{\text{sky}} \sin^2\alpha + \text{Tb}_{\text{veg}}(1 - \sin^2\alpha). \end{aligned} \quad \text{(A2)}$$

With the following identity

$$\sin^2\alpha = \frac{d^2}{d^2 + h^2} = \frac{1}{1 + (h/d)^2} \quad \text{(A3)}$$

we obtain the following:

$$\text{Tb}_{\downarrow} = \text{Tb}_{\text{sky}} \frac{1}{1 + (h/d)^2} + \text{Tb}_{\text{veg}} \frac{1}{1 + (d/h)^2}. \quad \text{(A4)}$$

In Fig. 9, the fraction of the vegetation contribution is 1.9 times more important than the fraction of the sky contribution, thus it is nonnegligible.

This article has been accepted for inclusion in a future issue of this journal. Content is final as presented, with the exception of pagination.



## ACKNOWLEDGMENT

The authors would like to thank Dr. A. Rees and J. Lemmetyinen for providing the Tb measurements and the MEMLS input parameters for the Daring Lake sites. The authors would like to gratefully acknowledge colleagues for assistance during the field campaigns. The authors would also like to thank both anonymous reviewers for their contribution to the improvement of this paper.

## REFERENCES

[1] L. Arnaud, G. Picard, N. Champollion, F. Domine, J.-C. Gallet, E. Lefebvre, M. Fily, and J. M. Barnola, "Instruments and methodes: Measurement of vertical profiles of snow specific surface area with 1 cm resolution using infrared reflectance: Instrument description and validation," *J. Glaciol.*, vol. 57, no. 201, pp. 17–29, Feb. 2011.

[2] K. Asmus and C. Grant, "English surface based radiometer sbr data acquisition system," *Int. J. Remote Sens.*, vol. 20, nos. 15–16, pp. 3125–3129, 1999.

[3] A. Bartsch, T. Kumpula, B. Forbes, and F. Stammler, "Detection of snow surface thawing and refreezing in the eurasian arctic with quikscat: Implications for reindeer herding," *Ecological Appl.*, vol. 20, no. 8, pp. 2346–2358, 2010.

[4] L. Brucker, G. Picard, and M. Fily, "Snow grain-size profiles deduced from microwave snow emissivities in antarctica," *J. Glaciol.*, vol. 56, no. 197, pp. 514–526, 2010.

[5] L. Brucker, A. Royer, G. Picard, A. Langlois, and M. Fily, "Hourly simulations of seasonal snow microwave brightness temperature using coupled snow evolution-emission models in Quebec, Canada," *Remote Sens. Environ.*, vol. 115, pp. 1966–1977, May 2011.

[6] M. Butt and R. Kelly, "Estimation of snow depth in the UK using the HUT snow emission model," *Int. J. Remote Sens.*, vol. 29, no. 14, pp. 4249–4267, Jan. 2008.

[7] P. Debye, H. Anderson, Jr., and H. Brumberger, "Scattering by an inhomogeneous solid. II. the correlation function and its application," *J. Appl. Phys.*, vol. 28, no. 6, pp. 679–683, Jan. 1957.

[8] C. Derksen, P. Toose, J. Lemmetyinen, J. Pulliainen, A. Langlois, N. Rutter, and M. Fuller, "Evaluation of passive microwave brightness temperature simulations and snow water equivalent retrievals through a winter season," *Remote Sens. Environ.*, vol. 117, pp. 236–248, Feb. 2012.

[9] F. Domine, A. Cabanes, A.-S. Taillandier, and L. Legagneux, "Specific surface area of snow samples determined by CH4 adsorption at 77 k and estimated by optical microscopy and scanning electron microscopy," *Environ. Sci. Technol.*, vol. 35, no. 4, pp. 771–780, Feb. 2001.

[10] F. Domine, R. Salvatori, L. Legagneux, R. Salzano, M. Fily, and R. Casacchia, "Correlation between the specific surface area and the short wave infrared swir reflectance of snow," *Cold Regions Sci. Technol.*, vol. 46, no. 1, pp. 60–68, 2006.

[11] M. Durand, E. Kim, and S. Margulis, "Quantifying uncertainty in modeling snow microwave radiance for a mountain snowpack at the point-scale, including stratigraphic effects," *IEEE Trans. Geosci. Remote Sens.*, vol. 46, no. 6, pp. 1753–1767, Jun. 2008.

[12] M. Durand, E. Kim, and S. Margulis, "Radiance assimilation shows promise for snowpack characterization," *Geophys. Res. Lett.*, vol. 36, no. 2, p. L02503, Jan. 2009.

[13] M. Durand and D. Liu, "The need for prior information in characterizing snow water equivalent from microwave brightness temperatures," *Remote Sens. Environ.*, vol. 126, pp. 248–257, Nov. 2012.

[14] C. Fierz, R. Armstrong, Y. Durand, P. Etchevers, E. Greene, D. McClung, K. Nishimura, P. Satyawali, and S. Sokratov, *The International Classification for Seasonal Snow on the Ground*. London, U.K.: IACS, 2009.

[15] J.-C. Gallet, F. Domine, C. Zender, and G. Picard, "Rapid and accurate measurement of the specific surface area of snow using infrared reflectance at 1310 and 1550 nm," *Cryosphere Discussions*, vol. 3, no. 1, pp. 33–75, 2009.

[16] T. Grenfell and J. Putkonen, "A method for the detection of the severe rain-on-snow event on banks island, October 2003, using passive microwave remote sensing," *Water Resour. Res.*, vol. 44, no. 3, pp. 1–16, Nov. 2008.

[17] N. Grody, "Relationship between snow parameters and microwave satellite measurements: Theory compared with advanced microwave sounding unit observations from 23 to 150 ghz," *J. Geophys. Res.*, vol. 113, no. D22, pp. 1–23, Nov. 2008.

[18] B. Hansen, R. Aanes, I. Herfindal, J. Kohler, B. Saether, and M. Oli, "Climate, icing, and wild arctic reindeer: Past relationships and future prospects," *Ecology*, vol. 92, no. 10, pp. 1917–1923, 2011.

[19] A. Kontu and J. Pulliainen, "Simulation of spaceborne microwave radiometer measurements of snow cover using in situ data and brightness temperature modeling," *IEEE Trans. Geosci. Remote Sens.*, vol. 48, no. 3, pp. 1031–1044, Mar. 2010.

[20] A. Langlois, A. Royer, C. Derksen, B. Montpetit, F. Dupont, and K. Goïta, "Coupling the snow thermodynamic model snowpack with the microwave emission model of layered snowpacks for subarctic and arctic snow water equivalent retrievals," *Water Resour. Res.*, vol. 48, no. 12, pp. 1–30, Dec. 2012.

[21] A. Langlois, A. Royer, F. Dupont, A. Roy, K. Goïta, and G. Picard, "Improved corrections of forest effects on passive microwave satellite remote sensing of snow over boreal and subarctic regions," *IEEE Trans. Geosci. Remote Sens.*, vol. 49, no. 10, pp. 3824–3837, Oct. 2011.

[22] A. Langlois, A. Royer, and K. Goïta, "Analysis of simulated and spaceborne passive microwave brightness temperatures using in situ measurements of snow and vegetation properties," *Commun. J. Remote Sens.*, vol. 36, no. S1, pp. S135–S148, Jan. 2010.

[23] A. Langlois, A. Royer, B. Montpetit, G. Picard, L. Brucker, L. Arnaud, P. Harvey-Collard, M. Fily, and K. Goïta, "On the relationship between snow grain morphology and in-situ near infrared calibrated reflectance photographs," *Cold Regions Sci. Technol.*, vol. 61, no. 1, pp. 34–42, Apr. 2010.

[24] J. Lemmetyinen, A. Kontu, A. Rees, C. Derksen, and J. Pulliainen, "Comparison of multiple layer snow emission models," in *Proc. 11th Specialist Meeting Microw. Radiometry Remote Sens. Environ. MicroRad*, Mar. 2010, pp. 99–103.

[25] J. Lemmetyinen, J. Pulliainen, A. Rees, A. Kontu, Y. Qiu, and C. Derksen, "Multiple-layer adaptation of hut snow emission model: Comparison with experimental data," *IEEE Trans. Geosci. Remote Sens.*, vol. 48, no. 7, pp. 2781–3055, Jul. 2010.

[26] M. Matzl and M. Schneebeli, "Measuring specific surface area of snow by near-infrared photography," *J. Glaciol.*, vol. 52, no. 179, pp. 558–564, Dec. 2006.

[27] C. Mätzler, "Improved born approximation for scattering of radiation in a granular medium," *J. Appl. Phys.*, vol. 83, no. 11, pp. 6111–6117, Jun. 1998.

[28] C. Mätzler and P. Rosenkranz, "Dependence of microwave brightness temperature on bistatic surface scattering: Model functions and application to AMSU-A," *IEEE Trans. Geosci. Remote Sens.*, vol. 45, no. 7, pp. 2130–2138, Jul. 2007.

[29] C. Mätzler and A. Wiesmann, "Extension of the microwave emission model of layered snowpacks to coarse-grained snow," *Remote Sens. Environ.*, vol. 70, no. 3, pp. 317–325, Apr. 1999.

[30] C. Mätzler, *Microwave Properties of Ice and Snow*, vol. 227. Boston, MA, USA: Kluwer, 1998, pp. 241–257.

[31] C. Mätzler, "Relation between grain-size and correlation length of snow," *J. Glaciol.*, vol. 48, pp. 461–466, 2002.

[32] C. Mätzler, *Thermal Microwave Radiation: Applications for Remote Sensing* (IET electromagnetic waves series). Stevenage, U.K.: Institution of Engineering and Technology, May 2006.

[33] F. L. Miller, R. H. Russell, and A. Gunn, "The recent decline of peary caribou on western queen elizabeth islands of arctic Canada," *Polarforschung*, vol. 45, no. 1, pp. 17–21, 1975.

[34] B. Montpetit, A. Royer, A. Langlois, P. Cliche, A. Roy, N. Champollion, G. Picard, F. Domine, and R. Obbard, "New shortwave infrared albedo measurements for snow specific surface area retrieval," *J. Glaciol.*, vol. 58, no. 211, pp. 941–952, Sep. 2012.

[35] G. Picard, L. Arnaud, F. Domine, and M. Fily, "Determining snow specific surface area from near-infrared reflectance measurements: Numerical study of the influence of grain shape," *Cold Regions Sci. Technol.*, vol. 56, no. 1, pp. 10–17, Apr. 2009.

[36] C. Prigent, J.-P. Wigneron, W. Rossow, and J. Pardo-Carrion, "Frequency and angular variations of land surface microwave emissivities: Can we estimate SSM/T and amsu emissivities from SSM/I emissivities," *IEEE Trans. Geosci. Remote Sens.*, vol. 38, no. 5, pp. 2373–2386, Sep. 2000.

[37] J. T. Pulliainen, J. Grandell, and M. T. Hallikainen, "Hut snow emission model and its applicability to snow water equivalent retrieval," *IEEE Trans. Geosci. Remote Sens.*, vol. 37, no. 3, pp. 1378–1390, May 1999.

[38] J. Putkonen, H. Jacobson, and K. Rennert, "Brief communication 'modeled rain on snow in CLM3 warms soil under thick snow cover and cools it under thin'," *Cryosphere Discussions*, vol. 5, no. 5, pp. 2557–2570, Sep. 2011.

This article has been accepted for inclusion in a future issue of this journal. Content is final as presented, with the exception of pagination.



[39] A. Rees, J. Lemmetyinen, C. Derksen, J. Pulliainen, and M. English, "Observed and modelled effects of ice lens formation on passive microwave brightness temperatures over snow covered tundra," *Remote Sens. Environ.*, vol. 114, no. 1, pp. 116–126, 2010.
[40] K. Rennert, G. Roe, J. Putkonen, and C. Bitz, "Soil thermal and ecological impacts of rain on snow events in the circumpolar arctic," *J. Climate*, vol. 22, no. 9, pp. 2302–2315, May 2009.
[41] A. Roy, G. Picard, A. Royer, F. Dupont, A. Langlois, B. Montpetit, and C. Derksen, "Brightness temperature simulations of the canadian seasonal snowpack driven by measurements of the snow specific surface area," *IEEE Trans. Geosci. Remote Sens.*, vol. 51, no. 9, to be published [Online]. Available: ieeexplore.ieee.org
[42] A. Roy, A. Royer, J.-P. Wigneron, A. Langlois, J. Bergeron, and P. Cliche, "A simple parameterization for a boreal forest radiative transfer model at microwave frequencies," *Remote Sens. Environ.*, vol. 124, pp. 371–383, Jan. 2012.
[43] M. Serreze and R. Barry, "Processes and impacts of arctic amplification: A research synthesis," *Global Planetary Change*, vol. 77, nos. 1–2, pp. 85–96, May 2011.
[44] F. S. Solheim, "Use of pointed water vapor radiometers to improve gps surveying accuracy," Ph.D. dissertation, Dept. Phys., Univ. Colorado Boulder, Boulder, CO, USA, 1993.
[45] A. Stien, L. Loel, A. Mysterud, T. Severinsen, J. Kohler, and R. Langvatn, "Icing events trigger range displacement in a high-arctic ungulate," *Ecology*, vol. 91, no. 3, pp. 915–920, Mar. 2010.
[46] M. Takala, K. Luojus, J. Pulliainen, C. Derksen, J. Lemmetyinen, J.-P. Kärnä, J. Koskinen, and B. Bojkov, "Estimating northern hemisphere snow water equivalent for climate research through assimilation of space-borne radiometer data and ground-based measurements," *Remote Sens. Environ.*, vol. 115, no. 12, pp. 3517–3529, 2011.
[47] M. Tedesco and E. Kim, "Retrieval of dry-snow parameters from microwave radiometric data using a dense-medium model and genetic algorithms," *IEEE Trans. Geosci. Remote Sens.*, vol. 44, no. 8, pp. 2143–2151, Aug. 2006.
[48] A. Toure, K. Goïta, A. Royer, E. Kim, M. Durand, S. Margulis, and H. Lu, "A case study of using a multilayered thermodynamical snow model for radiance assimilation," *IEEE Trans. Geosci. Remote Sens.*, vol. 49, no. 8, pp. 2828–2837, Aug. 2011.
[49] L. Tsang, D. Liang, X. Xu, and P. Xu, "Microwave emission from snowpacks: Modelling the effects of volume scattering, surface scattering and layering," in *Proc. Microw. Radiometry Remote Sens. Environ.*, Mar. 2008, pp. 1–4.
[50] U. Wegmüller and C. Mätzler, "Rough bare soil reflectivity model," *IEEE Trans. Geosci. Remote Sens.*, vol. 37, no. 3, pp. 1391–1395, May 1999.
[51] A. Wiesmann, C. Fierz, and C. Mätzler, "Simulation of microwave emission from physically modeled snowpacks," *Ann. Glaciol.*, vol. 31, no. 1, pp. 397–401, Jan. 2000.
[52] A. Wiesmann and C. Mätzler, "Microwave emission model of layered snowpacks," *Remote Sens. Environ.*, vol. 70, no. 3, pp. 307–316, Dec. 1999.
[53] J.-P. Wigneron, A. Chanzy, Y. Kerr, H. Lawrence, J. Shi, M. Escorihuela, V. Mironov, A. Mialon, F. Demontoux, P. De Rosnay, and K. Saleh-Contell, "Evaluating an improved parameterization of the soil emission in l-meb," *IEEE Trans. Geosci. Remote Sens.*, vol. 49, no. 4, pp. 1177–1189, Apr. 2011.
[54] H. Ye, D. Yang, and D. Robinson, "Winter rain on snow and its association with air temperature in northern eurasia," *Hydrol. Process.*, vol. 22, no. 15, pp. 2728–2736, 2008.

**Benoit Montpetit** received the B.Sc. degree in physics from Université de Sherbrooke, Sherbrooke, QC, Canada, in 2009, where he is currently pursuing the Ph.D. degree in remote sensing.

He participated in multiple snow studies with the Centre d'Applications et de Recherches en Télédétection, Université de Sherbrooke, and with the Laboratoire de Glaciologie et de Géophysique de l'Environnement, Grenoble, France. His current research interests include snow and soil microwave emission modeling, snow grain size measurements, and ice lens modeling and detection within snowpacks.

**Alain Royer** received the Ph.D. degree in geophysics from the University of Grenoble, Grenoble, France, in 1981.

He was a Natural Sciences and Engineering Research Council Fellow with the Centre d'Applications et de Recherches en Télédétection, Université de Sherbrooke, Sherbrooke, QC, Canada, from 1983 to 1988, where he has been a Professor since 1988. From 2000 to 2010, he was the Director of Cartel. He was involved in the IPY Canadian Cryosphere project from 2008 to 2011 and leads several projects for improving methods for snow modeling and remote sensing, based on passive microwave radiometry, recently over Arctic (Churchill, Ma, 2009, Baffin Island, Nu, 2011), subarctic (Nunavik, 2008–2013) and Antarctic (Dome C, 2012) regions. His current research interests include environmental geophysics from space, including the development of surface parameter retrieval algorithms from remote sensing data applied to northern climate change analysis.

**Alexandre Roy** received the B.Sc. degree in physical geography from the Université de Montréal, Montréal, QC, Canada, in 2002, and the M.Env. degree in remote sensing from the Université de Sherbrooke, Sherbrooke, QC, in 2009, where he is currently pursuing the Ph.D. degree in remote sensing.

His current research interests include snow, passive microwave, radar, land surface schemes and water cycles.

**Alexandre Langlois** received the B.Sc. degree in physical geography and the M.Sc. degree in remote sensing from the Université de Sherbrooke, Sherbrooke, QC, Canada, in 2001 and 2003, respectively. He conducted his Ph.D. work from 2004 to 2007 with the University of Manitoba, Winnipeg, MB, Canada, where he focused on the analysis of snow over sea ice using passive microwave radiometry.

He has participated in numerous field campaigns with the Canadian and European Arctic. He is currently a Professor with the Centre d'Applications et de Recherches en Télédétection, Département de Géomatique Appliquée, Université de Sherbrooke, where his current work focuses on snow and passive microwaves' model coupling over land.

Dr. Langlois has been an active member on the executive of the Eastern Snow Conference since 2009.

**Chris Derksen** received the B.E.S., M.A., and Ph.D. degrees from the University of Waterloo, Waterloo, ON, Canada, in 1997, 1998, and 2001, respectively.

He is a Research Scientist with the Climate Research Division, Environment Canada, and an Adjunct Faculty with the Department of Geography and Environmental Management, University of Waterloo. His current research interests include microwave remote sensing of the cryosphere, and the use of satellite derived datasets to identify cryosphere-climate interactions.

# 6 Résultats : Étude et création d'un indice de détection des croutes de glace par télédétection MOP

## 6.1 Introduction

Dans une optique de suivi des milieux arctiques par télédétection MOP, il est important de pouvoir détecter la formation de croutes de glace dans le couvert nival. Plusieurs produits de suivi de l'état du couvert nival comme l'ÉEN, l'épaisseur de la neige ou l'étendue de la neige sont obtenus par télédétection MOP. Comme il a été démontré précédemment, la présence de croutes de glace affecte fortement le signal MOP et induit donc des erreurs sur les paramètres de la neige mesurés. De plus, ces croutes de glace affectent les mœurs des communautés arctiques et menacent même la survie de différentes espèces de la faune arctique (Hansen *et al.*, 2011; Miller *et al.*, 1975; Rennert *et al.*, 2009; Serreze et Barry, 2011; Putkonen et Roe, 2003). Comme la densité de stations d'observations dans l'arctique est faible (Figure 1.1), il est important de développer un indice de détection des croutes de glace par télédétection afin de corriger les effets de ces croutes et ainsi corriger les produits du couvert nival. Grenfell et Putkonen (2008) ont étudié un événement de pluie hivernale survenu en octobre 2003 sur l'île Banks (Territoires du Nord-Ouest), au Canada. Ils ont démontré que la formation de la croute de glace à l'intérieur du couvert de neige a fortement modifié le rapport de polarisation (PR). Cette observation est confirmée par l'étude de sensibilité présentée à la section IV de Montpetit *et al.* (2013).

## 6.2 Rapport de polarisation

Le rapport de polarisation (PR) pour une fréquence $f$ est décrit par l'équation suivante (Cavalieri *et al.*, 1984; Grenfell et Putkonen, 2008) :

$$PR(f) = \frac{T_B(f, V-Pol) - T_B(f, H-Pol)}{T_B(f, V-Pol) + T_B(f, H-Pol)} \tag{6.2.1}$$

Comme démontré à la section IV de Montpetit *et al.* (2013), la $T_B$ du couvert de neige en H-Pol est nettement plus atténuée par la présence d'une croute de glace que la $T_B$ en V-Pol. Ceci est principalement dû au coefficient de réflexion entre les interfaces du manteau neigeux (sol-

neige, neige-neige, neige-air) qui est plus fort en H-Pol qu'en V-Pol. Ces coefficients de réflexion sont obtenus à l'aide des équations de Fresnel. La figure 6.1 montre la sensibilité des coefficients de Fresnel d'une interface de neige ayant une constante diélectrique $\epsilon'_{neige}$ allant de 1.25 (une couche de neige ayant une densité de 150 kg m$^{-3}$, Mätzler (1996)) à 1.55 (une couche de neige ayant une densité de 300 kg m$^{-3}$) et un milieu incident ayant une constante diélectrique allant de la constante diélectrique de l'air ($\epsilon'_{air} = 1$) jusqu'à la constante diélectrique de la glace pure ($\epsilon'_{glace} = 3.2$).

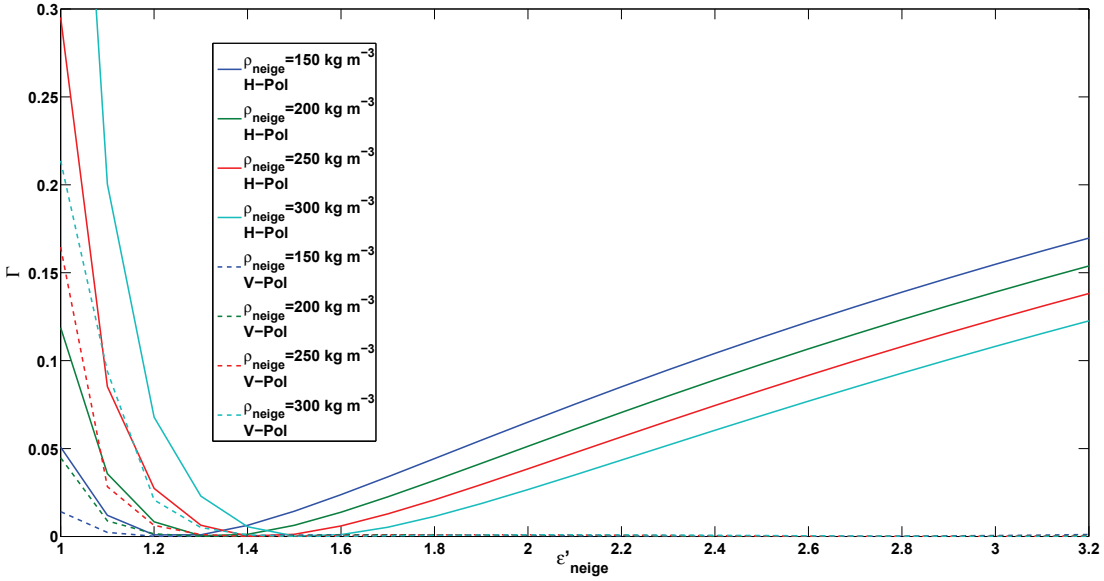


Figure 6.1 – Sensibilité des coefficients de Fresnel en H-Pol (trait plein) et V-Pol (trait pointillé) à la constante diélectrique du milieu incident. Le milieu de réflexion est considéré comme étant de la neige avec un $\epsilon'_{neige}$ allant de 1.25 à 1.53 et l'angle d'incidence est de 55 $^o$.

On observe dans la figure 6.1 que la réflectivité en H-Pol est davantage affectée par le contraste diélectrique entre la neige et le milieu incident que la réflectivité en V-Pol. Ceci implique donc que lorsqu'il y a formation d'une croute de glace, particulièrement à la surface du couvert neigeux, la $T_B$ en V-Pol sera moins atténuée que la $T_B$ en H-Pol. Ainsi, le PR (Éq. 6.2.1) subira une forte augmentation suite à la formation d'une croute de glace.

Il est vrai que du simple point de vue de l'atténuation de la $T_B$ , le PR n'est pas nécessaire et que la différence entre les deux $T_B$ peut bien décrire la présence de croutes de glace. Dans le domaine des MOP, la $T_B$ pour une fréquence $f$ et une polarisation $p$ est décrite par l'approximation de Rayleigh-Jeans :

$$T_B(f,p) = e(f,p)T_{neige} \tag{6.2.2}$$

où $e(f,p)$ et $T_{neige}$ sont respectivement l'émissivité et la température du couvert de neige. Comme la température de la neige peut varier d'un hiver à l'autre et même au cours d'une seule période hivernale, la différence de polarisation peut être plus difficile à évaluer dans une optique d'étude temporelle à long terme. Le PR quant à lui minimise l'impact de la température de la neige jusqu'à l'éliminer dans l'approximation où la $T_B$ n'est pas affectée par des contributions externes comme l'atmosphère et que la seule composante des $T_B$ du PR est la contribution du couvert de neige. Ainsi, le PR fourni un paramètre normalisé qui peut être étudié sur une période temporelle plus longue.

## 6.3 Validation de MEMLS pour simuler la $T_B$ de la neige avec des croutes de glace

Suite aux campagnes de terrain Baie James et Umiujuaq (section 2.1), les Figures 3 et 5 de l'article Montpetit *et al.* (2013) ont pu être complétées avec de nouvelles données radiométriques sur deux nouveaux sites en ajoutant des mesures à 10.7 GHz en plus des mesures à 19 et 37 GHz. La Figure 6.2 montre la comparaison entre les $T_B$ mesurées et simulées à l'aide de MEMLS pour des sites où il n'y avait pas de croutes de glace dans le couvert de neige. La Figure 6.3 montre la comparaison entre les $T_B$ mesurées et simulées à l'aide de MEMLS pour des sites où il y avait présence de croutes de glace dans le couvert de neige. La Figure 6.3(a) présente les simulations où les croutes de glace ont été omises et la Figure 6.3(b) présente les simulations où les croutes de glace ont été simulées (Montpetit *et al.*, 2013) avec leurs propriétés mesurées (température, épaisseur et position). Le paramètre de taille de grains de neige a été corrigé par le facteur $\phi$, déterminé à la section 3.2 et la contribution du sol a été simulé à l'aide des paramètres obtenus à la section 4.

Le tableau 6.1 donne les erreurs quadratiques moyennes (RMSE) entre les $T_B$ mesurées et simulées des Figures 6.2 et 6.3. Comme dans la section 5, on remarque que lorsqu'on omet les croutes de glace lorsqu'on simule la $T_B$ du couvert nival ayant des croutes de glace, il y a une très grande erreur entre les mesures et les simulations (RMSE=24.9 K). Toutefois, lorsqu'on simule ces mêmes sites avec des croutes de glace, on retrouve l'erreur obtenue pour les simulations de couverts de

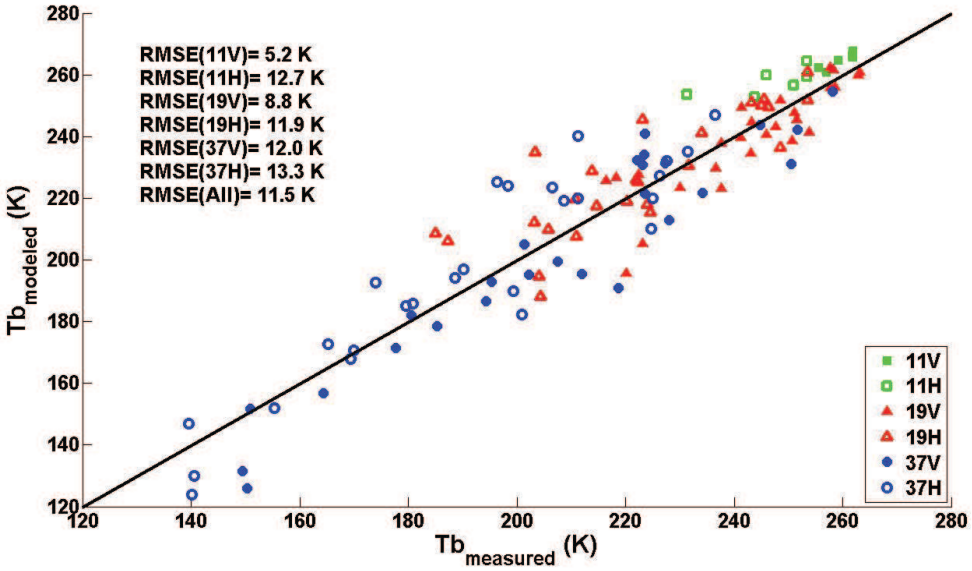


Figure 6.2 – Simulations des $T_B$ des couverts de neige sans présence de croutes de glace à l'aide du modèle MEMLS. Le facteur de correction $\phi = 1.3$ de la taille des grains de neige a été appliqué (section 3.2) et la contribution du sol a été simulée à l'aide des travaux de la section 4. — Simulations using MEMLS of snowpacks where no ice lenses were measured. The snow grain size correction factor $\phi = 1.3$ was applied and the soil contribution was modeled using the results presented in section 4.

neige n'ayant pas de croutes (Figure 6.2). Ceci indique donc que l'erreur restante des simulations des couverts nivaux ayant des croutes de glace est plutôt due aux erreurs de modélisation de la neige qu'aux erreurs de modélisation des croutes de glace. On peut donc conclure qu'avec une erreur globale de 11.3 K, il est possible de simuler la $T_B$ de couverts nivaux avec ou sans croutes de glace à l'aide de MEMLS.

## 6.4 Étude de la sensibilité du PR aux paramètres d'une croute de glace

Afin d'évaluer l'effet des croutes de glace sur le PR, 23 sites de la campagne de terrain 2010-2011 à Churchill (Manitoba), au Canada ont été sélectionnés. Ces sites ont comme particularité d'être des clairières (aucune présence de végétation) et le sol est organique. Ces sites ont été mesurés de janvier à avril 2010 et la base de données comprend une grande variété de propriétés de couverts nivaux représentatifs des régions arctiques du Canada. Le tableau 6.2 présente les valeurs moyennes et les écart-types des propriétés mesurées du couvert nival.

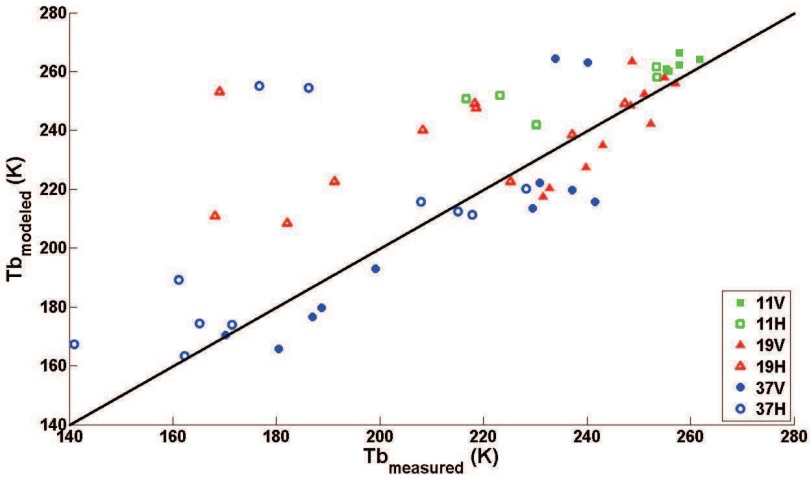


(a)

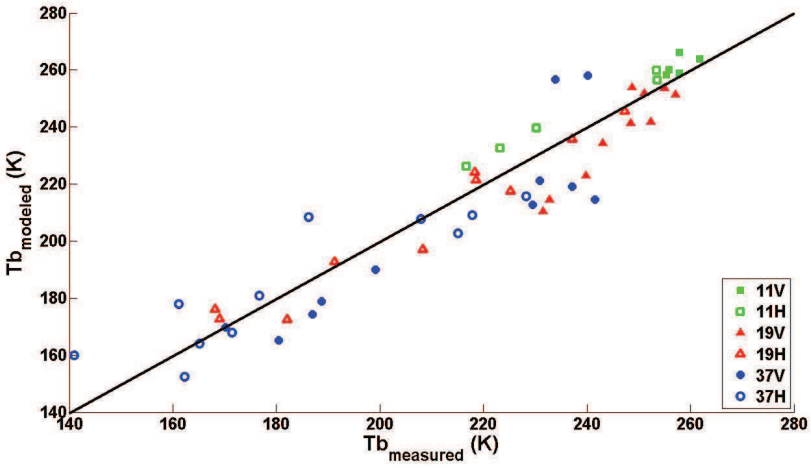


(b)

Figure 6.3 – Simulations des $T_B$ des couverts de neige présentant des croutes de glace à l'aide du modèle MEMLS. Le facteur de correction $\phi = 1.3$ de la taille des grains de neige a été appliqué (section 3.2) et la contribution du sol a été simulée à l'aide des travaux de la section 4. Les croutes de glace ont été omises dans les simulations (a) et ensuite simulées avec leurs propriétés mesurées (b). — Simulations using MEMLS where ice lenses were measured. The snow grain size correction factor $\phi = 1.3$ was applied and the soil contribution was modeled using the results presented in section 4. The ice lenses were first omitted from the simulations (a) and then included with their measured properties (b).

Pour chacun des sites, les PR ont été simulés pour 4 scénarios, soit : 1) sans croute de glace, 2) avec une croute de glace insérée sous le couvert nival soit à l'interface sol-neige, 3) avec une croute de

Tableau 6.1 – Erreur quadratique moyenne entre les $T_B$ mesurées et simulées à l'aide de MEMLS (Figure 6.3). — Root mean square error between the measured and modeled $T_B$ using MEMLS (Figure 6.3).

| Canal | RMSE (K) Neige (Figure 6.2) | Sans glace (Figure 6.3(a)) | Avec glace (Figure 6.3(b)) |
|---|---|---|---|
| 11V | 5.2 | 5.4 | 4.5 |
| 11H | 12.7 | 20.9 | 7.9 |
| 19V | 8.8 | 9.5 | 11.7 |
| 19H | 11.9 | 36.6 | 6.4 |
| 37V | 12.0 | 17.0 | 16.1 |
| 37H | 13.3 | 33.8 | 12.2 |
| Tous | 11.5 | 24.9 | 11.3 |

glace insérée au milieu du couvert nival à un interface neige-neige et 4) à la surface du couvert nival à l'interface neige-air. De plus, des croutes de glace d'une épaisseur de 0 à 1 cm ont été simulées pour chacun des quatre scénarios. Pour ces simulations, la contribution du sol a été simulée à l'aide des résultats obtenus à la section 4 (Montpetit *et al.*, En Revision), la taille des grains de neige a été corrigée à l'aide du facteur $\phi$, obtenu dans la section 3.2, et la contribution atmosphérique à été simulée pour une gamme de valeurs de vapeur d'eau précipitable allant de 1 à 25 mm et les propriétés atmosphériques (la $T_B$ descendante : $T_{B,\downarrow}$) et la transmissivité ($\tau_{atm}$) de l'atmosphère ont été calculées à l'aide des régressions linéaires présentées par Roy (2014). Les $T_B$ simulées pour une fréquence $f$ et une polarisation $p$ peuvent être traduites par l'équation suivante :

$$T_B(f,p) = e_{neige}(f,p)T_{neige} + (1 - e_{neige}(f,p))T_{B\downarrow}(f) \tag{6.4.1}$$

où $e_{neige}$ est l'émissivité effective du couvert nival simulée par MEMLS, $T_{neige}$ est la température effective du couvert nival simulée par MEMLS et $T_{B\downarrow}$ est la température de brillance atmosphérique descendante simulée à l'aide des régressions linéaires de Roy (2014). Par la suite, les PR ont été calculés (Éq. 6.2.1) à l'aide de ces $T_B$ à 10.7 GHz (PR11), 19 GHz (PR19) et 37 GHz (PR37). La figure 6.4 présente les PR simulés dans l'espace 3D des PR11, PR19 et PR37. On remarque que les simulations sans glace (cercles noirs) se retrouvent surtout vers l'origine. Les simulations avec une croute de glace à l'interface sol-neige (cercles rouges) sont légèrement décalées des simulations sans glace (noir) sur l'axe des PR11 et s'étendent vers des valeurs supérieures à ces dernières

Tableau 6.2 – Hauteur de neige ($H_{neige}$), température moyenne de la neige ($T_{neige}$), densité moyenne de la neige ($\rho_{neige}$) et la SSA moyenne de la neige et leurs écart-types (entre parenthèses) pour les 23 sites sélectionnés de la campagne 2009-2010 à Churchill (Manitoba), Canada. — Snow height ($H_{neige}$), mean snow temperature ($T_{neige}$), mean snow density ($\rho_{neige}$) and the mean snow SSA with their standard deviations (in parenthesis) for the 23 selected sites of the 2009-2010 Chuchill (Manitoba), Canada field campaign.

| # de site | $H_{neige}$ (cm) | $T_{neige}$ (K) | $\rho_{neige}$ (kg m$^{-3}$) | SSA (kg m$^{-2}$) |
|---|---|---|---|---|
| 1 | 43.0 | 260.7 (6.3) | 279.0 (78.8) | 13.2 (6.3) |
| 2 | 19.0 | 258.5 (2.6) | 266.7 (43.6) | 9.8 (0.9) |
| 3 | 33.0 | 254.1 (3.1) | 377.6 (119.4) | 17.0 (2.1) |
| 4 | 56.0 | 259.9 (5.6) | 319.1 (68.1) | 13.7 (4.1) |
| 5 | 48.0 | 255.5 (7.1) | 260.4 (27.2) | 9.0 (0.8) |
| 6 | 45.0 | 258.5 (7.8) | 236.7 (27.9) | 11.0 (3.1) |
| 7 | 44.0 | 252.2 (8.7) | 285.9 (49.4) | 11.9 (1.6) |
| 8 | 86.0 | 257.5 (7.8) | 285.9 (49.4) | 14.7 (1.7) |
| 9 | 51.0 | 260.2 (8.1) | 278.2 (50.7) | 15.0 (10.9) |
| 10 | 46.0 | 258.7 (7.5) | 242.6 (42.2) | 20.3 (10.7) |
| 11 | 22.0 | 263.2 (3.4) | 262.4 (23.6) | 13.0 (0.0) |
| 12 | 25.0 | 263.2 (3.4) | 277.7 (41.7) | 15.6 (0.7) |
| 13 | 33.0 | 267.0 (2.9) | 291.7 (65.7) | 8.9 (0.9) |
| 14 | 118.0 | 269.7 (2.6) | 373.6 (47.1) | 15.4 (4.9) |
| 15 | 82.0 | 265.3 (4.1) | 284.5 (65.2) | 25.3 (24.8) |
| 16 | 91.0 | 268.1 (3.7) | 309.3 (80.4) | 26.4 (22.8) |
| 17 | 96.0 | 267.5 (5.7) | 291.1 (58.3) | 47.9 (76.2) |
| 18 | 86.0 | 267.0 (5.9) | 293.6 (61.7) | 76.2 (47.7) |
| 19 | 174.0 | 268.1 (4.8) | 388.0 (72.7) | 20.8 (14.4) |
| 20 | 180.0 | 268.7 (5.1) | 286.6 (82.8) | 18.2 (9.6) |
| 21 | 150.0 | 267.4 (5.1) | 381.9 (92.6) | 21.7 (15.8) |
| 22 | 119.0 | 266.7 (4.4) | 353.6 (89.2) | 36.2 (25.5) |
| 23 | 57.0 | 261.0 (7.2) | 309.0 (71.6) | 12.3 (4.0) |

sur les axes des PR19 et PR37. Les simulations pour les croutes de glace à l'interface neige-neige (cercles bleu) sont, quant à elles, beaucoup plus distribuées sur l'axe des PR11 et PR19, mais restent dans des valeurs similaires de PR37 que les simulations avec une croute à l'interface sol-neige (rouge). Finalement, on observe que les simulations pour les croutes à l'interface neige-air (cercles verts) se démarquent des autres scénarios de simulation sur l'axe des PR37.

La Figure 6.5 montre les distributions des différences entre les PR de la Figure 6.4 et la moyenne des PR du scénario sans glace de la Figure 6.4. Les différents scénarios ont les mêmes codes de

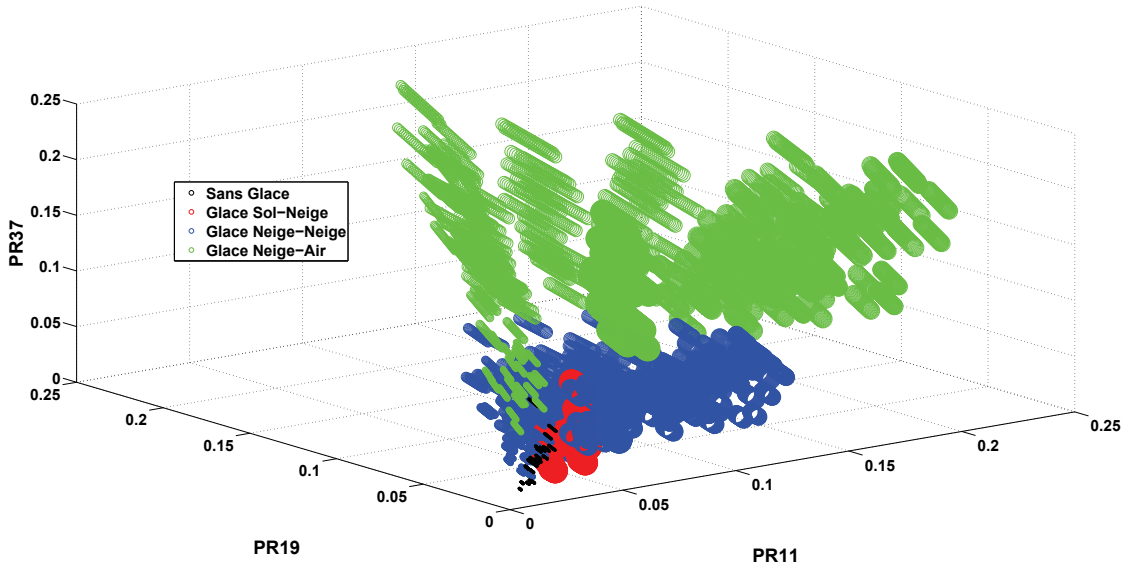


Figure 6.4 – Représentation 3D des PR simulés pour les sites Churchill sélectionnée (Tableau 6.2) à 10.7 GHz (PR11), 19 GHz (PR19) et 37 GHz (PR37). Les simulations sans glace sont représentés par des cercles noirs, les simulations avec une croute de glace à l'interface sol-neige en rouge, les simulations avec une croute de glace à l'interface neige-neige en bleu et les simulations avec une croute à l'interface neige-air en vert. La taille des cercles est proportionnelle à l'épaisseur des croutes de glace. — 3D representation of the simulated PR for the selected Churchill sites (Table 6.2) at 10.7 GHz (PR11), 19 GHz (PR19) and 37 GHz (PR37). The simulations with no ice lenses within the snowpack are represented by black circles, simulations with an ice lens at the soil-snow interface by red circles, simulations with an ice lens at the snow-snow interface by blue circles and simulations with an ice lens at the snow-air interface by green circles.

couleurs que la Figure 6.4. La différence à la moyenne des PR a été choisie afin de permettre l'étude des PR sur de multiples sites indépendamment des conditions de neige. Ces figures permettent de mieux cerner les effets des paramètres des croutes de glace sur les PR. On observe que pour le PR11, les simulations sont beaucoup plus dispersées que pour les autres PR. Le PR11 permet aussi de mieux délimiter les simulations sans croute de glace (noir) et les simulations avec une croute de glace à l'interface sol-neige (rouge) que les autres PR, particulièrement que le PR37. En effet, les simulations du PR37 se retrouvent surtout en deçà de 0.05 pour les scénarios sans glace, avec glace à l'interface sol-neige et à l'interface neige-neige. Toutefois, le PR37 est celui qui discrimine le mieux le scénario des simulations avec une croute de glace à l'interface neige-air. Ces caractéristiques du PR37 peuvent être expliquées par la plus faible profondeur de pénétration du signal à 37 GHz et il est donc plus affecté par les changements des propriétés de surface que les

deux autres fréquences étudiées ici.

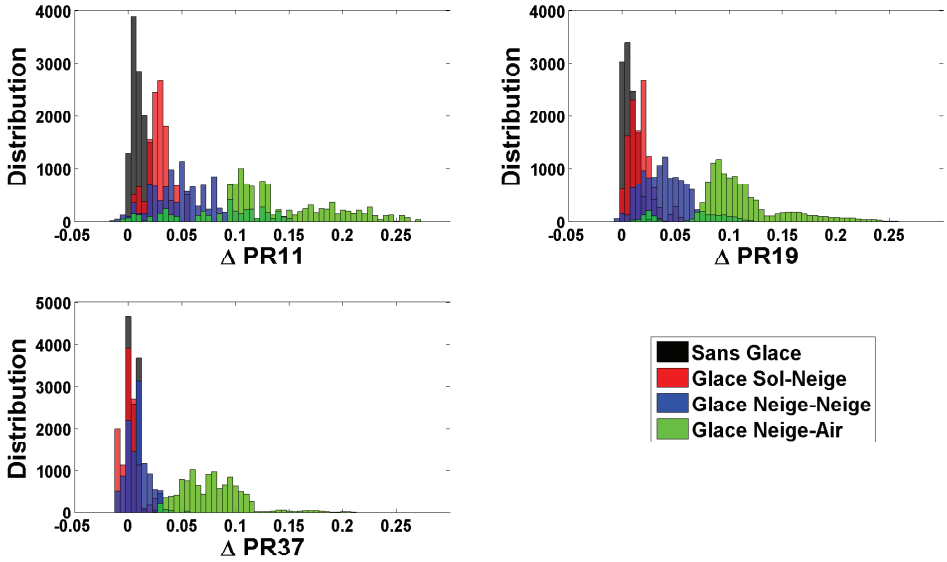


Figure 6.5 – Histogrammes de distribution des différences entre les PR simulés pour les sites Churchill sélectionnée (Tableau 6.2) et la moyenne des PR du scénario sans neige à 10.7 GHz (PR11), 19 GHz (PR19) et 37 GHz (PR37). Le code de couleur est identique à celui de la Figure 6.4. Afin de normaliser les distributions des quatres scénarios, la distribution du scénario sans glace a été dupliquée pour avoir le même nombre de points que les autres scénarios ayant 20 fois plus de points étant donné les simulations pour les différentes épaisseurs de glace. — Histogramme distribution of the difference between the simulated PR of the selected Churchill sites (Table 6.2) and the mean PR values of the ice free simulations at 10.7, (PR11), 19 (PR19) and 37 GHz (PR37). The color code is the same as Figure 6.4. To normalise the distributions of all four scenarios, the simulations for the ice free scenario were duplicated 20 times in order to have the same number of points as the other three scenarios.

Avec ces histogrammes, il est donc possible de déterminer des seuils où il est plus probable d'observer des couverts de neige sans glace ou avec glace aux différentes interfaces. Le Tableau 6.3 présente ces seuils. Ces derniers ont été déterminés à l'aide des simulations où les simulations indiquaient un plus grand nombre de résultats pour le scénario (sans glace, glace aux interfaces sol-neige, neige-neige et neige-air) que pour la somme des résultats des trois autres scénarios. Puisque les simulations du PR37 sans glace et celles avec une croute de glace à l'interface sol-neige sont indiscernables, aucun seuil pour détecter les croutes à l'interface sol-neige n'a été déterminé pour le PR37. Les Tableaux 6.4 à 6.6 présentent les matrices de confusion si les seuils du Tableau 6.3 sont appliqués aux simulations de la Figure 6.4.

Tableau 6.3 – Seuils de détection de croutes de glace des PR à 10.7 (PR11), 19 (PR19) et 37 GHz (PR37) pour les simulations de la Figure 6.4.

| | Seuils | | |
|---|---|---|---|
| Scénarios | PR11 | PR19 | PR37 |
| Glace sol-neige | 0.020 | 0.050 | 0.100 |
| Glace neige-neige | 0.015 | 0.030 | 0.070 |
| Glace neige-air | — | 0.015 | 0.035 |

Tableau 6.4 – Matrice de confusion des seuils du PR11. — Confusion matrix for the PR11 thresholds.

| | | Scénarios de référence | | | | | |
|---|---|---|---|---|---|---|---|
| | | Sans Glace | Glace sol-neige | Glace neige-neige | Glace neige-air | Total | Omission (%) |
| Scénarios Produits (seuils) | Sans Glace | 10500 | 1000 | 0 | 0 | 11500 | 8.7 |
| | Glace sol-neige | 1880 | 9120 | 500 | 0 | 11500 | 20.7 |
| | Glace neige-neige | 1241 | 3627 | 5077 | 1555 | 11500 | 55.9 |
| | Glace neige-air | 475 | 675 | 1394 | 8956 | 11500 | 22.12 |
| | Total | 14096 | 14422 | 6971 | 10511 | 46000 | |
| | Commission (%) | 25.5 | 36.8 | 27.2 | 14.8 | | $\kappa = 0.482$ |

Tableau 6.5 – Matrice de confusion des seuils du PR19. — Confusion matrix for the PR19 thresholds.

| | | Scénarios de référence | | | | | |
|---|---|---|---|---|---|---|---|
| | | Sans Glace | Glace sol-neige | Glace neige-neige | Glace neige-air | Total | Omission (%) |
| Scénarios Produits (seuils) | Sans Glace | 10480 | 760 | 260 | 0 | 11500 | 8.9 |
| | Glace sol-neige | 5360 | 4980 | 1160 | 0 | 11500 | 56.7 |
| | Glace neige-neige | 1358 | 2518 | 6506 | 1118 | 11500 | 43.4 |
| | Glace neige-air | 49 | 428 | 216 | 10807 | 11500 | 6.0 |
| | Total | 17247 | 8686 | 8142 | 11925 | 46000 | |
| | Commission (%) | 39.2 | 42.7 | 20.1 | 9.4 | | $\kappa = 0.462$ |

On remarque que le seuil ayant le meilleur indice $\kappa$ de Cohen est le PR11. Ceci peut être expliqué par le fait que le signal à 10.7 GHz a une plus grande profondeur de pénétration et peut donc mieux discerner les changements de stratigraphie au fondu du couvert nival. On remarque que les trois PR présentent de faibles pourcentages d'omission ($< 10$ %). Toutefois, les erreurs de commission sont plus élevées, surtout pour le PR37 (66.2 %). Ceci indique donc qu'il est possible que des couverts

Tableau 6.6 – Matrice de confusion des seuils du PR37. — Confusion matrix for the PR37 thresholds

| | | Scénarios de référence | | | | | |
|---|---|---|---|---|---|---|---|
| | | Sans Glace | Glace sol-neige | Glace neige-neige | Glace neige-air | Total | Omission (%) |
| Scénarios produits (Seuils) | Sans Glace | 11000 | 0 | 500 | 0 | 11500 | 4.4 |
| | Glace sol-neige | 11000 | 0 | 500 | 0 | 11500 | 100.0 |
| | Glace neige-neige | 8684 | 0 | 2684 | 132 | 11500 | 76.7 |
| | Glace neige-air | 0 | 0 | 392 | 11108 | 11500 | 3.4 |
| | Total | 30684 | 0 | 4076 | 11240 | 46000 | |
| | Commission (%) | 66.2 | — | 44.0 | 1.7 | | $\kappa = 0.289$ |

de neige sans glace présentent des propriétés affectant les PR de façon similaire à des couverts de neige ayant des croutes de glace. Ces erreurs plus grandes proviennent surtout des scénarios où les croutes de glace se retrouvent aux interfaces sol-neige et neige-neige. En effet, ceci est de plus confirmé par les grandes erreurs ($> 20$ %) de commission/omission des simulations où il y avait des croutes de glace aux interfaces sol-neige et neige-neige en plus du fait que le PR37 ne peut détecter les croutes de glace lorsqu'elles sont situées à l'interface sol-neige. Ceci peut être expliqué par le fait que les contrastes diélectriques entre les interfaces sol-glace et glace-neige ne sont pas aussi prononcés et différents des contrastes diélectriques des interfaces sol-neige et neige-neige. Mis à part l'erreur d'omission du PR11, les erreurs d'omission/commission pour les simulations des couverts de neige avec une croute à l'interface neige-air sont faibles ($< 15$ %). La plus grande erreur d'omission du PR11 pour ce scénario peut être expliqué par le fait que le signal MOP à 10.7 GHz a une plus grande profondeur de pénétration et il est moins affecté par les changements de propriétés de surface que les signaux à 19 et 37 GHz. Les très faibles erreurs d'omission/commission (3.4 % et 1.7 % respectivement) du PR37 pour les simulations avec une croute à l'interface neige-air confirme son grand potentiel à discriminer les croutes de surfaces. Une approche utilisant les trois PR, semble efficace pour détecter la présence de glace sans spécifier son emplacement dans le couvert nival.

## 6.5 Validation de l'indice de détection des croutes de glace sur des données MOP satellitaires

Afin de valider l'indice de détection des croutes de glace, des mesures MOP satellitaires (section 2.2) du NSIDC ont été utilisées. Ces données ont été ré-échantillonnées sur le EASE-Grid du NSIDC, ce qui permet de comparer le même pixel sur les données SMMR, SSM/I et AMSR-E de 1978 à 2011. Afin de bien valider les seuils de la section précédente sur les PR satellitaires, des corrections atmosphériques ont dues être apportées à l'aide des mesures de ré-analyse atmosphériques NARR (section 2.3). Ainsi, les $T_{Bsat}$ satellitaires à la fréquence $f$ et polarisation $p$ ont été corrigées à l'aide de l'équation suivante :

$$T_B(f,p) = \frac{T_{Bsat}(f,p) - T_{B\uparrow}(f,p)}{\tau_{atm}(f,p)} \tag{6.5.1}$$

où $T_B(f,p)$ est la $T_B$ équivalente qui serait mesurée à la surface de la Terre, $T_{B\uparrow}(f,p)$ est la $T_B$ atmosphérique ascendente ($\approx T_{B\downarrow}$) et $\tau_{atm}(f,p)$ est la transmissivité atmosphérique calculée à l'aide des régressions linéaires de Roy (2014). La Figure 6.6 présente la série temporelle des PR11, PR19 et PR37 satellitaires pour les deux pixels choisis (section 2.2). De plus, les moyennes hivernales (les mois de décembre, janvier et février) pour chaque capteur (SMMR, SSM/I et AMSR-E) sont indiquée par des traits pointillés horizontaux. Afin d'éliminer les événements de croutes de glace dans le calcul de la moyenne, une méthode itérative a été utilisée où, pour chaque itération, les PR ayant une valeur supérieure à la moyenne ($\bar{PR}_i$) plus un écart-type ($\sigma_{PR_i}$) de l'itération précédente ($PR_i > \bar{PR}_{i-1} + \sigma_{PR_{i-1}}$) sont retirés du calcul. Ainsi, après trois itérations, les valeurs extrêmes des PR ont pu être retirées du calcul de la moyenne hivernale finale. Le premier pixel situé au Nunavik (Québec, Canada) a été choisi puisqu'il démontrait des caractéristiques d'occupation du sol similaires à celles observées à Churchill (Manitoba, Canada) qui est le site d'étude de la section précédente. Le deuxième pixel, situé sur l'île Banks (Territoires du Nord-Ouest, Canada) a été choisi parce qu'un événement de pluie hivernale suivi de la formation d'une croute de glace en octobre 2003 a été répertorié par Grenfell et Putkonen (2008). Ainsi, l'indice de détection de croutes de glace pourra être validé sur un site arctique.

Les deux séries temporelles $T_B$ de la Figure 6.6 montrent les mesures des orbites ascendants et descendants des capteurs. Ainsi, des épisodes de regel nocturne au printemps pourraient être détectés. Comme ces pixels couvrent une superficie de 25 km x 25 km, un seul seuil glace/non glace a été

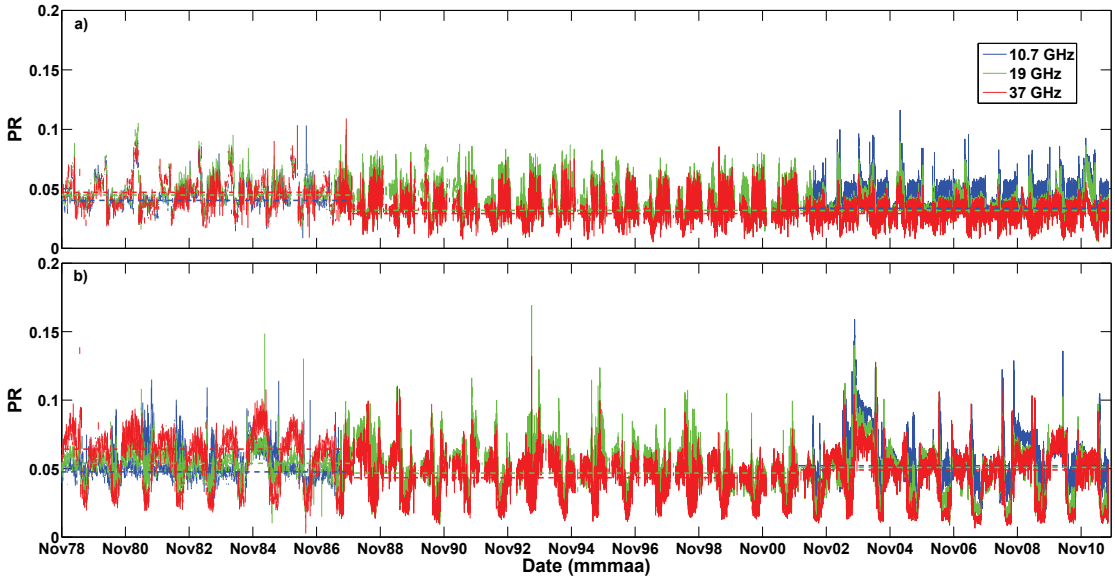


Figure 6.6 – Séries temporelles des PR satellitaires à 10.7 (bleu), 19 (vert) et 37 GHz (rouge) pour les sites du Nunavik, Québec, Canada (a) et l'île Banks, Territoires-du-Nord-Ouest, Canada (b). Les mesures des années 1978 à 1987 ont été acquises du capteur SMMR, de 1987 à 2001 du capteur SSM/I et de 2001 à 2011 du capteur AMSR-E. — Satellite PR timeseries at 10.7 (blue), 19 (green) and 37 GHz (red) for the Nunavik, Quebec, Canada site (a) and for the Banks island, North-West-Territories, Canada (b). The data for the years 1978-1987 were acquired by the SMMR sensor, the years 19987-2001 by the SSM/I sensor and the years 2001-2011 by the AMSR-E sensor.

utilisé comme il serait plus complexe de déterminer l'emplacement d'une croute de glace dans le couvert nival sur une si grande superficie. Ces seuils ont été déterminés à l'aide des simulations de la Figure 6.4 et sont présentés dans le Tableau 6.7.

Tableau 6.7 – Seuils de détection de croutes de glace des PR à 10.7 (PR11), 19 (PR19) et 37 GHz (PR37) pour les simulations de la Figure 6.4 pour la détection de présence de croute de glace. — Ice lens detection thresholds for the PR11, PR19 and PR37 of Figure 6.4.

| | Seuils | | |
|---|---|---|---|
| Scénarios | $\Delta$ PR11 | $\Delta$ PR19 | $\Delta$ PR37 |
| Sans Glace | $<$0.020 | $<$0.010 | $<$0.015 |
| Avec Glace | $>$0.020 | $>$0.010 | $>$0.015 |

Ces seuils indiquent que le nombre de simulations sans glace est inférieur à la somme des nombres de simulations des 3 autres scénarios. La figure 6.7 présente les données de la figure 6.6 pour la

période de 2002 à 2005. Sur la figure 6.7, les moyennes hivernales (traits pointillés) ainsi que les seuils de l'indice de détection de glace (traits pleins) sont illustrés. Les ellipses noires présentent des périodes où aucune croute n'a été détectée et les ellipses rouges montrent les périodes où il y a eu détection de croutes de glace. La Figure 6.8 montre les événements détectés par le PR37 (magenta), PR19 (cyan), PR11 (rouge), les 3 PR (vert) et les PR pour 3 jours consécutifs (bleu) pour le pixel Nunavik (a) et le pixel Banks (b). Les événements affichés sont ceux entre les mois de novembre et mars. Les événements de croutes de glace détectés par Roy (2014) sur le pixel du Nunavik dans le cadre de ses travaux de thèse (Figure 7.6, Roy (2014)) sont confirmés par la Figure 6.8, où les seuils indiquent la présence de croutes de glace pour les hivers 2002-2003, 2003-2004, 2004-2005, 2006-2007, 2009-2010 et 2010-2011.

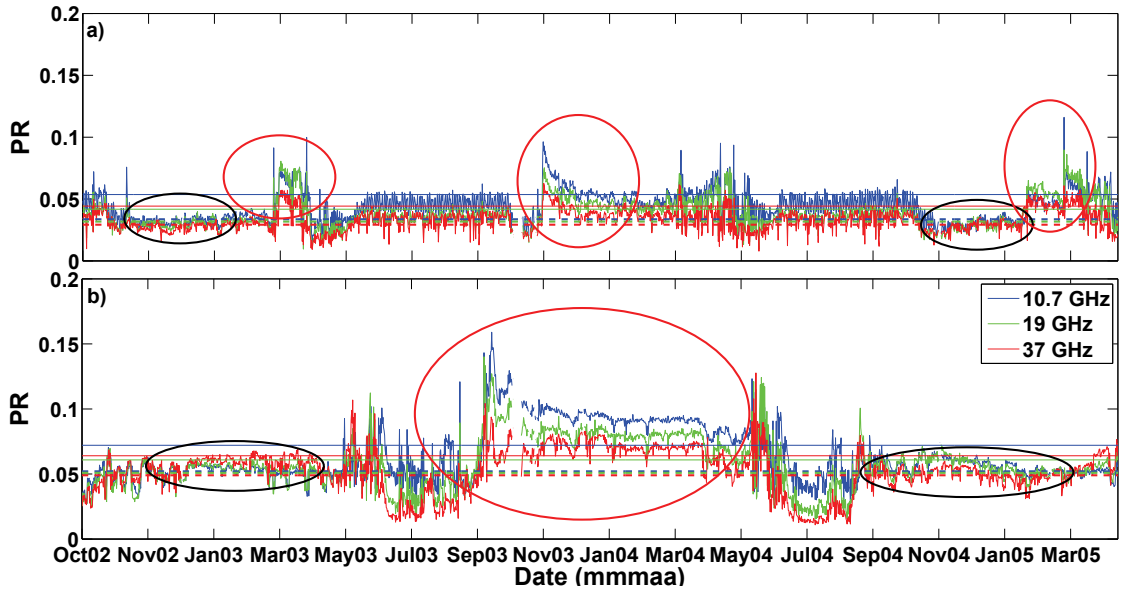


Figure 6.7 – Séries temporelles des PR satellitaires AMSR-E à 10.7 (bleu), 19 (vert) et 37 GHz (rouge) pour les sites du Nunavik, Québec, Canada (a) et l'île Banks, Territoires-du-Nord-Ouest, Canada (b) pour la période de 2002 à 2005. Les traits pointillés horizontaux montrent la moyenne hivernale (décembre, janvier, février) des PR et les traits pleins horizontaux présentent les seuils à franchir. Les ellipses noires présentent les périodes où il n'y a pas présence de glace et les ellipses rouges présentent les périodes où des croutes de glace sont détectées. — Satellite AMSR-E PR timeseries at 10.7 (blue), 19 (green) and 37 GHz (red) for the Nunavik, Quebec, Canada site (a) and for the Banks island, North-West-Territories, Canada (b) for the 2002-2005 years. The horizontal dotted lines are the winter (december, january, march) PR means and the full lines show the thresholds of the ice index. The black ellipses show periods where no ice is detected and the red ellipses show periods where ice is detected.

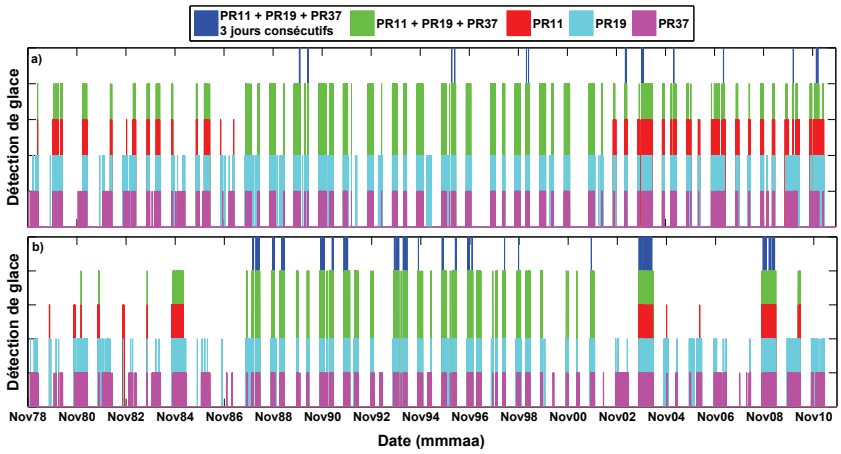


Figure 6.8 – Détection de la présence de croute de glace par les seuils des PR du Tableau 6.7 pour (a) le pixel du Nunavik et (b) le pixel de l'île Banks. — Ice lens detection with the thresholds of Table 6.7 for (a) the Nunavik pixel and (b) the Banks pixel.

Les travaux de Roy (2014) étaient de simuler les $T_B$ AMSR-E à l'aide du schéma de surface du modèle climatique *Canadian LAnd Surface Scheme* (CLASS) comme intrants au modèle de TR MOP DMRT-ML. Il a démontré que le seul moyen de retrouver les $T_B$ pour ce pixel pour ces années était de simuler une croute de glace dans le couvert nival. Ainsi, les observations de Roy (2014) sont confirmées par l'indice de détection des croutes de glace développé dans cette thèse où on retrouve de la glace dans le couvert nival pour au moins 3 jours consécutif sur les trois PR.

Comme des événements détectés durant les années 1990 n'ont pas de PR11, il est difficile de conclure que ce sont bien des détections de croutes de glace puisqu'il y a plusieurs événements qui font grimper les PR19 et PR37 au-delà de leur seuil et où le PR11 demeure en deçà de son seuil. Des données de validation terrain seraient nécessaires et comme aucune station météorologique ne se trouve à proximité du pixel, il est difficile de conclure que ces événements sont bien causés par la présence de croutes de glace dans le couvert nival.

La Figure 6.8b montre bien que l'événement répertorié par Grenfell et Putkonen (2008) sur l'île Banks est détecté par les seuils du Tableau 6.7. De plus, on remarque que des événements sont survenus durant l'hiver 2008-2009. En regardant la Figure 6.6, on remarque que pour cette année, les PR AMSR-E se comportent comme pour l'année 2003 où les PR sont nettement supérieurs à la moyenne hivernale. Comme pour le pixel du Nunavik, il est difficile de conclure sur la présence de croutes de glace pour les années 1990 puisqu'il n'y a pas de PR11. Toutefois, les PR19 et PR37

semblent franchir les seuils pour plusieurs jours consécutifs. Ceci pourrait être dû à la présence de croutes de neige formée par le vent. La Figure 6.9 présente la sensibilité des PR11, PR19 et PR37 à la densité d'une couche de neige. On remarque que pour des couches de neige très denses ($>$ 350 kg m$^{-3}$), les PR ont des valeurs similaires aux valeurs d'un couvert de neige ayant une croute de glace.

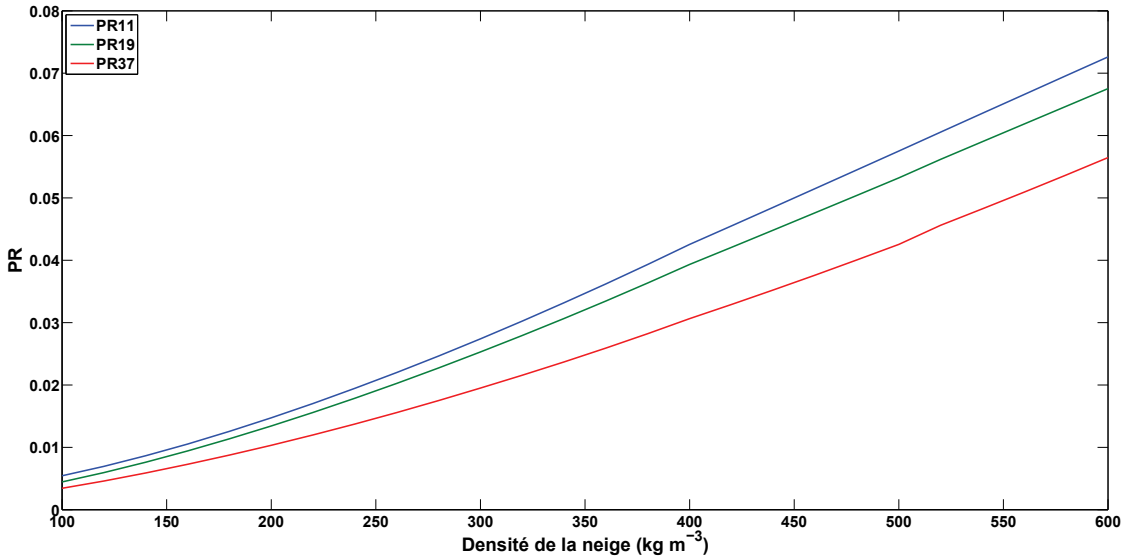


Figure 6.9 – Sensibilité des PR11 (bleu), PR19 (vert) et PR37 (rouge) à la densité d'un couvert de neige de 50 cm, $T_{neige} = 250$ K et $p_c = 0.15$ mm — Sensitivity of the PR11 (blue), PR19 (green) and PR37 (red) to snow density for a snowpack of 50 cm, $T_{snow} = 250$ K and $p_c = 0.15$ mm

Aussi, on remarque que pour les années où il n'y a pas de croutes de glace, les valeurs des trois PR sont très similaires tandis que lorsqu'il y a détection de croutes de glace, il y a un écart prononcé entre les trois PR. Pour certains hivers des années 1990, il ne semble pas y avoir d'écarts significatifs entre les PR19 et PR37. Il se pourrait donc que la détection des croutes de glace par seulement deux PR soit de faux positifs et ne soit pas aussi précis qu'avec trois PR. Pour les années 1980, on remarque que les trois PR détectent des croutes mais ces détections ne semblent pas se produire pour trois journées consécutives. En regardant de plus près, il est possible de voir des fluctuations journalières où les PR franchissent les seuils et retombent sous la valeur des seuils. Ceci peut être expliqué par le fait que l'angle d'incidence du capteur SMMR est plus faible et plus éloigné de l'angle de Brewster et ainsi est plus sensible aux différentes fluctuations journalières du PR causées par une moins grande différence entre les $T_B$ en V-Pol et H-Pol. La Figure 6.10 montre la série temporelle des PR de la Figure 6.4 pour l'île Banks ainsi que les températures minimales

et maximales mesurées à la station d'Environnement Canada de Sachs Harbour (Territoires du Nord-Ouest, Canada).

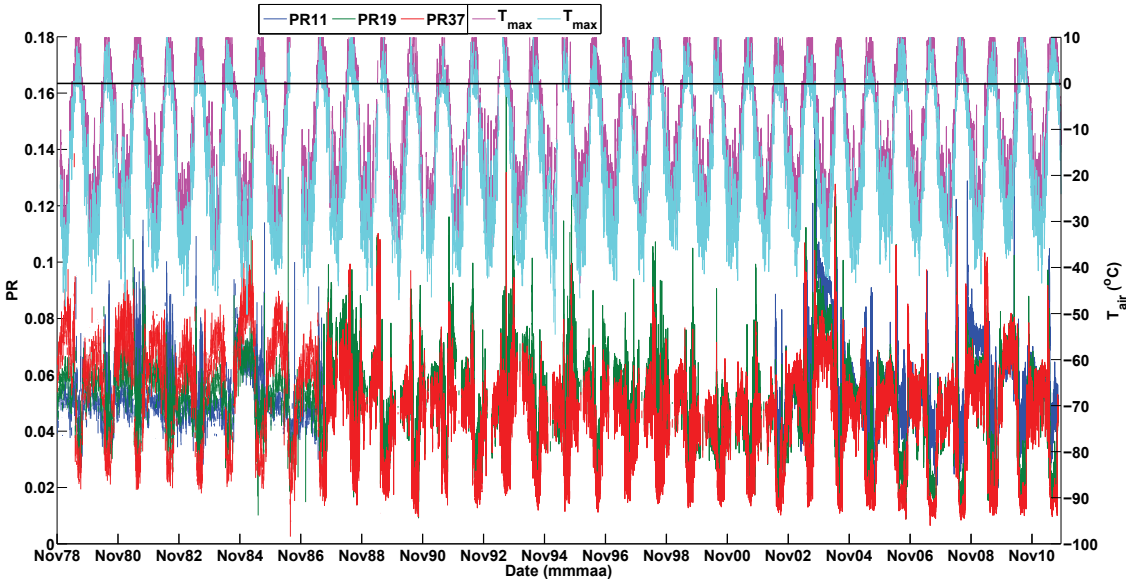


Figure 6.10 – Série temporelle des PR11 (bleu), PR19 (vert) et PR37 (rouge) du pixel de l'île Banks ainsi que les températures de l'air minimales (cyan) et maximales (magenta) prises à la station de Sachs Harbour d'Environnement Canada (Territoires-du-Nord-Ouest, Canada) (http ://climat.meteo.gc.ca/). — Timeseries of the PR11 (blue), PR19 (green) and PR37 (red) of the Banks island pixel with the minimum (cyan) and maximum (magenta) air temperatures measured at the Environment Canada weather station in Sachs Harbour (North-West-Territories, Canada)(http ://climat.meteo.gc.ca/).

En regardant les températures mesurées à Sachs Harbour, on remarque que les événements détectés par les PR de la Figure 6.8 correspondent à des températures mesurées légèrement au-dessus du point de congélation qui chutent rapidement sous le point de congélation par la suite. Ces phénomènes se produisent surtout durant les premiers mois de la saison soit octobre et novembre. Comme les données de précipitations n'ont pas été acquises à cette station, il est impossible de le confirmer avec les données actuelles mais il est plausible qu'il y ait eu des précipitations sous forme liquide et que suite à la chute rapide des températures, cette eau ait formé une croute de glace comme il a été observé par Grenfell et Putkonen (2008).

La figure 6.11 présente le nombre d'événements détectés par année pour chaque pixel de 1979 à 2011 (33 hivers). Le nombre d'événements total (en vert) inclus les événements détectés par la passe ascendante et descendante du capteur. Le tableau 6.8 résume les statistiques de la figure 6.11.

Les événements diurnes correspondent aux événements qui ont été détectés par seulement l'une des deux passes (ascendante ou descendante) du capteur au cours d'une même journée. Afin de discriminer les événements importants, la courbe bleue montre les événements qui ont perduré 3 jours consécutifs ou plus.

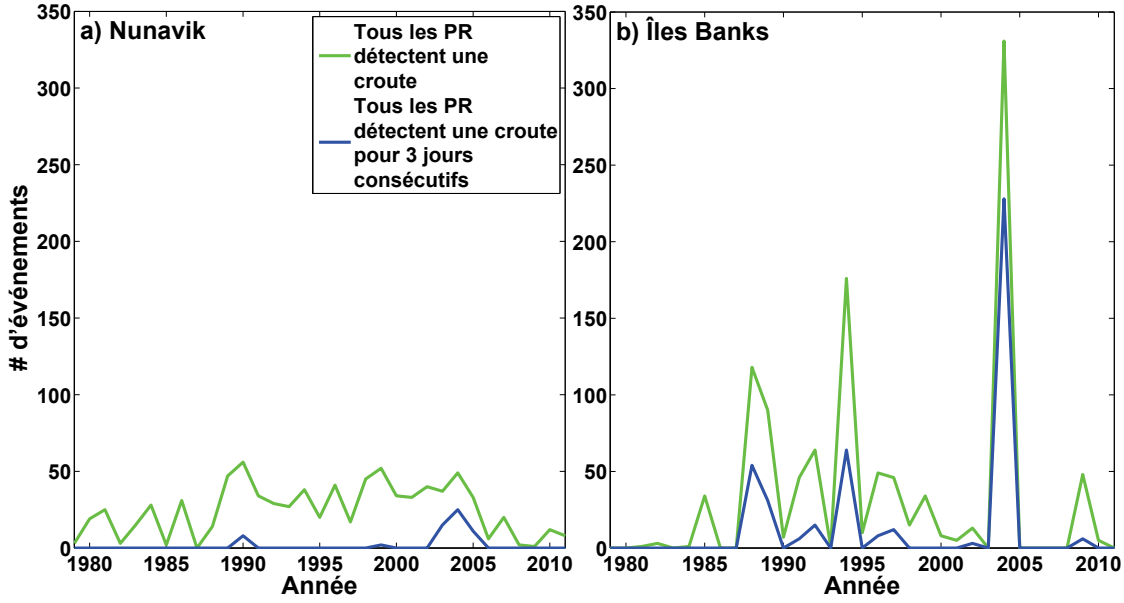


Figure 6.11 – Nombres d'événements détectés par les seuils du tableau 6.7 par année. — Number of events detected by the thresholds of table 6.7 each year.

La figure 6.11a montre qu'il y a beaucoup d'événements sur le pixel du Nunavik mais ceux-ci ne semblent pas perdurer plus de 3 jours. Ceci peut-être dû au couvert de neige plus épais dans cette région (Roy, 2014) qui diminue la sensibilité du PR37 à la croute de glace lorsque cette dernière est couverte par un couvert de neige suffisamment épais. Toutefois, on peut noter un plus grand nombre d'événements pour les années 1990 ainsi que le début des années 2000. La figure 6.11b montre qu'il y a des années extrêmes pour chacune des décennies (1988, 1994 et 2004) avec l'année 2003-2004 étant l'année ayant le plus d'événements détectés (Grenfell et Putkonen, 2008). Aucune tendance n'a pu être observée à l'échelle de ces deux pixels. Une étude à plus grande échelle spatiale permettrait peut-être de découvrir des tendances.

Tableau 6.8 – Nombres d'événements détectés par les seuils du tableau 6.7 ainsi que le nombre d'hivers où aucune croute n'a été détectée. — Number of events detected by the thresholds of table 6.7 and the number of winters without ice lenses detected.

| | Nunavik | Île Banks |
|---|---|---|
| Événements totaux | 844 | 1105 |
| Événements diurnes | 260 | 141 |
| Hivers sans croutes | 28 | 23 |

# 7 Conclusions et travaux futurs

L'étude des changements climatiques est très important au niveau social, économique et environnemental. La neige est un excellent indicateur des changements climatiques et la télédétection est un excellent outil d'étude de l'évolution du couvert nival. Cette thèse a donc pour but d'analyser le transfert radiatif MOP du sol, de la neige et de la glace afin de développer un indice de détection des croutes de glace dans le couvert nival par télédétection micro-ondes passives satellitaires. Pour ce faire, la modélisation du TR MOP du couvert nival a dû être améliorée afin de minimiser les erreurs de modélisation et ainsi modéliser et comprendre les effets des croutes de glace sur la $T_B$ émise par le couvert nival. Pour ce faire, la modélisation de la contribution du sol sous le couvert nival a été améliorée. Aussi, la mesure du paramètre géophysique de la neige le plus sensible dans la modélisation du TR MOP, i.e. la taille des grains de neige, a été améliorée et sa paramétrisation dans le modèle MEMLS a aussi été optimisée. La caractérisation des croutes de glace dans la modélisation du TR MOP a aussi été améliorée et validée à l'aide de mesures radiométriques et géophysiques in-situ de la neige et de la glace.

Deux nouveaux instruments ont été développés au CARTEL pour la mesure de la surface spécifique de la neige (SSA) pour paramétriser la taille des grains de neige. Le premier, IRIS, a été développé d'après le concept de l'instrument *DUal Frequencies Integrating Sphere for Snow Specific Surface area* (Gallet *et al.*, 2009). Le deuxième, la SWIRcam, est un nouvel appareil qui capte des photographies infrarouges à 1.3 $\pm 0.1 \mu$m et permet de caractériser la SSA des profils de neige en deux dimensions. Les deux instruments démontrent une grande reproductibilité et une précision de 10% sur la mesure de la SSA. Par la suite, ce paramètre à été validé pour la modélisation du TR MOP du couvert nival dans le modèle MEMLS. Il a été démontré que la SSA traduite en longueur de corrélation, paramètre de taille de grains de neige de MEMLS, nécessitait une correction afin de minimiser l'erreur sur la modélisation de la $T_B$ du couvert nival par rapport aux mesures de $T_B$ in-situ. Cette correction est un facteur multiplicatif de la longueur de corrélation de $\phi$=1.3 et

permet de minimiser l'erreur quadratique moyenne (RMSE) entre les mesures et les simulations du couvert nival à 11.6 K.

Par la suite, il a été démontré qu'il est possible, avec des mesures de températures ainsi que des mesures radiométriques du sol gelé, d'optimiser le modèle de réflectivité du sol de Wegmüller et Mätzler (1999) pour retrouver des paramètres effectifs de constantes diélectriques et de rugosité de surface du sol. Des constantes diélectriques effectives de 3.20, 3.45 et 4.53 pour des fréquences de 10.7, 19 et 37 GHz ont été trouvées. De plus, une rugosité de surface effective de 0.19 cm a été obtenue suite à l'optimisation des paramètres de sol. Ces paramètres effectifs permettent de réduire la RMSE entre les mesures et simulations des $T_B$ du sol à 4.65 K. De plus, avec la base de données PORTOS-93, il a été possible d'évaluer deux modèles de réflectivité du sol. Le premier est celui de Wegmüller et Mätzler (1999) et le second est celui de Wang et Choudhury (1981). Cette base de données est unique puisqu'elle regroupe des données multi-angles et multi-fréquences (1.41 à 90 GHz) pour une grande gamme de conditions de sols nus. Il a été démontré que les deux modèles évalués, avec les bons scénarios d'optimisations, étaient équivalents et qu'il était possible de réduire les biais entre les $T_B$ mesurées et simulées autour de 10.0 K.

Avec les différentes contributions du TR MOP du couvert de neige optimisées, il a été possible d'implémenter un module de TR MOP de la glace dans le modèle MEMLS et de valider ce dernier avec des mesures radiométriques et géophysiques de couverts nivaux ayant des croutes de glace à l'intérieur. Il a été démontré que dans la limite où la densité de la couche simulée est celle de la glace pure (917 kg $m^{-3}$) et que la longueur de corrélation est nulle, l'approximation de Borne (Mätzler, 1998) implémentée dans MEMLS est équivalente à simuler une croute de glace pure avec les équations du TR MOP de la glace pure. En effet, une différence de 0.3 K entre les RMSE simulées avec l'approximation de Borne et les équations du TR de la glace pure a été observée. Dans ce même travail, il a été démontré qu'en simulant une croute de glace pure, avec les propriétés géophysiques mesurées in-situ dans le couvert nival, à l'aide de MEMLS, il est possible de minimiser l'erreur des simulations des couverts nivaux avec des croutes de glace à une erreur comparable aux simulations des couverts nivaux n'ayant pas de croute de glace (RMSE= 11.3 K).

Avec le modèle MEMLS validé pour la modélisation de couverts de neiges ayant des croutes de glace, il a été possible de modéliser les effets des croutes de glace sur le signal MOP émis par le couvert nival. Il a été démontré que le ratio de polarisation est fortement affecté par la présence de croutes de glace. Il a été possible de démontrer que le PR à 37 GHz (PR37) était très sensible à la présence de croutes de glace à la surface du couvert nival. De plus, le PR à 10.7 GHz (PR11) semble

être le meilleur indice pour déterminer s'il y a des croutes de glace en profondeur du couvert de neige. Ces effets des croutes de glace étaient déjà connus mais les travaux de cette thèse ont permis de les démontrer et les expliquer par des simulations, ce qui n'avait jamais été fait auparavant. Avec des simulations des PR sur les sites Churchill, il a été possible de déterminer trois seuils où les PR indiquaient la présence de croutes de glace. Ces seuils ont été appliqués à une série temporelle de près de 34 ans sur un pixel démontrant une occupation du sol similaire aux sites de mesures à Churchill. Plusieurs croutes de glace ont été découvertes depuis les années 1990 sur ce pixel où les indices franchissaient les seuils pour trois jours consécutifs. Les mêmes événements détectés par Roy (2014) ont été détectés sur ce pixel. À l'aide de données de validation in-situ, il serait possible d'affirmer l'efficacité des indices PR. Cependant, selon Roy (2014), les événements détectés par AMSR-E ne pourraient être expliqué que par la présence d'une croute de glace.

Finalement, ces indices PR ont été testés sur un pixel satellitaire de l'île Banks en Territoires-du-Nord-Ouest, Canada. Il a été démontré que l'événement répertorié par Grenfell et Putkonen (2008) en 2003 a été détecté par les seuils des PR. De plus, des comportements des PR observés ont fourni des indices quant au développement d'un indice de détection de croutes de glace pour ces régions. En effet, en moyenne, durant l'hiver où il n'y a pas de croute de glace, l'écart entre les PR11, PR19 et PR37 n'est pas très prononcé. Toutefois, pour l'hiver 2002-2003, où un événement de croute de glace a été répertorié par Grenfell et Putkonen (2008), un très grand écart entre les différents PR a été observé. Cet écart a aussi été observé à plusieurs reprise durant les années 1980 et la fin des années 2000. Ces événements détectés ont suivi une période de refroidissement rapide. Il est donc possible qu'il y ait eu formation de glace dans le couvert nival. Toutefois, sans l'aide de données de validation terrain, il est impossible de valider parfaitement ces observations.

Dans le contexte de changements climatiques que l'on connaît, il est important de bien comprendre les environnements arctiques. Dans le futur, il serait très intéressant d'acquérir des données radiométriques et géophysiques du sol, de la neige et de la glace dans les régions arctiques afin de pouvoir bien simuler les différentes conditions de neige. Ainsi, il serait possible de simuler et de comprendre le signal MOP satellitaire mesuré dans ces régions. Le modèle MEMLS comme d'autres modèles de TR MOP, ont démontré qu'il est possible de modéliser la $T_B$ du couvert de neige à de multiples fréquences et pour de multiples conditions de neige. De plus, l'utilisation de signaux MOP à des fréquences plus faibles pourrait apporter beaucoup d'information à la détection des croutes de glace dans le couvert nival. Par exemple, la bande L ($\approx$1.41GHz), avec sa grande profondeur de pénétration, permet de détecter les propriétés du sol sous le couvert de neige (Brown *et al.*, 2013). Il serait intéressant de simuler les effets d'une croute de glace sur le signal en bande L autant sur les MOP que sur le signal actif RADAR afin de déterminer si le capteur de

la mission *Soil Moisture Active and Passive* (SMAP) pourrait être utilisé pour apporter davantage d'information. De plus, il serait possible de faire de l'assimilation de données multi-sources afin de simuler le signal MOP et tenter de confirmer la présence de croutes de glace. Ainsi, les travaux de cette thèse ont permis de déterminer que le modèle MEMLS est capable de simuler la $T_B$ du couvert de neige à de multiples fréquences. De plus, il a été démontré qu'avec des données in-situ de qualité, il est possible de calibrer des modèles afin de minimiser les erreurs de simulation. Ainsi, il a été démontré que la modélisation du TR du couvert nival est un outil puissant pour comprendre les comportements des signaux satellitaires aux différentes propriétés géophysiques du couvert nival.

# 8 Références de la thèse (hors article publiés en tant qu'auteur)


T. AOKI, T. AOKI, M. FUKABORI, A. HACHIKUBO, Y. TACHIBANA et F. NISHIO : Effects of snow physical parameters on spectral albedo and bidirectional reflectance of snow surface. *Journal of Geophysical Research D : Atmospheres*, 105(D8):10219–10236, 2000. ISSN 01480227.

Richard L. ARMSTRONG et Eric BRUN : *Snow and Climate : Physical Processes, Surface Energy Exchange and Modeling*. Cambridge University Press, 2008.

L. ARNAUD, G. PICARD, N. CHAMPOLLION, F. DOMINE, J.-C. GALLET, E. LEFEBVRE, M. FILY et J. M. BARNOLA : Instruments and methodes : Measurement of vertical profiles of snow specific surface area with 1 cm resolution using infrared reflectance : instrument description and validation. *Journal of Glaciology*, 57(201):17–29, 2011.

M.E. BROWN, V. ESCOBAR, S. MORAN, D. ENTEKHABI, P.E. O'NEILL, E.G. NJOKU, B. DOORN et J.K. ENTIN : Nasa's soil moisture active passive (smap) mission and opportunities for applications users. *Bulletin of the American Meteorological Society*, 94(8):1125–1128, 2013. ISSN 00030007.

L. BRUCKER, G. PICARD, L. ARNAUD, J.-M. BARNOLA, M. SCHNEEBELI, H. BRUNJAIL, E. LEFEBVRE et M. FILY : Modeling time series of microwave brightness temperature at dome c, antarctica, using vertically resolved snow temperature and microstructure measurements. *Journal of Glaciology*, 57(201):171–182, 2011. ISSN 00221430.

J.C. CALVET, J.P. WIGNERON, A. CHANZY et D. HABOUDANE : Retrieval of surface parameters from microwave radiometry over open canopies at high frequencies. *Remote Sensing of Environment*, 53(1):46–60, 1995. ISSN 00344257.

D.J. CAVALIERI, P. GLOERSEN et W.J. CAMPBELL : Determination of sea ice parameters with the nimbus 7 smmr. *Journal of Geophysical Research*, 89(D4):5355–5369, 1984.

A.T.C. CHANG, J.L. FOSTER, D.K. HALL, A. RANGO et B.K. HARTLINE : Snow water equivalent estimation by microwave radiometry. *Cold Regions Science and Technology*, 5(3):259–267, 1982. ISSN 0165232X.

S. CHEN et I. BAKER : Evolution of individual snowflakes during metamorphism. *Journal of Geophysical Research D : Atmospheres*, 115(21):1–9, 2010. ISSN 01480227.

C. DERKSEN : The contribution of amsr-e 18.7 and 10.7 ghz measurements to improved boreal forest snow water equivalence retrievals. *Remote Sensing of Environment*, 112(5):2701–2710, 2008. ISSN 00344257.

C. DERKSEN, S.L. SMITH, M. SHARP, L. BROWN, S. HOWELL, L. COPLAND, D.R. MUELLER, Y. GAUTHIER, C.G. FLETCHER, A. TIVY, M. BERNIER, J. BOURGEOIS, R. BROWN, C.R. BURN, C. DUGUAY, P. KUSHNER, A. LANGLOIS, A.G. LEWKOWICZ, A. ROYER et A. WALKER : Variability and change in the canadian cryosphere. *Climatic Change*, 115(1):59–88, 2012. ISSN 01650009.

F. DOMINÉ, M. ALBERT, T. HUTHWELKER, H.-W. JACOBI, A. A. KOKHANOVSKY, M. LEHNING, G. PICARD et W. R. SIMPSON : Snow physics as relevant to snow photochemistry. *Atmospheric Chemistry and Physics*, 8:171–208, 2008.

F. DOMINÉ, A. CABANES, A.-S. TAILLANDIER et L. LEGAGNEUX : Specific surface area of snow samples determined by ch4 adsorption at 77 k and estimated by optical microscopy and scanning electron microscopy. *Environmental Science and Technology*, 35(4):771–780, 2001. ISSN 0013936X.

M. DURAND, E.J. KIM et S.A. MARGULIS : Quantifying uncertainty in modeling snow microwave radiance for a mountain snowpack at the point-scale, including stratigraphic effects. *IEEE Transactions on Geoscience and Remote Sensing*, 46(6):1753–1767, 2008. ISSN 01962892.

C. FIERZ, R.L. ARMSTRONG, Y. DURAND, P. ETCHEVERS, E. GREENE, D.M. MCCLUNG, K. NISHIMURA, P.K. SATYAWALI et S.A. SOKRATOV : *The International Classification for Seasonal Snow on the Ground*. IHP-VII Technical Documents in Hydrology N 83, 2009.

C.G. FLETCHER, P.J. KUSHNER, A. HALL et X. QU : Circulation responses to snow albedo feedback in climate change. *Geophysical Research Letters*, 36(9), 2009. ISSN 00948276.

J.-C. GALLET, F. DOMINE, C.S. ZENDER et G. PICARD : Rapid and accurate measurement of the specific surface area of snow using infrared reflectance at 1310 and 1550 nm. *Cryosphere Discussions*, 3(1):33–75, 2009. ISSN 19940432.

M.A. GOODBERLET et J.B. MEAD : Improved models of soil emission for use in remote sensing of soil moisture. *IEEE Transactions on Geoscience and Remote Sensing*, 50(10 PART2):3991–3999, 2012. ISSN 01962892.

T.C. GRENFELL et J. PUTKONEN : A method for the detection of the severe rain-on-snow event on banks island, october 2003, using passive microwave remote sensing. *Water Resources Research*, 44(3), 2008. ISSN 00431397.

Norman GRODY : Relationship between snow parameters and microwave satellite measurements : Theory compared with advanced microwave sounding unit observations from 23 to 150 ghz. *JOURNAL OF GEOPHYSICAL RESEARCH*, 113:D22108, 2008.

B.B. HANSEN, R. AANES, I. HERFINDAL, J. KOHLER, B.E. SAETHER et M.K. OLI : Climate, icing, and wild arctic reindeer : Past relationships and future prospects. *Ecology*, 92(10):1917–1923, 2011. ISSN 00129658.

J.A. JONES et R.M. PERKINS : Extreme flood sensitivity to snow and forest harvest, western cascades, oregon, united states. *Water Resources Research*, 46(12), 2010. ISSN 00431397.

R.E. KELLY, A.T. CHANG, L. TSANG et J.L. FOSTER : A prototype amsr-e global snow area and snow depth algorithm. *IEEE Transactions on Geoscience and Remote Sensing*, 41(2 PART 1):230–242, 2003. ISSN 01962892.

N.P. KLINGAMAN, B. HANSON et D.J. LEATHERS : A teleconnection between forced great plains snow cover and european winter climate. *Journal of Climate*, 21(11):2466–2483, 2008. ISSN 08948755.

A. LANGLOIS, A. ROYER, C. DERKSEN, B. MONTPETIT, F. DUPONT et K. GOÏTA : Coupling the snow thermodynamic model snowpack with the microwave emission model of layered snowpacks for subarctic and arctic snow water equivalent retrievals. *Water Resour. Res.*, 48(12), 2012. ISSN 0043-1397. URL `http://dx.doi.org/10.1029/2012WR012133`.

A. LANGLOIS, A. ROYER et K. GOÏTA : Analysis of simulated and spaceborne passive microwave brightness temperatures using in situ measurements of snow and vegetation properties. *Canadian Journal of Remote Sensing*, 36(SUPPL.):S135–S148, 2010a. ISSN 07038992.

A. LANGLOIS, A. ROYER, B. MONTPETIT, G. PICARD, L. BRUCKER, L. ARNAUD, P. HARVEY-COLLARD, M. FILY et K. GOÏTA : On the relationship between snow grain morphology and in-situ near infrared calibrated reflectance photographs. *Cold Regions Science and Technology*, 61:34–42, 2010b.

J. LEMMETYINEN, A. KONTU, A. REES, C. DERKSEN et J. PULLIAINEN : Comparison of multiple layer snow emission models. *In 11th Specialist Meeting onMicrowave Radiometry and Remote Sensing of the Environment, MicroRad 2010- Proceedings*, pages 99–103, 2010a.

Juha LEMMETYINEN, Jouni PULLIAINEN, Andrew REES, Anna KONTU, Yubao QIU et Chris DERKSEN : Multiple-layer adaptation of hut snow emission model : Comparison with experimental data. *IEEE TRANSACTIONS ON GEOSCIENCE AND REMOTE SENSING*, 48:2781–3055, 2010b.

G.E. LISTON et C.A. HIEMSTRA : The changing cryosphere : Pan-arctic snow trends (1979-2009). *Journal of Climate*, 24(21):5691–5712, 2011. ISSN 08948755.

M. MATZL et M. SCHNEEBELI : Measuring specific surface area of snow by near-infrared photography. *Journal of Glaciology*, 52(179):558–564, 2006. ISSN 00221430.

M. MATZL et M. SCHNEEBELI : Stereological measurement of the specific surface area of seasonal snow types : Comparison to other methods, and implications for mm-scale vertical profiling. *Cold Regions Science and Technology*, 64(1):1–8, 2010. ISSN 0165232X.

C. MÄTZLER : Improved born approximation for scattering of radiation in a granular medium. *Journal of Applied Physics*, 83(11):6111–6117, 1998. ISSN 00218979.

Christian MÄTZLER : Microwave permittivity of dry snow. *IEEE Transactions on Geoscience and Remote Sensing*, 34:573–581, 1996.

Christian MÄTZLER : Relation between grain-size and correlation length of snow. *Journal of Glaciology*, 48:461–466, 2002.

F. L. MILLER, R. H. RUSSELL et A. GUNN : The recent decline of peary caribou on western queen elizabeth islands of arctic canada. *Polarforschung*, 45:17–21, 1975.

B. MONTPETIT, A. ROYER, A. LANGLOIS, P. CLICHE, A. ROY, N. CHAMPOLLION, G. PICARD, F. DOMINE et R. OBBARD : New shortwave infrared albedo measurements for snow specific surface area retrieval. *Journal of Glaciology*, 58(211):941–952, 2012. ISSN 00221430.

B. MONTPETIT, A. ROYER, A. ROY et A. LANGLOIS : In-situ passive microwave parameterization of sub-arctic frozen organic soils. *Geoscience and Remote Sensing Letters*, xxx:xxx, En Revision.

B. MONTPETIT, A. ROYER, A. ROY, A. LANGLOIS et C. DERKSEN : Snow microwave emission modeling of ice lenses within a snowpack using the microwave emission model for layered snowpacks. *Geoscience and Remote Sensing, IEEE Transactions on*, 51(9):4705–4717, 2013. ISSN 0196-2892.

B. MONTPETIT, A. ROYER, J.-P. WIGNERON, A. CHANZY et A. MIALON : Evaluation of multi-frequencybare soil passive microwave reflectivity models. *Remote Sensing of Environment*, 162: 186–195, 2015.

H.S. NEGI et A. KOKHANOVSKY : Retrieval of snow albedo and grain size using reflectance measurements in himalayan basin. *Cryosphere*, 5(1):203–217, 2011. ISSN 19940416.

National Climatic Data Center NOAA : State of the climate : National snow & ice for annual 2013. `http://www.ncdc.noaa.gov/sotc/snow/2013/13`, December 2013. published online December 2013, retrieved on November 12, 2014.

OAR/ESRL PSD NOAA : North american regional reanalysis. http ://www.esrl.noaa.gov/psd, September 2014.

National Snow NSIDC et Ice Data CENTER : Ease-grid 2.0 brightness temperature data. nsidc.org, Septembre 2014.

T.H. PAINTER, N.P. MOLOTCH, M. CASSIDY, M. FLANNER et K. STEFFEN : Instruments and methods : Contact spectroscopy for determination of stratigraphy of snow optical grain size. *Journal of Glaciology*, 53(180):121–127, 2007. ISSN 00221430.

Ghislain PICARD, Ludovic BRUCKER, Alexandre ROY, Florent DUPONT, Michel FILY et Alain ROYER : Simulation of the microwave emission of multi-layered snowpacks using the dense media radiative transfer theory : the dmrt-ml model. *Geoscientific Model Development*, 6:1061–1078, 2013.

C. PRIGENT, J.-P. WIGNERON, W.B. ROSSOW et J.R. PARDO-CARRION : Frequency and angular variations of land surface microwave emissivities : Can we estimate ssm/t and amsu emissivities from ssm/i emissivities ? *IEEE Transactions on Geoscience and Remote Sensing*, 38(5 II):2373–2386, 2000. ISSN 01962892.

J. PULLIAINEN et M. HALLIKAINEN : Retrieval of regional snow water equivalent from space-borne passive microwave observations. *Remote Sensing of Environment*, 75(1):76–85, 2001. ISSN 00344257.

Jouni T. PULLIAINEN, Jochen GRANDELL et Martti T. HALLIKAINEN : Hut snow emission model and its applicability to snow water equivalent retrieval. *IEEE TRANSACTIONS ON GEOSCIENCE AND REMOTE SENSING*, 37:1378–1390, 1999.

J. PUTKONEN, H.P. JACOBSON et K. RENNERT : Brief communication "modeled rain on snow in clm3 warms soil under thick snow cover and cools it under thin". *Cryosphere Discussions*, 5 (5):2557–2570, 2011. ISSN 19940432.

J. PUTKONEN et G. ROE : Rain-on-snow events impact soil temperatures and affect ungulate survival. *Geophysical Research Letters*, 30(4):37–1, 2003. ISSN 00948276.

X. QU et A. HALL : What controls the strength of snow-albedo feedback ? *Journal of Climate*, 20 (15):3971–3981, 2007. ISSN 08948755. cited By (since 1996) 13.

Andrew REES, Juha LEMMETYINEN, Chris DERKSEN, Jouni PULLIAINEN et Micheal ENGLISH : Observed and modelled effects of ice lens formation on passive microwave brightness temperatures over snow covered tundra. *Remote Sensing of Environment*, 114:116–126, 2010.

K.J. RENNERT, G. ROE, J. PUTKONEN et C.M. BITZ : Soil thermal and ecological impacts of rain on snow events in the circumpolar arctic. *Journal of Climate*, 22(9):2302–2315, 2009. ISSN 08948755.

A. ROY, G. PICARD, A. ROYER, B. MONTPETIT, F. DUPONT, A. LANGLOIS, C. DERKSEN et N. CHAMPOLLION : Brightness temperature simulations of the canadian seasonal snowpack driven by measurements of the snow specific surface area. *Geoscience and Remote Sensing, IEEE Transactions on*, 51(9):4692–4704, 2013. ISSN 0196-2892.

Alexandre ROY : *Modélisation de l'émission micro-onde hivernale en forêt boréale á l'aide du couplage d'un modèle de transfert radiatif avec un schéma de modèle climatique (CLASS)*. Thèse de doctorat, Université de Sherbrooke, 2014.

M.C. SERREZE et R.G. BARRY : Processes and impacts of arctic amplification : A research synthesis. *Global and Planetary Change*, 77:85–96, 2011. ISSN 09218181.

A.-S. TAILLANDIER, F. DOMINE, W.R. SIMPSON, M. STURM et T.A. DOUGLAS : Rate of decrease of the specific surface area of dry snow : Isothermal and temperature gradient conditions. *Journal of Geophysical Research F : Earth Surface*, 112(3), 2007. ISSN 01480227.

A.B. TAIT : Estimation of snow water equivalent using passive microwave radiation data. *Remote Sensing of Environment*, 64(3):286–291, 1998. ISSN 00344257.

R. TURCOTTE, L.-G. FORTIN, V. FORTIN, J.-P. FORTIN et J.-P. VILLENEUVE : Operational analysis of the spatial distribution and the temporal evolution of the snowpack water equivalent in southern québec, canada. *Nordic Hydrology*, 38:211–234, 2007.

F. VACHON, K. GOÏTA, D. DE SÈVE et A. ROYER : Inversion of a snow emission model calibrated with in situ data for snow water equivalent monitoring. *IEEE Transactions on Geoscience and Remote Sensing*, 48(1):59–71, 2010. ISSN 01962892.

S. VAVRUS : The role of terrestrial snow cover in the climate system. *Climate Dynamics*, 29 (1):73–88, 2007. ISSN 09307575.

A.E. WALKER et B.E. GOODISON : Discrimination of a wet snow cover using passive microwave satellite data. *Annals of Glaciology*, 17:307–311, 1993. ISSN 02603055.

J. R. WANG et B. J. CHOUDHURY : Remote sensing of soil moisture content over bare field at 1.4 ghz frequency. *Journal of Geophysical Research*, 86(C6):5277–5282, 1981. ISSN 01480227.

U. WEGMÜLLER et C. MÄTZLER : Rough bare soil reflectivity model. *IEEE Transactions on Geoscience and Remote Sensing*, 37(3):1391–1395, 1999. ISSN 01962892.

Andreas WIESMANN et Christian MÄTZLER : Microwave emission model of layered snowpacks. *Remote Sensing of Environment*, 70:307–316, 1999.

J.-P. WIGNERON, A. CHANZY, Y.H. KERR, H. LAWRENCE, J. SHI, M.J. ESCORIHUELA, V. MIRONOV, A. MIALON, F. DEMONTOUX, P. DE ROSNAY et K. SALEH-CONTELL : Evaluating an improved parameterization of the soil emission in l-meb. *IEEE Transactions on Geoscience and Remote Sensing*, 49(4):1177–1189, 2011. ISSN 01962892.

J.-P. WIGNERON, L. LAGUERRE et Y.H. KERR : A simple parameterization of the l-band microwave emission from rough agricultural soils. *IEEE Transactions on Geoscience and Remote Sensing*, 39(8):1697–1707, 2001. ISSN 01962892.

# A Annexe : Modélisation de l'émissivité du sol non gelé humide

Dans certaines régions de la cryosphère, il n'est pas rare d'observer un sol non-gelé sous le couvert nival. Ceci rend le modèle de Montpetit *et al.* (En Revision) de la section précédente invalide. Plusieurs études ont été faites sur la modélisation de l'émissivité MOP du sol non gelé (Wigneron *et al.*, 2011; Goodberlet et Mead, 2012). Toutefois, ces études se concentrent principalement sur des mesures à basses fréquences (bande L). Pour l'étude du couvert neigeux, des fréquences allant jusqu'à 37 GHz sont souvent utilisées. L'amélioration de la modélisation de l'émissivité du sol humide à haute fréquence s'inscrit donc dans l'objectif général de cette thèse qui est d'améliorer la modélisation du TR MOP du couvert neigeux. Wegmüller et Mätzler (1999), Prigent *et al.* (2000) et Calvet *et al.* (1995) ont démontré qu'il est possible de modéliser l'émissivité MOP du sol à plus haute fréquence mais que les modèles nécessitent des modifications. Ce travail vise à analyser et comparer ces différents modèles, ce qui n'a jamais été fait. Les données utilisées pour cette partie du travail ont été acquises par l'Institut National de Recherche Agronomique (INRA) Avignon en France lors de la campagne PORTOS-93 en avril 1993. Ces données ont été pré-traitées et fournies par Jean-Pierre Wigneron de l'INRA. La base de données comprend les mesures géophysiques du sol tel que : la densité du sol (en g cm$^{-3}$), des paramètres de rugosité de surface comme l'écart-type de hauteur (en mm, référé par $\sigma_{sol}$ ou $\sigma$ dorénavant) et la longueur de corrélation (en mm), l'humidité du sol (en m$^3$ m$^{-3}$) et la température du sol (en K) à différentes profondeurs. De plus, des données radiométriques de $T_B$ à 1.41, 10.65, 23.8, 36.5 et 90 GHz ont été acquises simultanément aux mesures géophysiques. Ces mesures ont été effectuées sur 7 sites ayant des caractéristiques distinctes. Ces mesures et ces sites sont décrits en détails dans Wigneron *et al.* (2011) et Wigneron *et al.* (2001) et se retrouvent également dans l'article Montpetit *et al.* (2015) présenté à la section A. Le travail d'analyse et d'optimisation des données fait l'objet d'un article publié dans le journal *Remote Sensing of Environment* (Montpetit *et al.*, 2015). Ce travail démontre qu'il est possible d'optimiser un modèle d'émission MOP du sol afin d'obtenir un biais moyen de $\pm$ 0.2 K et un écart-type $\approx$ 10.75 K et que les modèles de Wegmüller et Mätzler (1999) et Wang et Choudhury (1981) sont équivalent sous différents scénarios d'optimisation de leurs paramètres. Les travaux d'analyses de la base de données PORTOS-93, d'optimisation des modèles, de la production des résultats, la rédaction de l'article (Montpetit *et al.*, 2015) ainsi que les révisions de l'article (avec l'aide des co-auteurs) ont été faites par l'auteur principal dans le cadre de cette thèse. L'originalité de cet article est la calibration de deux modèles d'émission MOP de sol simultanément sur la même base de données multi-angles et multifréquences.

## A.1 Article : Evaluation of multi-frequency bare soil passive microwave reflectivity models

Remote Sensing of Environment 162 (2015) 186–195

Contents lists available at ScienceDirect

Remote Sensing of Environment

journal homepage: www.elsevier.com/locate/rse

# Evaluation of multi-frequency bare soil microwave reflectivity models

B. Montpetit [a,*], A. Royer [a], J.-P. Wigneron [b], A. Chanzy [c], A. Mialon [d]

[a] Centre d'Applications et de Recherches en Télédétection, Université de Sherbrooke, Québec, Canada
[b] INRA, Bordeaux science Agro, UMR 1391 ISPA, 33140 Villenave d'Ornon Cedex, France
[c] INRA, Domaine Saint-Paul — Site Agroparc, 84914 Avignon, France
[d] Centre d'Etudes Spatiales de la BIOsphère, Toulouse, France

ARTICLE INFO

*Article history:*
Received 8 July 2014
Received in revised form 9 February 2015
Accepted 11 February 2015
Available online xxxx

*Keywords:*
Passive microwaves
Bare soil
Rough soil reflectivity model

ABSTRACT

Passive microwave remote sensing is commonly used to monitor the hydrological processes of the earth's surface (soil moisture) as well as key surface environmental processes (vegetation dynamics, snow cover, etc.). For many applications, it is important to model the effects of surface roughness. This study focuses on the unique PORTOS-93 measurement campaign that covered a wide range of bare soil conditions in terms of moisture, temperature and surface roughness. The PORTOS-93 campaign covers a frequency range from 1.41 to 90 GHz. In this study, based on the PORTOS-93 dataset, we compare the Wegmüller & Mätzler (1999) model (referred to as WM99) with the Wang & Choudhury (1981) model (referred to as QHN) and evaluate their abilities to simulate the soil surface brightness temperature ($T_B$). We show that improved results were obtained by tuning the parameters of the two models to the entire PORTOS-93 dataset for each frequency separately compared to the model tuned independently of frequency. In addition we found that the Mironov et al. (2009) soil permittivity model is slightly more accurate at lower frequencies (<11 GHz) for simulating soil permittivity than the Dobson et al. (1985) soil permittivity model for the PORTOS-93 site. We also found that both of these permittivity models need to be tuned at higher frequencies (>20 GHz) and that using the Wang & Schmugge (1980) model tuned using parameters derived by Calvet et al. (1995a) at higher frequencies for the PORTOS-93 dataset gives best results. Using the proposed tuned reflectivity models for each frequency separately, we obtained an overall bias of −0.20 K and 0.21 K for the WM99 and QHN models respectively between the measured and modelled brightness temperatures. This corresponds to a significant improvement in comparison to the use of the tuned WM99 model independently of the frequency (bias = −38.08 K).

© 2015 Elsevier Inc. All rights reserved.

## 1. Introduction

Passive microwave remote sensing is commonly used to monitor hydrological processes as in the European Space Agency's (ESA) Soil Moisture and Ocean Salinity (SMOS) mission (Kerr et al., 2001) and the National Aeronautics and Space Administration's (NASA) upcoming Soil Moisture Active and Passive (SMAP) mission (Brown et al., 2013). These missions mainly concentrate on L-band (1.41 GHz) microwave brightness temperatures ($T_B$) to retrieve the soil moisture ($SM$). In order to extract $SM$, the contribution from the soil to the overall $T_B$ has to be isolated from other contributions such as the atmosphere (Kerr & Njoku, 1990), the vegetation (Wigneron et al., 2003) and the snow cover (Rautiainen et al., 2012). This signal also needs to take into account the soil surface properties such as surface roughness (Escorihuela et al., 2007; Wigneron et al., 2011) and soil texture (Njoku & Entekhabi, 1996; Wigneron et al., 2003).

The NASA National Snow and Ice Data Center (NSIDC) and the Japan Aerospace Exploration Agency (JAXA) provide standard soil moisture products from the Advanced Microwave Scanning Radiometer—Earth Observing System (AMSR-E) (Njoku, Jackson, Lakshmi, Chan, & Nghiem, 2003; Shibata, Imaoka, & Koike, 2003). The NSIDC AMSR-E Level 3 soil moisture product (Njoku et al., 2003) is based on an inversion algorithm from the 10.7 GHz and 18.7 GHz brightness temperature data using the empirical soil permittivity model of Wang and Schmugge (1980) and semi-empirical equations based on the Wang and Choudhury (1981) roughness model with three free parameters (hereinafter referred to as the QHN model): the roughness height ($H_R$), a polarisation mixing parameter ($Q_R$) and a parameter accounting for the angular dependency of the reflectivity ($N_R$). The JAXA product is based on the discrete ordinate method proposed by Tsang and Kong (1977) and the soil permittivity model of Dobson, Ulaby, Hallikainen, and El-Rayes (1985), hereafter referred to as the Soil Moisture Dielectric Mixing (SMDM) model. Validation studies show that the algorithms currently in use by JAXA and NASA still need improvements (see Jackson et al., 2010).

Studies for other environmental applications (land surface parameter retrieval such as vegetation and snow cover dynamics, or vegetation

* Corresponding author at: Centre d'Applications et de Recherches en Télédétection (CARTEL), Département de Géomatique Appliquée, Université de Sherbrooke, Sherbrooke, Québec J1K 2R1, Canada.
*E-mail address:* Benoit.Montpetit2@USherbrooke.ca (B. Montpetit).

http://dx.doi.org/10.1016/j.rse.2015.02.015
0034-4257/© 2015 Elsevier Inc. All rights reserved.

water content) based on higher frequencies (from 6 to 90 GHz) need accurate estimates of the soil signal under the canopy or the snow (e.g. Mätzler, 2006). In most of these studies, the soil contribution brings uncertainties that must be taken into account to improve the retrievals (see for example Calvet et al., 2011; Prigent, Wigneron, Rossow, & Pardo-Carrion, 2000).

Ground-based microwave experiments in combination with ground-truth measurements have been conducted to elaborate methods to relate *SM* to the L-band $T_B$ such as PORTOS (Wigneron, Laguerre, & Kerr, 2001), SMOSREX (de Rosnay et al., 2006) and also airborne campaigns such as SMEX03 (Jackson et al., 2005), CanEx-SM10 (Magagi et al., 2013) and SMAPEx (Panciera et al., 2014). These studies have mainly proposed soil surface roughness corrections to the L-band $T_B$ (Escorihuela et al., 2007; Schwank et al., 2010; Shi et al., 2002; Wang & Choudhury, 1981; Wigneron et al., 2011) but only a few studies have tried to apply these corrections to $T_B$ at higher frequencies (>1.4 GHz, Calvet, Wigneron, Chanzy, & Haboudane, 1995; Prigent et al., 2000; Wang, O'Neill, Jackson, & Engman, 1983; Wegmüller & Mätzler, 1999).

For example the PORTOS-93 (Wigneron et al., 2011) and SMOSREX (Escorihuela et al., 2007) campaigns were conducted to relate the bare soil geophysical parameters (soil moisture, temperature, surface roughness, textural composition, etc.) to the simulated soil reflectivity at L-band using the QHN roughness model. Analysis of the PORTOS-93 data showed that the last two parameters could be neglected ($N_R = Q_R = 0$) with a low impact on the accuracy of the *SM* retrievals (Lawrence, Wigneron, Demontoux, Mialon, & Kerr, 2013). The SMOSREX study also showed that $Q_R$ could be neglected but suggested that $N_R$ had to be specific for a given polarisation and found that $N_{RV} = -1$ and $N_{RH} = 1$ (Escorihuela et al., 2007). Nonetheless, the values of $N_{RV}$ and $N_{RH}$ at L-band are not yet well established (Lawrence et al., 2013; Wigneron et al., 2007). Prigent et al. (2000) have shown that for higher frequencies (23.8 GHz and higher), to use such a QHN approach, all three parameters ($H_R$, $Q_R$ and $N_R$) had to be considered. They have also shown that all three parameters were dependent upon the surface properties and type (smooth soil, rough soil or covered with vegetation) meaning that these parameters needed to be tuned for each area and can vary in time depending on the surface type (texture, roughness, etc.). Goodberlet and Mead (2014) suggested that to model the effects of soil surface roughness at L-band, the $Q_R$ parameter should be considered and that it is related empirically to the surface roughness. Also, they suggested that $H_R$ depended not only on the surface roughness but also on the Fresnel reflectivity (based on the soil surface permittivity which depends on soil moisture). This last result differs from previous studies. Finally, they showed that $N_{RV} = -2$ and $N_{RH} = 1$ which is similar to what Escorihuela et al. (2007) suggested. These different studies showed that there is a need to further investigate the effects of surface roughness on the soil reflectivity since there are still many questions concerning the calibration of the surface roughness parameters.

Other studies focusing mainly on vegetated areas used a similar approach to extract soil surface parameters from passive microwave $T_B$ at higher frequencies. Calvet, Wigneron, Chanzy, and Haboudane (1995) showed that it is possible to retrieve $Q_R$ and $H_R$ at 23.8, 36.5 and 90 GHz for fields covered by sorghum and wheat canopies and estimate the soil contribution to the measured $T_B$. The latter study also showed that the soil dielectric properties could be modelled for silt–loam soils using the model of Wang and Schmugge (1980) (hereafter referred to as WS80), provided that it has been calibrated to the specific conditions of the fields. In this study, the three frequencies had to be treated separately.

Pellarin, Kerr, and Wigneron (2006) simulated $T_B$ at C- (6.6 GHz) and X-bands (10.7 GHz) at global scale using the QHN model and have evaluated these simulations with the Scanning Multichannel Microwave Radiometer (SMMR) satellite $T_B$. They showed that the QHN model was able to reproduce realistic values of $T_B$ at a global scale. Roy et al. (2012) showed that an optimization of the reflectivity model on the AMSR-E $T_B$ converged to specific values of $H_R$ and $Q_R$ at 19 and 37 GHz over Canadian boreal forest sites. These last studies were conducted over vegetated areas where the soil contribution to the measured satellite $T_B$ is attenuated by the overlaying canopy making the retrieval of soil parameters more complex.

The most complete study at higher frequencies (>10 GHz) was done by Wegmüller and Mätzler (1999) who developed a reflectivity model (hereinafter referred to as the WM99 model) that is based on the Mo and Schmugge (1987) parameterization for the frequency range of 1 to 100 GHz and incidence angle range of 20 to 70° for rough bare soils. They showed that the vertical (V-Pol) and horizontal polarisation (H-Pol) reflectivities were strongly correlated and that only one polarisation had to be modelled (either V or H) as a function of the soil variables, while the other could be derived from the former. Mo and Schmugge (1987) and Wegmüller and Mätzler (1999) found that it is preferable to model the H-Pol reflectivity as a function of the soil variables (soil roughness, moisture and temperature) and, in a second step, the V-Pol reflectivity can be computed from the modelled H-Pol reflectivity. Contrary to what was discussed by Calvet, Wigneron, Chanzy, Raju, and Laguerre (1995), they did not consider the reflectivities at different frequencies separately. This is mainly due to the fact that Wegmüller and Mätzler (1999) used the SMDM soil dielectric model (Dobson et al., 1985), whereas Calvet, Wigneron, Chanzy, Raju, and Laguerre (1995) used an empirical soil dielectric permittivity mixing model (Wang & Schmugge, 1980). More recently, a new soil permittivity model, referred to as the Generalized Refractive Mixing Dielectric Model (GRMDM), was developed (Mironov, Kerr, Wigneron, Kosolapova, & Demontoux, 2012; Mironov, Kosolapova, & Fomin, 2009). Recent studies (Goodberlet & Mead, 2014; Mialon et al., 2014; Wigneron et al., 2011, 2012) found that this new model provides accurate simulations of the soil dielectric constant in comparison to the SMDM model at L-band.

Here, we propose to evaluate the WM99 and QHN models using the unique PORTOS-93 multi-angular, bi-polarisation and multi-frequency dataset. To do so, 1) an evaluation of the permittivity modelling based on the SMDM, GRMDM and WS80 models was made in the 1–90 GHz range of frequencies, 2) then, we evaluated and compared the two semi-empirical soil reflectivity models (WM99 and QHN) and 3) finally a comparison between different tuned approaches of the WM99 and QHN models was made.

## 2. Materials and methods

### 2.1. Experimental dataset

The PORTOS-93 dataset is thoroughly described in Wigneron et al. (2001) and only a short description of the measurements will be given here. The measurements were taken over seven bare fields at the Institut National de la Recherche Agronomique (INRA) Avignon Remote Sensing test site during the period of April 20th to July 10th, 1993 (Table 1). The sites are silty clay loam fields with a textural

**Table 1**
Measured surface roughness parameter ($\sigma$), soil moisture (*SM*) and effective soil temperature ($T_{soil}$) over the different fields for the entire measurement campaign. The mean and standard deviation of the measurements over each field are given.

| Field no. | Std deviation of height $\sigma$ (mm) | | Soil moisture *SM* ($m^3\ m^{-3}$) | | Soil temperature $T_{soil}$ (K) | |
|---|---|---|---|---|---|---|
| | Mean | Std | Mean | Std | Mean | Std |
| 6 | 59.37 | 13.77 | 0.15 | 0.09 | 298.68 | 2.01 |
| 9 | 4.76 | 1.89 | 0.19 | 0.07 | 298.15 | 3.67 |
| 11 | 8.39 | 1.24 | 0.20 | 0.04 | 297.71 | 3.43 |
| 15 | 8.96 | 2.84 | 0.18 | 0.11 | 299.36 | 3.25 |
| 16 | 47.43 | 4.76 | 0.15 | 0.16 | 302.94 | 6.85 |
| 17 | 4.57 | 1.98 | 0.14 | 0.10 | 300.50 | 6.44 |
| 18 | 19.15 | 5.08 | 0.15 | 0.16 | 305.75 | 7.27 |

composition of 62% silt, 11% sand and 27% clay. The surface roughness parameters are given in Table 1. The surface roughness varied from very smooth surfaces to freshly ploughed fields. Field 17 was crushed and compressed by a roadroller to obtain the smoothest surface of all seven fields and field 6 was ploughed using a spading machine at a fast pace to get the roughest surface of the seven fields (Table 1). Alongside the radiometric measurements, soil moisture (*SM*) and temperature profiles ($T_{soil}$) were acquired. Measured effective soil moisture ranged from 0.01 to 0.38 $m^3$ $m^{-3}$ and effective soil temperature (noted $T_{soil}$) (Wigneron et al., 2001) ranged from 290.68 to 318.00 K and was calculated by:

$$T_{Soil}(\theta) = \int_0^{\infty} T_{soil}(z)\,\frac{\kappa_s(z)}{\cos(\theta')}\exp\left[-\int_0^{z}\frac{\kappa_s(z')}{\cos(\theta')}dz'\right]dz \quad (1)$$

where $\kappa_s(z) = \mathrm{Im}\sqrt{\varepsilon_s(T_{Soil}(z), SM(z), f)}$ is the normalized attenuation coefficient at depth $z$ at frequency $f$. *SM* and $T_{Soil}$ were sampled every 0.5 cm for the first cm, every cm from 1 to 10 cm, 15, 20 and 50 cm deep. The sampling depth for each frequency and site was then determined using Eq. (1). The mean and standard deviation for each measured soil parameter per field for the measurement campaign are given in Table 1.

The data used to compute the soil reflectivities in this study were the brightness temperatures ($T_B$) acquired by the PORTOS radiometers at four incidence angles (10°, 20°, 30° and 40°) and 5 different frequencies (1.41, 10.65, 23.8, 36.5 and 90 GHz) in both horizontal (H-Pol) and vertical (V-Pol) polarisations. The radiometers were mounted on a 20 m high crane boom and the observations were done over 18 × 40 m fields. The 3 and 20 dB beamwidths were respectively, 12.5° and 30.0° at 1.41 GHz, 13.0° and 39.2° at 10.65 GHz, 10.3° and 31.8° at 23.8 GHz, 9.6° and 31.5° at 36.5 GHz and 11.3° and 32.8° at 90 GHz. This corresponds to a footprint of about 7 to 10 m wide at nadir for the 3 dB beamwidth. The radiometers were regularly calibrated (every 2–3 weeks) using calm water surfaces and eccosorb surfaces (emissivity close to 1 in the microwave domain) at ambient temperature or immersed in liquid nitrogen (77 K) (Asmus & Grant, 1999). The overall accuracy at all frequencies was estimated at 3 K using a single calibration rule for the whole campaign. The measured $T_B$ can be modelled using the following equation (assuming that the cosmic downwelling radiation is negligible):

$$T_B = (1-\Gamma_P)T_{Soil} + \Gamma_P T_B^{Sky} \quad (2)$$

where $\Gamma_P$ is the bare-soil reflectivity at polarisation "*P*" and $T_B^{Sky}$ is the downwelling sky brightness temperature. The latter was modelled following Kerr and Njoku (1990) with the operational outputs of the Météo-France 15 level weather forecast model PERIDOT (Calvet, Wigneron, Chanzy, & Haboudane, 1995).

### 2.2. Models

#### 2.2.1. Soil permittivity model

In this study, three permittivity models were used. The first one was developed by Dobson et al. (1985) based on a semi-empirical mixing dielectric model (SMDM) using as inputs: soil moisture (*SM*), soil temperature, soil texture (% clay and % sand) and soil bulk density ($\rho_b$ in g/$cm^3$). The second model is the empirical model of Wang and Schmugge (1980) which uses the same inputs as the SMDM model. At high frequencies (23.8, 36.5 and 90 GHz), we used the Wang and Schmugge (1980) model tuned by Calvet, Wigneron, Chanzy, and Haboudane (1995). The third model is the generalized refractive mixing dielectric model (GRMDM) developed by Mironov et al. (2009) which requires the soil humidity, temperature and clay content as inputs.

#### 2.2.2. Soil reflectivity models

Two soil roughness models were analysed in this study. The first one is the model developed by Wegmüller and Mätzler (1999) (hereafter referred to as WM99). The general equations of the WM99 model are

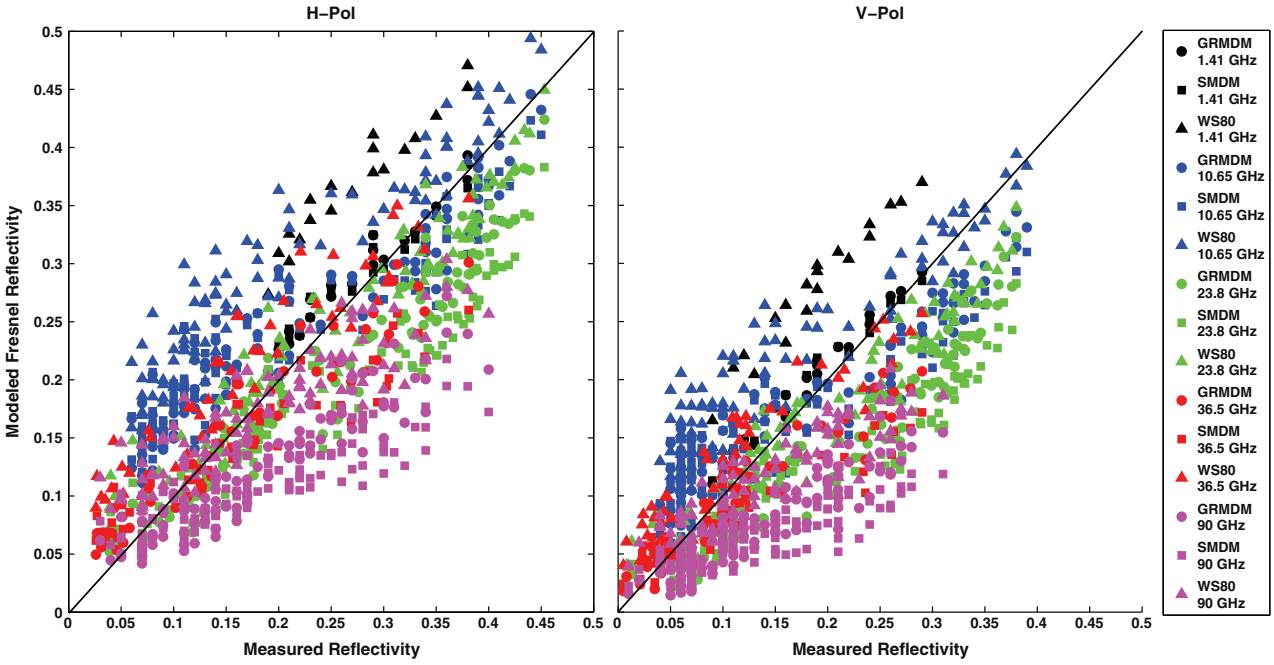


**Fig. 1.** Comparison of the soil permittivity relationships with soil moisture (*SM*) for the retrieved permittivities (Table 2) (triangles), the modelled permittivities with GRMDM (circles) and SMDM (squares) for sites with low surface roughness ($\sigma < 5$ mm) at 1.41 (black), 10.65 (blue), 23.8 (green), 36.5 (red) and 90 GHz (magenta), at both H-Pol (a) and V-Pol (b) polarisations. (For interpretation of the references to colour in this figure legend, the reader is referred to the web version of this article.)

**Table 2**
Bias and standard deviation (parentheses) between the measured reflectivities of sites 9 and 17 (Table 1) and the modelled reflectivities using the SMDM, GRMDM and WS80 permittivity models and the Fresnel equations. The selected models are in bold.

| f (GHz) | GRMDM H-Pol | GRMDM V-Pol | GRMDM | SMDM H-Pol | SMDM V-Pol | SMDM | WS80 H-Pol | WS80 V-Pol | WS80 |
|---|---|---|---|---|---|---|---|---|---|
| 1.41 | −0.02 | −0.02 | **−0.02** | −0.01 | −0.01 | −0.01 | −0.10 | −0.09 | −0.09 |
| | (0.01) | (0.01) | **(0.01)** | (0.02) | (0.01) | (0.01) | (0.02) | (0.01) | (0.01) |
| 10.65 | −0.03 | −0.01 | **−0.02** | −0.03 | −0.00 | −0.02 | −0.09 | −0.05 | −0.07 |
| | (0.05) | (0.05) | **(0.05)** | (0.06) | (0.06) | (0.06) | (0.05) | (0.04) | (0.05) |
| 23.8 | 0.05 | 0.06 | 0.05 | 0.06 | 0.08 | 0.07 | 0.01 | 0.03 | **0.02** |
| | (0.04) | (0.04) | (0.04) | (0.05) | (0.05) | (0.05) | (0.04) | (0.03) | **(0.04)** |
| 36.5 | 0.01 | 0.02 | 0.01 | 0.02 | 0.03 | 0.03 | −0.04 | −0.02 | **−0.03** |
| | (0.03) | (0.03) | (0.03) | (0.05) | (0.05) | (0.05) | (0.04) | (0.03) | **(0.03)** |
| 90 | 0.06 | 0.06 | 0.06 | 0.07 | 0.07 | 0.07 | 0.01 | 0.03 | **0.02** |
| | (0.04) | (0.04) | (0.04) | (0.06) | (0.05) | (0.06) | (0.05) | (0.04) | **(0.05)** |
| All | 0.02 | 0.03 | 0.03 | 0.03 | 0.04 | 0.04 | −0.03 | −0.01 | −0.02 |
| | (0.06) | (0.05) | (0.05) | (0.07) | (0.06) | (0.07) | (0.06) | (0.05) | (0.06) |

defined by four parameters ($A_0$, $A_2$, $A_3$ and $\beta$), related by the following equations for a given incidence angle ($\theta$):

$$\Gamma_H = \Gamma_H^{Fresnel} \exp\left(-A_0(k\sigma)^{A_1}\right) \tag{3}$$

$$A_1 = A_2 \cos^{A_3}\theta \tag{4}$$

$$\Gamma_V = \Gamma_H(\cos\theta)^{\beta} \tag{5}$$

where $k$ is the vacuum wavenumber at a given wavelength $\lambda$ ($\frac{2\pi}{\lambda}$) and $\sigma$ is the standard deviation of surface height (surface roughness). Eqs. (3) and (4) were determined empirically with ground measurements of reflectivity in the 1–100 GHz range and soil measurements similar to the ones in this study. These equations are based on Mo and Schmugge (1987) and Wegmüller and Mätzler (1999). The original WM99 model is defined by the following parameters: $A_0 = 1$, $A_2 = \sqrt{0.1}$, $A_3 = 0.5$ and $\beta = 0.655$ (Wegmüller & Mätzler, 1999). Eq. (5) accounts for the strong correlation between the observed V-Pol and H-Pol reflectivities.

The second rough soil reflectivity model used in this study is based on the model developed by Wang and Choudhury (1981) (hereafter referred to as QHN). The equations are defined by four empirical parameters ($Q_R$, $H_R$, $N_{RV}$, and $N_{RH}$) related to the reflectivity ($\Gamma_p$) for a given incidence angle ($\theta$) and polarisation $p$:

$$\Gamma_p = \left[(1-Q_R)\Gamma_p^* + Q_R\Gamma_q^*\right] \exp\left(-H_R \cos^{N_{Rp}}\theta\right) \tag{6}$$

where $\Gamma_p^*$ and $\Gamma_q^*$ are the Fresnel reflectivities at polarisation $p$ and $q$ (e.g. $q$ = V if $p$ = H and vice versa). To relate the four parameters of Eq. (6) to the soil properties, empirical equations are generally used. The base formulation of the QHN model used in this study is the one proposed by Wigneron et al. (2011) which was optimized on the PORTOS-93 dataset at L-band. They found that $Q_R = N_{RV} = N_{RH} = 0$ and that $H_R$ could be related to surface roughness by:

$$H_R = \left(\frac{a_1\,\sigma}{a_2\sigma + a_3}\right)^6 \tag{7}$$

where $a_1 = 0.9437$, $a_2 = 0.8865$ and $a_3 = 2.2913$ for $\sigma$ values ranging from 4.57 to 59.37 mm.

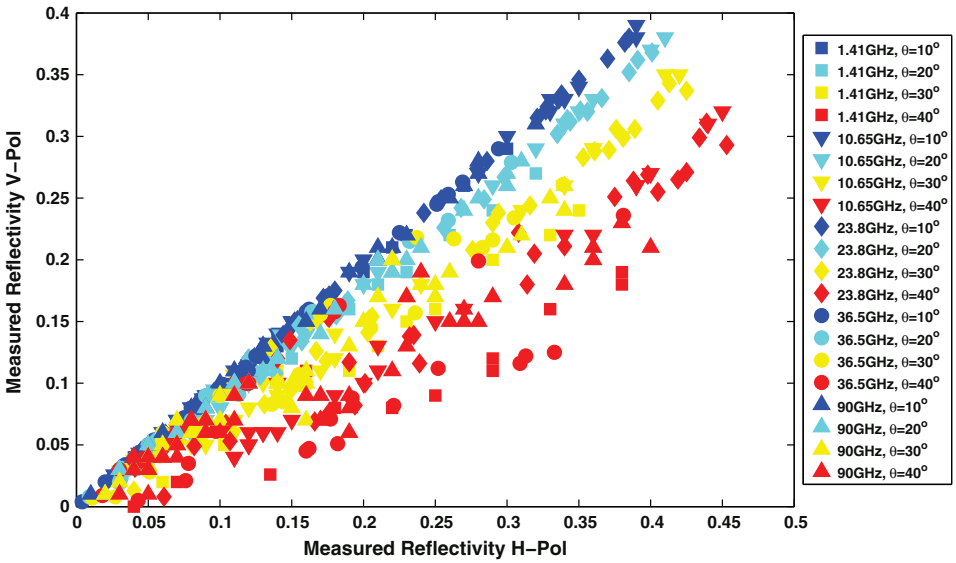


**Fig. 2.** Relationship between the measured reflectivities in V-Pol and H-Pol at 1.41 (squares), 10.65 (upside down triangles), 23.8 (diamonds), 36.5 (circles) and 90 GHz (triangles) for incidence angles of 10° (blue), 20° (cyan), 30° (yellow) and 40° (red) for all sites. (For interpretation of the references to colour in this figure legend, the reader is referred to the web version of this article.)

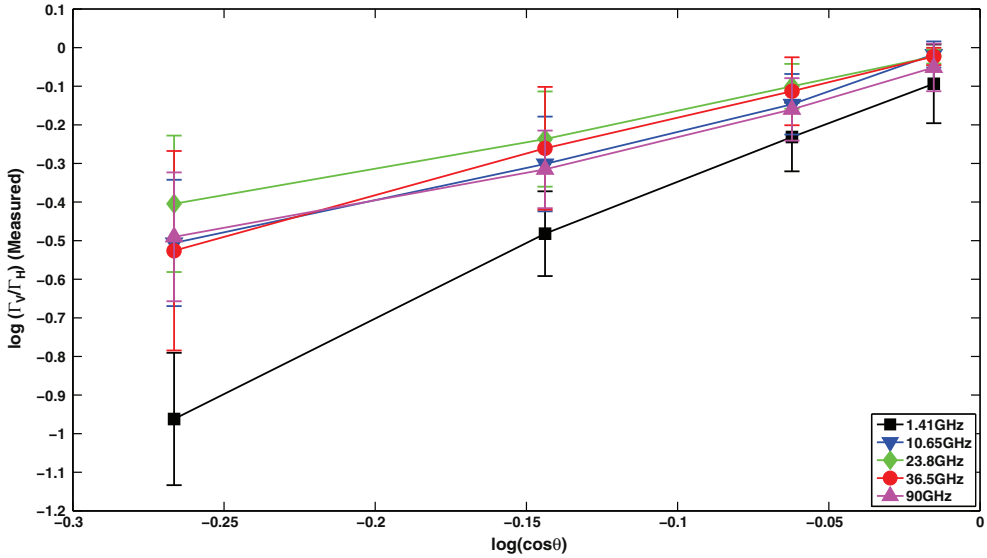


**Fig. 3.** Comparison of the mean reflectivity ratio (V-Pol/H-Pol) and the cosine of the incidence angle in logarithmic scale at 10°, 20°, 30° and 40°.

### 2.3. Methodology

The first step in this study was to select a soil permittivity model to compute the Fresnel soil reflectivity. To do so, we assumed that the reflectivity of very smooth bare soils ($\sigma < 5$ mm, and correlation length $l > 60$ mm) was accurately modelled using the Fresnel equations (sites 9 and 17, Table 1). According to Mo and Schmugge (1987), a surface is considered smooth when the ratio $m = \sigma / l < 0.1$. If this criterion is applicable to higher frequencies, site 9 ($m = 0.07$) and site 17 ($m = 0.02$) can be considered smooth and well represented by the Fresnel equations. The Fresnel reflectivities using the three soil permittivity models (SMDM, GRMDM or WS80) were compared to the measured reflectivities, in order to evaluate which models provided lowest simulation errors.

In a second step, to evaluate the representation of the polarisation effects in the WM99 model (Eq. (5)), a comparison between the measured reflectivities in V-Pol and H-Pol was made for all the measured sites. Each incidence angle was considered separately to determine if there was a linear relationship between the reflectivities measured at the two H and V polarisations. Then, each frequency was considered separately to determine if there is a need to consider $\beta$ as frequency dependent.

In a third step, for the WM99 model, we tuned the parameters of Eqs. (3) to (5) independently of frequency (referred to as WM99fi) and for each frequency separately (referred to as WM99fd) using the least square minimization algorithm of Levenberg–Marquardt (Marquardt, 1963; hereafter referred as LM63). For this tuning, the most accurate soil permittivity model (SMDM, GRMDM or WS80) was used according to the results obtained in step one. The same tuning process was performed for the QHN model using Eqs. (6) and (7) (referred similarly to as QHNfi and QHNfd).

Finally, for both the WM99 and QHN models, the evaluation of the two scenarios (frequency independent and frequency independent) was conducted by comparing the measured and the modelled $T_B$ values.

## 3. Results

### 3.1. Evaluation of the permittivity models

To evaluate the performance of the SMDM, GRMDM and WS80 models, the soils with a smooth surface were chosen ($\sigma < 5$ mm and $l > 60$ mm, e.g. sites 9 and 17 in Table 1). The modelled reflectivities using the different permittivity models and the Fresnel equations were compared to the measured reflectivities at all the five frequencies and for both H and V polarisations (Fig. 1).

Table 2 presents the mean biases and the associated standard deviations between the modelled and measured reflectivities shown in Fig. 1. For the selected smooth sites, the SMDM and GRMDM model provide similar results at lower frequencies (<11 GHz). Overall, the GRMDM model has a lower standard deviation for the lower frequencies and this is why this model was chosen for the remaining analysis of this study for frequencies lower than 11 GHz. At higher frequencies (>23 GHz), the empirical WS80 model tuned by Calvet, Wigneron, Chanzy, and Haboudane (1995) on sites 9 and 17 of the current study shows the lowest biases and standard deviations overall. Although the GRMDM model shows better results at 36.5 GHz than the WS80 model, the latter was chosen for the remaining analysis of this study in order to stay consistent over the higher frequency range. Note that the modelled reflectivities are sensitive to the downwelling sky $T_B$ values used. To assess the accuracy of the weather forecast model PERIDOT data (Calvet, Wigneron, Chanzy, & Haboudane, 1995) as inputs, the downwelling sky $T_B$ was modelled using the ERA-Interim reanalysis data (Dee et al., 2011) as inputs in the same Kerr and Njoku (1990) atmospheric model. A standard deviation of 0.22 K, 5.92 K, 15.88 K, 13.15 K and 27.52 K at 1.41, 10.65, 23.8, 36.5 and 90 GHz respectively was observed between both modelled downwelling sky $T_B$. This corresponds to a variability (mean difference between both $T_B$ simulations divided by the mean value modelled using the PERIDOT

**Table 3**
Retrieved parameters and optimization statistics of the frequency independent optimization (WM99fi) and the frequency dependent optimization (WM99fd).

| | f (GHz) | $A_0$ | $A_2$ | $A_3$ | $\beta$ | Bias | Std |
|---|---|---|---|---|---|---|---|
| WM99fi | All | 0.039 | 0.872 | −0.016 | 2.140 | −0.002 | 0.058 |
| WM99fd | 1.41 | 0.610 | 1.203 | 0.362 | 2.948 | −0.001 | 0.019 |
| | 10.65 | 0.080 | 0.935 | 0.302 | 1.890 | −0.012 | 0.052 |
| | 23.8 | 0.026 | 1.181 | −0.054 | 1.349 | 0.011 | 0.046 |
| | 36.5 | 0.063 | 0.806 | −0.022 | 2.433 | −0.004 | 0.035 |
| | 90 | 0.004 | 1.266 | −0.104 | 1.869 | 0.003 | 0.049 |

**Table 4**
Same as Table 3 for the QHN model.

| | f (GHz) | $a_1$ | $a_2$ | $a_3$ | $Q$ | $N_V$ | $N_H$ | Bias | Std |
|---|---|---|---|---|---|---|---|---|---|
| QHNfi | All | 0.887 | 0.796 | 3.517 | 0.075 | 1.503 | 0.131 | −0.003 | 0.042 |
| QHNfd | 1.41 | 0.903 | 0.829 | 3.434 | 0.366 | −0.099 | 0.000 | 0.002 | 0.016 |
| | 10.65 | 0.880 | 0.838 | 3.280 | 0.657 | 3.209 | 0.178 | 0.012 | 0.047 |
| | 23.8 | 0.880 | 0.775 | 3.748 | −0.100 | 1.619 | 0.134 | −0.019 | 0.041 |
| | 36.5 | 0.938 | 0.868 | 2.506 | −0.545 | 1.876 | 0.054 | 0.007 | 0.032 |
| | 90 | 0.867 | 0.734 | 4.275 | −0.012 | 2.404 | 0.145 | −0.008 | 0.046 |

data) of 5.6%, 4.3%, 9.1%, 7.5% and 16.3% on the measured surface reflectivity at 1.41, 10.65, 23.8, 36.5 and 90 GHz respectively.

### 3.2. Evaluation of the reflectivity polarisation ratios

To evaluate the accuracy of the roughness models (WM99 or QHN) to simulate the soil reflectivity, an analysis of the reflectivity polarisation ratio ($\Gamma_V/\Gamma_H$) was performed. Fig. 2 compares the measured V-Pol reflectivity to the measured H-Pol reflectivity for all the sites (see Table 1).

As expected with Eq. (5), a linear relationship between the H and V reflectivities is found for a given incidence angle ($R^2 > 0.86$). At lower incidence angles ($\leq 20°$), the linear correlation ($R^2 = 0.99$) is stronger than at higher incidence ($\geq 30°$) where there is more variability. The reasons for this high variability at higher incidence angles are discussed in Section 4. Fig. 3 shows the mean polarisation ratio compared to the cosine of the incidence angle on a log scale. The polarisation ratios were all averaged for a given incidence angle and a given frequency. Fig. 3 shows that there is a need to consider the frequency dependence of $\beta$ (Eq. (5)) to properly model the polarisation ratio at different frequencies considered here. The ratio at 1.41 GHz is clearly lower than at the four other frequencies (at 10.65, 23.8 36.5 and 90 GHz) which have comparable ratios.

### 3.3. Evaluation of the reflectivity models

The results for $T_B$ modelling of both tuned reflectivity models (WM99 and QHN) in the frequency independent (fi) and frequency dependent (fd) scenarios will be presented in the following.

#### 3.3.1. Optimization results

Table 3 presents the tuned parameters of the WM99 in the frequency independent (WM99fi) and frequency dependent (WM99fd) scenarios.

The use of the WM99fi scheme led to a low bias between the measured and modelled reflectivities but it led a high standard deviation (Std) which is 40% of the overall averaged measured reflectivity. The WM99fd tuning gives similar biases but gives lower Std except at 90 GHz (variability of 13.3%, 29.4%, 27.8%, 27.3% and 38.5% of the mean measured reflectivity at 1.41, 10.65, 23.8, 36.5 and 90 GHz respectively). The $\beta$ value obtained in the WM99fi scheme is comparable to the mean $\beta$ value obtained in the WM99fd scheme. The $A_0$ obtained at 1.41 GHz is much higher than that obtained at other frequencies for the WM99fd scheme. We could also note the low value of $A_0$ ($A_0 = 0.004$) at 90 GHz for the WM99fd scheme meaning a low sensitivity to surface roughness effects at 90 GHz (see Eq. (5)). The value of the $A_3$ parameter is much greater at lower frequencies (<11 GHz) and becomes negative at higher frequencies (>23 GHz) which indicates a different angular dependency of the modelled reflectivity in H-Pol between the two frequency ranges in relation with their dependency to the surface roughness. Table 4 gives the tuned parameters for both the QHNfi and QHNfd schemes.

Considering the results of the QHN model in Table 4, it can be seen that the parameters of Eq. (7) obtained here are similar to the ones obtained by Wigneron et al. (2011) and are very similar for both the QHNfi and QHNfd models. This indicates that the roughness dependency of the QHN model is almost frequency independent. The retrieved $N_V$ and $N_H$ values at 1.41 GHz are close to 0.00. Also, as seen with the WM99 model, there is a sign difference in the $Q$ parameter between the low

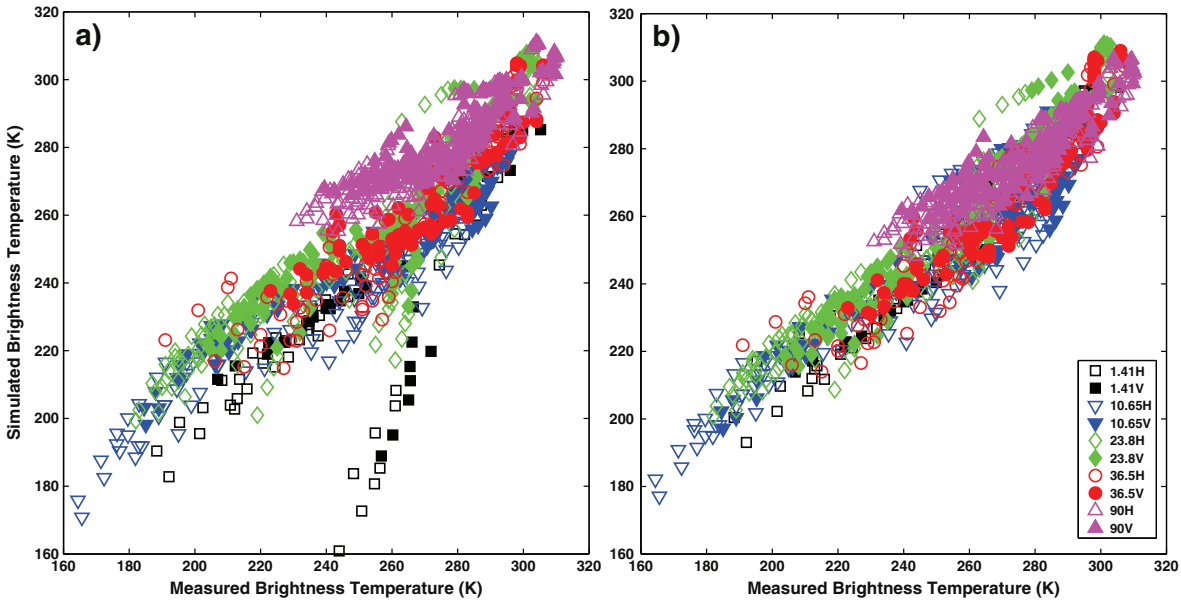


**Fig. 4.** Simulated $T_B$ using the WM99 (a) and QHN (b) models compared to the measured $T_B$ at 1.41 (squares), 10.65 (reversed triangles), 23.8 (diamonds), 36.5 (circles) and 90 GHz (triangles) at both V-Pol (filled) and H-Pol (empty) polarisation for all sites and measurements.

**Table 5**
Biases and standard deviation of the difference between the measured and simulated $T_B$ using the WM99fi and QNHfi models for the frequency independent scenario.

| Channel | WM99fi | | QHNfi | |
|---|---|---|---|---|
| | Bias (K) | Std (K) | Bias (K) | Std (K) |
| 1.41H | −19.78 | 23.05 | 2.08 | 6.41 |
| 1.41V | −18.39 | 17.33 | −3.41 | 5.47 |
| 10.65H | −7.54 | 14.87 | −1.97 | 15.21 |
| 10.65V | −6.53 | 14.24 | −2.77 | 12.79 |
| 23.8H | 2.94 | 15.11 | 5.97 | 10.95 |
| 23.8V | 2.53 | 10.65 | 3.59 | 7.82 |
| 36.5H | −4.87 | 10.61 | −3.79 | 9.37 |
| 36.5V | −4.83 | 8.74 | −4.67 | 8.03 |
| 90H | 6.87 | 9.89 | 1.10 | 9.20 |
| 90V | 5.42 | 8.44 | 1.54 | 7.43 |
| 1.41H&V | −19.09 | 20.30 | −0.66 | 6.54 |
| 10.65H&V | −7.03 | 14.53 | −2.37 | 14.03 |
| 23.8H&V | 2.73 | 13.05 | 4.78 | 9.57 |
| 36.5H&V | −4.85 | 9.70 | −4.23 | 8.71 |
| 90H&V | 6.15 | 9.21 | 1.32 | 8.35 |
| H-Pol | −1.41 | 15.99 | 0.89 | 11.44 |
| V-Pol | −1.60 | 13.28 | −0.37 | 9.36 |
| All | −1.51 | 14.69 | 0.26 | 10.46 |

and high frequencies. All these results will be further discussed in Section 4.

### 3.3.2. Frequency independent optimization

Fig. 4 shows the comparison between the measured and modelled $T_B$ using the WM99fi (Table 3) model (Fig. 4a) and the QHNfi (Table 4) model (Fig. 4b).

From Fig. 4, it can be seen that the WM99fi model does not accurately simulate the $T_B$ values at 1.41 GHz and 23.8 GHz where some points in the plot are further from the 1:1 line. Table 5 gives the bias and Std between the measured and modelled $T_B$ for the WM99fi and QHNfi models.

The biases of both models are generally low (−1.51 and 0.26 K for the WM99fi and QHNfi models respectively), except at 1.41 GHz for the WM99fi scheme, but both the bias and standard deviation are generally lower for the QHNfi model. The higher errors can be seen at 1.41, 10.65 and 90 GHz for the WM99fi model while higher errors can be noted at 23.8 and 36.5 GHz for the QHNfi model. A single dataset is not sufficient to simulate a broad range of frequencies but better results are found with the QHN model with the PORTOS-93 dataset which are good for all the measured frequencies.

### 3.3.3. Frequency dependent optimization

Fig. 5 shows the comparison between the measured $T_B$ and the modelled $T_B$ using the WM99fd model (Fig. 5a) and the QHNfd model (Fig. 5b).

Fig. 5a shows some improvement for the WM99fd compared to the WM99fi model (Fig. 4a) since the simulations are closer generally to the 1:1 line. No significant improvement can be seen between the QHNfi (Fig. 4b) and the QHNfd (Fig. 5b) models. Table 6 gives the bias and Std between the measured and modelled $T_B$ of the WM99fd and QHNfd models.

Table 6 shows that the overall biases (±0.2 K) and Std (~10 K) are similar for both the WM99 and QHN models. When looking at the different frequencies separately, it can be seen that the biases are smaller for the WM99fd model compared to the QHNfd model but the Std are higher.

### 3.3.4. Reflectivity modelling sensitivity

Fig. 6 shows the sensitivity of the WM99fd model to the soil moisture (*SM*) for low surface roughness conditions ($\sigma$ = 0.05 mm, Fig. 6a) and high surface roughness conditions ($\sigma$ = 30 mm; Fig. 6b) and the sensitivity to surface roughness for low soil moisture conditions (*SM* = 0.05 $m^3$ $m^{-3}$, Fig. 6c) and high soil moisture conditions (*SM* = 0.20 $m^3$ $m^{-3}$). The WM99fd model was chosen mainly because of its lower overall standard deviation compared to the other optimizations.

Fig. 6a and b shows that the modelled reflectivity increases with increasing values of *SM* at every frequency and both low and high surface roughness conditions. The decrease in the slopes of Fig. 6a and b with frequency indicates that the sensitivity to *SM* decreases with frequency.

Fig. 6c and d shows that the modelled reflectivity decreases with increasing $\sigma$ values. Fig. 6c shows that there is not much difference in the relationship between the different frequencies and polarisations for low soil moisture conditions. On the contrary, Fig. 6d shows that for high *SM* values, there is a lot of variation between the results for the different frequencies at H-Pol but not at V-Pol. The sensitivity of the simulated reflectivities to surface roughness is similar for each frequency (slope is similar) but the modelled reflectivity seems to decrease with

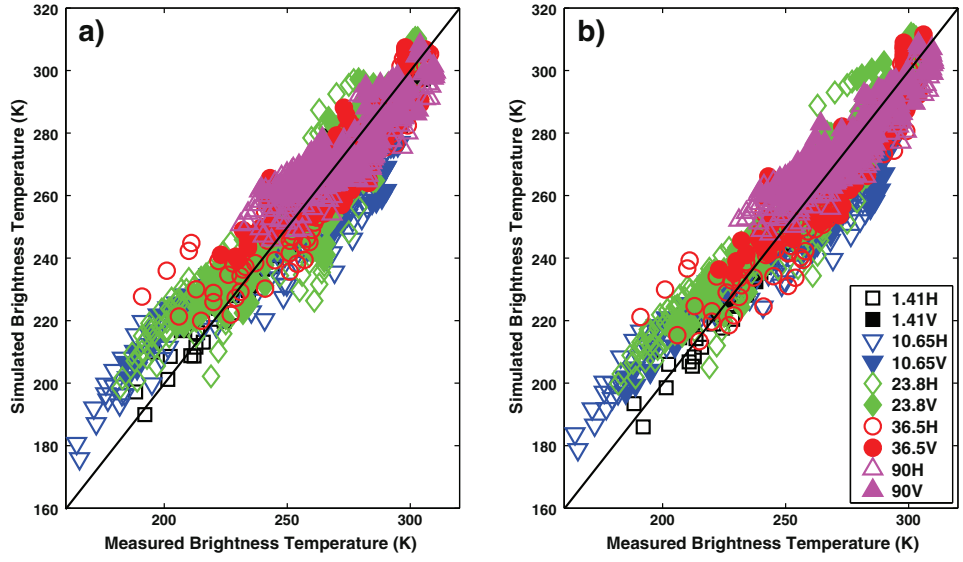


**Fig. 5.** Same as Fig. 4 but for the WM99fd (a) and QHNfd (b) scenarios.

**Table 6**
Same as Table 5 but for the WM99fd and QHNfd scenarios.

| Channel | WM99fd | | QHNfd | |
|---|---|---|---|---|
| | Bias (K) | Std (K) | Bias (K) | Std (K) |
| 1.41H | −0.87 | 5.87 | −1.42 | 5.43 |
| 1.41V | −0.24 | 6.15 | −0.40 | 4.28 |
| 10.65H | −3.04 | 15.02 | −2.55 | 14.46 |
| 10.65V | −4.37 | 14.44 | −5.09 | 11.96 |
| 23.8H | 5.08 | 13.05 | 5.33 | 11.33 |
| 23.8V | 0.67 | 9.83 | 3.91 | 7.64 |
| 36.5H | −1.08 | 10.52 | −3.59 | 9.82 |
| 36.5V | −1.00 | 9.26 | −1.39 | 8.41 |
| 90H | 0.57 | 9.85 | 0.83 | 9.25 |
| 90V | −0.13 | 8.17 | 1.67 | 7.33 |
| 1.41H&V | −0.56 | 5.99 | −0.91 | 4.89 |
| 10.65H&V | −3.70 | 14.71 | −3.82 | 13.30 |
| 23.8H&V | 2.88 | 11.74 | 4.62 | 9.67 |
| 36.5H&V | −1.04 | 9.88 | −2.49 | 9.19 |
| 90H&V | 0.22 | 9.04 | 1.25 | 8.35 |
| H-Pol | 0.55 | 12.06 | 0.27 | 11.33 |
| V-Pol | −0.94 | 10.29 | 0.14 | 9.08 |
| All | −0.20 | 11.23 | 0.21 | 10.26 |

frequency as confirmed by Fig. 6a and b. The sensitivity to surface roughness in V-Pol is very similar for low *SM* values (Fig. 6c) and high *SM* values (Fig. 6d) which indicates that the sensitivity to $\sigma$ in V-Pol does not depend on *SM* for the WM99fd model.

## 4. Discussion

In this section, the results highlighted in the previous section are discussed in more details.

### 4.1. Soil permittivity modelling

In this study, three permittivity models were used to model the Fresnel reflectivity of smooth bare soils. As shown in Table 2, the good agreement at lower frequencies (<11 GHz) between the modelled Fresnel reflectivity and the measured reflectivity of the smooth soils for the SMDM and GRMDM models was expected since the surface roughness has less impact at these frequencies and the very low surface roughness of sites 9 and 17 can be properly modelled by the Fresnel reflectivity. Also, both permittivity models were developed in frequency ranges (1–18 GHz for both models, see Mironov et al., 2013 for the GMRMD model and Dobson et al., 1985 for the SMDM model) including these frequencies. At higher frequencies (>23 GHz) the surface smoothness criterion of Mo and Schmugge (1987) may not apply and the surface reflectivity may not be properly modelled by the Fresnel reflectivity. Hence higher errors are observed in Table 2 for these frequencies for both these models. At higher frequencies, the soil reflectivity is more affected by the values of the downwelling sky $T_B$. Since no measurements of the atmospheric conditions were acquired during the PORTOS-93 campaign, it is difficult to accurately determine the downwelling sky contribution to the measured $T_B$ signal. There is an increased uncertainty on the measured reflectivity at higher frequencies especially at 23.8 GHz which is known to be used to monitor atmospheric water vapour (Kerr & Njoku, 1990).

### 4.2. Soil reflectivity modelling

Figs. 2 and 3 show that the measured reflectivity in H-Pol is highly correlated to the reflectivity in V-Pol which shows the pertinence of a model based on a relationship such as Eq. (5) (WM99 model) to model the polarisation ratio. This suggests that the number of parameters to determine in the QHN model could be reduced since there would not be a need to determine a series of $Q_R$, $H_R$ and $N_R$ parameters for each polarisation as suggested by Goodberlet et al. (2012). Nonetheless, at higher incidence ($\geq 30°$), there is more variability due to the stronger polarisation difference and higher sensitivity of the measured signal to the soil properties increasing the measurement noise.

### 4.3. $T_B$ modelling

As shown in Figs. 4 and 5, both the WM99 and QHN models have similar accuracies to simulate the soil $T_B$. Since no significant improvement could be seen between the QHNfd and QHNfi schemes, there is no need to use the QHNfd scheme since it requires a set of parameters for each frequency, a total of 30 parameters, with no significant added value. The results for the QHNfd models in Table 4 show that the parameters of Eq. (6) are very similar for each frequency suggesting that Eq. (6) is almost frequency independent. Nonetheless, this relationship

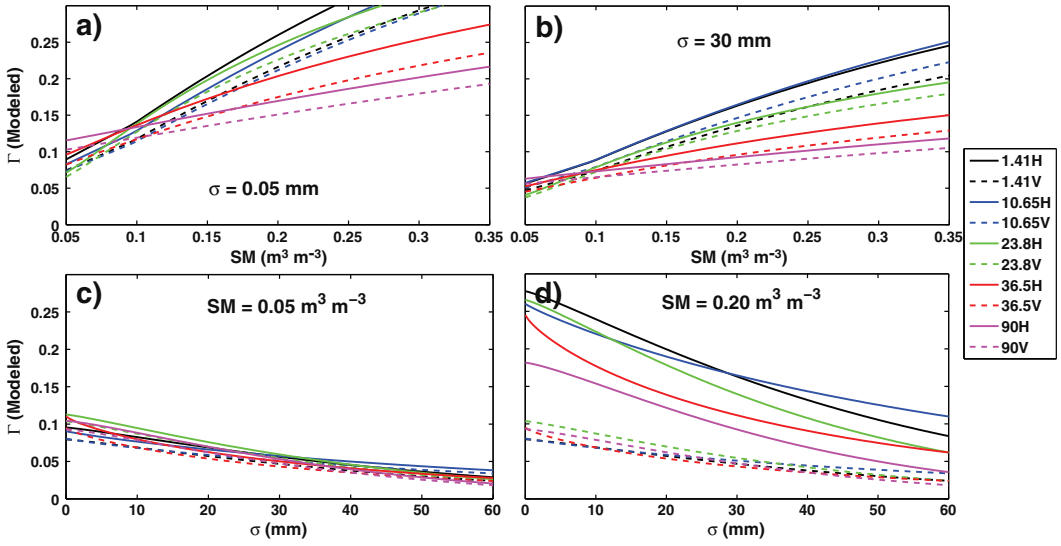


**Fig. 6.** Modelled reflectivity using the WM99fde formulation at H-Pol (solid line) and V-Pol (dashed line) at 1.41 (black), 10.65 (blue), 23.8 (green), 36.5 (red) and 90 GHz (magenta) as a function of a) soil moisture (*SM*) for a low soil surface roughness ($\sigma$), b) *SM* for a high $\sigma$ value, c) $\sigma$ for a low *SM* value and d) $\sigma$ for a high *SM* value. $\theta = 20$ ° and $T_{soil} = 300$ K for all simulations. (For interpretation of the references to colour in this figure legend, the reader is referred to the web version of this article.)

might be site dependent and should be evaluated over other sites before it can be used operationally.

To obtain the accuracy of the QHNfi model with the WM99 model, there is a need to determine a set of parameters for each frequency (20 parameters total). The number of parameters can be reduced to 17 since, as shown by Table 3 and Fig. 3, two $\beta$ values can simulate the polarisation ratio without loss in accuracy.

With a good precision and fewer parameters to determine for all frequencies, the QHN model seems to be a better model for operational implementation. Its frequency independence properties make it simpler than the WM99 model adapted to each frequency for a total of 17 to 20 parameters.

## 5. Conclusion

The objective of this study was to evaluate two soil reflectivity models using the unique multi-angular and multi-frequency PORTOS-93 bare soil measurements and to obtain a simple and accurate surface reflectivity model to simulate the brightness temperature ($T_B$). Considering the $T_B$ measurements at H-Pol at 1.41, 10.65, 23.8, 36.5 and 90 GHz over smooth soil surfaces, it was found that the GRMDM model (Mironov et al., 2009) is more accurate to simulate the soil permittivity than the SMDM model (Dobson et al., 1985) at lower frequencies (<11 GHz). It was shown that both permittivity models still need improvement at higher frequencies (>23 GHz) and that the empirical permittivity WM80 model (Wang & Schmugge, 1980) tuned by Calvet, Wigneron, Chanzy, and Haboudane (1995) was more accurate at these frequencies. Also, the high correlation between the measured reflectivities at H and V polarisations shows that it is simpler to simulate the V-Pol reflectivity based on the simulated H-Pol reflectivity as opposed to simulating both polarisations separately.

With a least square error minimization algorithm, we computed optimized parameters of the WM99 and QHN models for each frequency channel of the PORTOS-93 database. We found that there was no major improvement to model the reflectivity considering each frequency independently for the QHN model but there were some strong improvements for the WM99 model. Nonetheless, even if it was shown that both models have similar accuracies with biases and standard deviations of $0.26 \pm 10.46$ K and $-0.20 \pm 11.23$ K for the QHNfi and WM99fd models respectively, the QHN model was found more suitable for operational use with fewer parameters to optimize and its frequency independent behaviour.

Covering a large range of frequencies, from 1.41 to 90 GHz, and soil conditions (in terms of moisture content, temperature, surface roughness), the results are based on a unique soil type (a silty clay loam, see Wigneron et al., 2001). Other experimental datasets (from in situ or airborne measurements) are needed to fully validate the results obtained in this study over a larger range of soil types.

## Acknowledgements

The authors would like to thank Dr. Alexandre Roy for his helpful discussion which contributed to this paper. We also acknowledge the contribution of the National Sciences and Engineering Research Council of Canada for their funding, and INRA for the POSTOS-93 database.

## References

Asmus, K., & Grant, C. (1999). Surface based radiometer (SBR) data acquisition system. *International Journal of Remote Sensing, 20*, 3125–3129.

Brown, M., Escobar, V., Moran, S., Entekhabi, D., O'Neill, P., Njoku, E., Doorn, B., & Entin, J. (2013). NASA's soil moisture active passive (SMAP) mission and opportunities for applications users. *Bulletin of the American Meteorological Society, 94*, 1125–1128.

Calvet, J., Wigneron, J., Chanzy, A., & Haboudane, D. (1995). Retrieval of surface parameters from microwave radiometry over open canopies at high frequencies. *Remote Sensing of Environment, 53*, 46–60.

Calvet, J. -C., Wigneron, J. -P., Chanzy, A., Raju, S., & Laguerre, L. (1995). Microwave dielectric properties of a silt–loam at high frequencies. *IEEE Transactions on Geoscience and Remote Sensing, 33*, 634–642.

Calvet, J. -C., Wigneron, J. -P., Walker, J., Karbou, F., Chanzy, A., & Albergel, C. (2011). Sensitivity of passive microwave observations to soil moisture and vegetation water content: L-band to W-band. *IEEE Transactions on Geoscience and Remote Sensing, 49*, 1190–1199.

Dee, D. P., Uppala, S. M., Simmons, A. J., Berrisford, P., Poli, P., Kobayashi, S., Andrae, U., Balmaseda, M. A., Balsamo, G., Bauer, P., Bechtold, P., Beljaars, A. C. M., van de Berg, L., Bidlot, J., Bormann, N., Delsol, C., Dragani, R., Fuentes, M., Geer, A. J., Haimberger, L., Healy, S. B., Hersbach, H., Hólm, E. V., Isaksen, L., Kållberg, P., Köhler, M., Matricardi, M., McNally, A. P., Monge-Sanz, B. M., Morcrette, J. -J., Park, B. -K., Peubey, C., de Rosnay, P., Tavolato, C., Thépaut, J. -N., & Vitart, F. (2011). The ERA-Interim reanalysis: configuration and performance of the data assimilation system. *Quarterly Journal of the Royal Meteorological Society, 137*, 553–597. http://dx.doi.org/10.1002/qj.828.

de Rosnay, P., Calvet, J. -C., Kerr, Y., Wigneron, J. -P., Lemaître, F., Escorihuela, M., Sabater, J., Saleh, K., Barrié, J., Bouhours, G., Coret, L., Cherel, G., Dedieu, G., Durbe, R., Fritz, N., Froissard, F., Hoedjes, J., Kruszewski, A., Lavenu, F., Suquia, D., & Waldteufel, P. (2006). SMOSREX: A long term field campaign experiment for soil moisture and land surface processes remote sensing. *Remote Sensing of Environment, 102*, 377–389.

Dobson, M. C., Ulaby, F. T., Hallikainen, M. T., & El-Rayes, M. A. (1985). Microwave dielectric behavior of wet soil — Part II: Dielectric mixing models. *IEEE Transactions on Geoscience and Remote Sensing, GE-23*, 35–46.

Escorihuela, M., Kerr, Y., De Rosnay, P., Wigneron, J. -P., Calvet, J. -C., & Lemaître, F. (2007). A simple model of the bare soil microwave emission at L-band. *IEEE Transactions on Geoscience and Remote Sensing, 45*, 1978–1987.

Goodberlet, M., & Mead, J. (2012). Improved models of soil emission for use in remote sensing of soil moisture. *IEEE Transactions on Geoscience and Remote Sensing, 50*, 991–3999.

Goodberlet, M. A., & Mead, J. B. (2014). A model of surface roughness for use in passive remote sensing of bare soil moisture. *IEEE Transactions on Geoscience and Remote Sensing, 52*(9), 5498–5505.

Jackson, T., Bindlish, R., Gasiewski, A., Stankov, B., Klein, M., Njoku, E., Bosch, D., Coleman, T., Laymon, C., & Starks, P. (2005). Polarimetric scanning radiometer C- and X-band microwave observations during SMEX03. *IEEE Transactions on Geoscience and Remote Sensing, 43*, 2418–2429.

Jackson, T. J., Cosh, M. H., Bindlish, R. P. J., Bosch, D., Seyfried, M., Goodrich, D. C., Moran, M. S., & Du, J. Y. (2010). Validation of advanced microwave scanning radiometer soil moisture products. *IEEE Transactions on Geoscience and Remote Sensing, 48*(12), 4256–4272.

Kerr, Y. H., & Njoku, E. G. (1990). Semiempirical model for interpreting microwave emission from semiarid land surfaces as seen from space. *IEEE Transactions on Geoscience and Remote Sensing, 28*, 384–393.

Kerr, Y., Waldteufel, P., Wigneron, J. -P., Martinuzzi, J. -M., Font, J., & Berger, M. (2001). Soil moisture retrieval from space: The soil moisture and ocean salinity (SMOS) mission. *IEEE Transactions on Geoscience and Remote Sensing, 39*, 1729–1735.

Lawrence, H., Wigneron, J. -P., Demontoux, F., Mialon, A., & Kerr, Y. H. (2013). Evaluating the semiempirical H–Q model used to calculate the L-band emissivity of a rough bare soil. *IEEE Transactions on Geoscience and Remote Sensing, 51*(7), 4075–4084.

Magagi, R., Berg, A., Goita, K., Belair, S., Jackson, T., Toth, B., Walker, A., McNairn, H., O'Neill, P., Moghaddam, M., Gherboudj, I., Colliander, A., Cosh, M., Burgin, M., Fisher, J., Kim, S. -B., Mladenova, I., Djamai, N., Rousseau, L. -P., Belanger, J., Shang, J., & Merzouki, A. (2013). Canadian experiment for soil moisture in 2010 (CanEx-SM10): Overview and preliminary results. *IEEE Transactions on Geoscience and Remote Sensing, 51*, 347–363.

Marquardt, D. (1963). An algorithm for least-squares estimation of nonlinear parameters. *SIAM Journal of Applied Mathematics, 11*, 431–441.

Mätzler, C. (2006). *Thermal microwave radiation: Applications for remote sensing*. Institution of Engineering and Technology.

Mialon, A., Richaume, P., Leroux, D., Bircher, S., Al, Bitar A., Pellarin, T., Wigneron, J. -P., & Kerr, Y. (2014). Comparison of Dobson and Mironov dielectric models in the SMOS soil moisture retrieval algorithm. *IEEE Transactions on Geoscience and Remote Sensing*. http://dx.doi.org/10.1109/TGRS.2014.2368585.

Mironov, V., Kerr, Y., Wigneron, J. -P., Kosolapova, L., & Demontoux, F. (2013). Temperature and texture dependent dielectric model for moist soils at 1.4 GHz. *IEEE Geoscience and Remote Sensing Letters, 10*(3), 419–423.

Mironov, V., Kosolapova, L., & Fomin, S. (2009). Physically and mineralogically based spectroscopic dielectric model for moist soils. *IEEE Transactions on Geoscience and Remote Sensing, 47*, 2059–2070.

Mo, T., & Schmugge, T. J. (1987). Parameterization of the effect of surface roughness on microwave emission. *IEEE Transactions on Geoscience and Remote Sensing, GE-25*, 481–486.

Njoku, E., & Entekhabi, D. (1996). Passive microwave remote sensing of soil moisture. *Journal of Hydrology, 184*, 101–129.

Njoku, E. G., Jackson, T., Lakshmi, V., Chan, T., & Nghiem, S. (2003). Soil moisture retrieval from AMSR-E. *IEEE Geoscience and Remote Sensing Letters, 41*(2), 215–229.

Panciera, R., Walker, J., Jackson, T., Gray, D., Tanase, M., Ryu, D., Monerris, A., Yardley, H., Rüdiger, C., Wu, X., Gao, Y., & Hacker, J. (2014). The soil moisture active passive experiments (SMAPEx): Toward soil moisture retrieval from the SMAP mission. *IEEE Transactions on Geoscience and Remote Sensing, 52*, 490–507.

Pellarin, T., Kerr, Y., & Wigneron, J. -P. (2006). Global simulation of brightness temperatures at 6.6 and 10.7 GHz over land based on SMMR data set analysis. *IEEE Transactions on Geoscience and Remote Sensing, 44*, 2492–2505.

Prigent, C., Wigneron, J. -P., Rossow, W. B., & Pardo-Carrion, J. R. (2000). Frequency and angular variations of land surface microwave emissivities: Can we estimate SSM/T and AMSU emissivities from SSM/I emissivities? *IEEE Transactions on Geoscience and Remote Sensing, 38*, 2373–2386.

Rautiainen, K., Lemmetyinen, J., Pulliainen, J., Vehvilainen, J., Drusch, M., Kontu, A., Kainulainen, J., & Seppänen, J. (2012). L-band radiometer observations of soil processes in boreal and subarctic environments. *IEEE Transactions on Geoscience and Remote Sensing, 50*, 1483–1497.

Roy, A., Royer, A., Wigneron, J. -P., Langlois, A., Bergeron, J., & Cliche, P. (2012). A simple parameterization for a boreal forest radiative transfer model at microwave frequencies. *Remote Sensing of Environment, 124*, 371–383.

Schwank, M., Völksch, I., Wigneron, J. -P., Kerr, Y., Mialon, A., De Rosnay, P., & Mätzler, C. (2010). Comparison of two bare-soil reflectivity models and validation with L-band radiometer measurements. *IEEE Transactions on Geoscience and Remote Sensing, 48*, 325–337.

Shi, J., Chen, K., Li, Q., Jackson, T., O'Neill, P., & Tsang, L. G. (2002). A parameterized surface reflectivity model and estimation of bare-surface soil moisture with L-band radiometer. *IEEE Transactions on Geoscience and Remote Sensing, 40*, 2674–2686.

Shibata, A., Imaoka, K., & Koike, T. (2003). AMSR/AMSR-E level 2 and 3 algorithm developments and data validation plans of NASDA. *IEEE Transactions on Geoscience and Remote Sensing, 41*(2), 195–203.

Tsang, L., & Kong, J. (1977). Thermal microwave emission from a random inhomogeneous layer over a homogeneous medium using the method of invariant imbedding. *Radio Science, 12*, 185–194.

Wang, J. R., & Choudhury, B. (1981). Remote sensing of soil moisture content over bare field at 1.4 GHz frequency. *Journal of Geophysical Research, 86*, 5277–5282.

Wang, J. R., O'Neill, E., Jackson, T. J., & Engman, E. T. (1983). Multifrequency measurements of the effects of soil moisture, soil texture, and surface roughness. *IEEE Transactions on Geoscience and Remote Sensing, GE21*, 44–51.

Wang, J. R., & Schmugge, T. J. (1980). Empirical model for the complex dielectric permittivity of soils as a function of water content. *IEEE Transactions on Geoscience and Remote Sensing, GE-18*, 288–295.

Wegmüller, U., & Mätzler, C. (1999). Rough bare soil reflectivity model. *IEEE Transactions on Geoscience and Remote Sensing, 37*, 1391–1395.

Wigneron, J. -P., Calvet, J. -C., Pellarin, T., Van de Griend, A., Berger, M., & Ferrazzoli, P. (2003). Retrieving near surface soil moisture from microwave radiometric observations: Current status and future plans. *Remote Sensing of Environment, 85*, 489–506.

Wigneron, J. -P., Chanzy, A., Kerr, Y., Lawrence, H., Shi, J., Escorihuela, M., Mironov, V., Mialon, A., Demontoux, F., De Rosnay, P., & Saleh-Contell, K. (2011). Evaluating an improved parameterization of the soil emission in L-MEB. *IEEE Transactions on Geoscience and Remote Sensing, 49*, 1177–1189.

Wigneron, J. -P., Kerr, Y., Waldteufel, P., Saleh, K., Escorihuela, M. -J., Richaume, P., Ferrazzoli, P., de Rosnay, P., Gurney, R., Calvet, J. -C., Grant, J. P., Guglielmetti, M., Hornbuckle, B., Mätzler, C., Pellarin, T., & Schwank, M. (2007). L-band microwave emission of the biosphere (L-MEB) model: Description and calibration against experimental data sets over crop fields. *Remote Sensing of Environment, 107*, 639–655.

Wigneron, J. -P., Laguerre, L., & Kerr, Y. (2001). A simple parameterization of the L-band microwave emission from rough agricultural soils. *IEEE Transactions on Geoscience and Remote Sensing, 39*, 1697–1707.

Wigneron, J. -P., Schwank, M., Lopez Baeza, E., Kerr, Y. H., Novello, N., Millan, C., Moisy, C., Richaume, P., Mialon, A., Al Bitar, A., Cabot, F., Lawrence, H., Guyon, D., Calvet, J. -C., Grant, J. P., Casal, T., de Rosnay, P., Saleh, K., Mahmoodi, A., Delwart, S., & Mecklenburg, S. (2012). First evaluation of the SMOS observations over the VAS site in the Mediterranean region. *Remote Sensing of Environment, 124*, 26–37.

# B Annexe : Autres collaborations scientifiques en tant que co-auteur

Dans cette annexe, les travaux connexes à ceux présentés dans cette thèse sont présentés. Les contributions faites dans le cadre de la thèse sont aussi spécifiées.

## B.1 Article : Coupling the snow thermodynamic model SNOWPACK with the microwave emission model of layered snowpacks for subarctic and arctic snow water equivalent retrievals

En 2011, le professeur Alexandre Langlois a publié un article présentant les résultats du couplage de MEMLS avec le modèles thermodynamique de neige SNOWPACK pour évaluer l'ÉEN. Il a été démontré dans ce travail que le couplage de ces deux modèles pour minimiser l'erreur de la taille des grains de neige sur la simulation de la $T_B$ MOP permet d'améliorer l'estimation de l'ÉEN. Ce travail cadre avec les travaux de cette thèse puisqu'il tente d'améliorer les simulations de la $T_B$ en couplant différents modèles de neige losrque des données in-situ ne sont pas disponibles. Pour ce travail, le traitement des données de taille des grains de neige ainsi que la révision de l'article par des échanges et discussions entre les co-auteurs ont été effectué dans le cadre de cette thèse.

# Coupling the snow thermodynamic model SNOWPACK with the microwave emission model of layered snowpacks for subarctic and arctic snow water equivalent retrievals

A. Langlois,[1] A. Royer,[1] C. Derksen,[2] B. Montpetit,[1] F. Dupont,[3] and K. Goïta[1]

Received 14 March 2012; revised 6 November 2012; accepted 7 November 2012; published 20 December 2012.

[1] Satellite-passive microwave remote sensing has been extensively used to estimate snow water equivalent (SWE) in northern regions. Although passive microwave sensors operate independent of solar illumination and the lower frequencies are independent of atmospheric conditions, the coarse spatial resolution introduces uncertainties to SWE retrievals due to the surface heterogeneity within individual pixels. In this article, we investigate the coupling of a thermodynamic multilayered snow model with a passive microwave emission model. Results show that the snow model itself provides poor SWE simulations when compared to field measurements from two major field campaigns. Coupling the snow and microwave emission models with successive iterations to correct the influence of snow grain size and density significantly improves SWE simulations. This method was further validated using an additional independent data set, which also showed significant improvement using the two-step iteration method compared to standalone simulations with the snow model.

**Citation:** Langlois, A., A. Royer, C. Derksen, B. Montpetit, F. Dupont, and K. Goïta (2012), Coupling the snow thermodynamic model SNOWPACK with the microwave emission model of layered snowpacks for subarctic and arctic snow water equivalent retrievals, *Water Resour. Res.*, *48*, W12524, doi:10.1029/2012WR012133.

## 1. Introduction

[2] Seasonal snow cover plays an important role in the surface energy balance [e.g., *Male and Granger*, 1981; *Arons and Colbeck*, 1995; *Gustafsson et al.*, 2001] through its high albedo, low thermal conductivity, and diffusivity [e.g., *Li and Zhou*, 2001; *Albert*, 2002; *Lemke et al.*, 2007]. Furthermore, snow is a key hydrological variable, acting as an important freshwater reservoir [e.g., *Barnett et al.*, 2005], necessary for the health of ecosystems and energy production (e.g., hydroelectricity). Variability in snow melt and snow melt timing has major implications for permafrost regimes [*Romanovsky et al.*, 2010] and associated geochemical cycling.

[3] Large uncertainties remain with regard to the effect of snow on climatological cooling and heating patterns [*Fletcher et al.*, 2009]. Furthermore, the lack of proper snow depth and snow water equivalent (SWE) information within global circulation models lead to uncertainties in climate predictions [*Essery*, 1998; *Brown et al.*, 2003; *Hardiman et al.*, 2008; *Dutra et al.*, 2010]. The uncertainties are larger in northern latitudes where the observed warming is strongest [i.e., *Kaufman et al.*, 2009] due to a lack of in situ snow and meteorological observations used to drive the models. A realistic representation of snow (e.g., SWE) is therefore imperative to make reliable projections about the response of the northern environment to a warming climate. This was addressed in numerous studies using various remote sensing methods to monitor snow cover extent using visible-near infrared remote sensing [e.g., *Hall et al.*, 1995; *Maurer et al.*, 2003; *Salomonson and Appel*, 2004; *Frei and Lee*, 2010]. However, those methods do not allow the retrieval of SWE, a crucial parameter related to cryospheric energy and water budgets. The use of spaceborne passive microwave measurements has proven to be a useful tool in determining SWE over land [e.g., *Chang et al.*, 1982; *Foster et al.*, 1997; *Pulliainen and Hallikainen*, 2001; *Derksen et al.*, 2005, 2010] and sea ice [e.g., *Markus and Cavalieri*, 2000; *Langlois et al.*, 2007, 2010a], but the satellite sensor coarse spatial resolution ($\sim$625 km$^2$) combined with high spatial variability of snow and vegetation properties [e.g., *Foster et al.*, 2005; *Langlois et al.*, 2011] introduces random and systematic uncertainties that can produce high error values for retrieval methods that rely solely on passive microwave measurements.

[4] Recently, multilayered thermodynamic snow models such as SNOWPACK [*Bartelt and Lehning*, 2002] have demonstrated potential in SWE predictions [e.g., *Langlois et al.*, 2009]. The coupling of such models with climatological

[1]Centre d'Applications et de Recherches en Télédétection, Université de Sherbrooke, Sherbrooke, Québec, Canada.
[2]Climate Research Division, Environment Canada, Toronto, Ontario, Canada.
[3]Laboratoire de Glaciologie et Géophysique de l'Environnement (LGGE) UMR 5183, UJF—Grenoble 1/CNRS, Grenoble, France.

Corresponding author: A. Langlois, Département de Géomatique Appliquée, Centre d'Applications et de Recherches en Télédétection (CARTEL), Université de Sherbrooke, Office A4-280, Sherbrooke, Québec J1K 2R1, Canada. (a.langlois2@usherbrooke.ca)

©2012. American Geophysical Union. All Rights Reserved.
0043-1397/12/2012WR012133

reanalysis data such as the North American Regional Reanalysis (NARR) showed reasonable SWE predictions in northeastern Canada, and the use of reanalysis data to drive snow models can address the spatial limitations of driving the model with meteorological observations, given the sparse spatial coverage of stations across Canada (about 25 stations per 100,000 km$^2$; *Metcalfe and Goodison* [1993]). Modeled snow information coupled with passive microwave radiative transfer models such as the microwave emission model of layered snowpacks (MEMLS) [*Wiesmann and Mätzler*, 1999] could further improve our understanding of retrieval accuracy and hence regional SWE variability.

[5] Recent work using passive microwave data has shown potential in retrieving SWE [*Andreadis and Lettenmaier*, 2006; *Pulliainen*, 2006; *Pardé et al.*, 2007; *Durand and Margulis*, 2007; *Touré et al.*, 2011; *Takala et al.*, 2011]. However, most iteration procedures using passive microwave data are conducted solely on SWE, while large uncertainties still remain with regard to snow grain size parameterization. Grain size is by far the most significant variable affecting radiative transfer in the microwave models and yet is ignored or simply treated in recent studies. Those large uncertainties could lead to bias in SWE retrievals such as systematic overestimation or underestimation, by compensating for errors due to poor snow grain parameterization through SWE. Thus, it becomes necessary to assess the retrieval of snow grain size information in current models, which is hampered by a lack of field measurements arising from sampling constraints. Some of the literature suggests that "grain size" is poorly defined and measured with repeatability problems [e.g., *Domine et al.*, 2006]. Since the morphology is extremely variable and can change in a matter of hours [e.g., *Colbeck*, 1983; *Arons and Colbeck*, 1995; *Domine et al.*, 2008; *Langlois et al.*, 2008], validation of such models with accurate field measurements is yet to be done. Of particular relevance, most SWE algorithms make use of passive microwave radiative transfer principles, where large uncertainties are related to the poor definition of snow grain size profiles [e.g., *Grenfell and Warren*, 1999; *Mätzler and Wiesmann*, 1999; *Roy et al.*, 2004; *Foster et al.*, 2005]. In fact, it was shown using various radiative transfer models such as MEMLS [*Durand et al.*, 2008; *Langlois et al.*, 2010a], Helsinki University of Technology [*Butt and Kelly*, 2008; *Kontu and Pulliainen*, 2010; *Derksen et al.*, 2012a], and Dense Media Radiative Transfer (DMRT) [*Tedesco and Kim*, 2006; *Grody*, 2008; *Brucker et al.*, 2010] that simulated $T_b$ are very sensitive to snow grain size, and yet this variable is poorly characterized. Promising results from various methods show that near-infrared reflectance can be linked to specific surface area of snow grains [*Matzl and Schneebeli*, 2006; *Domine* et al., 2006; *Picard et al.*, 2010; *Langlois et al.*, 2010b]. Results from those methods, along with the coupling of a snow and microwave emission model, would allow an improved assessment of the snow grain information from snow model, with related uncertainties, and a more accurate retrieval of snow variables such as SWE.

[6] While satellite microwave brightness temperatures exhibit strong sensitivity to the scattering properties of terrestrial snow, SWE retrieval solutions based solely on empirical relationships between microwave brightness temperature and SWE still perform poorly. Data iteration approaches, however, that can include a physical snowpack model coupled with a radiative transfer scheme are a possible solution [*Durand et al.*, 2008]. With this goal in mind, the present study evaluates the feasibility of driving a physical snowpack model (SNOWPACK) with the NARR, the outputs of which will be coupled with the MEMLS. The model SNOWPACK is appropriate, since it produces detailed snowpack information far beyond bulk properties like density, depth, and SWE. Radiometric models require stratigraphy and grain size information that are produced by this model. Hence, our main objective is to reduce the uncertainties in SWE simulated by snow models by incorporating passive microwave observations within an iterative scheme (i.e., iteration until error is minimized), which is completely independent from field measurements. Specifically, we want to (a) couple the thermodynamic multilayer snow model (SNOWPACK) to MEMLS, (b) quantify and correct the uncertainty related to poor snow grain information initially predicted by SNOWPACK, and (c) to correct modeled SWE from SNOWPACK-MEMLS and measured in situ/airborne brightness temperature data.

## 2. Data and Methods

### 2.1. International Polar Year and Cold Regions Hydrology High-Resolution Observatory Field Campaigns

[7] Data for this study were collected during two intensive Canadian field campaigns, namely the Canadian International Polar Year (IPY) project "Variability and Change in the Canadian Cryosphere," which took place in northern Québec in February of 2008, and the Canadian Cold Regions Hydrology High-resolution Observatory (CoReH2O) Snow and Ice Experiment throughout the winter 2009–2010 in Churchill (CH), Manitoba.

[8] The IPY intensive field campaign took place in February 2008 and included four high-resolution sampling sites located at Sept-Îles (SI—boreal: 50.3N–66.3W), Schefferville (SC—taiga: 54.8N–66.7W), Kuujjuaq (KU—taiga and tundra: 58.1N–68.6W), and Puvirnituq (POV—open tundra: 59.8N–76.4W), and five flight lines for airborne measurements (Figure 1). At the high-resolution sampling sites, snow and vegetation properties were measured every kilometer within a grid of 8 km × 16 km. Airborne passive microwave measurements along the flight lines were acquired from a Twin Otter equipped with radiometers at 19 and 37 GHz (both horizontal and vertical polarizations). A helicopter crew measured snow and vegetation properties every 40 km between SI and Kangirsuk (KG—open tundra). This ~2000 km transect spanned the transition in vegetation from dense boreal forest to open tundra (Figure 1). More details on the measurement campaign can be found in *Langlois et al.* [2010a, 2011].

[9] The CoReH2O campaign took place between November 2009 and May 2010 in CH, Manitoba [*Derksen et al.*, 2012b] (Figure 1), during which spatially intensive and temporally extensive observation periods were conducted. The data used in this article were collected during four intensive observation periods (IOPs) of 2–3 weeks in January (IOP 1), February (IOP 2), March (IOP 3), and April/May (IOP 4) 2010. Throughout these periods, sites were revisited to capture the temporal evolution of snow physical properties, and their impact on passive microwave

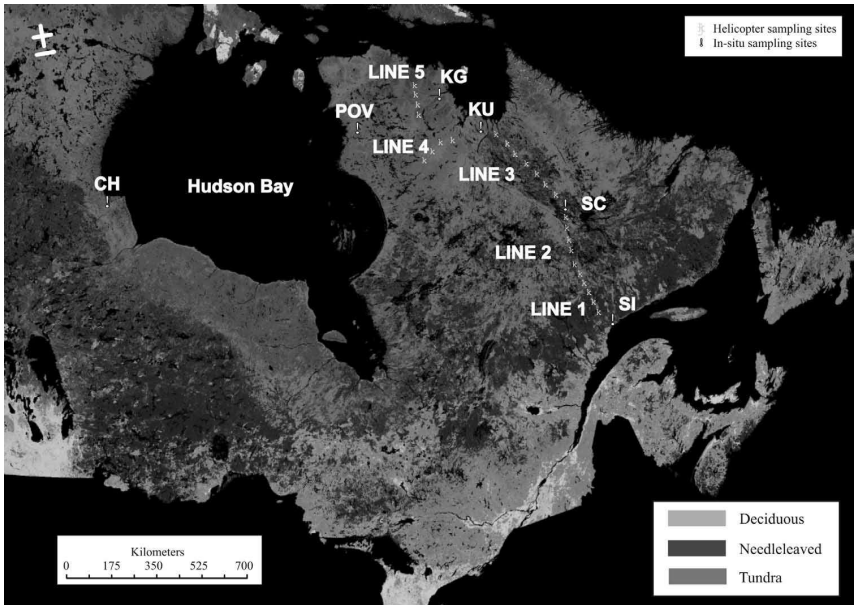


**Figure 1.** Location of the IPY and CoReH2O field campaign flight lines and sampling sites. The background map is derived from the MODIS land cover product with aggregated classes for clarity.

brightness temperatures measured with sled-based radiometers over various surfaces (clearing in a forested stand, dry/wet fen, and lake ice).

### 2.2. Snow Properties

[10] Snowpits were dug at each site such that direct solar illumination of the snow wall was avoided. Layered density profiles were obtained by extracting snow samples at 3 cm intervals from the surface to the snow/soil interface using a 192 $cm^3$ density cutter and weighed using a Pesola light series scale ($\pm$0.5 g). Bulk SWE and density were measured from a snow core at each site. Density was also determined from the product of measured layer density and thickness through each snowpit. Temperature profiles were measured at 3 cm intervals using a Traceable 2000 digital temperature probe ($\pm$0.1°C). The number of sampled sites is given in Table 1.

[11] Snow grain size, a critical parameter strongly affecting microwave snow emission [e.g., *Mätzler*, 1987], was measured (in CH only) using the shortwave InfraRed Integrating Sphere (IRIS) system, similar to the one developed by *Gallet et al.* [2009], which uses an integrating sphere (Labsphere®, 10cm diameter) mounted with two ports on the equator of the sphere at 0° and 90° and one port at the top. The first port located on the equator of the sphere is for the illumination source from a 1.3 μm laser with a 1 cm beam expander. The second port on the equator of the sphere is located in front of the laser and placed in front of the target (snow sample) and the third one at 90° is for an InGaAs photodiode detector. A diaphragm is put in front of the laser beam to measure the dark current and possible parasitic light coming into the sphere. Subtracting the dark current and parasitic light from the measured signal of the sample without the diaphragm allows the clean measurement of the signal reflected by the snow sample. The IRIS system is calibrated to albedo for each snowpit using reference Spectralon targets (0.06, 0.25, 0.59, 0.79, and 0.99 at 1300 nm), taking into account any possible shift in the laser illumination between every snowpit measurement. For more details on the IRIS system, please refer to *Montpetit et al.* [2011] or *Gallet et al.* [2010].

### 2.3. Moderate Resolution Imaging Spectroradiometer Vegetation Product and Passive Microwave Measurements

[12] Only vegetation-free (forest fraction, $F = 0$) airborne brightness temperatures were used in this study. To identify which sampling sites had available $T_b$ where $F = 0$, we used satellite-derived land cover type and forest fraction maps. The land cover type was determined from the Land Cover Map of Canada 2005, produced by the Canadian Center for Remote Sensing (Natural Resources Canada, Ottawa, Canada) [*Latifovic et al.*, 2004]. The data set encompasses land cover at 250 m spatial resolution, including water fraction. As for the vegetation fraction, values were extracted from the Moderate Resolution Imaging Spectroradiometer (MODIS) vegetation continuous fields available from the Global Land Cover Facility [*Hansen et al.*, 2002]. The vegetation continuous field collection

**Table 1.** Sampling Sites for the IPY and CoReH2O Campaigns Where $T_b$, Snow, and Vegetation Properties Data Are Available

| Data Set | Dominant Land Cover | Number of Sampling Sites |
|---|---|---|
| IPY | Dense boreal forest, taiga, and open tundra | 36 |
| CoReH2O | Taiga; open wetland | 16 |

contains proportional estimates for vegetative cover types gathered into three general classes: woody vegetation (forest), herbaceous vegetation, and bare ground.

[13] For the airborne passive microwave measurements, the radiometers were mounted on the National Research Council Twin Otter aircraft, which is described in detail by *Walker et al.* [2002]. The airborne radiometers were precalibrated and postcalibrated each flight using warm (ambient temperature microwave absorber) and cold (liquid nitrogen) targets as described by *Solheim* [1993] and *Asmus and Grant* [1999]. Uncertainty in the measurement of the calibration target temperature was estimated at $\pm 2$ K. The 19 and 37 GHz radiometers were calibrated simultaneously, so the same target temperature uncertainties for a given calibration apply to both frequencies. Estimates of intercalibration receiver drift were made by examining the preflight and postflight calibration target brightness temperatures. Radiometer stability depended on frequency, but overall uncertainty was estimated at $\pm 2$ K at 19 GHz and $<1$ K at 37 GHz. The aircraft flew over the high-resolution grids at an altitude of 914 m, while the sites sampled by helicopter access were flown at an altitude of 305 m. The ground field of view at 53° incidence angle was approximately 290 m $\times$ 490 m and 120 m $\times$ 200 m for the two altitudes, respectively. One should note that the sites used in this article (Table 1) showed no evidence of melt and contained no ice lenses. The presence of ice lenses complicates MEMLS simulations [*Rees et al.*, 2010], and thus sites where ice was present were removed from the data set. The surface-based measurements conducted in CH used the same set of radiometers mounted on a sled and pulled by a snowmobile. The radiometers were also precalibrated and postcalibrated using warm and cold targets everyday for the duration of the campaign [*Derksen et al.*, 2012b].

## 2.4. Models

### 2.4.1. SNOWPACK Simulations Driven by NARR

[14] Snow thermodynamic models require meteorological information as input, which are sparse in northern regions. Regional reanalysis data such as the NARR available (1979–present) from the Environmental Modeling Center, National Centers for Environmental Prediction, represent a good alternative and were used to drive SNOWPACK. The horizontal resolution is 0.3° (approximately 32 km) and the temporal resolution is eight times daily (every 3 h). To simulate snow cover evolution, the model requires, at each time step (set every 3 h), mean values of air (2-m) and surface temperatures (°C), relative humidity (%), wind speed ($\mathrm{m \cdot s^{-1}}$), incoming/reflected shortwave and incoming longwave radiation ($\mathrm{W \cdot m^{-2}}$), and cumulative precipitation over the 3 h period ($\mathrm{kg \cdot m^{-2}}$ or mm). A local validation of NARR can be found in *Langlois et al.* [2009], which found that basic meteorological parameters (temperature, humidity, radiation) are fairly well simulated in southern Québec and that promising results are found in northern regions such as KU and SC; however, further investigation is required with regard to precipitation. Thermophysical processes of interest in SWE studies such as phase change, water vapor transport (i.e., metamorphism), and loss (runoff, evaporation, and sublimation) are included within SNOWPACK. The details on the internal models will not be given here; they can be found elsewhere [*Lehning et al.*, 2002; *Bartelt and Lehning*, 2002].

[15] Model settings were specified, given the input data availability mentioned above. Two main types of output data can be visualized through user-friendly software, namely scalar and vector data [*Spreitzhofer et al.*, 2004]. The scalar data are related to individual layers of the snowpack such as the simulated vertical profiles of snow density, temperature, grain size, and shape, whereas vector data are attributed to snow cover evolution, such as depth and SWE. The amount of layers varies, given the number of precipitation events and the predicted snow depth. The transition between solid and liquid precipitation occurs at $+1.2$°C.

### 2.4.2. Microwave Emission Model of Layered Snowpacks

[16] The MEMLS can be used in the frequency range between 5 and 100 GHz [*Mätzler and Wiesmann*, 1999; *Wiesmann and Mätzler*, 1999]. The model is based on radiative transfer theory, which allows the scattering coefficient to be predicted from physical snow parameters and the absorption coefficient from dielectric properties of ice. Snow cover is considered as a series of horizontal layers ($L$) each characterized by thickness, reflectivity ($r_L$), emissivity ($e_L$), transmissivity ($t_L$), and temperature ($T_L$). The model automatically computes these parameters using snow information as input. To obtain accurate characterizations of $r_L$, $e_L$, and $t_L$, a six-flux three-dimensional approach is used within each layer. The horizontal fluxes represent radiation that is trapped in the snow cover and cannot exit at incidence angles ($\theta$) larger than the critical angle $\theta_c$. The vertical fluxes represent the radiation that escapes the snow cover at $\theta < \theta_c$. Further details on the radiation transfer theory used in MEMLS can be found in *Mätzler and Wiesmann* [1999] and *Wiesmann and Mätzler* [1999]. The primary input profile data are density ($\rho_s$), snow temperature ($T_s$), liquid water content ($W_s$), correlation length ($l_c$), vertical extent ($z_L$), physical ground temperature ($T_g$), and snow-ground interface reflectivity ($r_0$), which were derived through the NARR-SNOWPACK coupling and field observations. From these primary parameters, the dielectric properties (for dry and wet snow) as well as the absorption ($\gamma_a$) and scattering ($\gamma_s$) coefficients can be derived. The soil parameters in MEMLS were set using the soil reflectivity model of *Wegmüller and Mätzler* [1999].

### 2.4.3. Correction of Simulated Snow Grains

[17] The output of the SNOWPACK simulations driven by NARR were used as input to MEMLS. We kept the same number of layers as predicted by SNOWPACK (which were not constrained and so were different for each site, given the variability in the number of precipitation events and the predicted snow thickness), but the snow grain optical diameter values (from SNOWPACK, $d_{\mathrm{opt}}$) were replaced by correlation length values (requested in MEMLS, $l_c$) such that

$$l_c = \frac{2}{3} \cdot \left(1 - \frac{\rho_{\mathrm{snow}}}{\rho_{\mathrm{ice}}}\right) \cdot d_{\mathrm{opt}}, \tag{1}$$

where $\rho_{\mathrm{snow}}$ and $\rho_{\mathrm{ice}}$ are, respectively, snow and ice density in $\mathrm{kg \cdot m^{-3}}$ [*Mätzler*, 1992a]. Using the NARR forced snow information from SNOWPACK as input to MEMLS, a two-step iteration process for SWE retrieval was developed

such that simulated snow grain size was corrected using measured and simulated $T_b$ (first iteration) prior to retrieving SWE (second iteration), also using measured and simulated $T_b$ (Figure 2).

[18] By doing so, we avoid compensation through SWE for poor snow grain parameterization. We compared simulated and measured $T_b$ and applied a correction factor (multiplying factor $\varphi$, as depicted in Figure 2) on simulated correlation length ($l_c$) values until a minimum root-mean-square error (RMSE) was reached. It was demonstrated by *Lundy* [2000] that SNOWPACK is able to predict the trends in density with some degree of accuracy ($R^2$: 0.83, mean-square error: 66 kg·m$^{-3}$), but uncertainties are related to incorrect calculation of grain size and bond. Predicting the rate of grain growth during equilibrium and kinetic-growth metamorphism is a complex task, and the physics used by SNOWPACK have not been extensively validated due to the complexity of measuring snow grains properly (lack of reference data). Another possible problem lies in the assignment of the initial grain size of new snow, which is set constant (i.e., standard value). Since the model only allows grain growth, no grain sizes less than this initial value are ever predicted (which leads to systematic overestimation of grain size), leading to low $T_b$ simulations (i.e., through loss due to excessive scattering) and very large RMSE. Snow grain simulations from SNOWPACK [*Huang et al.*, 2012] or other multilayered snow thermodynamic models such as CROCUS were investigated in other studies [*Morin et al.*, 2012; *Brucker et al.*, 2010]. They outline the problem of different definitions of "grain size" and treatment of its growth, leading to the need for adjustment prior to be coupled with a snow emission model. Thus, before focusing on the objective of this study (i.e., retrieve SWE), it appears necessary to show whether the snow model overestimates or underestimates snow grain size when compared to available in situ measurements, using which this bias can be corrected with passive microwave measurements.

## 3. Results and Discussion

### 3.1. Snow Properties

[19] We selected sampling sites at which vegetation-free airborne brightness temperatures ($T_{b\text{-SNOW}}$) were available. At each site, SWE was measured and compared to NARR-SNOWPACK runs. Results are highlighted in Table 2 for both IPY and CoReH2O campaigns. The differences between measured and modeled SWE values are highly variable from one site to another, and the relationship between modeled and measured SWE is depicted in Figure 3.

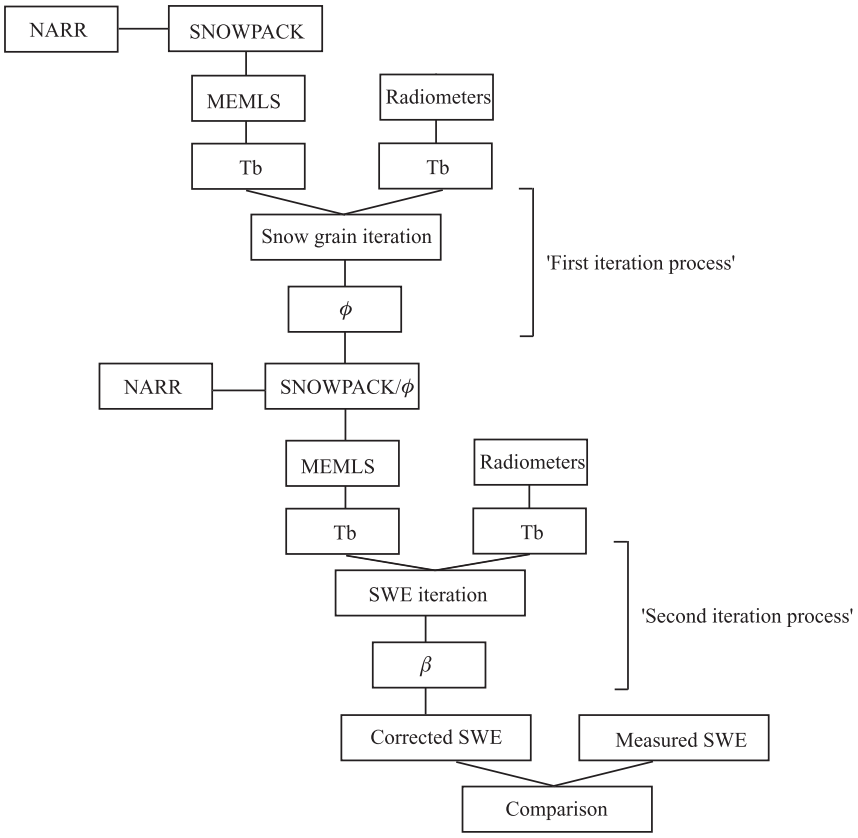


**Figure 2.** Two-step iteration method using measured and simulated brightness temperatures for predicted snow grain correction and SWE retrieval.

**Table 2.** Measured and Modeled SWE (NARR-SNOWPACK) for the IPY and CoReH2O Data Sets

| | | SWE (mm) | | | | | |
|---|---|---|---|---|---|---|---|
| | | Measured | | | SNOWPACK | | |
| Data Set | *n* Sites | Min. | Max. | Avg. | Min. | Max. | Avg. |
| IPY | 36 | 43.6 | 450.8 | 189.2 | 125.4 | 256.9 | 173 |
| CoReH2O | 16 | 56.6 | 334.2 | 154.2 | 81.5 | 146.7 | 112.7 |

[20] The initial SWE predictions from NARR-SNOWPACK (no passive microwave measurements considered) are quite poor with a slope of 0.23, a *y*-axis intercept (offset) of 108.9 mm of SWE, an RMSE of 79.4 mm, and a mean bias of 26.5 mm. Overall, SNOWPACK largely underestimates SWE, and improving on this result using an iterative scheme to retrieve SWE from measured and modeled passive microwave brightness temperatures is the main objective of this article. It would be difficult to identify the forcing process behind the large modeled underestimation compared to observations. The performance of SNOWPACK in predicting SWE can vary from one site to another and is different from year to year [*Langlois et al.*, 2009]. One of the potential explanations is that local precipitation gauge measurements are highly uncertain in remote northern locations, and systematic biases can be significant [*Yang et al.*, 1999]. Northern areas are usually open, and wind disturbance can be significant, leading to lower catch efficiencies by the gauges (i.e., lower measured precipitation), which, in turn, leads to systematically smaller precipitation values in NARR and hence SWE values in SNOWPACK. This is in agreement with *Langlois et al.* [2009] that found more accurate SWE simulations in southern Québec at a research station with proper maintenance and protected from wind disturbance. Because of its recent release, the strengths and weaknesses of NARR are largely undocumented [*Mesinger et al.*, 2006]. Although NARR provides much improved representation of precipitation when compared to other reanalysis products [*Bukovsky and Karoly*, 2007], *Mesinger* et al. [2006] identified some of the known weaknesses, including precipitation inaccuracies over Canada. Although it is hard to quantify the exact uncertainties in high latitude precipitation data, the work by *Langlois et al.* [2009] has shown reasonable NARR precipitation estimates over seasonal time scales in some areas. Furthermore, Figure 3 clearly shows important variability in measured SWE within one NARR pixel (i.e., one simulated SWE value by SNOWPACK). This variability is explained by different environments in which sampling occurred (fen, forest, open tundra). Hence, changing precipitations would only move the cluster up or down as shown in Figure 3, when clear improvement is needed on the slope. The SWE simulations need to be improved individually at each site (i.e., at the model level) rather than on precipitations that

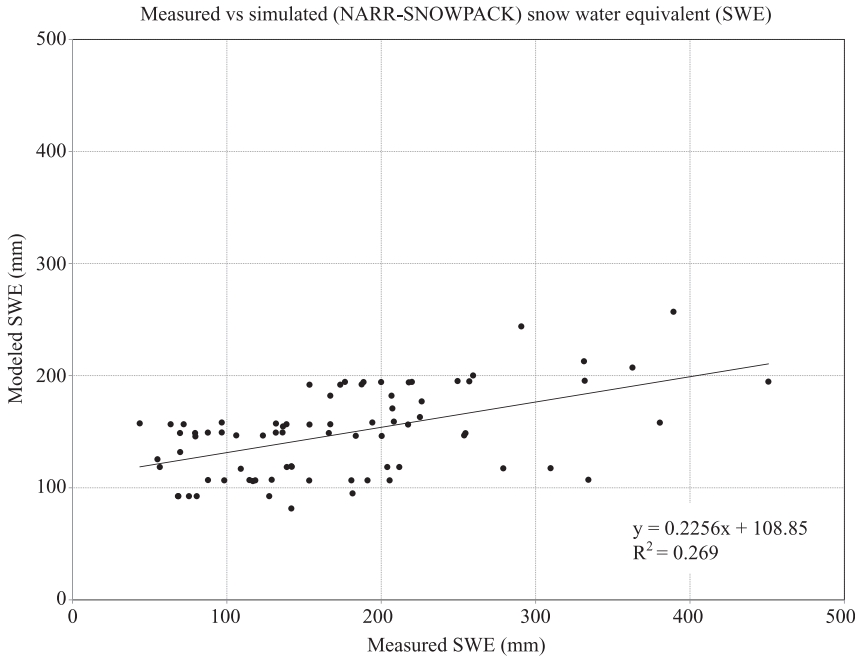


**Figure 3.** Comparison between initial modeled SWE values from NARR-SNOWPACK (without consideration of passive microwave measurements) and field-measured values.

would logically not improve the above results. Finally, the modeled density values from SNOWPACK are generally underestimated, where the underestimation increases with increasing thickness. This leads to larger underestimation in SWE for deep snow, as discussed in Figure 6. The new snow density is a function of air and surface temperatures (range −12°C to +2°C), wind speed, and relative humidity. The snow density estimations are based on statistical relationships from the Alps, and their applicability to other regions presented in this article needs further evaluation [*Lehning et al.*, 2002].

### 3.2. Simulated Snow Grain Size Correction

[21] The initial MEMLS $T_b$ with SNOWPACK-derived grain size (no correction) varied between 80 and 150 K, which are unrealistically low values for these conditions. The SNOWPACK $l_c$ values were initially predicted with an average of 0.82 mm, with values up to 1.9 mm. However, it was shown by *Wiesmann et al.* [1998] that typical snow has $l_c$ values ranging between 0.06 mm (new snow) and 0.25 mm (depth hoar), which are much lower than those simulated by SNOWPACK. Hence, the resulting scattering from overestimated $l_c$ values is significant when MEMLS is coupled directly to SNOWPACK.

[22] To address this issue, we coupled snowpit measurements (temperature, density, depth) with simulated (NARR-SNOWPACK) correlation length values and used the data as input to MEMLS to find an optimal scaling coefficient ($\varphi$), which provides the lowest RMSE values between simulated and measured $T_b$. Initial RMSE values (i.e., $\varphi = 1$, no correction on grain size) ranged between 136 and 170 K at 19 and 37 GHz (V and H pol.), as shown in Table 3. The minimum RMSE between simulated (using snowpit information and SNOWPACK $l_c$ predicted values) and measured $T_b$ was obtained with a $\varphi = 0.1$ at all frequencies and polarizations, which produced RMSE values of 7.8, 8.1, 26, and 26.8 K at 19V, 19H, 37V, and 37H, respectively (Table 3). The corrected $l_c$ values (SNOWPACK $l_c$ reduced by ∼90%) are closer to what was determined by *Wiesmann et al.* [1998]. Furthermore, the corrected $l_c$ values are in agreement with IRIS measurements conducted in CH (Table 4). The high sensitivity of the IRIS system to grain size under controlled illumination provides improved retrievals of snow grain size information [e.g., *Domine et al.*, 2006; *Montpetit et al.*, 2011]. The reason why IRIS was not used to determine the $\varphi$ is that the overarching goal is to be completely independent from field measurements (presented in the first iteration process; Figure 2). Nonetheless, $l_c$ values from Table 4 are well below the initial values simulated by SNOWPACK ($\varphi = 1$) but agree quite well with the corrected values using $\varphi = 0.1$ obtained through the $T_b$ iteration. This demonstrates just how important such a correction is, prior to any further iteration.

**Table 4.** Correlation Length Derived From IRIS Measurements in CH Compared to Scaled SNOWPACK $l_c$ Values

| | Correlation Length, $l_c$ (mm) | | |
|---|---|---|---|
| Method | Min. | Max. | Average |
| IRIS (197 measurements) | 0.017 | 0.306 | 0.161 |
| SNOWPACK $l_c$–$\varphi$ | 0.020 | 0.175 | 0.118 |

[23] Once the snow grain size information is corrected, the obtained RMSE in the SNOWPACK-MEMLS $T_b$ includes errors related to other snow properties, but primarily to the density because the dielectric constant is largely controlled by density in dry snow conditions [e.g., *Tiuri et al.*, 1984; *Hallikainen et al.*, 1986; *Mätzler*, 1987; *Huining et al.*, 1999]. Hence, some differences in SNOWPACK modeled density were found in the initial runs when compared against field measurements (density generally underestimated by SNOWPACK), which can explain some of the differences between modeled and measured SWE (Figure 3). Hence, these differences were addressed by a second modeling iteration to retrieve SWE (see the flowchart in Figure 2). Assimilating SWE values without prior correction of unrealistic grain size representation would produce heavily biased simulations, so the $\varphi$ correction factor was included in the SWE iteration. The use of simultaneous (two free variables: grain size and SWE) iteration method as proposed by *Pardé et al.* [2007] leads to larger errors than those proposed here. The successive iteration presented in this article (first snow grain size, then SWE) was already addressed in previous studies using spaceborne data [e.g., *Pulliainen*, 2006], but the results highlighted the difficulty of using such an iteration scheme in mixed pixels (i.e., given the low spatial resolution of passive microwave satellite data, many spatial features contribute to the signal). This constraint is well addressed in this article by using high spatial resolution airborne data with relatively homogeneous pixels.

### 3.3. SWE Retrievals Using Modeled and Airborne $T_b$ Iteration

#### 3.3.1. SWE Iteration Range

[24] Previous studies have shown that $T_b$ values at 37 GHz typically decrease, as the scattering volume (i.e., SWE) increases, which is the basis behind most SWE algorithms using the difference between 19 and 37 GHz, $\Delta T_b$ (a larger $\Delta T_b$ due to decreasing brightness temperatures at 37 GHz with increasing snow depth) [e.g., *Chang et al.*, 1982; *Mätzler*, 1987]. However, with large values of SWE, this scattering behavior is no longer evident because the 37 GHz

**Table 3.** Initial RMSE Values Between Measured and Modeled Brightness Temperatures and Associated Values After $\varphi$ Correction (Scaling Factor) on $l_c$ Values

| | | RMSE (K) | | | | | | | |
|---|---|---|---|---|---|---|---|---|---|
| | | 19V | | 19H | | 37V | | 37H | |
| Source | $\varphi$ | Initial | With $\varphi$ | Initial | With $\varphi$ | Initial | With $\varphi$ | Initial | With $\varphi$ |
| Snowpit-SNOWPACK | 0.1 | 169.7 | 7.8 | 154.9 | 8.1 | 146 | 26 | 136.2 | 26.8 |

brightness temperature increases with higher SWE due to emission from the snowpack itself that masks the large scattering from large depth hoar grains [e.g., *Rosenfeld and Grody*, 2000; *Dong et al.*, 2005] (Figure 4). This reversal from the "classical" $\Delta T_b$ pattern can cause ambiguity in SWE retrievals. Hence, to improve the accuracy of the SWE retrieval iteration, we limited consideration to cases where the effect mentioned above was not observed. By looking at the brightness temperature, we found that the reversal slope of the $T_b$ versus SWE relationship occurs at measured SWE values larger than 148 mm (up to a measured maximum of 290 mm). This corresponds to snow depths of 65–105 cm at an average density of 250 kg·m$^{-3}$. The 148 mm threshold was determined using the minimal $T_b$ values of a second-degree polynomial fit on averaged ranges of SWE with 25 mm increment (which did not show statistical significance).

[25] Obviously, the slope reversal depends upon snow physical properties (i.e., grain size; stratigraphic properties) and dielectric properties that are highly variable spatially and temporally. For instance, *Qiu et al.* [2011] demonstrated that this reversal can be highly dependent on snow grain size where the reversal occurs at relatively deeper snow with small snow grain size values. However, many differences exist between various studies. Most differences arise from the different polarizations (V versus H, with lower penetration depth for H-polarized $T_b$ causing an earlier reversal, as seen in Figure 4). Also, given the environment (boreal, taiga, tundra, sea ice, etc.), large differences in $T_b$ can be measured arising from highly variable dielectric properties, which are governed by density, temperature, and wetness. For instance, *Markus et al.* [2006] simulated a slope reversal using $\Delta T_{b19H\text{-}37H}$ at about 90 cm of snow depth (SWE of 245 mm for density of 250 kg·m$^{-3}$), whereas the limit is set at 50 cm (SWE of 140 mm for density of 250 kg·m$^{-3}$) in *Kelly et al.* [2003]. Using Special Sensor Microwave/Imager (SSM/I) data, *Rosenfeld and*

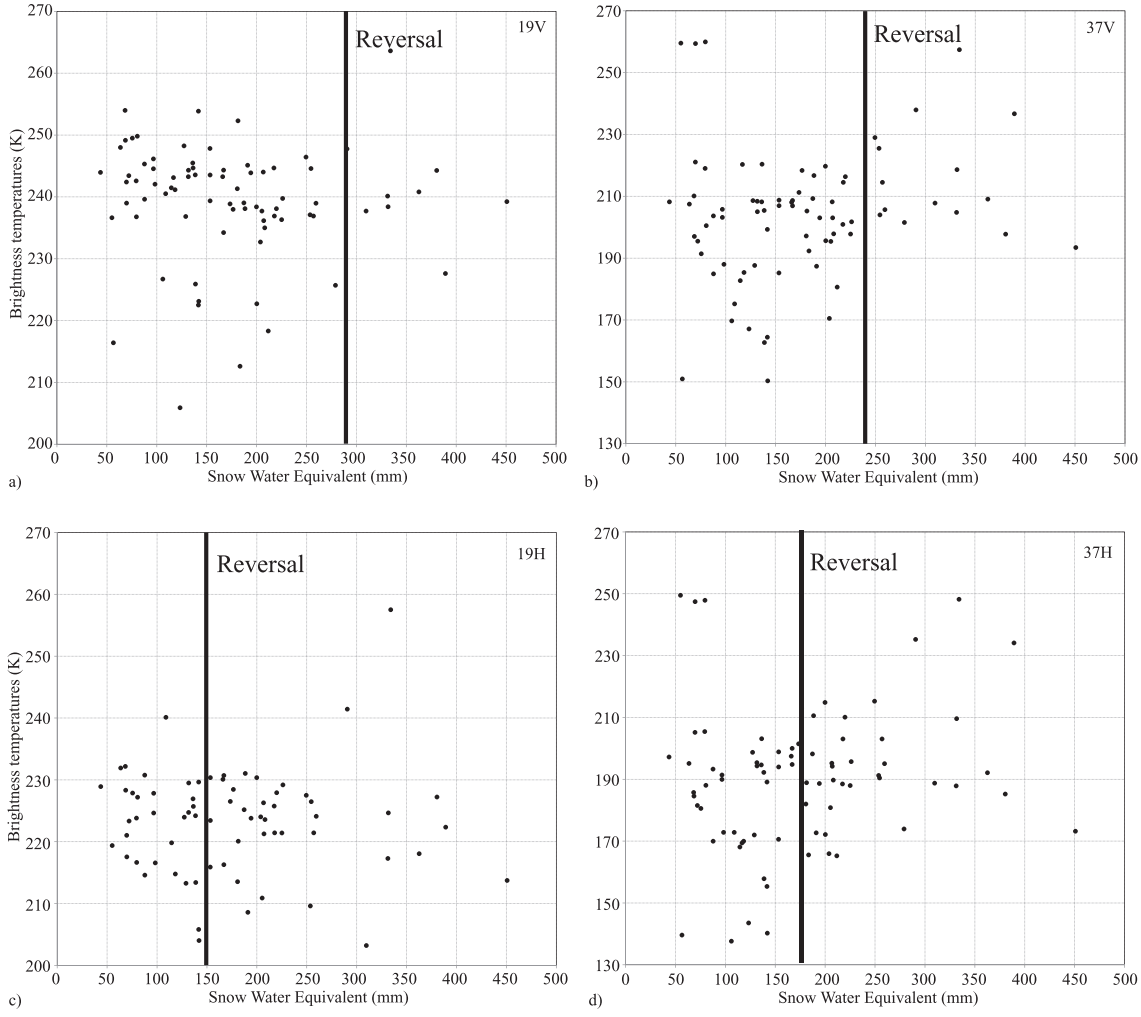


**Figure 4.** Measured brightness temperature (ground and airborne) as a function of SWE at 19 GHz in the vertical polarization, (a) 19V, (b) 37V, (c) 19H, and (d) 37H. The slope reversal in brightness temperature versus SWE is marked by the bold vertical line.

*Grody* [2000] observed the reversal at 37V at depths of 40–50 cm. However, one must be careful comparing these findings, since most of evaluations do not take into account vegetation contributions to the signal [e.g., *Kruopis et al.*, 1999; *Pampaloni*, 2004; *Pardé et al.*, 2005; *Lemmetyinen et al.*, 2009; *Langlois et al.*, 2010b, 2011], nor atmospheric effects [e.g., *Kerr and Njoki*, 1990; *Mätzler*, 1992b]. Both effects, which can be neglected in our study since we are using ground and airborne radiometer measurements over vegetation-free areas, can have a significant impact on $T_b$, leading to a biased slope reversal threshold. In fact, *Derksen* et al. [2010] showed that the reversal occurred at ~130 mm using airborne data, whereas lower SWE threshold was observed using satellite measurements. In light of this, we corrected SWE using measured and modeled brightness temperatures at all frequencies and polarizations, and best results were obtained combining 19V and 37V. From this result, we conducted the second iteration over the 0–290 mm SWE range (290 mm being the limit observed for 19V in Figure 4a).

#### 3.3.2. $\beta$ Correction Factor for SWE Retrieval

[26] As highlighted in Figure 2, we modified the SNOWPACK-modeled SWE values (using a $\beta$ factor: when $\beta SWE_{SNOWPACK} = SWE_{measured}$) using an iterative scheme (minimizing RMSE between observed and modeled $T_b$ by changing SWE values in the input SNOWPACK data) using the snow grain corrected ($\varphi$) MEMLS output data from the first iteration process (Figure 2). Two different approaches were tested:

[27] 1. A fixed correction factor, $\beta$, was applied to the SNOWPACK-modeled SWE ("$\beta$ fixed" in Table 5). The $\beta$ is obtained when the RMSE between measured (radiometer) and simulated (MEMLS) $T_b$ is minimized for all sites combined (i.e., same correction on SWE for each site).

[28] 2. Adjustable $\beta$ values were computed individually at each site to minimize the difference between $T_{b\text{-rad.}}$ and $T_{b\text{-MEMLS}}$.

[29] From the first approach, the lowest RMSE value on $T_b$ obtained from the iteration was with $\beta = 1.35$ (i.e., modeled SWE values multiplied by 1.35; Figure 5). Although this correction method improves the slope (from 0.23 in Figure 2 to 0.53 in Figure 5), the RMSE (from 79 to 55 mm), and $R^2$ (from 0.27 to 0.45), the offset increases from 109 to 121 mm, highlighting the need for further improvement.

[30] It appears that the difference between measured and modeled SWE varies with the magnitude of the in situ SWE measurements, which largely explains the poor results in Figure 5. The correlation observed between the measured and modeled SWE differences with the in situ SWE measurements (Figure 6) shows that measured values below 148 mm (corresponding to 148 mm modeled) are lower than predicted values from SNOWPACK. Hence, a more appropriate strategy would be to obtain a $\beta$ correction factor individually for each site providing the lowest RMSE value between modeled and measured $T_b$ (i.e., SWE value where $T_{b\text{-MEMLS}} \approx T_{b\text{-MEASURED}}$). To establish the reliable range variation of the $\beta$ correction factor, we computed the optimal $\beta$ values that would provide the perfect match obtained with $SWE_{measured}/SWE_{SNOWPACK}$. Those values ranged between 0.4 and 1.9, where values below 1 decrease modeled SWE. We then coupled SNOWPACK and MEMLS using the whole $\beta$ range (0.4–1.9, step of 0.1) and used the $\beta$ value as a free parameter that provided the best simulation (i.e., where MEMLS $T_b$ was closest to radiometer measurements).

[31] Since predicted SWE values below 148 mm (value derived from regression in Figure 6) are overestimated by SNOWPACK (Figure 6), their $\beta$ correction factor should theoretically be <1, whereas modeled values over 148 mm should have a $\beta > 1$. Hence, for sites where $\beta$ values obtained through the iteration did not obey that rule, we simply applied a fixed negative/positive $\beta$ value ($\beta = 0.7$ for sites that obtained a $\beta > 1$ for SWE < 150 mm, and $\beta = 1.45$ for sites that obtained a $\beta < 1$ for SWE > 148 mm). Such cases can occur under various circumstances of which further analysis is beyond the scope of this article. The forcing values of 0.7 and 1.45 provided the best results, and the obtained corrected modeled SWE values are improved further when compared to a fixed $\beta = 1.35$ (slope, $y$-axis intercept, and $R^2$) as shown in Figure 7 and Table 5 ("$\beta$ adjustable" in Table 5).

[32] The relationship between predicted values (with $\varphi$ and $\beta$) shows an improved slope, $R^2$, and $y$-axis offset and an RMSE of 65.4 mm (Table 5). Thus, the method suggested here improves SWE predictions compared to standalone simulations with a physical snow model driven by regional reanalysis. A similar approach was developed by *Foster et al.* [2011]; however; their approach requires in situ information (not always representative), whereas our methodology is completely independent from surface observations.

**Table 5.** Summary of Initial and Corrected SWE Simulation Statistics Compared to Field Measurements

| SWE Simulations | Slope | $y$-Axis Offset (mm) | $R^2$ | RMSE (mm) |
|---|---|---|---|---|
| Initial | 0.226 | 108.85 | 0.269 | 79.4 |
| $\beta$ fixed | 0.532 | 121.13 | 0.447 | 54.9 |
| $\beta$ adjustable | 0.891 | 23.474 | 0.404 | 65.4 |

### 3.4. Validation

[33] The method developed above was tested against an independent data set, also acquired during the 2008 IPY campaign near the community of POV (59.8 N–76.45W; see Figure 1). Coincident airborne brightness temperatures and in situ SWE measurements were collected along a transect, spanning two NARR pixels (hence, two NARR-SNOWPACK SWE values). Nearly 5000 snow depths were measured in 5 days, then converted to SWE using average density determined from snow core measurements and were also measured along the snow depth transects (see *Derksen et al.* [2010] for a complete description). The airborne radiometer footprint was about 100 m, within which measured SWE values were averaged (between 10 and 85 SWE measurements in each footprint), leading to a total of 109 points used in the validation.

[34] Obviously, one can expect a poor relationship between NARR-SNOWPACK modeled versus measured SWE (Figure 8a), given that only two modeled SWE values are available and compared against 109 in situ measurements, which were strongly affected by local-scale variability. This is also the reason why no validation was conducted using Advanced Microwave Scanning Radiometer–EOS data. However, for each of the 109 footprints, $\beta$ values were found using the methodology presented in this article. We

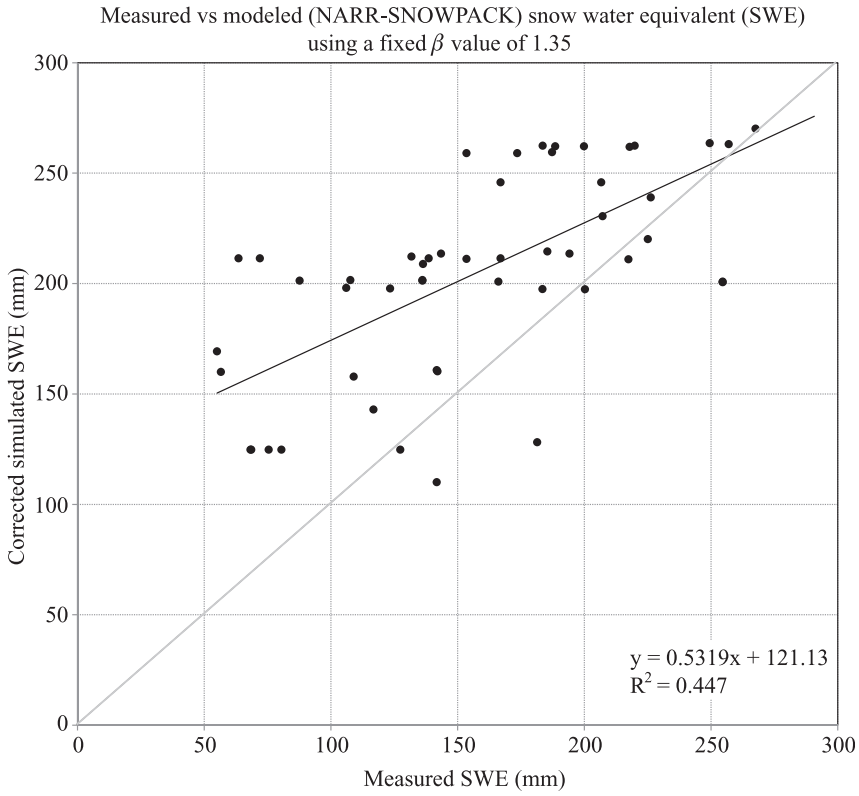


**Figure 5.** Comparison between modeled SWE values from NARR-SNOWPACK ($\varphi$ scaling applied to grain size) using a fixed $\beta$ value of 1.35 (multiplying factor) and measured values.

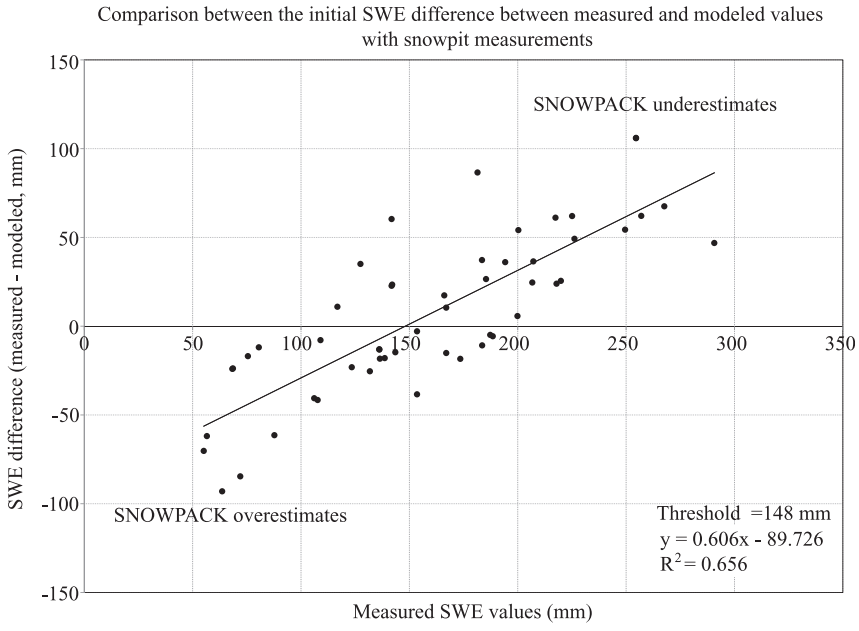


**Figure 6.** Difference between measured and modeled SWE as a function of measured SWE.

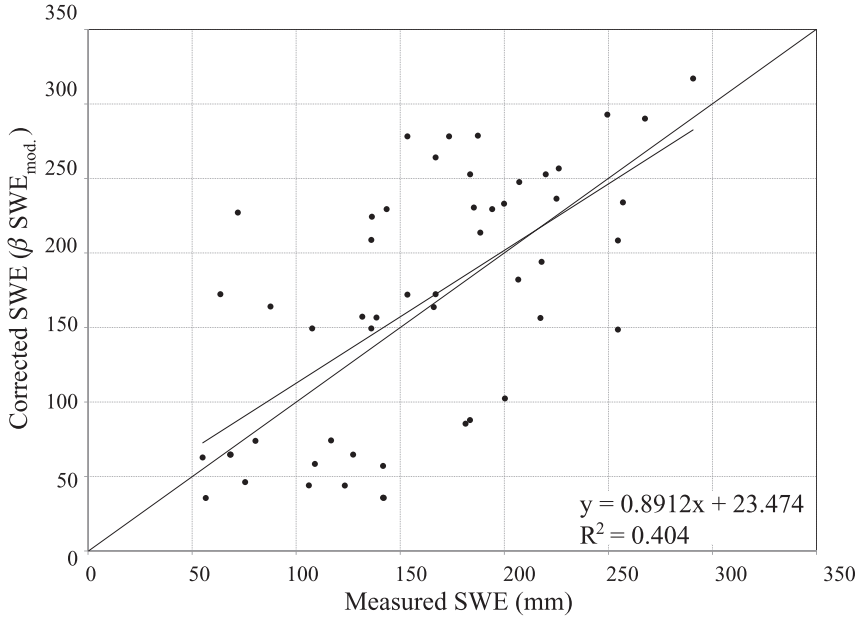


**Figure 7.** Comparison between modeled SWE values from NARR-SNOWPACK ($\varphi$ scaling factor applied to grain size) using variable $\beta$ values (multiplying factor) for each site using a 148 mm threshold (second iteration process, see Figure 2).

retrieved corrected modeled SWE and compared them against field measurements (Figure 8b). Results show that our method clearly improves SWE simulations from SNOWPACK, even with the very high spatial variability measured on the ground. The average standard deviation of measured SWE within the two NARR pixels is 57 mm (min. 14 mm, max. 148 mm).

[35] However, potential sources of error can arise from field measurements of SWE and the inherent spatial variability. Although the latter cannot be corrected but only quantified, it remains a potential source of error. As displayed in Figure 8 for the validation, this spatial variability varied between 14% and 99% within the radiometer footprints (approximately 100 m × 100 m). *Shook and Gray* [1996] measured the standard deviation of snow depth at sampling distances ranging between 1 m and 1 km and showed that the standard deviation within distances of about 30 m is representative of larger scales [*Clark et al.*, 2011]. However, this specific 30 m spatial variability was not systematically measured on the field and has to be measured in tundra environments. This is crucial to SWE retrievals using coarse spatial resolution passive microwave satellite data and can account for observed biases and explain some of the errors observed in Figures 7 and 8, given the scale differences between snowpit measurements (local) and simulations (NARR-SNOWPACK at ~32 km).

## 4. Conclusions

[36] We coupled a snow thermodynamic model (SNOWPACK) driven by regional reanalysis data (NARR) with a layered snow emission model (MEMLS) to improve simulations of SWE, completely independent from any surface observations (using the $\beta$ values from section 3.3.2 considered to be representative). To evaluate the snow model, simulations were compared to in situ measurements from two different field campaigns. We first showed that the initial SWE simulations (without the use of any passive microwave measurements) contained large errors with a regression slope of 0.23 and a $y$-axis offset of 109 mm. The initial $R^2$ and RMSE were measured 0.27 and 79 mm, respectively.

[37] To improve this result, we coupled the snow model output to a layered microwave snow emission model. First, the poor grain characterization by the snow model was corrected using an iterative scheme where the simulated snow grain was modified (scaling factor, $\varphi$) until a minimum difference in brightness temperatures ($\Delta T_{b\text{-MIN}}$) was found between measured (radiometer) and modeled (MEMLS) data. The most appropriate scaling factor was found to be 0.1 for all sites, which was then applied to the snow model output. The SNOWPACK output data (with corrected snow grain size using $\varphi$) was again coupled to MEMLS for a second iteration to retrieve SWE (i.e., modifying SWE until $\Delta T_{b\text{-MIN}}$ was found). A scaling factor for SWE ($\beta$) was found for all sites collectively (minimum RMSE) at 1.35. Further improvement occurred when using two $\beta$ values for underestimated and overestimated SWE values, which produced significant improvement on the slope, $y$-axis intercept, $R^2$, and RMSE between modeled SWE (with the two iteratively determined scaling factors) and measured SWE.

[38] It is important to understand that the rather large uncertainties in snow model predictions of SWE and grain size (in our case: SNOWPACK) can be attributed to (1) the model itself and how it treats physical processes such as metamorphism and compaction and (2) the input meteorological

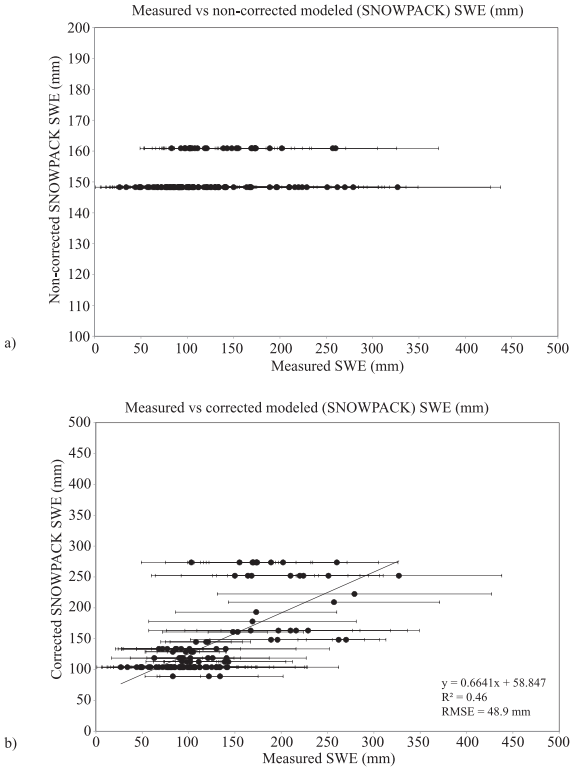


**Figure 8.** Comparison between modeled and measured SWE (a) before and (b) after the iterations with measured brightness temperatures. Measurements are from transects near the POV (Figure 1). In (a), data span two NARR pixels (therefore, two NARR SWE values). Horizontal lines correspond to the standard deviation of the in situ SWE measurements.

data. It is thus hard to compare and identify key components of the models that are problematic. The overall objective of this article was not to identify and correct weaknesses in SNOWPACK but rather to investigate if $T_b$ can be used to correct initial biases in the snow model whether they come from the model of the input data and without any other source of information on the snowpack. A comparison between similar snow models was conducted in the framework of Snow Model Intercomparison Project (SnowMIP) and by *Langlois et al.* (2009). In this latter analysis, results showed similar biases in three models, namely, SNOWPACK, CROCUS, and SNTHERM. The use of another model performing better in SWE of snow grain simulations would simply change the level of correction needed ($\varphi$, $\beta$), but the overall improvement would not necessarily change. Improving the physical treatment of SNOWPACK is out of the scope of this study.

[39] Validation using an independent snow survey data set over tundra with strong local-scale variability showed promising results, with a RMSE of 49 mm, and we showed that our method can be applied over a wide range of SWE values (45–260 mm). Furthermore, most studies presented in section 1 are using satellite-passive microwave data, which include $T_b$ contributions from various surface characteristics such as roughness, spatial variation in snow thickness and thermophysical properties, and snow grain size. Hence, the exact nature of each contribution is hard to quantify at the satellite scale and remains poorly studied. The airborne-derived brightness temperatures used in this article are generally more sensitive to plot-scale characteristics, increasing the challenge of SWE retrieval. On the other hand, this increased sensitivity to snow properties allowed the correction for poor grain simulations by the snow model ($\varphi$), which represents a step forward for iterative schemes (for future spaceborne retrievals). We showed that coupling a snow thermodynamic model with a microwave snow emission model without accounting for poor grain parameterization uncertainty leads to very large errors, with RMSE $>$100 K in brightness temperatures. A simple two-step iterative procedure (first iteration on snow grains and second on SWE) driven by meteorological reanalysis and without any in situ snow information allows similar SWE retrieval accuracy when compared to an assimilation scheme that requires in situ snow information [*Takala et al.*, 2011]. The *Takala et al.* [2011] study identified RMSE values ranging between 23 and 73 mm over Eurasia (depending on the season) and between 21 and 70 mm over Canada (depending on land cover).

[40] In this study, we covered a wide range of measurements from very low values that can be expected in the fall to high values expected at the end of winter. Furthermore, we covered an extensive area ($>$2000 km) encompassing several environments (boreal, taiga, tundra) with specific physical processes governing snow accumulation and transport. This said, with proper assessment of the various contributions to $T_b$ (i.e., topography, vegetation, atmosphere), we believe the data set to be representative of subarctic regions and that the method and threshold can be regionally applied. Prior to doing so, the next intuitive step would be to extend the validation of the method using a multiscale (in situ, airborne, spaceborne) approach. The differences in errors observed at the various scales using the same field SWE reference measurements averaged at the different scales will explain the potential source of errors at the satellite scale. The proposed simplified approach could also be applied regionally with a snow model or within the land surface scheme of a regional climate model to potentially improve snow monitoring. Furthermore, the physical processes driving the initial SNOWPACK model biases in SWE such as precipitation parameterization, treatment of albedo and density (starting values and temporal evolution), sublimation/erosion, and their seasonal evolution should be addressed in a dedicated study.

[41] **Acknowledgments.** The authors thank the Churchill Northern Studies Centre and Environment Canada staff that participated in the project for their collaboration and support. The authors acknowledge the generous contributions of G. Picard, L. Arnaud, L. Brucker, N. Champollion, J.-D. Giguère, A. Roy, S. Crête-d'Avignon, C. Rivest, M. Chum, P. Harvey-Collard, and S. Langlois for helping to collect the data in harsh arctic winter conditions. Special thanks to Peter Toose and Arvids Silis from Environment Canada, M. Dufour, and Heli-Excel for making the ambitious helicopter transect possible and to the McGill Subarctic Research Station and Makivik Corporation staff for essential logistical support. This project was funded through the Canadian IPY project-Environment Canada, the National Sciences and Engineering Research Council of Canada, the Collaboration Québec-France, Le Centre Jacques Cartier and the French Remote Sensing program (Programme National de Télédétection Spatiale), and the Canadian Space Agency.

## References


Albert, M. R. (2002), Effects of snow and firn ventilation on sublimation rates, *Ann. Glaciol.*, *35*, 510–514.

Andreadis, K., and D. Lettenmaier (2006), Trends in 20th century drought over the continental United States, *Geophys. Res. Lett.*, *33*, L10403, doi:10.1029/2006GL025711.

Arons, E. M., and S. C. Colbeck (1995), Geometry of heat and mass transfer in dry snow: A review of theory and experiment, *Rev. Geophys.*, *33*, 463–493.

Asmus, K., and C. Grant (1999), Surface based radiometer (SBR) data acquisition system, *Int. J. Remote Sens.*, *20*, 3125–3129.

Barnett, T. P., J. C. Adam, and D. P. Lettenmaier (2005), Potential impacts of a warming climate on water availability in snow-dominated regions, *Nature*, *438*, 303–309, doi:10.1038/nature04141.

Bartelt, P. B., and M. Lehning (2002), A physical SNOWPACK model for avalanche warning services. Part I: Numerical model, *Cold Reg. Sci. Technol.*, *35*(3), 123–145.

Brown, R. D., B. Brasnett, and D. Robinson (2003), Gridded North American monthly snow depth and snow water equivalent for GCM evaluation, *Atmos. Ocean*, *41*, I–14.

Brucker, L., A. Royer, G. Picard, A. Langlois, and M. Fily (2010), Hourly simulations of seasonal snow microwave brightness temperature using coupled snow evolution-emission models in Québec, Canada, *Remote Sens. Environ.*, *115*, 1966–1977.

Bukovsky, M. S., and D. J. Karoly (2007), A brief evaluation of precipitation from the North American regional reanalysis, *J. Hydrometeorol.*, *8*(4), 837–847.

Butt, M., and R. E. J. Kelly (2008), Monitoring snowcover in the UK using passive microwave remote sensing observations and the HUT model, *Int. J. Remote Sens.*, *29*(14), 4249–4267, doi:10.1080/01431160801891754.

Chang, A. T. C., J. L. Foster, D. K. Hall, A. Rango, and B. K. Hartline (1982), Snow water equivalent estimation by microwave radiometry, *Cold Reg. Sci. Technol.*, *5*(3), 259–267.

Clark, M. P., J. Hendrikx, A. G. Slater, D. Kavetski, B. Anderson, N. J. Cullen, T. Kerr, E. Örn Hreinsson, and R. A. Woods (2011), Representing spatial variability of snow water equivalent in hydrologic and land-surface models: A review, *Water Resour. Res.*, *47*, W07539, doi:10.1029/2011WR010745.

Colbeck, S. C. (1983), Theory of metamorphism of dry snow, *J. Geophys. Res.*, *88*, 5475–5482.

Derksen, C., A. Walker, and B. Goodison (2005), Evaluation of passive microwave snow water equivalent retrievals across the boreal forest/tundra transition of western Canada, *Remote Sens. Environ.*, *96*(3–4), 315–327.

Derksen, C., P. Toose, A. Rees, L. Wang, M. English, A. Walker, and M. Sturm (2010), Development of a tundra-specific snow water equivalent retrieval algorithm for satellite passive microwave data, *Remote Sens. Environ.*, *114*, 1699–1709.

Derksen, C., P. Toose, J. Lemmetyinen, J. Pulliainen, A. Langlois, N. Rutter, and M. Fuller (2012a), Evaluation of passive microwave brightness temperature simulations and snow water equivalent retrievals through a winter season, *Remote Sens. Environ.*, *117*, 236–248.

Derksen, C., et al. (2012b), Variability and change in the Canadian cryosphere, *Clim. Change*, *115*, 59–88, doi:10.1007/s10584-012-0470-0.

Domine, F., R. Salvatori, L. Legagneux, R. Salzano, M. Fily, and R. Casacchia (2006), Correlation between the specific surface area and the short wave infrared (SWIR) reflectance of snow, *Cold Reg. Sci. Technol.*, *46*, 60–68.

Domine, F., M. Albert, T. Huthwelker, H.-W. Jacobi, A. A. Kokhanovsky, M. Lehning, G. Picard, and W. R. Simpson (2008), Snow physics as relevant to snow photochemistry, *Atmos. Chem. Phys.*, *8*, 171–208.

Dong, J., J. P. Walker, and P. R. Houser (2005), Factors affecting remotely sensed snow water equivalent uncertainty, *Remote Sens. Environ.*, *97*(1), 68–82.

Durand, M., and S. A. Margulis (2007), Correcting first-order errors in snow water equivalent estimates using a multifrequency, multiscale radiometric data assimilation scheme, *J. Geophys. Res.*, *112*, D13121, doi:10.1029/2006JD008067.

Durand, M., E. J. Kim, and S. A. Margulis (2008), Quantifying uncertainty in modeling snow microwave radiance for a mountain snowpack at the point-scale, including stratigraphic effects, *IEEE Trans. Geosci. Remote Sens.*, *46*(6), 1753–1767.

Dutra, E., G. Balsamo, P. Viterbo, P. M. A. Miranda, A. Beljaars, C. Schär, and K. Elder (2010), An improved snow scheme for the ECMWF land surface model: Description and offline validation, *J. Hydrometeorol.*, *11*(4), 899–916, doi:10.1175/2010JHM1249.1.

Essery, R. (1998), Boreal forests and snow in climate models, *Hydrol. Process.*, *12*(10–11), 1561–1567.

Fletcher, C. G., P. J. Kushner, A. Hall, and X. Qu (2009), Circulation responses to snow albedo feedback in climate change, *Geophys. Res. Lett.*, *36*, L09702, doi:10.1029/2009GL038011.

Foster, J. L., A. T. C. Chang, and D. K. Hall (1997), Comparison of snow mass estimates from a prototype passive microwave snow algorithm, a revised algorithm and a snow depth climatology, *Remote Sens. Environ.*, *62*, 132–142.

Foster, J. L., C. Sun, J. P. Walker, R. Kelly, A. T. C. Chang, J. Dong, and H. Powell (2005), Quantifying the uncertainty in passive microwave snow water equivalent observations, *Remote Sens. Environ.*, *94*(2), 187–203.

Foster, J. L., et al. (2011), A blended global snow product using visible, passive microwave and scatterometer satellite data, *Int. J. Remote Sens.*, *32*(5), 1371–1395.

Frei, A., and S. Lee (2010), A comparison of optical-band based snow extent products during spring over North America, *Remote Sens. Environ.*, *114*, 1940–1948.

Gallet, J.-C., F. Domine, C. S. Zender, and G. Picard (2009), Measurement of the specific surface area of snow using infrared reflectance in an integrating sphere at 1310 and 1550 nm, *Cryosphere*, *3*, 167–182.

Gallet, J.-C., F. Domine, L. Arnaud, G. Picard, and J. Savarino (2010), Vertical profiles of the specific surface area of the snow at Dome C, Antarctica, *Cryosphere Discuss.*, *4*, 1647–1708.

Grenfell, T. C., and S. G. Warren (1999), Representation of a nonspherical ice particle by a collection of independent spheres for scattering and absorption of radiation, *J. Geophys. Res.*, *104*, 31,697–31,708.

Grody, N. (2008), Relationship between snow parameters and microwave satellite measurements: Theory compared with Advanced Microwave Sounding Unit observations from 23 to 150 GHz, *J. Geophys. Res.*, *113*, D22108, doi:10.1029/2007JD009685.

Gustafsson, D., M. Stähli and P.-E. Jansson (2001), The surface energy balance of a snow cover: Comparing measurements to two different simulation models, *Theor. Appl. Climatol.*, *70*, 81–96.

Hall, D. K., G. A. Riggs, and V. V. Salomonson (1995), Development of methods for mapping global snow cover using moderate resolution imaging spectroradiometer data, *Remote Sens. Environ.*, *54*, 27–140.

Hallikainen, M., F. T. Ulaby, and M. Abdelrazik (1986), Dielectric properties of snow in the 3 to 37 GHz range, *IEEE Trans. Ant. Propag.*, *34*, 1329–1340.

Hansen, M., R. DeFries, J. R. G. Townshend, R. Sohlberg, C. Dimiceli, and M. Carroll (2002), Towards an operational MODIS continuous fields of percent tree cover algorithm: Example using AVHRR and MODIS data, *Remote Sens. Environ.*, *83*, 303–319.

Hardiman, S. C., P. J. Kushner, and J. Cohen (2008), Investigating the ability of general circulation models to capture the effects of Eurasian snow cover on winter climate, *J. Geophys. Res.*, *113*, D21123, doi:10.1029/2008JD010623.

Huang, C., S. A. Margulis, M. T. Durand, and K. N. Musselman (2012), Assessment of snow grain-size model and stratigraphy representation impacts on snow radiance assimilation: Forward modeling evaluation, *IEEE Trans. Geosci. Remote Sens.*, *50*, 4551–4561, doi:10.1109/TGRS.2012.2192480.

Huining, W., J. Pulliainen, and M. Hallikainen (1999), Effective permittivity of dry snow in the 18 to 90 GHz range, *Prog. Electromagn. Res.*, *24*, 119–138.

Kaufman, D. S., et al. (2009), Recent warming reverses long-term Arctic cooling, *Science*, *325*(5945), 1236–1239.

Kelly, R., A. T. C. Chang, L. Tsang, and J. Foster (2003), A prototype AMSR-E global snow area and snow depth algorithm, *IEEE Trans. Geosci. Remote Sens.*, *41*(2), 230–242.

Kerr, Y. H., and E. G. Njoki (1990), A semiempirical model for interpreting microwave emission from semiarid land surfaces as seen from space, *IEEE Trans. Geosci. Remote Sens.*, *28*(3), 384–393.

Kontu, A., and J. Pulliainen (2010), Simulation of spaceborne microwave radiometer measurements of snow cover using in situ data and brightness temperature modeling, *IEEE Trans. Geosci. Remote Sens.*, *48*(3), 1031–1044.

Kruopis, N., J. Praks, A. N. Arslan, H. Alasalmi, J. Koskinen, and M. Hallikainen (1999), Passive microwave measurements of snow-covered forest areas in EMAC'95, *IEEE Trans. Geosci. Remote Sens.*, *37*(6), 2699–2705.

Langlois, A., D. G. Barber, and B. J. Hwang (2007), Development of a snow water equivalent algorithm using passive microwave data over first-year sea ice, *Remote Sens. Environ.*, *106*(1), 75–88.

Langlois, A., T. Fisico, D. G. Barber, and T. N. Papakyriakou (2008), The response of snow thermophysical processes to the passage of a polar low-pressure system and its impact on in-situ passive microwave data: A case study, *J. Geophys. Res.*, *113*, C03S04, doi:10.1029/2007JC004197.

Langlois, A., L. Brucker, J. Kohn, A. Royer, C. Derksen, P. Cliche, G. Picard, M. Fily, and J.-M. Willemet (2009), Regional retrieval of snow water equivalent (SWE) using thermodynamic snow models in Québec, Canada, *J. Hydrometeorol.*, *10*(6), 1447–1463.

Langlois, A., A. Royer, and K. Goïta (2010a), Linkages between simulated and spaceborne passive microwave brightness temperatures with in-situ measurements of snow and vegetation properties, *Can. IPY Spec. Issue Can. J. Remote Sens.*, *36*(1), 135–148.

Langlois, A., A. Royer, B. Montpetit, G. Picard, L. Brucker, L. Arnaud, K. Goïta, and M. Fily (2010b), On the relationship between measured and modeled snow grain morphology using infrared reflectance, *Cold Reg. Sci. Technol.*, *61*, 34–42.

Langlois, A., A. Royer, F. Dupont, A. Roy, K. Goïta, and G. Picard (2011), Improved vegetation corrections for satellite passive microwave remote sensing using airborne radiometer data, *IEEE Trans. Geosci. Remote Sens.*, *49*(10), 3824–3837.

Latifovic, R., Z.-L. Zhu, J. Cihlar, C. Giri, and I. Olthof (2004), Land cover mapping of North and Central America—Global land cover 2000, *Remote Sens. Environ.*, *89*(1), 116–127.

Lehning, M., P. B. Bartelt, R. L. Brown, C. Fierz, and P. Satyawali (2002), A physical SNOWPACK model for the Swiss Avalanche Warning Services. Part III: Meteorological boundary conditions, thin layer formulation and evaluation, *Cold Reg. Sci. Technol.*, *35*(3), 169–184.

Lemke, P., et al. (2007), Observations: Changes in snow, ice and frozen ground, in: Climate Change 2007: The Physical Science Basis, in *Contribution of Working Group I to the Fourth Assessment Report of the Intergovernmental Panel on Climate Change*, edited by S. Solomon, et al., Cambridge Univ. Press, New York.

Lemmetyinen, J., C. Derksen, J. Pulliainen, W. Strapp, P. Toose, A. Walker, S. Tauriainen, J. Pihlflyckt, J.-P. Kärnä, and M. T. Hallikainen (2009), A comparison of airborne microwave brightness temperatures and snowpack properties across the boreal forests of Finland and Western Canada, *IEEE Trans. Geosci. Remote Sens.*, *47*(3), 965–978.

Li, S., and X. Zhou (2001), Derivation of surface direct beam spectral albedo for a wide range of incident angles from spectral reflectance measurements under overcast conditions, paper presented at IEEE 2001 International Geoscience and Remote Sensing Symposium (IGARSS 2001), Sydney, Australia, 9–13 July, pp. 1801–1803.

Lundy, C. C. (2000), Statistical validation of a numerical snow cover model and preliminary experimental results to facilitate model improvement, M.Sc. thesis, Dept. Civil. Eng., Mont. State Univ., Bozeman, Mont.

Male, D. H., and R. J. Granger (1981), Snow surface energy exchange, *Water Resour. Res.*, *17*, 609–627.

Markus, T., and D. Cavalieri (2000), An enhancement of the NASA Team Sea Ice Algorithm, *IEEE Trans. Geosci. Remote Sens.*, *38*, 1387–1398.

Markus, T., D. C. Powell, and J. R. Wang (2006), Sensitivity of passive microwave snow depth retrievals to weather effects and snow evolution, *IEEE Trans. Geosci. Remote Sens.*, *44*, 68–77.

Matzl, M., and M. Schneebeli (2006), Areal measurement of specific surface area in snow profiles by near infrared reflectivity, *J. Glaciol.*, *52*(179), 558–564.

Mätzler, C. (1987), Applications of the interaction of microwaves with natural snow cover. *Remote Sens. Rev.*, *2*(1), 259–387.

Mätzler, C. (1992a), Relation between grain-size and correlation length of snow, *J. Glaciol.*, *48*(162), 461–466.

Mätzler, C. (1992b), Ground-based observations of atmospheric radiation at 5, 10, 21, 35, and 94 GHz, *Radio Sci.*, *27*(3), 403–415.

Mätzler, C., and A. Wiesmann (1999), Extension of the microwave emission model of layered snowpacks to coarse-grained snow, *Remote Sens. Environ.*, *70*(3), 317–325.

Maurer, E. P., J. D. Rhoads, R. O. Dubayah, and D. P. Lettenmaier (2003), Evaluation of the snow-covered area data product from MODIS, *Hydrol. Process.*, *17*, 59–71.

Mesinger, F., et al. (2006), North American Regional Reanalysis, *Bull. Am. Meteorol. Soc.*, *87*(3), 343–360.

Metcalfe, J. R., and B. E. Goodison (1993), Correction of Canadian winter precipitation data, paper presented at Eighth Symposium on Meteorological Observations and Instrumentation, Anaheim, Calif., AMS, Boston, Mass.

Montpetit, B., A. Royer, A. Langlois, P. Cliche, A. Roy, N. Champollion, G. Picard, F. Domine, and R. Obbard (2011), New short-wave infrared albedo measurements for snow specific surface area retrieval, *J. Glaciol.*, *58*, 941–952.

Morin, S., F. Domine, A. Dufour, Y. Lejeune, B. Lesaffre, J.-M. Willemet, C. M. Carmagnola, and H.-W. Jacobi (2012), Measurements and modeling of the vertical profile of specific surface area of an alpine snowpack, *Adv. Water Resour.*, doi:10.1016/j.advwatres.2012.01.010, in press.

Pampaloni, P. (2004), Microwave radiometry of forests, *Waves Random Complex Medium*, *14*, 275–298.

Pardé, M., K. Goïta, A. Royer, and F. Vachon (2005), Boreal forest transmissivity in the microwave domain using ground-based measurements, *IEEE Trans. Geosci. Remote Sens.*, *2*(2), 169–171.

Pardé, M., K. Goïta, and A. Royer (2007), Inversion of a passive microwave snow emission model for water equivalent estimation using airborne and satellite data, *Remote Sens. Environ.*, *111*, 346–356.

Picard, G., L. Arnaud, F. Domine, and M. Fily (2010), Determining snow specific surface area from near-infrared reflectance measurements: Numerical study of the influence of grain shape, *Cold Reg. Sci. Technol.*, *56*, 10–17.

Pulliainen, J. (2006), Mapping of snow water equivalent and snow depth in boreal and sub-arctic zones by assimilating space-borne microwave radiometer data and ground-based observations, *Remote Sens. Environ.*, *101*(2), 257–269.

Pulliainen, J., and M. Hallikainen (2001), Retrieval of regional snow water equivalent from space-borne passive microwave observations, *Remote Sens. Environ.*, *75*(1), 76–85.

Qiu, Y., H. Guo, J. Shi, S. Kang, J. Lemmetyinen, and J. R. Wang (2011), Analysis of the passive microwave high-frequency signal in the shallow snow retrieval, in *Geoscience and Remote Sensing Symposium (IGARSS), 2011*, IEEE International, 24–29 July 2011, pp. 3863–3866.

Rees, A., J. Lemmetyinen, C. Derksen, J. Pulliainen, and M. English (2010), Observed and modelled effects of ice lens formation on passive microwave brightness temperatures over snow covered tundra, *Remote Sens. Environ.*, *114*, 116–126.

Romanovsky, V. E., S. L. Smith, and H. H. Christiansen (2010), Permafrost thermal state in the polar northern hemisphere during the International Polar Year 2007–2009: A synthesis, *Permafrost Periglacial Process.*, *21*(2), 106–116.

Rosenfeld, S., and N. Grody (2000), Anomalous microwave spectra of snow cover observed from special sensor microwave/imager measurements, *J. Geophys. Res.*, *105*(D11), 14,913–14,925.

Roy, V., K. Goïta, A. Royer, A. Walker, and B. Goodison (2004), Snow water equivalent retrieval in a Canadian boreal environment from microwave measurements using the HUT snow emission model, *IEEE Trans. Geosci. Remote Sens.*, *42*(9), 1850–1859.

Salomonson, V. V., and I. Appel (2004), Estimating fractional snow cover from MODIS using the normalized difference snow index, *Remote Sens. Environ.*, *89*, 351–360.

Shook, K., and D. M. Gray (1996), Small-scale spatial structure of shallow snowcovers, *Hydrol. Process.*, *10*, 1283–1292.

Solheim, F. 1993, Use of pointed water vapor radiometers to improve GPS surveying accuracy, Ph.D. dissertation, Univ. of Colo., Boulder, Colo., December.

Spreitzhofer, G., C. Fierz, and M. Lehning (2004), SN_GUI: A graphical user interface for snow pack modeling, *Comput. Geosci.*, *30*(8), 809–816.

Takala, M., K. Luojus, J. Pulliainen, C. Derksen, J. Lemmetyinen, J.-P. Kärnä, J. Koskinen, and B. Bojkov (2011), Estimating northern hemisphere snow water equivalent for climate research through assimilation of space-borne radiometer data and ground-based measurements, *Remote Sens. Environ.*, *115*(12), 3517–3529.

Tedesco, M., and E. J. Kim (2006), Intercomparison of electromagnetic models for passive microwave remote sensing of snow, *IEEE Trans. Geosci. Remote Sens.*, *44*(10–1), 2654–2666.

Tiuri, M. E., A. H. Sihlova, E. G. Nyfors, and M. T. Hallikainen (1984), The complex dielectric constant of snow at microwave frequencies, *IEEE J. Ocean. Eng.*, *9*(5), 377–382.

Touré, A. M., K. Goïta, A. Royer, E. J. Kim, M. Durand, S. A. Margulis, and H. Lu (2011), A case study of using a multilayered thermodynamical snow model for radiance assimilation, *IEEE Trans. Geosci. Remote Sens.*, *49*(8), 2828–2837.

Walker, A., J. W. Strapp, and I. MacPherson. (2002) A Canadian Twin Otter microwave radiometer installation for airborne remote sensing of snow, ice and soil moisture, paper presented at International Geoscience and Remote Sensing Symposium [CD-ROM], Toronto, Ont., June.

Wegmüller, U., and C. Mätzler (1999), Rough bare soil reflectivity model, *IEEE Trans. Geosci. Remote Sens.*, *37*(3), 1391–1395.

Wiesmann, A., and C. Mätzler (1999), Microwave emission model of layered snowpacks, *Remote Sens. Environ.*, *70*(3), 307–316.

Wiesmann, A., C. Mätzler, and T. Weise (1998), Radiometric and structural measurements of snow samples, *Radio Sci.*, *33*(2), 273–289.

Yang, D., S. Ishida, B. E. Goodison, and T. Gunther (1999), Bias correction of daily precipitation for Greenland, *J. Geophys. Res.*, *104*(D6), 6171–6181.

## B.2 Article : Brigthness Temperature Simulations of the Canadian Seasonal Snowpack Driven by Measurements of the Snow Specific Surface Area

En 2013, conjointement avec l'article (Montpetit *et al.*, 2013), Alexandre Roy a publié un ouvrage sur les simulations de la $T_B$ à l'aide de la SSA et des modèles DMRT-ML et HUT pour des sites où il n'y avait pas de croutes de glace. Il a été démontré dans ce travail que les modèles DMRT-ML et HUT nécessitaient eux aussi des corrections à la taille des grains de neige afin de minimiser l'erreur sur la $T_B$ simulée. Ce travail est très similaire aux travaux d'optimisation de la $T_B$ du couvert nival sans glace effectués dans cette thèse et cadre donc bien avec les travaux présentés ici. De multiple échange avec Alexandre Roy ont eu lieu afin de déterminer les méthodes d'optimisation du sol et de la taille des grains de neige. Ainsi, les structures des deux articles se ressembles en ce sens. La validation des résultats par des échanges et discussions entre les co-auteurs de l'ouvrage ainsi que les révisions ont été réalisées dans le cadre de cette thèse.

This article has been accepted for inclusion in a future issue of this journal. Content is final as presented, with the exception of pagination.



# Brightness Temperature Simulations of the Canadian Seasonal Snowpack Driven by Measurements of the Snow Specific Surface Area

Alexandre Roy, *Graduate Student Member, IEEE*, Ghislain Picard, Alain Royer, Benoit Montpetit, Florent Dupont, Alexandre Langlois, Chris Derksen, and Nicolas Champollion

***Abstract*—Snow grain size is the snowpack parameter that most affects the microwave snow emission. The specific surface area (SSA) of snow is a metric that allows rapid and reproducible field measurements and that well represents the grain size. However, this metric cannot be used directly in microwave snow emission models (MSEMs). The aim of this paper is to evaluate the suitability and the adaptations required for using the SSA in two MSEMs, i.e., the Dense Media Radiative Theory-Multilayer model (DMRT-ML) and the Helsinki University of Technology model (HUT n-layer), based on *in situ* radiometric measurements. Measurements of the SSA, using snow reflectance in the shortwave infrared, were taken at 20 snowpits in various environments (e.g., grass, tundra, and dry fen). The results show that both models required a scaling factor for the SSA values to minimize the root-mean-square error between the measured and simulated brightness temperatures. For DMRT-ML, the need for a scaling factor is likely due to the oversimplified representation of snow as spheres of ice with a uniform radius. We hypothesize that the need for a scaling factor is related to the grain size distribution of snow and the stickiness between grains. For HUT n-layer, using the SSA underestimates the attenuation by snow, particularly for snowpacks with a significant amount of depth hoar. This paper provides a reliable description of the grain size for DMRT-ML, which is of particular interest for the assimilation of satellite passive microwave data in snow models.**

***Index Terms*—Dense Media Radiative Theory-Multilayer (DMRT-ML), Helsinki University of Technology (HUT) n-layer, *in situ* measurements, microwave snow emission model (MSEM), snow grains specific surface area (SSA).**

Manuscript received June 13, 2012; revised October 26, 2012 and December 10, 2012; accepted December 16, 2012. This work was supported in part by the Fond Québécois de la Recherche sur la Nature et les Technologies (FQRNT) through the Global Environmental and Climate Change Centre (GEC3) and the Commission Permanente de Coopération Franco-Québécoise (CPCFQ), by the National Sciences and Engineering Research Council of Canada (NSERC), by Environment Canada—Climate Research Division, by the Canadian Space Agency, and by the French Programme National de Télédétection Spatiale.

A. Roy, A. Royer, B. Montpetit, and A. Langlois are with the Centre d'Applications et de Recherches en Télédétection (CARTEL), Université de Sherbrooke, Sherbrooke, QC J1K 2R1, Canada (e-mail: Alexandre.R.Roy@USherbrooke.ca; Alain.Royer@USherbrooke.ca; Benoit.Montpetit2@USherbrooke.ca; A.Langlois2@USherbrooke.ca).

G. Picard and N. Champollion are with the Laboratoire de Glaciologie et Géophysique de l'Environnement (LGGE), Université Joseph Fourier/CNRS, UMR 5183, 38041 Grenoble, France (e-mail: Ghislain.Picard@ujf-grenoble.fr; Nicolas.Champollion@lgge.obs.ujf-grenoble.fr).

F. Dupont is with the Centre d'Applications et de Recherches en Télédétection (CARTEL), Université de Sherbrooke, Sherbrooke, QC J1K 2R1, Canada, and also with the Laboratoire de Glaciologie et Géophysique de l'Environnement (LGGE), Université Joseph Fourier/CNRS, UMR 5183, 38041 Grenoble, France (e-mail: Florent.Dupont@lgge.obs.ujf-grenoble.fr).

C. Derksen is with the Climate Research Division, Environment Canada, Toronto, ON, Canada and also with the Department of Geography and Environment Management, University of Waterloo, Waterloo, ON N2L 3G1, Canada (e-mail: Chris.Derksen@ec.gc.ca).

Color versions of one or more of the figures in this paper are available online at http://ieeexplore.ieee.org.

Digital Object Identifier 10.1109/TGRS.2012.2235842

## I. Introduction

THE characterization of snow properties (e.g., accumulation, albedo, snow water equivalent, depth, melt, and temperature) is a major challenge in the prediction of energy and water budgets in cold regions. Because the albedo of snow is initially very high, a change of its optical characteristics resulting from metamorphosis or changes in its spatial coverage lead to significant climatic feedbacks [28], [46], [68]. Water stored in the form of snow, potentially for many months before entering runoff, can also significantly affect soil moisture and river runoff, including the occurrence of flood events [51], [66].

Passive microwave remote sensing is an appealing approach for characterizing the properties of snow at the synoptic scale; images are available at least twice a day for northern regions where meteorological stations and networks are generally sparse. Several studies have demonstrated the potential for using passive microwave measurements to estimate the snow water equivalent (SWE) [7], [9], [27], [45], [67] in midlatitude zones where the snow cover is seasonal and several empirical algorithms based on linear relationships between the SWE and the spectral difference of brightness temperatures have been proposed (e.g., [56]). It has however been demonstrated that using constant empirical relationships is often inaccurate because of interannual variability in the seasonal metamorphosis of snow grains [50]. One of the options to overcome this problem (see the review of Dietz *et al.* [10]) is to use a microwave snow emission model (MSEM) to understand the different contributions to the microwave signal. Different assimilation methods can then allow the coupling of a snow evolution model and an MSEM to correct the snow parameters by using brightness temperature observations [14], [15], [31], [58], [60].

It has been shown that the snow grain size is one of the key parameters of snow emission. This has been illustrated through different radiative transfer models, e.g., Helsinki University of Technology (HUT) [6], [30], [48], [53], Dense Media

0196-2892/$31.00 © 2013 IEEE

This article has been accepted for inclusion in a future issue of this journal. Content is final as presented, with the exception of pagination.



Radiative Theory (DMRT) [3], [22], [59], [64], and Microwave Emission Model of Layered Snowpacks (MEMLS) [16], [31], [61], [72]. However, grain size is a parameter that is difficult to accurately characterize and measure in the field, and it is not operationally measured at weather stations. Even the definition of snow grain size is ambiguous [1], [39]; a widely measured metric is the maximum diameter of grains $D_{\max}$ [17]. However, an accurate and objective measurement of this parameter is difficult to obtain given the wide variety of snow grain shapes. In addition, snow grains cannot always be clearly identified in the snow layer when the boundaries between grains are difficult to identify [12]. For instance, Kontu and Pulliainen [30] estimated that in their case, for a visual assessment (snow grains placed on a 1-mm grid) of the longest dimension of a grain $D_{\max}$, the accuracy for grains larger than 1 mm is $\pm 0.5$ mm and that for grains smaller than 1 mm is $\pm 0.25$ mm.

In contrast, the specific surface area (SSA) of a snow grain, which represents the ratio of the area of ice per unit of mass of ice (SSA $= (A/\rho_{\rm ice}V)$, units in $\mathrm{m^2 kg^{-1}}$), is a well-defined parameter that represents the geometric characteristics of a porous medium such as snow [13]. Methods based on snow reflectance in the short-wave infrared (SWIR) can now provide rapid and reproducible field measurements of the SSA [2], [19], [42] with an accuracy value within 12% compared with reference measurements made by methane adsorption [13].

In addition, significant progress has been made in modeling the evolution of the SSA in physical snow models [8], [25], [34], [57]. These studies propose simple approaches to simulate the SSA, and they are straightforward to implement in a snow model. Often, these models use, as their input, parameters that are already calculated by a traditional snow model. The SSA is also calculated in some existing snow models such as Crocus [44].

Thus, considering that the measurement of the SSA is well defined, its measurement is rapid and accurate, and modeling the SSA is possible, it is important to examine the use of this snow microstructure metric in an MSEM [3], [24], [39], [61]. However, the parameters representing the snow grain size in MSEM differ from the SSA concept, which is also different from the grain size measurements traditionally used [33]. It thus appears necessary to adapt the MSEM to derive an effective grain size from SSA.

For Antarctica, Brucker *et al.* [3] used SSA measurements based on near-infrared reflectance photography as input to a multilayer (ML) MSEM, i.e., DMRT-ML. They found that using the optical radius defined as

$$R_0 = \frac{3}{\rho_{\rm ice} SSA} \tag{1}$$

where $\rho_{\rm ice}$ is the ice density $= 917$ kg m$^{-3}$, was inadequate as input for their model based on DMRT. A scaling factor of $\phi = 2.85$ was applied to minimize the difference between the simulated brightness temperature $T_B$ and data from the Advanced Microwave Scanning Radiometer for the Earth Observing System (AMSR-E)

$$R_{\rm eff} = \frac{3}{\rho_{\rm ice} SSA}\phi \tag{2}$$

where $R_{\rm eff}$ is the effective radius in the microwave range. The climatic conditions and the types of snow in Antarctica are different from the seasonal snow found in midlatitude and subarctic environments; hence, the relationship between SSA and $R_{\rm eff}$ may be different and thus deserves further analysis in the context of seasonal snow. Furthermore, soil emission may be a significant contribution to the signal emerging from the surface in environments with seasonal snow, whereas it is neglected in Antarctica [4] since snowpack depth is much larger than the microwave penetration depth at the frequencies considered here.

Kontu and Pulliainen [30] proposed another approach to parameterize grain size in MSEM. They presented an empirical formula for calculating an effective diameter $D_{\rm eff}$ derived from $D_{\max}$, which improves $T_B$ simulations with the one-layer HUT model. The aim of their approach is to decrease the relative contribution of thick hoar layers (consisting of large grains at the bottom of the snowpack) in the calculation of the average snow grain size. This formula (with the same empirical coefficients) is also directly used in the HUT n-layer version, where it reduces the effect of large values on the observed grain size [58]. It should however be noted that the empirical relation between grain sizes and the extinction coefficient was derived with grain sizes smaller than 1.6 mm [23].

The objective of this paper is to evaluate the performance of two well-known ML MSEMs, namely, DMRT-ML and HUT n-layer, using SSA measurements and measured $T_B$ at 18.7 and 36.5 GHz. We first present the data, models, and SSA adaptation method, followed by the results. In the discussion, we propose several physical explanations for the SSA adaptations. We also discuss various approaches for integrating the SSA values in both MSEMs.

## II. Field Sites and Data Description

Snowpit measurements were acquired for four types of land cover, namely, open tundra, snow drifts on tundra, dry tundra fen, and midlatitude open grassy sites. The first three sites were located close to the Churchill Northern Studies Centre (58.73° N, 93.81° W) in Manitoba, Canada. The data were collected during the Canadian CoReH20 Snow and Ice (CAN-CSI) campaign in the winter of 2010, which included four periods of intensive field sampling (beginning of January, mid-February, end of March, and mid-April). Full details of the campaign are provided in [8]. During the winter of 2011, the grassy sites were located at the *Site Interdisciplinaire de Recherche en Environnement Extérieur* (SIRENE) experimental station at the Université de Sherbrooke (45.37° N, 71.92° W) and at Saint-Romain (80 km northeast of Sherbrooke) in Québec, Canada. The grassy sites have generally less aged snow. All snowpits were located in large open areas to avoid the effect of vegetation emission reflected by the snow, which could influence the radiometric measurements Kruopis *et al.* [32], [52], [73]. None of the snowpits had ice lenses, which can strongly influence the emissivity of the snow cover [40], [43], [49].

$T_B$ measurements in Churchill were taken for every snowpit at 19 and 37 GHz in vertical polarization (V-pol) and horizontal

This article has been accepted for inclusion in a future issue of this journal. Content is final as presented, with the exception of pagination.



TABLE I
AVERAGE VALUES FOR SNOWPIT PROPERTIES. SITE TYPE: TUNDRA [1], DRIFT TUNDRA [2], DRY TUNDRA FEN [3], AND MIDLATITUDE OPEN GRASSY SITES [4] (CH = CHURCHILL, S-R = SAINT-ROMAIN, AND SIR = SIRENE). $T_{\rm snow}$ IS THE MEAN SNOWPACK TEMPERATURE; DENSITY IS THE MEAN SNOWPACK DENSITY; $R_o$ IS THE MEAN OPTICAL RADIUS; $T_{\rm soil}$ IS THE SOIL SURFACE TEMPERATURE; $T_B$ IS THE *IN SITU* RADIOMETRIC MEASUREMENT; DATE IS WHEN THE MEASUREMENTS WERE TAKEN.

| # | Site Type | Snow depth (m) | Tsnow (K) | Density (kg/m3) | $R_o$ (mm) | Tsoil (K) | $T_B$ 37V | $T_B$ 37H | $T_B$ 19V | $T_B$ 19H | Date |
|---|---|---|---|---|---|---|---|---|---|---|---|
| 1 | 1 [CH] | 0.37 | 259.4 | 235.4 | 0.24 | 267.9 | 177.7 | 169.4 | 243.1 | 220.3 | 09/02/2010 |
| 2 | 1 [CH] | 0.48 | 255.2 | 261.4 | 0.36 | 269.6 | 150.3 | 140.2 | 223.1 | 204.0 | 24/03/2010 |
| 3 | 1 [CH] | 0.45 | 258.7 | 229.8 | 0.38 | 270.3 | 149.5 | 140.5 | 220.2 | 204.4 | 24/03/2010 |
| 4 | 1 [CH] | 0.44 | 252.5 | 284.6 | 0.29 | 269.8 | 164.4 | 155.3 | 222.5 | 205.8 | 26/03/2010 |
| 5 | 2 [CH] | 0.70 | 257.3 | 311.4 | 0.21 | 270.3 | 218.7 | 201.0 | 250.7 | 224.0 | 10/02/2010 |
| 6 | 2 [CH] | 1.18 | 269.4 | 372.6 | 0.22 | 272.7 | 223.2 | 208.7 | 247.6 | 222.0 | 18/03/2010 |
| 7 | 2 [CH] | 0.82 | 265.3 | 284.0 | 0.21 | 271.8 | 211.9 | 199.4 | 236.6 | 224.6 | 20/03/2010 |
| 8 | 2 [CH] | 0.91 | 267.1 | 324.8 | 0.23 | 272.5 | 201.4 | 190.2 | 230.0 | 211.0 | 20/03/2010 |
| 9 | 2 [CH] | 0.83 | 268.3 | 292.8 | 0.25 | 272.9 | 207.5 | 188.7 | 237.7 | 203.2 | 20/03/2010 |
| 10 | 2 [CH] | 1.74 | 266.0 | 380.3 | 0.17 | 272.8 | 244.9 | 227.7 | 251.2 | 231.6 | 22/03/2010 |
| 11 | 2 [CH] | 1.80 | 266.8 | 367.8 | 0.18 | 272.9 | 227.3 | 206.6 | 241.4 | 203.4 | 22/03/2010 |
| 12 | 2 [CH] | 1.50 | 266.4 | 380.9 | 0.20 | 272.7 | 222.2 | 198.4 | 243.2 | 213.8 | 22/02/2010 |
| 13 | 2 [CH] | 1.19 | 265.8 | 351.4 | 0.18 | 272.5 | 223.5 | 196.3 | 245.9 | 222.4 | 22/03/2010 |
| 14 | 3 [CH] | 0.51 | 258.5 | 308.4 | 0.21 | 269.7 | 195.4 | 180.8 | 237.7 | 210.9 | 13/02/2010 |
| 15 | 3 [CH] | 0.34 | 258.6 | 262.7 | 0.20 | 267.2 | 185.3 | 170.0 | 241.2 | 214.8 | 13/02/2010 |
| 16 | 3 [CH] | 0.57 | 259.3 | 328.0 | 0.28 | 270.1 | 180.6 | 165.2 | 218.3 | 187.3 | 23/03/2010 |
| 17 | 3 [CH] | 0.19 | 259.1 | 263.2 | 0.38 | 264.6 | 150.9 | 139.6 | 216.4 | 185.0 | 23/03/2010 |
| 18 | 4 [SIR] | 0.21 | 266.3 | 241.4 | 0.14 | 272.3 | 251.7 | 231.5 | 263.2 | 245.1 | 17/01/2011 |
| 19 | 4 [SIR] | 0.33 | 271.6 | 254.6 | 0.17 | 273.0 | 250.5 | 226.3 | 262.9 | 243.2 | 27/01/2011 |
| 20 | 4 [S-R] | 0.47 | 269.4 | 179.2 | 0.09 | 273.5 | 258.1 | 236.5 | 258.3 | 246.4 | 08/12/2010 |

polarization (H-pol) at a height of approximately 2 m above the ground and at an angle of 53° with a PR-series field radiometer (Radiometrics Corporation, Boulder, CO) close to the angle used by satellites. The footprint of the measurements at the snow surface of snow was approximately 0.6 m × 0.6 m. Radiometer calibration was based on one measurement taken with Eccosorb at the ambient temperature (i.e., warm reference) and another measurement taken over a surface of liquid nitrogen (i.e., cold reference) (see [69]). In the worst case, the measurement error for the calibration target was estimated as ±2 K. Ambient and cold point measurements from before and after each measurement period (typically separated by three to five days) were used to produce a final calibrated $T_B$ data set. For the snowpits at SIRENE, the $T_B$ measurements were taken at 19 and 37 GHz at an angle of 54° and at a height of approximately 1.5 m above the ground. The radiometers were calibrated before and after the winter season using ambient and cold targets.

For each site, profiles of snow temperature, snow density, and SSA were taken at a vertical resolution of 5 cm in the footprint of the radiometric measurements. The density was measured with a 185-cm$^3$ density cutter, and the samples were weighed with a 100-g Pesola light series scale with an accuracy value of 1 g. The temperature was measured with a Traceable 2000 digital temperature probe ($\pm 0.1$ °C). The soil surface temperature was also measured. The SSA was measured with the shortwave InfraRed Integrating Sphere (IRIS) system [42], which is based on the principle described in [19], which exploits the relationship between the SWIR snow reflectance and the SSA [29]. A snow sample obtained using a cylindrical snow sampler with a 10-cm diameter (parallel to the snow surface) and 6 cm long was placed directly under the opening of the integrating sphere in a closed box. The snow was then illuminated with a 1.33-$\mu$m laser, and the signal reflected in the sphere was recorded by an InGaAs photodiode, which generates a voltage. Calibration with Lambertian targets with known reflectances (Spectralon: 0.06, 0.25 0.60, 0.79, and 0.98 at 1.33 $\mu$m) allowed the measured voltages to be related to the snow reflectance. From the reflectance, the SSA was calculated with the [29] theoretical model as described by Montpetit *et al.* [42]. A summary of the average measurements of the 20 snowpits used is given in Table I.

## III. MODELS AND SSA ADAPTATION APPROACH

### A. Models

This section describes the two MSEMs used in this paper, i.e., DMRT-ML and HUT n-layer. The same soil emission model was used for the two models.

*1) DMRT-ML:* DMRT-ML [47] is an ML MSEM based on the DMRT [63]. Several studies have used this theory to examine the passive microwave emission from snow-covered ground [22], [34], Tedesco and Kim [36], [38], [65], [74].

The DMRT assumes that the snow cover is composed of ice spheres. Permittivity is calculated using the first-order quasi-crystalline approximation and the Percus–Yevick approximation. It has been shown that the DMRT is in agreement with numerical solutions of the 3-D Maxwell equations up to a density of 275 kg m$^{-3}$ [7], [65], which is a relatively low density for snow particularly when late in the snow season and at high latitudes.

This article has been accepted for inclusion in a future issue of this journal. Content is final as presented, with the exception of pagination.



The propagation of energy between the different snow layers is calculated with the DIScrete Ordinate Radiative Transfer (DISORT) method [26]. In this paper, the propagation of electromagnetic radiation was calculated for 32 streams. Brucker *et al.* [3] and [5] used this model in a study on Antarctic snow. The version used in this paper includes a soil reflectivity model (see Section III-A3), which is available online (http://lgge.osug.fr/~picard/dmrtml/).

*2) HUT n-layer:* The HUT n-layer model [58] is an extension of the semi-empirical HUT model that calculates the emission of a one-layer snow cover [48]. The attenuation coefficient of snow is calculated using an empirical equation given the frequency and the grain size ($D_{\text{eff}}$ is the microwave effective grain size, often derived from $D_{\max}$, which is the longest diameter of the observed snow grain).

The ML model is based on a two-flux approximation for each layer. The model calculates the upwelling and downwelling fluxes for each layer before it calculates the upwelling emission at the surface of the snow cover.

*3) Soil Emission Model:* The [70] model calculates the soil reflectivity for a rough surface. H-pol reflectivity $r_H$ is calculated as follows:

$$r_H = r_{H,\text{Fresnel}} \cdot \exp\left(-(k\sigma)^{\sqrt{-0.1\cos\theta}}\right) \tag{3}$$

where $k$ is the wavenumber, $\sigma$ is the standard deviation of the surface height (in meters), $\theta$ is the nadir angle (in degrees), and $r_{H,\text{Fresnel}}$ is the Fresnel coefficient. This equation is valid for $\theta$ smaller than 60°. The Fresnel coefficients were calculated using the soil permittivity calculated following [11]. Because soil properties were not measured (except for soil temperature), soil moisture was set to 0.35 and the soil was considered as nonfrozen (soil temperature at the SIRENE site close to 0 °C) and liquid water was present, whereas at the Churchill sites, soil temperatures was above the limit of $-5$ °C to $-7$ °C proposed by Mironov *et al.* [41] for complete freezing of tundra soil. The reflectivity of the soil in V-pol $r_V$ is derived from $r_H$ as follows:

$$r_V = r_H \cdot (\cos\theta)^{0.655}. \tag{4}$$

### *B. Grain Size Correction Factor $\phi$ and Retrieval of Soil Parameters*

The overall approach for adapting the MSEM to an effective snow grain metric derived from SSA measurements consists of optimizing a constant and frequency-independent factor $\phi$ applied to the optical radius [see (2)] following [3]. However, the [3] study was in central Antarctica where the snow depth is several orders of magnitude deeper than the microwave penetration depth. In the case of a seasonal snowpack, soil emission can be significant, and it depends on parameters that are rarely measured, such as roughness parameter, soil moisture, and freezing state. Optimizing the grain size correction factor and the soil parameter(s) in one operation is not the most appropriate approach because the uncertainty in the observations and the model approximations will be compensated for by uncertainty and interdependence between the optimized parameters. A more physically based approach consists of optimizing the $\phi$ factor by selecting the situations where the soil has the least contribution and using only the highest frequency at 37 GHz. The soil parameters are optimized in a second step using the opposite situation, i.e., the shallowest snowpits and the lowest frequency at 19 GHz. The validation then includes all of the sites and both frequencies.

To find sites where the soil had a small contribution at 37 GHz [weak soil contribution (WSC)], a sensitivity test with DMRT-ML for the simulated $T_{\text{B}}$ was carried out for a very rough soil (i.e., low soil reflectivity) and a very smooth soil (i.e., high soil reflectivity) with an initial value of $\phi = 2.85$ [3]. Without a reference value for $\phi$ when using the SSA as a grain size parameter in HUT n-layer (no previous studies have been conducted on this specific topic), these same WSC sites were used for the analysis of the HUT n-layer model.

Once the sites were selected, there were three phases for each of the two MSEMs.

*Phase 1 Optimization of $\phi$:* This phase consisted of calculating $\phi$ [see (2)] at 37 GHz in V-pol with an initial value for the soil roughness $\sigma$ of 0.5 cm for WSC sites. Some studies consider a soil roughness value of 1 cm [70], Ferrazzoli *et al.* [75], whereas the HUT model generally considers 0.3 cm (Pulliainen [76]). Hence, 0.5 cm can be considered as a plausible median value. By considering WSC at 37 GHz, we were able to properly optimize $\phi$ without compensating for errors related to the soil. Note that this approach applies a constant correction to each layer in the snowpack. An iterative process with an increment of 0.1 was used to calculate $\phi$ that minimized the root-mean-square error (RMSE) between the measured and simulated $T_B$ at 37 GHz in V-pol for the WSC sites such that

$$\text{RMSE}_\phi = \sqrt{\frac{\sum_{i=1}^{N}\left(T_{B\,\text{sim};i}^{37V} - T_{B\,\text{mes};i}^{37V}\right)^2}{N}} \tag{5}$$

where $N$ is the total number of sites. Only the V-pol was used to avoid the increased sensitivity to the effect of snow stratification at H-pol [16]. However, the values for H-pol were used for the validation in phase 3.

*Phase 2 Optimization of the Soil Parameters:* Using optimized factor $\phi$, the surface roughness parameter $\sigma$ for each site was optimized at 19 GHz (V-pol and H-pol) for the grassy sites (SIRENE and Saint-Romain) and the tundra sites (Churchill). To minimize the compensation of error between optimizations for phases 1 and 2, the sites used in phase 1 (WSC sites) were discarded in phase 2. Thus, only the sites where the soil contribution was more important were considered [strong soil contribution (SSC)]. We used an increment of 0.01 cm to find the $\sigma$ values that minimized $\text{RMSE}_\sigma$ calculated as a function of the measured $T_{\text{B}}$ ($T_{\text{B\,mes}}$) and the simulated $T_{\text{B}}$ ($T_{\text{B\,sim}}$) in V-pol and H-pol as follows:

$$\text{RMSE}_\sigma = \sqrt{\frac{\sum_{i=1}^{N}\left(T_{B\,\text{sim};i}^{19V} - T_{B\,\text{mes};i}^{19V}\right)^2 + \left(T_{B\,\text{sim};i}^{19H} - T_{B\,\text{mes};i}^{19H}\right)^2}{2N}}. \tag{6}$$

This article has been accepted for inclusion in a future issue of this journal. Content is final as presented, with the exception of pagination.



TABLE II
$T_B$ (K) SIMULATIONS FOR THE DMRT-ML MODEL WITH $\phi = 2.85$ AND $T_B$ AT 37 GHZ FOR A SMOOTH SOIL $T_B$ ($\sigma_0 : \sigma = 0$ cm) AND A ROUGH SOIL $T_B$ ($\sigma_{10} : \sigma = 10$ cm). COLUMNS 6 AND 7 ARE THE DIFFERENCE BETWEEN THESE SIMULATED $T_B$ AT V-POL AND H-POL, RESPECTIVELY. THE SSC SITES ARE HIGHLIGHTED IN GRAY

| Sites # | $T_B$V ($\sigma_0$) | $T_B$H ($\sigma_0$) | $T_B$V ($\sigma_{10}$) | $T_B$H ($\sigma_{10}$) | $T_B$V($\sigma_{10}$)-$T_B$V($\sigma_0$) | $T_B$H($\sigma_{10}$)-$T_B$H($\sigma_0$) |
|---|---|---|---|---|---|---|
| 1 | 202.7 | 187.4 | 217.0 | 203.7 | 14.3 | 16.3 |
| 2 | 148.7 | 138.1 | 151.9 | 141.3 | 3.2 | 3.2 |
| 3 | 137.2 | 127.9 | 139.3 | 129.9 | 2.0 | 2.0 |
| 4 | 187.5 | 170.7 | 195.3 | 178.8 | 7.8 | 8.1 |
| 5 | 226.3 | 205.6 | 234.0 | 214.1 | 7.7 | 8.5 |
| 6 | 250.0 | 231.4 | 251.1 | 232.6 | 1.1 | 1.2 |
| 7 | 216.5 | 201.3 | 219.9 | 205.1 | 3.4 | 3.7 |
| 8 | 220.2 | 202.5 | 221.6 | 203.9 | 1.4 | 1.4 |
| 9 | 215.9 | 201.5 | 217.5 | 203.1 | 1.6 | 1.6 |
| 10 | 256.1 | 240.2 | 256.9 | 241.1 | 0.8 | 0.8 |
| 11 | 252.7 | 239.2 | 253.5 | 240.2 | 0.8 | 1.0 |
| 12 | 251.5 | 237.6 | 252.4 | 238.6 | 0.9 | 1.0 |
| 13 | 245.5 | 231.1 | 247.5 | 233.3 | 2.0 | 2.2 |
| 14 | 219.8 | 201.6 | 229.7 | 212.6 | 9.9 | 11.0 |
| 15 | 218.4 | 197.1 | 234.9 | 215.0 | 16.5 | 18.0 |
| 16 | 204.1 | 182.6 | 208.1 | 186.6 | 4.0 | 4.1 |
| 17 | 176.5 | 160.5 | 186.0 | 170.2 | 9.5 | 9.7 |
| 18 | 237.8 | 226.1 | 264.9 | 256.8 | 27.1 | 30.7 |
| 19 | 239.9 | 229.2 | 259.5 | 252.2 | 19.6 | 23.0 |
| 20 | 233.3 | 220.2 | 267.8 | 262.4 | 34.4 | 42.2 |

*Phase 3:* Using the optimized parameters for certain sites ($\phi$ for phase 1 and $\sigma$ for phase 2), validation was performed for all sites, both frequencies, and both polarizations. Calculations of RMSE were used to evaluate the error.

## IV. RESULTS

### A. Identification of the Sites Where the Soil had a Low Impact

To retrieve the $\phi$ factor at 37 GHz in V-pol, snowpits where the soil had a low impact had to be identified (WSC sites). To identify these WSC snowpits, we used an initial value of $\phi$ of 2.85 [3], and we calculated $T_\mathrm{B}$ with DMRT-ML for two extreme soil conditions: 1) smooth soil (or "cold soil") with low reflectivity and $\sigma = 0$; and 2) rough soil (or "warm soil") with high reflectivity and $\sigma = 10$ cm. The sites where the difference in $T_B$ for both polarizations was smaller than 5 K were considered as WSC sites (see Table II). This selection process identified 11 WSC sites (2, 3, 6, 7, 8, 9, 10, 11, 12, 13, and 16).

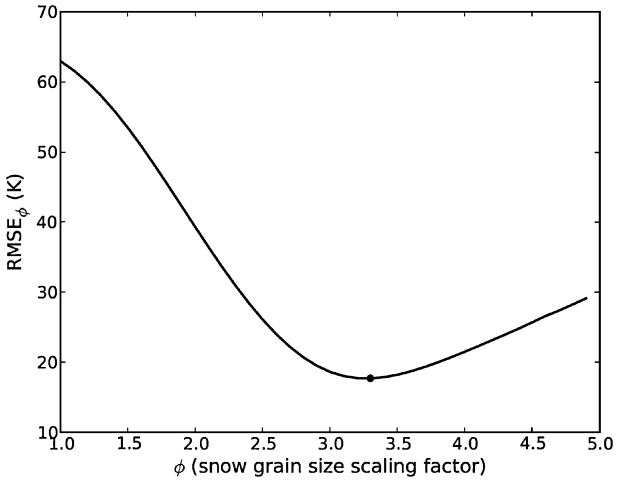


Fig. 1. RMSEs (RMSE$_\phi$) for the DMRT-ML model simulations as a function of grain size scaling factor $\phi$, which was applied to the optical radius [see (2)]. RMSE$_\phi$ are calculated for all the 11 WSC sites at 37-GHz V-pol. (Black dot) The minimum RMSE$_\phi$ = 17.7 K is at $\phi = 3.3$.

### B. Adaptation of Measured SSA for DMRT-ML

*Phase 1:* Using a surface roughness value of 0.5 cm, we calculated the $\phi$ that minimized the RMSE between the measured and simulated $T_\mathrm{B}$ at 37 GHz in V-pol [see (5)] for the 11 WSC sites. Fig. 1 shows that, without a correction for $R_o$, there is a very large RMSE$_\phi$ of 63.0 K. It also shows that there is an optimal value for the correction factor corresponding to $\phi = 3.3$ and a minimum RMSE$_\phi$ of 17.7 K. This value is slightly higher than that found by Brucker *et al.* [3]. However, the factor varies between $\phi = 2.9$ and $\phi = 3.7$ for RMSE$_\phi$ more than 2 K over the minimum RMSE$_\phi$, thus showing the possible variation of $\phi$.

*Phase 2:* In order to evaluate the ratio $r_V/r_H$ in the soil model [see (4)] using $\phi = 3.3$, the surface roughness of every site $\sigma$ was then separately calculated by minimizing the residual error between the measurements and simulations at 19 GHz. Table III shows the optimal values for $\sigma$ and the reflectivity values that minimized the differences between the simulated and measured $T_\mathrm{B}$ at 19 GHz in V-pol and H-pol separately. There is large variability in the $\sigma$ values between the different snowpits. The error related to modeling the snow, and more

This article has been accepted for inclusion in a future issue of this journal. Content is final as presented, with the exception of pagination.



TABLE III
OPTIMIZED DMRT-ML SOIL ROUGHNESS ($\sigma$ cm) FOR EVERY SITE AND REFLECTIVITY ($r_V$ AND $r_H$) AT 19 GHz. COLUMN 6 IS THE RATIO BETWEEN $r_V$ AND $r_H$. THE SSC SITES ARE HIGHLIGHTED IN GRAY

| Sites # | $\sigma_V$(cm) | $\sigma_H$(cm) | $r_V$ | $r_H$ | $r_V/r_H$ |
|---|---|---|---|---|---|
| 1 | 0.474 | 0.153 | 0.080 | 0.136 | 0.59 |
| 2 | 0.137 | 0.093 | 0.114 | 0.146 | 0.78 |
| 3 | 1.133 | 0.754 | 0.065 | 0.087 | 0.74 |
| 4 | 0.009 | 0.032 | 0.178 | 0.179 | 0.99 |
| 5 | 0.732 | 0.319 | 0.065 | 0.104 | 0.63 |
| 6 | 0.052 | 0.013 | 0.127 | 0.186 | 0.68 |
| 7 | 0.119 | 0.427 | 0.124 | 0.107 | 1.16 |
| 8 | 0.008 | 0.039 | 0.178 | 0.165 | 1.08 |
| 9 | 0.137 | 0.001 | 0.113 | 0.258 | 0.44 |
| 10 | 0.090 | 0.103 | 0.119 | 0.136 | 0.87 |
| 11 | < 0.001 | - | 0.205 | 0.426 | 0.48 |
| 12 | 0.011 | < 0.001 | 0.169 | 0.284 | 0.59 |
| 13 | 0.139 | 0.044 | 0.117 | 0.178 | 0.65 |
| 14 | 0.072 | 0.020 | 0.121 | 0.180 | 0.67 |
| 15 | 0.179 | 0.088 | 0.096 | 0.137 | 0.70 |
| 16 | < 0.001 | < 0.001 | 0.221 | 0.284 | 0.78 |
| 17 | 0.001 | < 0.001 | 0.187 | 0.271 | 0.69 |
| 18 | 2.383 | 0.500 | 0.032 | 0.076 | 0.42 |
| 19 | 2.324 | 0.295 | 0.034 | 0.095 | 0.36 |
| 20 | 1.396 | 0.842 | 0.057 | 0.088 | 0.65 |
| | | | | Mean $r_v/r_h$ ratio | 0.70 |
| | Mean $r_v/r_h$ ratio SSC sites (1, 4, 5, 14,15, 17, 18, 19, 20) | | | | 0.63 |

specifically the grain size, can nevertheless have a strong impact on the inverted roughness when the snow is deep and/or when the grains are large (greater effect of extinction) (see Table I). In one extreme case (site 10), it was impossible to converge toward the measured $T_\mathrm{B}$ at H-pol because the optimal soil reflectivity values were lower than the Fresnel coefficients (reflectivity of a plane surface), which is impossible with the selected soil emission model. A possible reason is an overestimation of the Fresnel coefficient due to uncertainty of the soil permittivity. Thus, the sites with deep snow cover or with large grains (WSC) were more influenced by the error related to the snow simulation (grain size) than by the soil roughness. Differences between simulated $T_B$ for low reflectivity of the soil ($\sigma = 0$) and high reflectivity ($\sigma = 10$ cm) at 19 GHz are significantly lower for WSC sites (29.8 K) than for SSC sites (46.1 K). The roughness values calculated at these sites were thus strongly biased, but the impact on the $T_B$ simulations was rather low.

Table III also shows that there was a significant variation in the ratio $r_V/r_H$. The $r_V/r_H$ values were lower for some locations such as the SIRENE sites (0.39), whereas there was strong variability for all of the tundra sites ($0.74 \pm 0.20$). The average $r_V/r_H$ was very similar to that used in (4) (0.71 for an incidence angle of 54°). The average ratio $r_V/r_H$ for the SSC sites was relatively similar at 0.63 (see Table III). However, for the grassy sites (all considered as SSC sites), the averaged ratio was significantly lower (0.47). These differences might impact the results mainly at 19 GHz where the soil contribution is generally larger.

As a further step, a unique value for the surface roughness was optimized for the grassy sites and another for the Churchill sites using only the SSC sites, which were the sites that were not chosen for optimizing $\phi$. The $\sigma$ that minimized the RMSE

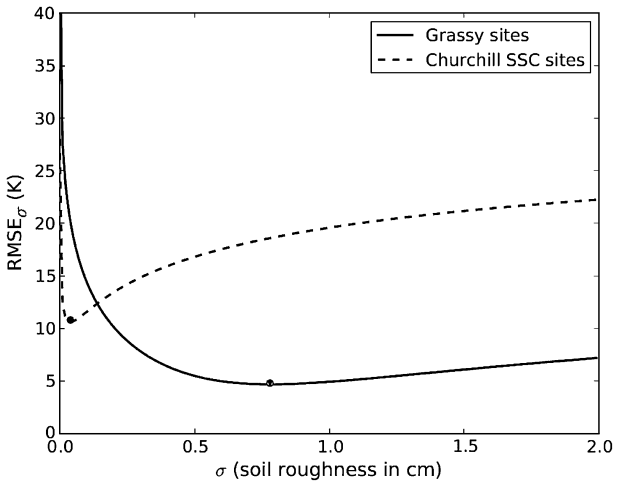


Fig. 2. RMSE ($\mathrm{RMSE}_\sigma$) for the optimization of the soil roughness parameter $\sigma$ at 19 GHz using the DMRT-ML model. Grassy sites are represented by the solid line and tundra sites by the dashed line [(gray point) grassy: $\sigma = 0.78$ cm; (black point) tundra: $\sigma = 0.04$ cm]. $\mathrm{RMSE}_\sigma$ is calculated from (6).

for $T_\mathrm{B}$ at 19 GHz [see (6)] was $\sigma = 0.78$ cm for the grassy sites (i.e., 18, 19, and 20) and $\sigma = 0.04$ cm for the tundra sites (i.e., 1, 4, 5, 14, 15, and 17) (see Fig. 2). The curve for the grassy sites does not show a pronounced minimum RMSE mainly because the reflectivity varied less strongly as a function of the roughness for larger $\sigma$ values (see Fig. 2). It should be noted that the difference between both $\sigma$ values may be due to the poor representation of soil moisture and texture, which were considered identical for both sites. The optimized $\sigma$ values should be also considered as an effective parameter (see Section V-C).

*Phase 3:* Fig. 3 shows the results for simulations using $\phi = 3.3$ and the optimized soil roughness values. The RMSE at 37 GHz is higher than that at 19 GHz for both polarizations [see Fig. 3(a)]. This difference is mainly due to sites where the wind had greatly increased the density of the topmost snow layers and the snow depth was the deepest. The smaller snow grains mainly at the surface (shallower penetration depth at 37 GHz) appear to cause an underestimation of the signal attenuation at these sites, which can result in an $R_\mathrm{eff}$ that is too low. Fig. 3(b) shows that the simulated ratios of 19H-pol/19V-pol are slightly higher than measurements. This difference may be due to the soil ratio $r_V/r_H$ [see (4)] in the soil model, which was slightly lower for our sites (0.63 for SSC sites [see Table III] compared to the [70] model value of 0.71 calculated from (4) for an incidence angle of 54°). Fig. 3(c) and (d), where simulated and measured $T_B$ behaviors are similar, shows the coherency of simulations and indicates that the scaling factor of $\phi = 3.3$ is valid at 37 and 19 GHz.

The effect of snow depth can be explained by the predominance of thick upper layers with small grains that caused the extinction to be underestimated. Kontu and Pulliainen [30] proposed a correction for the maximum extent $D_\mathrm{max}$ that reduces the weight of large grains and increases the weight of small grains. In this paper, to test this approach, we applied

This article has been accepted for inclusion in a future issue of this journal. Content is final as presented, with the exception of pagination.



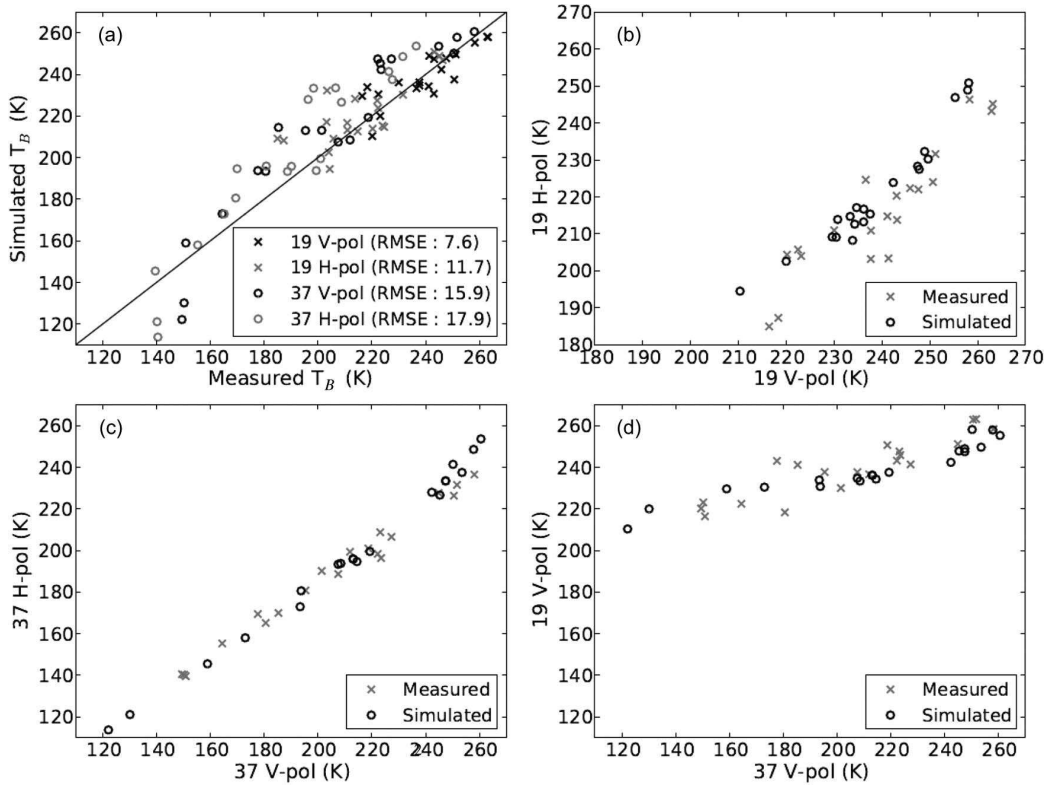


Fig. 3. DMRT-ML model simulations for a grain size correction factor of $\phi = 3.3$ and optimized $\sigma$ for all 20 snowpits at 19 and 37 GHz and two polarizations. (Upper left) Simulated brightness temperatures $T_B$ compared with measured $T_B$. In the inset, the RMSE (in kelvin) for each frequency and polarization is given. (Upper right) $T_B$ at 19-GHz H-pol versus $T_B$ at 19-GHz V-pol. (Bottom left) $T_B$ at 37-GHz H-pol versus $T_B$ at 37-GHz V-pol. (Bottom right) $T_B$ at 19-GHz V-pol versus $T_B$ at 37-GHz V-pol.

a similar formulation to the optical radius $R_o$ in DMRT-ML such that

$$R_{\text{eff}} = a\,[1 - \exp(-bR_0)] \tag{7}$$

where $a$ and $b$ are empirical parameters. Because of the shallow penetration depth (mainly at 37 GHz) for sites with a deep snowpack, this approach tends to increase the extinction by the smallest grains at the top layers relative to the largest grains and thus decreases the simulated $T_B$.

Using the same previous 11 WSC sites, parameters $a$ and $b$ were optimized (surface roughness was 0.5 cm). The values obtained were $a = 1.1$ and $b = 8.2$. The surface roughness values were then optimized for the tundra sites ($\sigma = 0.04$ cm) and the grassy sites ($\sigma = 1.1$ cm).

Fig. 4 shows that giving a higher weight to the smallest grains using the approach in [30] improves the RMSE at 37 GHz, principally in H-pol. The improvements in H-pol mainly result from the improvement of the four sites where $T_B$ were the highest (10, 18, 19, and 20) (see Table I) and from two other sites with coarse grains. There was also an improvement at 37 GHz for the most dense snowpack. However, for the three grassy sites, the results were poorer at V-pol. The RMSEs at 19 GHz were also slightly poorer. These results show that the Kontu and Pulliainen approach [30] for an ML model improves the simulations only under certain conditions. Part of this improvement may result because of the larger number of optimized parameters (two instead of one). This issue requires further investigation with a larger observational database.

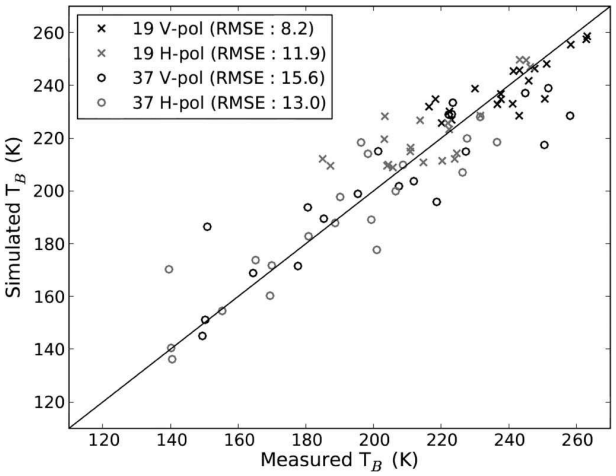


Fig. 4. DMRT-ML model simulations for a grain size correction with (7) ($a = 1.1$ and $b = 8.2$) and optimized soil roughness for all 20 snowpits at 19 and 37 GHz and two polarizations. In the inset, the RMSE (in kelvin) for each channel is given.

### C. Adaptation of Measured SSA for HUT n-Layer

Because there are no other studies that use the SSA as input data for HUT n-layer, it was difficult to choose an initial value

This article has been accepted for inclusion in a future issue of this journal. Content is final as presented, with the exception of pagination.



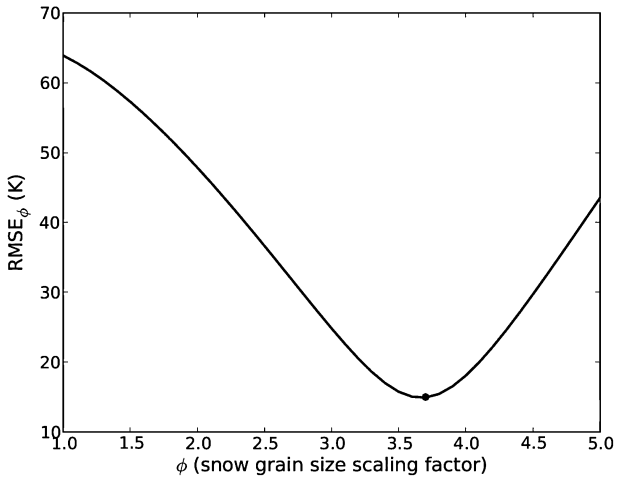


Fig. 5. RMSEs (RMSE$_\phi$) for the HUT n-layer model simulations as a function of grain size correction factor $\phi$, which was applied to the optical radius [see (2)]. Results are shown for the 11 WSC sites. (Black dot) The minimum RMSE$_\phi$ was 15.0 K at $\phi = 3.7$.

for $\phi$ for HUT n-layer in order to identify WSC sites. The same WSC sites used for DMRT-ML were thus used to optimize $\phi$ for HUT n-layer.

*Phase 1:* For an initial value of the surface roughness ($\sigma = 0.5$ cm), the optimized factor using (5) was $\phi = 3.7$ (see Fig. 5). This value is slightly sensitive to the choice of the initial value (for example, using an initial value of $\sigma = 0.01$ cm gives $\phi = 3.5$, whereas it gives $\phi = 3.8$ for $\sigma = 50$ cm). The choice of initial value of $\sigma = 0.5$ cm is based on previous studies. However, if we choose $\sigma = 0.04$ cm found at Churchill sites with DMRT-ML, we obtain $\phi = 3.5$. Thus, $\phi$ could slightly vary because of the initial $\sigma$ value.

As for DMRT-ML, to analyze the $r_V/r_H$ for the soil model [see (4)] using $\phi = 3.7$, the surface roughness for every site $\sigma$ was calculated separately. The results (not shown) were similar to those obtained with DMRT-ML with a mean ratio $r_V/r_H$ of 0.63 for all sites and 0.62 for the SSC sites.

The same SSC sites as for DMRT-ML were used to optimize $\sigma$ for the grassy and tundra sites. For the grassy sites, when minimizing the RMSE$_\sigma$ at 19 GHz [see (6)], we obtained $\sigma = 0.94$ cm. For the soil parameters for the Churchill sites, the $\sigma$ that minimized the RMSE$_\sigma$ was 0.06 cm. Thus, the $\sigma$ values that we obtained were again very similar to those obtained using DMRT-ML. Using the $\sigma$ values derived from HUT n-layer in DMRT-ML leads to small differences in RMSE at 19 GHz at V-pol (0.1 K) and H-pol (0.5 K) compared to using the values derived from DMRT-ML (see Section IV-B1). This shows that, by using two different snow models, we obtained almost the same soil parameters. This supports the reliability of the results for the soil parameters, the independence of the models, and the scaling factor for the snow grains.

Fig. 6(a) shows, however, that the RMSEs at 37 GHz are much higher than with DMRT-ML. HUT n-layer overestimated $T_B$, particularly for sites where $T_B$ was the lowest (containing the largest grains). It thus seems that the extinction by large grains was underestimated. This problem is probably due to the fact that HUT n-layer was initially designed to use $D_{\max}$ for the grain size parameter. Even with a scaling factor, $R_o$ will tend to underestimate the grains with a large $D_{\max}$ because the relationship between SSA and $D_{\max}$ is not linear [32]. Fig. 6(b) is similar to Fig. 3. Hence, it shows the possible high soil ratio $r_V/r_H$ [see (4)] in the soil model. Fig. 6(c) and (d) also shows similarity with Fig. 3. It indicates that the higher RMSE caused by attenuation underestimation is not reflected in HUT n-layer polarization and frequency coherency.

## V. Discussion

### A. Physical Basis for $\phi$ in the DMRT Model

The $\phi$ parameter introduced in this paper and in [3], which was adjusted in order to minimize the difference between the microwave observations and simulations, had a value much greater than unity and was different between the two studies (2.85 versus 3.3). Indeed, to use SSA measurements to drive DMRT-ML, as well as models based on the DMRT in general, it is important to understand the source of $\phi$ and to link its variability to measurable characteristics of snow. First, it is important to emphasize that, in agreement with the analysis by Durand *et al.* [16], measurement errors for other snowpack parameters having an influence on $T_B$ (e.g., density, depth, and stratigraphy) cannot explain an RMSE as high as 63 K that was obtained with $\phi = 1$ (see Fig. 1). In the following, we explore the possible sources influencing the magnitude of $\phi$. Second, we discuss the difference between $\phi$ from this paper and from measurements taken in Antarctica [3].

The DMRT version used in this paper assumes small homogeneous spheres, i.e., with $R_o$ much smaller than the wavelength [63]. These spheres all have the same radius, are randomly distributed, and are not necessarily in contact. If this was an accurate description of the microscopic structure of snow, then $R_{\text{eff}}$ in DMRT-ML would be equivalent to the radius of the spheres comprising our hypothetical snow, and we would obtain $\phi = 1$. However, this paper shows a significant departure of $\phi$ from unity that cannot be completely explained by measurement errors in the physical quantities of snow or in the microwave brightness temperature. It is thus clear that the difference between the microstructure of natural snow and the representation used in the DMRT is the principal cause of the high values of $\phi$. Two possible sources are discussed here, namely, the cohesion between the grains (stickiness) and the heterogeneity of snow grain size.

The position of snow grains is not random and independent because, among other things, the grains must physically touch each other to ensure the cohesion of the snow. In DMRT, this characteristic is modeled by using an attractive force between the spheres, which is parameterized by stickiness factor $\tau$ (see [64]). The resulting aggregation of grains forms clusters that interact with microwaves as objects that are larger than the spheres of which they are actually composed. This causes an increase in scattering, which is compatible with the high value of $\phi$ that is obtained when clustering is neglected. To test this hypothesis, DMRT-ML was modified to take into account stickiness in the simple case of "short range," i.e., the size of clusters is smaller than the wavelength. For 20 sites at 37 GHz

This article has been accepted for inclusion in a future issue of this journal. Content is final as presented, with the exception of pagination.



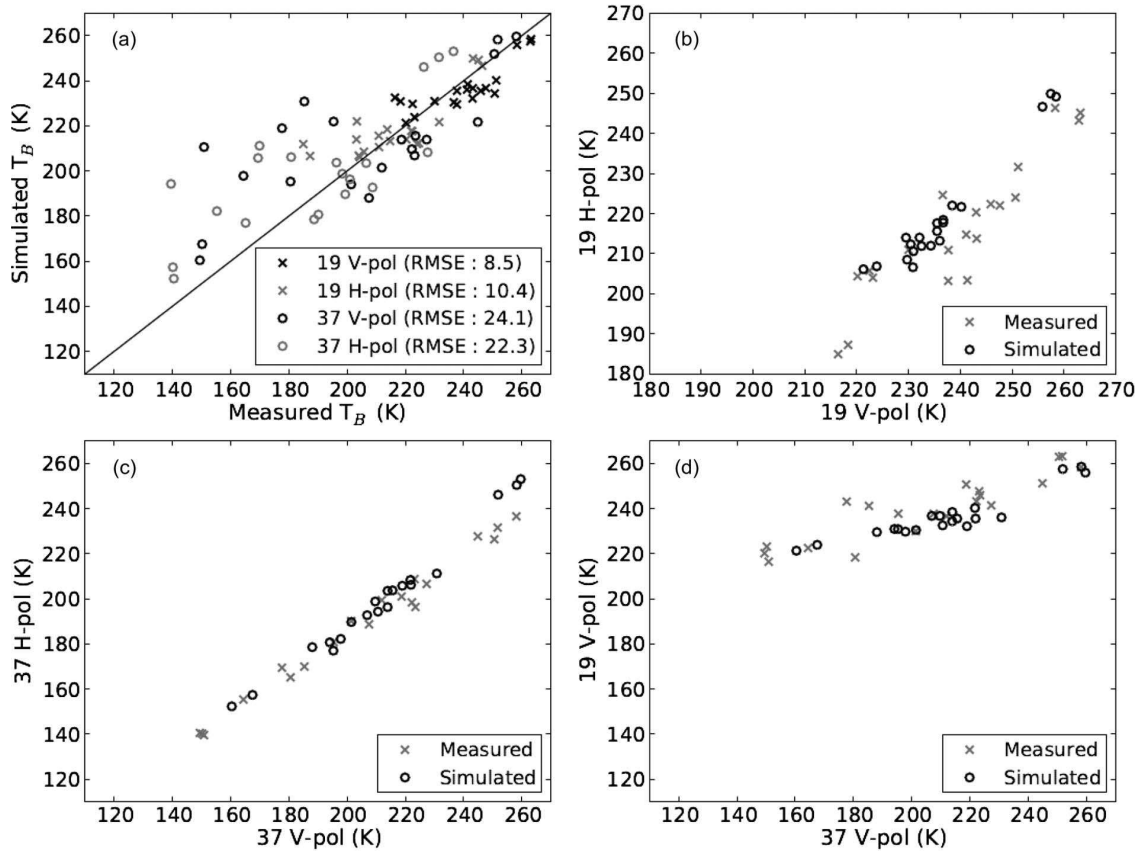


Fig. 6. HUT n-layer model simulations for a grain size correction factor of $\phi = 3.7$ and optimized $\sigma$ for all 20 snowpits at 19 and 37 GHz and two polarizations. In the inset, the RMSE (in kelvin) for each channel is given. (Upper left) Simulated brightness temperatures $T_B$ compared with measured $T_B$. (Upper right) $T_B$ at 19-GHz H-pol versus $T_B$ at 19-GHz V-pol. (Bottom left) $T_B$ at 37-GHz H-pol versus $T_B$ at 37-GHz V-pol. (Bottom right) $T_B$ at 19-GHz V-pol versus $T_B$ at 37-GHz V-pol.

and with the soil parameters optimized for DMRT-ML, a two-parameter ($\phi_{\text{sticky}}$ and $\tau$) optimization was carried out by a two-parameter space exploration (an increment of 0.1 for $\phi$ and 0.01 for $\tau$). The values that gave the lowest RMSE were $\phi_{\text{sticky}} = 2.6$ and $\tau = 0.44$ (see Fig. 7). These results show that stickiness could explain, in part, the value of $\phi = 3.3$ that was previously calculated. Fig. 7 also shows that, for a range of RMSE of $+1$ K over the minimal RMSE (14.5 K–15.5 K), we found a solution at $\phi_{\text{sticky}} = 1.4$ and $\tau = 0.13$, which is an interesting result that is discussed in more detail below. Note that the validity of the calculations for $\tau <\approx 0.3$ is not guaranteed for the "short-range" version of the stickiness implemented in DMRT-ML [7], [62]. In conclusion, even if the stickiness seems to be a pertinent physical explanation, in practice, its introduction poses difficulties because it is not a measurable quantity for natural snow and its optimization is not unequivocal, even in the simplified case that we considered here by using a constant value for the entire snowpack.

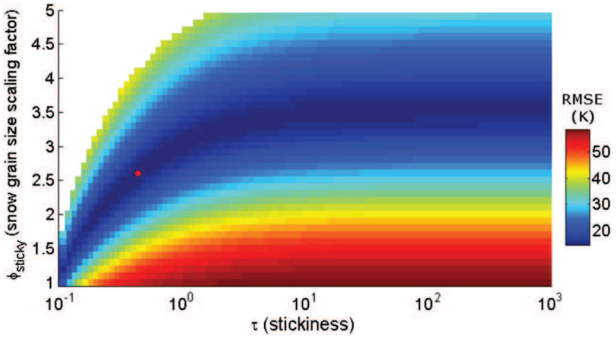


Fig. 7. RMSE (in kelvin) between DMRT-ML model $T_B$ simulations and $T_B$ measured as a function of grain size correction factor $\phi_{\text{sticky}}$ and stickiness $\tau$ (logarithmic scale). (White) Invalid result from DMRT-ML. (Red point) Minimum RMSE for $\phi_{\text{sticky}} = 2.6$ and $\tau = 0.44$.

Another factor that can explain the high value of $\phi$ is the heterogeneity of snow grains, particularly their size. This factor is important because the dependence of scattering on particle size is strongly nonlinear in the small particle range (for spheres and the frequencies examined in this paper, it varies with the cube of the radius) (e.g., [26]). As a result, large particles scatter much more than small particles. Thus, a collection of spheres with variable sizes has, in general, a larger scattering coefficient than a collection with the same SSA composed of identical spheres. In other words, the equivalent volume to surface area sphere approach that is valid in optics [21] is not valid in the microwave range [26].

This article has been accepted for inclusion in a future issue of this journal. Content is final as presented, with the exception of pagination.



To test the impact of the grain size distribution, we calculated the scattering and absorption coefficients (without stickiness) for sizes following the Rayleigh distribution in DMRT-ML; this distribution has a short upper tail, which permits the convergence of the calculation [71]. For this case, we obtained an optimal $\phi_{\mathrm{distribution}}$ of 2.4, which is a factor of 1.4 lower than the monodisperse case of $\phi = 3.3$ and confirms the result of Jin's work [26]. The precise value of $\phi_{\mathrm{distribution}}$ depends on the distribution chosen, which poses problems similar to stickiness because the grain size distribution may be variable depending on the type of snow, is difficult to measure in the field, may pose conceptual difficulties because the snow grains are not spherical, and sometimes may be hardly identifiable as individual grains.

The combination of the two factors described here seems to explain the high factor of 3.3. In fact, by setting $\tau = 0.13$, the product of $\phi_{\mathrm{sticky}}$ and $\phi_{\mathrm{distribution}}$ is 3.1, which is close to 3.3. However, this simple product is not rigorous, and the accurate calculation of the scattering and absorption coefficients for a size distribution of sticky spheres is not trivial [63] and it is not implemented in DMRT-ML.

It is quite possible that other factors contribute to coefficient $\phi$, such as the grain shape. To address this, our future research will determine whether $\phi$ varies depending on the type of snow, as suggested by the different $\phi$ obtained in this paper and in [3]. In fact, the parameters for the stickiness and the distribution of snow grain sizes may vary from one type of snow to another and have an influence on $\phi$. However, the difference obtained in both studies is not sufficiently large to exclude the uncertainty in the SSA or $T_B$ measurements. Indeed, the study in Antarctica used satellite-derived $T_B$ from kilometer-wide pixels compared to the point measurements of snow properties and $T_B$ used in this paper.

These are only qualitative explanations, and yet, given that the minimization previously obtained with $\phi = 3.3$ is reasonable from an assimilation perspective, the use of a fixed $\phi$ in the range of 2.8–3.5 is currently the most acceptable option.

### B. Analysis of $\phi$ for HUT n-Layer

The results obtained with the HUT n-layer model show that the SSA may not be a suitable parameter. As a semi-empirical model, HUT n-layer was parameterized as a function of measurements of $D_{\max}$. This difference in the conceptual characterization of snow grains may thus explain the higher RMSE with the HUT n-layer model compared with DMRT-ML, particularly for sites where there was a considerable fraction of depth hoar. It could also explain the higher value of $\phi = 3.7$ compared with $\phi = 3.3$ with DMRT-ML. Furthermore, we showed that the $\phi$ of HUT n-layer was slightly sensitive to soil parameterization. This sensitivity might be caused by the fact that the attenuation of large grains is underestimated by HUT n-layer at Churchill sites (as also illustrated in [8]) leading to an overestimation of the soil contribution. By using the $\sigma$ value derived from DMRT-ML, the $\phi$ value decreases to 3.5, whereas the RMSE remains almost the same. A simple adaptation of the HUT n-layer model to use the SSA as input is therefore not appropriate. It is thus necessary to find a parameterization of the model that is suitable.

TABLE IV
RMSE FOR HUT n-LAYER AND DIFFERENT CONFIGURATIONS OF THE DMRT-ML MODEL. IN PARENTHESES, THE CORRECTION APPLIED TO THE SNOW GRAINS IS SHOWN ($\phi$: (2); KONTU: (7); $\tau$: WITH STICKINESS; RAYLEIGH: RAYLEIGH GRAIN SIZE DISTRIBUTION)

| Models and approaches | 37V | 37H | 19V | 19H | Mean RMSE |
|---|---|---|---|---|---|
| **DMRT-ML ($\phi$ = 3.3)** | 15.9 | 17.9 | 7.6 | 11.7 | 13.3 |
| **DMRT-ML (Kontu: 1.1-8.2)** | 15.6 | 13.0 | 8.2 | 11.9 | 12.2 |
| **DMRT-ML ($\phi_{sticky}$ = 2.6; $\tau$ = 0.44)** | 14.5 | 16.0 | 7.9 | 10.8 | 12.3 |
| **DMRT-ML ($\phi$ = 2.4; Rayleigh)** | 14.3 | 16.2 | 7.6 | 11.2 | 12.3 |
| **HUT n-layer ($\phi$ = 3 .7)** | 24.1 | 22.3 | 8.5 | 10.4 | 16.3 |

### C. Soil Parameters

For the tundra sites, our study showed that the soil roughness had a low impact on $T_{\mathrm{B}}$ at 37 GHz. Even for sites where the snow depth was relatively shallow ($< 50$ cm), the attenuation by snow grains (principally by depth hoar) was sufficiently high to attenuate most of the contribution from the soil.

At 19 GHz, even if the grain size was the dominant factor, it was still necessary to take the soil into consideration. The average soil parameters for the grassy and tundra sites were retrieved for the case where the snow grain size had a low impact. There can nevertheless be considerable microvariability in the soil conditions (e.g., roughness, moisture, soil type, and litter) even within the same site [20], [54], [55]. Furthermore, considering the same soil moisture and texture for every site may lead to incorrect estimates of the soil permittivity property because of the Fresnel soil reflectivity. The calculated surface roughness becomes more like the average effective soil parameters for each site rather than true measurable roughness; further investigation will be needed to better understand the representation of this parameter. In addition, as shown in Table III, the ratio $r_V/r_H$ considered as constant in the roughness model of Wegmüller and Mätzler [70] may be different from one site to another as grassy sites exhibited a lower ratio.

### D. Synthesis of the Results

Several parameterizations for MSEM as a function of SSA measurements were evaluated in this paper and are summarized in Table IV. In terms of the average RMSE for the two frequencies and the two polarizations, the Kontu and Pulliainen approach [30], which was originally developed for HUT but applied to DMRT-ML in this paper, led to a slight improvement in the average RMSE compared with an approach with a fixed $\phi$ (see Table IV). The approaches with stickiness and the size distribution also led to an improvement of the average RMSE. The Kontu and Pulliainen approach [30] with the HUT n-layer model was not presented because the optimization of the $a$ and $b$ coefficients converged to a result equivalent to $\phi = 3.7$. The Kontu and Pulliainen approach [30] tends to increase the underestimation of extinction for large grains and thus overestimates the $T_B$ on snowpits having a large proportion of depth hoar.

This article has been accepted for inclusion in a future issue of this journal. Content is final as presented, with the exception of pagination.



## VI. Conclusion

The size of the scatterers in snow is the main parameter influencing the passive microwave emission. The objective of this paper was to parameterize two radiative transfer models (i.e., DMRT-ML and HUT n-layer) using snow SSA measurements to characterize grain size and ground-based radiometer measurements at 19 and 37 GH to evaluate the models.

For DMRT-ML, we found that a value of $\phi = 3.3$ minimized the RMSE between the simulated and measured $T_B$. This factor may be explained, in part, by the grain size distribution and the stickiness between grains that tends to form clusters with a large effective size. This paper has shown that at 37 GHz, the model had a very low sensitivity to the soil parameters for most snowpacks, particularly for the deepest snowpacks or those with depth hoar. At 19 GHz, although the transparency of the snow was higher, the grain size extinction has an important contribution. The approach of Kontu and Pulliainen [30], which gives a higher weight to small grains, led to an 8% decrease in the RMSE but required an optimization of two parameters instead of one. For HUT n-layer, a simple adaptation for the SSA does not allow good estimates of the extinction mostly at 37 GHz, particularly for sites containing coarse grains.

Our results show that a grain size metric derived from SSA for snow applied to DMRT-ML led to an average RMSE (19 and 37 GHz) of approximately 13 K. The results are comparable to other studies where the variety of types of snow and the range of measured $T_B$ were more limited [8]: 12.0 K; [30]: 9.3 K; [35]: 13.1 K. For HUT n-layer, we obtained higher overall RMSE (16.3 K), mainly due to the 37-GHz results (23.2 K). The results were derived from a unique data set that included precise snow measurements (e.g., SSA) for various types of snow cover, as well as colocated *in situ* radiometric measurements. An analysis of a much larger database from new field measurements may refine the optimization of $\phi$ and provide a better understanding of the physical basis of this parameter.

## Acknowledgment

This project was carried out in part during a visit of the first author to the Laboratoire de Glaciologie et Géophysique de l'Environnement (CNRS/Université Joseph Fourier). The authors would like to thank the Churchill Northern Studies Centre and the Environment Canada staff that participated in the project for their collaboration and support, J. Lemmetyinen for providing the HUT n-layer model, and the two reviewers who helped in improving the quality of the manuscript.

## References

[1] T. Aoki, M. Fukabori, A. Hachikubo, Y. Tachibana, and F. Nishio, "Effects of snow physical parameters on spectral albedo and bidirectional reflectance of snow surface," *J. Geophys. Res. D, Atmosp.*, vol. 105, no. D8, pp. 10 219–10 236, Jan. 2000.

[2] L. Arnaud, G. Picard, N. Champollion, F. Domine, J.-C. Gallet, E. Lefebvre, M. Fily, and J. M. Barnola, "Measurement of vertical profiles of snow specific surface area with a 1 cm resolution using infrared reflectance: Instrument description and validation," *J. Glaciol.*, vol. 57, no. 201, pp. 17–29, Feb. 2011.

[3] L. Brucker, G. Picard, L. Arnaud, J.-M. Barnola, M. Schneebeli, and H. Brunjail, "Modeling time series of microwave brightness temperature at dome C, Antarctica, using vertically resolved snow temperature and microstructure measurements," *J. Glaciol.*, vol. 57, no. 201, pp. 171–182, Feb. 2011.

[4] L. Brucker, A. Royer, G. Picard, A. Langlois, and M. Fily, "Hourly simulations of the microwave brightness temperature of seasonal snow in Quebec, Canada, using a coupled snow evolution-emission model," *Remote Sens. Environ.*, vol. 115, no. 8, pp. 1966–1977, Aug. 2011.

[5] L. Brucker, G. Picard, and M. Fily, "Snow grain-size profiles deduced from microwave snow emissivities in Antarctica," *J. Glaciol.*, vol. 56, no. 197, pp. 514–526, Aug. 2010.

[6] M. Butt and R. Kelly, "Estimation of snow depth in the UK using the HUT snow emission model," *Int. J. Remote Sens.*, vol. 29, no. 14, pp. 4249–4267, Jul. 2008.

[7] A. T. C. Chang, J. L. Foster, and D. K. Hall, "Nimbus-7 SMMR derived global snow cover parameters," *Ann. Glaciol.*, vol. 9, pp. 39–44, 1987.

[8] C. Derksen, P. Toose, J. Lemmetyinen, J. Pulliainen, A. Langlois, N. Rutter, and M. C. Fuller, "Evaluation of passive microwave brightness temperature simulations and snow water equivalent retrievals through a winter season," *Remote Sens. Environ.*, vol. 117, pp. 236–248, Feb. 2012.

[9] C. Derksen, A. Walker, and B. Goodison, "Evaluation of passive microwave snow water equivalent retrievals across the boreal forest–tundra transition of Western Canada," *Remote Sens. Environ.*, vol. 96, no. 3/4, pp. 315–327, Jun. 2005.

[10] A. J. Dietz, C. Kuenzer, U. Gessner, and S. Dech, "Remote sensing of snow—A review of available methods," *Int. J. Remote Sens.*, vol. 33, no. 13, pp. 4094–4134, Jul. 2012.

[11] M. C. Dobson, F. T. Ulaby, M. T. Hallikainen, and M. A. El-Rayes, "Microwave dielectric behavior of wet soil—Part II: Dielectric mixing models," *IEEE Trans. Geosci. Remote Sens.*, vol. GRS-23, no. 1, pp. 25–34, Jan. 1985.

[12] F. Domine, M. Albert, T. Huthwelker, H. Jacobi, A. A Kokhanovsky, M. Lehning, G. Picard, and W. R. Simpson, "Snow physics as relevant to snow photochemistry," *Atmos. Chem. Phys.*, vol. 8, no. 2, pp. 171–208, Jan. 2008.

[13] F. Domine, A. Cabanes, A. Taillandier, and L. Legagneux, "Specific surface area of snow samples determined by CH4 adsorption at 77 K and estimated by optical microscopy and scanning electron microscopy," *Environ. Sci. Technol.*, vol. 35, no. 4, pp. 771–780, Feb. 2001.

[14] M. Durand and D. Liu, "The need for prior information in characterizing snow water equivalent from microwave brightness temperatures," *Remote Sens. Environ.*, vol. 126, pp. 248–257, Nov. 2012.

[15] M. Durand, E. J. Kim, and S. A. Margulis, "Radiance assimilation shows promise for snowpack characterization," *Geophys. Res. Lett.*, vol. 36, no. 2, p. L02 503, Jan. 2009.

[16] M. Durand, E. J. Kim, and S. A. Margulis, "Quantifying uncertainty in modeling snow microwave radiance for a mountain snowpack at the point-scale, including stratigraphic effects," *IEEE Trans. Geosci. Remote Sens.*, vol. 46, no. 6, pp. 1753–1767, Jun. 2008.

[17] C. Fierz, R. L. Armstrong, Y. Durand, P. Etchevers, E. Greene, D. M. McClung, K. Nishimura, P. K. Satyawali, and S. A. Sokratov, "The international classification for seasonal snow on the ground," UNESCO-IHP, Paris, France, IHP-VII Technical Documents in Hydrology No.83, IACS Contribution No.1, 2009.

[18] M. G. Flanner and C. S. Zender, "Linking snowpack microphysics and albedo evolution," *J. Geophys. Res.*, vol. 111, no. D12, p. D12 208, Jun. 2006.

[19] J. Gallet, F. Domine, C. Zender, and G. Picard, "Measurement of the specific surface area of snow using infrared reflectance in an integrating sphere at 1310 and 1550 nm," *Cryosphere*, vol. 3, no. 2, pp. 167–182, Aug. 2009.

[20] J. P. Grant, A. A. Van de Griend, M. Schwank, and J.-P. Wigneron, "Observations and modeling of a pine forest floor at L-band," *IEEE Trans. Geosci. Remote Sens.*, vol. 47, no. 7, pp. 2024–2034, Jul. 2009.

[21] T. C. Grenfell and S. G. Warren, "Representation of a nonspherical ice particle by a collection of independent spheres for scattering and absorption of radiation," *J. Geophys. Res.*, vol. 104, no. D24, pp. 31 697–31 709, Jan. 1999.

[22] N. Grody, "Relationship between snow parameters and microwave satellite measurements: Theory compared with Advanced Microwave Sounding Unit observations from 23 to 150 GHz," *J. Geophys. Res.*, vol. 113, no. D22, p. D22 108, Nov. 2008.

[23] M. T. Hallikainen, F. T. Ulaby, and T. E. van Deventer, "Extinction behavior of dry snow in the 18- to 90-GHz range," *IEEE Trans. Geosci. Remote Sens.*, vol. GRS-25, no. 6, pp. 737–745, Nov. 1987.

[24] C. Huang, S. A Margulis, M. T. Durand, and K. N. Musselman, "Assessment of snow grain-size model and stratigraphy representation impacts on snow radiance assimilation: Forward modeling evaluation," *IEEE Trans. Geosci. Remote Sens.*, vol. 50, no. 11, pp. 4551–4564, Nov. 2012.

This article has been accepted for inclusion in a future issue of this journal. Content is final as presented, with the exception of pagination.




[25] H.-W. Jacobi, F. Domine, W. R. Simpson, T. A. Douglas, and M. Sturm, "Simulation of the specific surface area of snow using a one-dimensional physical snowpack model: Implementation and evaluation for subarctic snow in Alaska," *Cryosphere*, vol. 4, no. 1, pp. 35–51, Jan. 2010.

[26] Y. Jin, *Electromagnetic Scattering Modelling for Quantitative Remote Sensing*. Singapore: World Scientific, 1994.

[27] R. E. Kelly, A. T. C. Chang, L. Tsang, and J. L. Foster, "A prototype AMSR-E global snow area and snow depth algorithm," *IEEE Trans. Geosci. Remote Sens.*, vol. 41, no. 2, pp. 230–242, Feb. 2003.

[28] N. P. Klingaman, B. Hanson, and D. J. Leathers, "A teleconnection between forced great plains snow cover and European winter climate," *J. Climate*, vol. 21, no. 11, pp. 2466–2483, Jun. 2008.

[29] A. A. Kokhanovsky and E. P. Zege, "Scattering optics of snow," *Appl. Opt.*, vol. 43, no. 7, pp. 1589–1602, Mar. 2004.

[30] A. Kontu and J. T. Pulliainen, "Simulation of spaceborne microwave radiometer measurements of snow cover using in situ data and brightness temperature modeling," *IEEE Trans. Geosci. Remote Sens.*, vol. 48, no. 3, pp. 1031–1044, Mar. 2010.

[31] A. Langlois, A. Royer, C. Derksen, B. Montpetit, and K. Goïta, "Coupling of the snow thermodynamic model SNOWPACK with the microwave emission model for layered snowpacks (MEMLS) for subarctic and arctic snow water equivalent retrievals," *Water Resour. Res.*, vol. 48, no. 12, pp. W12 524-1–W12 524-14, Dec. 2012.

[32] A. Langlois, A. Royer, F. Dupont, A. Roy, K. Goïta, and G. Picard, "Improved corrections of forest effects on passive microwave satellite remote sensing of snow over boreal and subarctic regions," *IEEE Trans. Geosci. Remote Sens.*, vol. 49, no. 10, pp. 3824–3837, Oct. 2011.

[33] A. Langlois, A. Royer, B. Montpetit, G. Picard, L. Brucker, L. Arnaud, P. Harvey-Collard, M. Fily, and K. Goïta, "On the relationship between snow grain morphology and in-situ near infrared calibrated reflectance photographs," *Cold Reg. Sci. Technol.*, vol. 61, no. 1, pp. 34–42, Apr. 2010.

[34] L. Legagneux, A.-S. Taillander, and F. Domine, "Grain growth theories and the isothermal evolution of the specific surface area of snow," *J. Appl. Phys.*, vol. 95, no. 11, pp. 6176–6184, Jun. 2004.

[35] J. Lemmetyinen, J. Pulliainen, A. Rees, A. Kontu, Y. Qiu, and C. Derksen, "Multiple-layer adaptation of HUT snow emission model: Comparison with experimental data," *IEEE Trans. Geosci. Remote Sens.*, vol. 48, no. 7, pp. 2781–2794, Jul. 2010.

[36] D. Liang, X. Xu, L. Tsang, K. M. Andreadis, and E. G. Josberger, "The effects of layers in dry snow on its passive microwave emissions using dense media radiative transfer theory based on the quasicrystalline approximation (QCA/DMRT)," *IEEE Trans. Geosci. Remote Sens.*, vol. 46, no. 11, pp. 3663–3671, Nov. 2008.

[37] D. Liang, K. Tse, Y. Tan, L. Tsang, and K. H. Ding, "Scattering and emission in snow based on QCA/DMRT and numerical Maxwell model of 3Dimensional simulations (NMM3D)," in *Proc. IEEE 9th Spec. Meet. Microw. Radiometry Remote Sens. Environ. (MicroRad)*, San Juan, Puerto Rico, Feb. 28–Mar. 3, 2006, pp. 197–202.

[38] G. Macelloni, S. Paloscia, P. Pampaloni, and M. Tedesco, "Microwave emission from dry snow: A comparison of experimental and model results," *IEEE Trans. Geosci. Remote Sens.*, vol. 39, no. 12, pp. 2649–2656, Dec. 2001.

[39] C. Mätzler, "Relation between grain-size and correlation length of snow," *J. Glaciol.*, vol. 48, no. 162, pp. 461–466, Jun. 2002.

[40] C. Mätzler and U. Wëgmuller, "Dielectric properties of fresh-water ice at microwave frequencies," *J. Phys. D, Appl. Phys.*, vol. 20, no. 12, pp. 1623–1630, Dec. 1987.

[41] V. L. Mironov, R. D. De Roo, and I. G. Savin, "Temperature-dependable microwave dielectric model for an Arctic soil," *IEEE Trans. Geosci. Remote Sens.*, vol. 48, no. 6, pp. 2544–2556, Jun. 2010.

[42] B. Montpetit, A. Royer, A. Langlois, P. Cliche, A. Roy, N. Champollion, G. Picard, F. Domine, and R. Obbard, "New short wave infrared albedo measurements for snow specific surface area retrieval," *J. Glaciol.*, vol. 58, no. 211, pp. 941–952, Sep. 2012.

[43] B. Montpetit, A. Royer, A. Roy, A. Langlois, and C. Derksen, "Snow microwave emission modeling of ice lenses within the snowpack using the microwave emission model for layered snowpacks (MEMLS)," *IEEE Trans. Geosci. Remote Sens.*, to be published.

[44] S. Morin, F. Domine, A. Dufour, B. Lejeune, B. Lesaffre, J.-M. Willemet, C. M. Carmagnola, and H.-W. Jacobi, "Measurements and modeling of the vertical profile of specific surface area of an alpine snowpack," *Adv. Water Resour.*, 2013. [Online]. Available: http://dx.doi.org/10.1016/j.advwatres.2012.01.010

[45] M. Pardé, K. Goïta, and A. Royer, "Inversion of a passive microwave snow emission model for water equivalent estimation using airborne and satellite data," *Remote Sens. Environ.*, vol. 111, no. 2/3, pp. 346–356, Nov. 2007.

[46] G. Picard, F. Domine, G. Krinner, L. Arnaud, and E. Lefebvre, "Inhibition of the positive snow-albedo feedback by precipitation in interior Antarctica," *Nat. Climate Change*, vol. 2, no. 11, pp. 795–798, Jul. 2012.

[47] G. Picard, L. Brucker, A. Roy, F. Dupont, M. Fily, and A. Royer, "Simulation of the microwave emission of multi-layered snowpacks using dense media radiative transfer theory: The DMRT-ML model," *Geoscientific Model Dev. Discuss.*, vol. 5, no. 4, pp. 3647–3694, Nov. 2012.

[48] J. T. Pulliainen, J. Grandell, and M. T. Hallikainen, "HUT snow emission model and its applicability to snow water equivalent retrieval," *IEEE Trans. Geosci. Remote Sens.*, vol. 37, no. 3, pp. 1378–1390, May 1999.

[49] A. Rees, J. Lemmetyinen, C. Derksen, J. T. Pulliainen, and M. English, "Observed and modelled effects of ice lens formation on passive microwave brightness temperatures over snow covered tundra," *Remote Sens. Environ.*, vol. 114, no. 1, pp. 116–126, Jan. 2010.

[50] S. Rosenfeld and N. Grody, "Anomalous microwave spectra of snow cover observed from Special Sensor Microwave/Imager measurements," *J. Geophys. Res.*, vol. 105, no. D11, pp. 14 913–14 925, Jan. 2000.

[51] A. Roy, A. Royer, and R. Turcotte, "Improvement of springtime streamflow simulations in a boreal environment by incorporating snow-covered area derived from remote sensing data," *J. Hydrol.*, vol. 390, no. 1/2, pp. 35–44, Aug. 2010.

[52] A. Roy, A. Royer, J.-P. Wigneron, A. Langlois, J. Bergeron, and P. Cliche, "A simple parameterization for a boreal forest radiative transfer model at microwave frequencies," *Remote Sens. Environ.*, vol. 124, pp. 371–383, Sep. 2012.

[53] V. Roy, K. Goïta, A. Royer, A. E. Walker, and B. E. Goodison, "Snow water equivalent retrieval in a Canadian boreal environment from microwave measurements using the HUT snow emission model," *IEEE Trans. Geosci. Remote Sens.*, vol. 42, no. 9, pp. 1850–1859, Sep. 2004.

[54] K. Saleh, J.-P. Wigneron, P. de Rosnay, J.-C. Calvet, M.-J. Escorihuela, Y. H. Kerr, and P. Waldteufel, "Impact of rain interception by vegetation and mulch on the L-band emission of natural grass," *Remote Sens. Environ.*, vol. 101, no. 1, pp. 127–139, Mar. 2006.

[55] T. J. Schmugge, J. R. Wang, and G. Asrar, "Results from the push broom microwave radiometer flights over the Konza Prairie in 1985," *IEEE Trans. Geosci. Remote Sens.*, vol. 26, no. 5, pp. 590–596, Sep. 1998.

[56] P. R. Singh and T. Y. Gan, "Retrieval of snow water equivalent using passive microwave brightness temperature data," *Remote Sens. Environ.*, vol. 74, no. 2, pp. 275–286, Nov. 2000.

[57] A.-S. Taillandier, F. Domine, W. R. Simpson, M. Sturm, and T. A Douglas, "Rate of decrease of the specific surface area of dry snow: Isothermal and temperature gradient conditions," *J. Geophys. Res.*, vol. 112, no. F3, p. F03 003, Sep. 2007.

[58] M. Takala, K. Luojus, J. Pulliainen, C. Derksen, J. Lemmetyinen, J.-P. Kärnä, and J. Koskinen, "Estimating northern hemisphere snow water equivalent for climate research through assimilation of space-borne radiometer data and ground-based measurements," *Remote Sens. Environ.*, vol. 115, no. 12, pp. 3517–3529, Dec. 2011.

[59] M. Tedesco and E. J. Kim, "Intercomparison of electromagnetic models for passive microwave remote sensing of snow," *IEEE Trans. Geosci. Remote Sens.*, vol. 44, no. 10, pp. 2654–2666, Oct. 2006.

[60] A. M. Toure, K. Goïta, A. Royer, E. J. Kim, M. Durand, S. A. Margulis, and H. Lu, "A case study of using a multilayered thermodynamical snow model for radiance assimilation," *IEEE Trans. Geosci. Remote Sens.*, vol. 49, no. 8, pp. 2828–2837, Aug. 2011.

[61] A. M. Toure, K. Goïta, A. Royer, C. Mätzler, and M. Schneebeli, "Near-infrared digital photography to estimate snow correlation length for microwave emission modeling," *Appl. Opt.*, vol. 47, no. 36, pp. 6723–6733, Dec. 2008.

[62] L. Tsang, J. A. Kong, K.-H. Ding, and C. O. Ao, *Scattering of Electromagnetic Waves: Numerical Simulations*. New York, NY, USA: Wiley, 2001.

[63] L. Tsang and J. A. Kong, *Scattering of Electromagnetic Waves: Advanced Topics*. New York, NY, USA: Wiley, 2001.

[64] L. Tsang, C.-T. Chen, A. T. C. Chang, J. Guo, and K.-H. Ding, "Dense media radiative transfer theory based on quasicrystalline approximation with application to passive microwave remote sensing of new snow," *Radio Sci.*, vol. 35, no. 3, pp. 731–749, Jan. 2000.

[65] L. Tsang, D. Liang, X. Xu, and P. Xu, "Microwave emission from snowpacks: Modeling the effects of volume scattering, surface scattering and layering," in *Proc. 10th Spec. Meet. Microw. Radiometry Remote Sens. Environ. (MicroRad)*, Firenze, Italy, Mar. 11–14, 2008, pp. 1–4.

[66] R. Turcotte, L. G. Fortin, V. Fortin, J. P. Fortin, and J. P. Villeneuve, "Operational analysis of spatial distribution and the temporal evolution

This article has been accepted for inclusion in a future issue of this journal. Content is final as presented, with the exception of pagination.



of the snowpack water equivalent in southern Québec, Canada," *Nordic Hydrol.*, vol. 38, no. 3, pp. 211–234, 2007.
[67] F. Vachon, K. Goïta, D. De Sève, and A. Royer, "Geophysical inversion of a physical-based model combined with *in situ* data assimilation for snow water equivalent monitoring," *IEEE Trans. Geosci. Remote Sens.*, vol. 48, no. 1, pp. 59–71, Jan. 2010.
[68] S. Vavrus, "The role of terrestrial snow cover in the climate system," *Climate Dyn.*, vol. 29, no. 1, pp. 73–88, Jul. 2007.
[69] A. Walker, "Snow cover variations over the Mackenzie river basin from SSM/I passive 37 microwave satellite data," *Ann. Glaciol.*, vol. 34, pp. 8–14, 2002.
[70] U. Wegmüller and C. Mätzler, "Rough bare soil reflectivity model," *IEEE Trans. Geosci. Remote Sens.*, vol. 37, no. 3, pp. 1391–1395, May 1999.
[71] R. L. West, L. Tsang, and P. Winebrenner, "Dense medium radiative transfer theory for two scattering layers with a Rayleigh distribution of particle sizes," *IEEE Trans. Geosci. Remote Sens.*, vol. 31, no. 2, pp. 426–437, Mar. 1993.
[72] A. Wiesmann and C. Mätzler, "Microwave emission model of layered snowpacks," *Remote Sens. Environ.*, vol. 70, no. 3, pp. 307–316, Dec. 1999.
[73] N. Kruopis, J. Parks, A. Arslan, H. Alasalmi, J. Koskinen, and M. Hallikainen, "Passive microwave measurements of snow-covered forest areas in EMAC'95," *IEEE Trans. Geosci. Remote Sens.*, vol. 37, no. 5, pp. 2699–2705, Sep. 1999.
[74] M. Tedesco and J. K. Kim, "Intercomparison of electromagnetic models for passive microwave remote sensing of snow," *IEEE Trans. Geosci. Remote Sens.*, vol. 44, no. 10, pp. 2654–2666, Oct. 2006.
[75] P. Ferrazzoli, L. Guerriero, and J.-P. Wigneron, "Simulating L-band emission of forests in view of future satellite applications," *IEEE Trans. Geosci. Remote Sens.*, vol. 40, no. 12, pp. 2700–2708, Dec. 2002.
[76] J. Pulliainen, "Mapping of snow water equivalent and snow depth in boreal and sub-arctic zones by assimilating space-borne microwave radiometer data and ground-base observations," *Remote Sens. Environ.*, vol. 101, pp. 257–269, 2006.

**Alexandre Roy** (S'11) received the B.Sc. degree in physical geography in 2002 from the Université de Montréal, Montréal, QC, Canada, and the M.Env. degree in remote sensing in 2009 from the Université de Sherbrooke, Sherbrooke, QC, where he is currently working toward the Ph.D. degree in remote sensing.

His research interests include snow, passive microwave, radar, land surface schemes, and water cycles.

**Ghislain Picard**, photograph and biography not available at the time of publication.

**Alain Royer** received the Ph.D. degree in geophysics from the University of Grenoble, Grenoble, France, in 1981.

From 1983 to 1988, he was a Natural Sciences and Engineering Research Council Fellow with the Centre d'Applications et de Recherches en Télédétection (CARTEL), Université de Sherbrooke, Sherbrooke, QC, Canada. Since 1988, he is a Professor at the Université de Sherbrooke. Between 2000 and 2010, he was also the Director of Cartel. He was involved in Canada's International Polar Year cryosphere project (2008–2011), and he leads several projects for improving remote sensing of snow using passive microwave radiometry over Arctic (Baffin Island, 2011), Antarctic (Dome C, 2012), and subarctic (Nunavik, 2008–2013) regions. His research interests are environmental geophysics from space, including the development of surface parameter retrieval algorithms from remote sensing data applied to northern climate change analysis.

**Benoit Montpetit** received the B.Sc. degree in physics in 2009 from the Université de Sherbrooke, Sherbrooke, QC, Canada, where he is currently working toward the Ph.D. degree in remote sensing.

He participated in multiple snow studies in the Centre d'Applications et de Recherches en Télédétection (CARTEL), Université de Sherbrooke, and at the Laboratoire de Glaciologie et Géophysique de l'Environnement (LGGE), Grenoble, France. His research interests include snow and soil microwave emission modeling, snow grain size measurements, and ice lens modeling and detection within snowpacks.

**Florent Dupont** received the B.Sc. degree in physical geosciences and the M.Sc. degree in geophysics and climate from Université Joseph Fourier, Grenoble, France, in 2008 and 2010, respectively. He is currently working toward the Ph.D. degree in remote sensing and physical modeling of snow both in the Laboratoire de Glaciologie et Géophysique de l'Environnement, Université Joseph Fourier, and in the Centre d'Applications et de Recherches en Télédétection, Université de Sherbrooke, Sherbrooke, QC, Canada.

During his research, he participated in several field campaigns in the Arctic and in the Alps.

**Alexandre Langlois** received the B.Sc. degree in physical geography and the M.Sc. degree in remote sensing in 2001 and 2003, respectively, from the Université de Sherbrooke, Sherbrooke, QC, Canada, and the Ph.D. degree in 2007 from the University of Manitoba, Winnipeg, MB, Canada, where he focused on the analysis of snow over sea ice using passive microwave radiometry.

He participated in numerous field campaigns in the Canadian and European Arctic regions. He completed a postdoctoral research in the Centre d'Applications et de Recherches en Télédétection, Département de Géomatique Appliquée, Université de Sherbrooke, where he has been an Assistant Professor since 2012. His main work focuses on snow and passive microwaves' model coupling over land.

Dr. Langlois has been also an active member on the executive of the Eastern Snow Conference being a Steering Committee Member and the Proceedings Editor since 2009.

**Chris Derksen** received the B.E.S., M.A., and Ph.D. degrees from the University of Waterloo, Waterloo, ON, Canada, in 1997, 1998, and 2001, respectively.

He is a Research Scientist in the Climate Research Division, Environment Canada, Toronto, ON, and holds an adjunct faculty position with the Department of Geography and Environment Management, University of Waterloo. His research activities focus on remote sensing of terrestrial snow cover and the use of satellite-derived data sets to identify interactions between the climate system and the cryosphere.

**Nicolas Champollion** was born in Albertville, France, in 1986. He received the Master's degree (with good mention) specializing in earth and environment sciences, with particularly focus on ocean, atmosphere, and hydrology, and the Ph.D. degree, whose subject study is the microwave emission of snow near the surface at Dome C, Antarctica, with a modeling and field measurement approach from Université Joseph Fourier (UJF), Grenoble, France, in 2009 and 2012, respectively.

In summer of 2008 and from January to July 2009, he was with the Laboratoire de Glaciologie et Géophysique de l'Environnement (LGGE, which is a mixed research center between UJF and the Centre National de la Recherche Scientifique), Grenoble, where he worked on the microstructure of snow, particularly the specific surface area. During his Ph.D. studies, he participated in the LGGE laboratory council and the Ph.D. school council. More recently, he has been participating in the scientific council of UJF.

## B.3 Article : Snow Specific surface area simulation using the one-layer snow model in the Canadian LAnd Surface Scheme (CLASS)

En 2013, Alexandre Roy a publié un article sur la simulation de la SSA à l'aide du modèle de surface CLASS. Il a été démontré que le module de calcul de la SSA ajouté à CLASS en mode hors ligne permet de simuler la SSA avec une bonne précision (de l'ordre de 25%) en comparaison aux mesures au sol pour des neiges sèches. Les résultats sont cependant moins bons en neige humide. Ces travaux cadrent bien avec ceux de cette thèse puisqu'il vise à permettre d'utiliser un schéma de surface de modèle climatique comme CLASS afin de simuler une température de brillance grâce à l'ajout du calcul de la SSA. L'acquisition et le traitement des données acquises pour cette étude ainsi que la révision de l'article par des échanges entre les co-auteurs ont été faites dans le cadre de cette thèse.

The Cryosphere, 7, 961–975, 2013
www.the-cryosphere.net/7/961/2013/
doi:10.5194/tc-7-961-2013
© Author(s) 2013. CC Attribution 3.0 License.

The Cryosphere Open Access

# Snow specific surface area simulation using the one-layer snow model in the Canadian LAnd Surface Scheme (CLASS)

**A. Roy**[1], **A. Royer**[1], **B. Montpetit**[1], **P. A. Bartlett**[2], **and A. Langlois**[1]

[1]Centre d'Applications et de Recherches en Télédétection (CARTEL), Université de Sherbrooke, 2500 Boulder Université, J1K2R1 Sherbrooke, QC, Canada
[2]Climate Processes Section, Environment Canada, 4905 Dufferin street, M3H 5T4 Toronto, ON, Canada

*Correspondence to:* A. Roy (alexandre.r.roy@usherbrooke.ca)

Received: 27 November 2012 – Published in The Cryosphere Discuss.: 18 December 2012
Revised: 29 April 2013 – Accepted: 24 May 2013 – Published: 20 June 2013

**Abstract.** Snow grain size is a key parameter for modeling microwave snow emission properties and the surface energy balance because of its influence on the snow albedo, thermal conductivity and diffusivity. A model of the specific surface area (SSA) of snow was implemented in the one-layer snow model in the Canadian LAnd Surface Scheme (CLASS) version 3.4. This offline multilayer model (CLASS-SSA) simulates the decrease of SSA based on snow age, snow temperature and the temperature gradient under dry snow conditions, while it considers the liquid water content of the snowpack for wet snow metamorphism. We compare the model with ground-based measurements from several sites (alpine, arctic and subarctic) with different types of snow. The model provides simulated SSA in good agreement with measurements with an overall point-to-point comparison RMSE of 8.0 $m^2 kg^{-1}$, and a root mean square error (RMSE) of 5.1 $m^2 kg^{-1}$ for the snowpack average SSA. The model, however, is limited under wet conditions due to the single-layer nature of the CLASS model, leading to a single liquid water content value for the whole snowpack. The SSA simulations are of great interest for satellite passive microwave brightness temperature assimilations, snow mass balance retrievals and surface energy balance calculations with associated climate feedbacks.

## 1 Introduction

Snow grain size is of particular interest for microwave snow emission models, the surface energy balance (albedo and turbulent fluxes) and atmospheric–snow chemistry interactions (Domine et al., 2008). At high microwave frequencies (generally measured at 19 GHz and 37 GHz), snow grain size is an important variable affecting snowpack extinction and scattering properties (Kontu and Pulliainen, 2010; Grody, 2008; Durand et al., 2008; Roy et al., 2004). Thus, snow grain size must be considered in microwave snow emission models (MSEM) for the retrieval of snow properties from satellite passive microwave observations (Langlois et al., 2012; Huang et al., 2012; Pardé et al., 2007). Hence, in passive microwave applications, prior information such as snow grain size from a snowpack physical model is required for snow water equivalent (SWE) estimates (Durand and Liu, 2012). The surface albedo is also sensitive to the snow grain size and its vertical profile (Wiscombe and Warren 1980; Jin et al., 2008; Lyapustin et al., 2009; Aoki et al., 2011). Gardner and Sharp (2010) found that the broadband albedos of snowpacks show a logarithmic relationship with specific surface area (SSA). The thermal properties of snow, such as snow conductivity and diffusivity, are also related to snow microstructure (Domine et al., 2008; Adams and Sato, 1993). Surface albedo and snow conductivity are thus key parameters for modeling the surface energy balance in order to understand the impact of snow cover on global and regional climate dynamics (Armstrong and Brun, 2008). They also have a major impact on the prediction of the snow water equivalent as well as the timing of melt onset (Franz et al., 2010).

However, many snow evolution models do not take into account snow grain size. The Canadian LAnd Surface Scheme (CLASS: Verseghy, 1991; Verseghy et al., 1993) is used in the Canadian global circulation models (Scinocca et al., 2008) and the Canadian Regional Climate Model (CRCM:

Music and Caya, 2007; Caya and Laprise, 1999); it includes a one-layer snow model that does not simulate snow grain metamorphism. This is a major limitation for the assimilation of passive microwave brightness temperature ($T_B$) data for the improvement of snow simulations. In the context of data assimilation, where physical and emission models of snow are coupled, estimates of snow grain size are needed (Durand et al., 2009; Toure et al., 2011; Langlois et al., 2012). The implementation of snow grain metamorphism within CLASS is thus of particular interest for assimilation purposes. This implementation is not, however, straightforward in a one-layer snow model because snow metamorphism depends on many variables, such as snow age and the temperature gradient, which lead to a stratification of snow layers with different grain sizes. Thus, a major difficulty is that the vertical stratification is not considered in single-layer physical snow models. This study aims to address this issue, as simply as possible, using the CLASS one-layer snow evolution model. Even if one layer snow models are less physically correct then multi-layered models (Brun et al., 1992; Bartlelt et al., 2002; Bougamont et al., 2005; Ettema et al., 2010; Niwano et al., 2012), the SnowMIP experiments have shown that CLASS performs relatively well (Brown et al., 2006; Rutter et al., 2009). Furthermore, in climate and meteorological models, the errors in snow simulations are often related to the precipitation inputs. Hence, in these contexts, a more complex multi-layer model would not necessarily produce better results.

Grain size is a parameter that is difficult to characterize accurately and measure in the field. The specific surface area (SSA), which represents the ratio of the surface area per unit of mass, is a well-defined parameter representing the geometric characteristics of a porous medium, such as snow (Dominé et al., 2001). Methods based on snow reflectance in the shortwave infrared (SWIR) can now provide rapid and reproducible field measurements of SSA (Gallet et al., 2009; Arnaud et al., 2011; Montpetit et al., 2012), which can be related theoretically to grain size. SSA can be related to the radius of a monodisperse collection of ice spheres, each having the same surface area to volume ratio, called the optical radius ($R_{opt}$):

$$R_{opt} = \frac{3}{\rho_{ice}\mathrm{SSA.}} \quad (1)$$

Recent studies have shown that SSA offers a reliable representation of snow grain size in the context of microwave emission snow modeling (MESM) (Roy et al., 2013; Montpetit et al., 2013; Brucker et al., 2011). These studies showed that a scaling factor on $R_{opt}$ derived from SSA is required to simulate brightness temperatures in order oversimplification of snow grain representation in models. From a good representation of snow grain size in the snowpack for microwave emission simulations, it is possible to determinate which part of the signal is attributable to snow grain and which is attributable to other snow characteristics of interest like SWE.

Considering the importance of snow grain size and the advances made in snow microstructure characterization with the SSA metric, many studies have developed approaches for modeling the evolution of SSA throughout the winter season. Cabanes et al. (2003) first proposed an empirical exponential decay function of time and temperature for snow SSA. Legagneux et al. (2003) showed, using laboratory experiments under isothermal conditions, that the decreasing trend of SSA is best fitted using a logarithmic function. That trend has also been confirmed with X-ray microtomography measurements (Flin et al., 2004; Kaempfer and Schneebeli, 2007; Chen and Baker, 2010). Taillandier et al. (2007), using methane adsorption SSA measurements (Domine et al., 2001) in a taiga environment, proposed empirical relationships for the decrease of SSA as a function of time based on the snow age, snow temperature and the temperature gradient within the snowpack. A similar approach relating SSA to snow type (fresh snow, recognizable particles, aged and rounded crystals, aged and faceted crystals, and depth hoar) and snow density was developed by Domine et al. (2007). Jacobi et al. (2010) implemented these last two approaches in the Crocus multi-layer snow model (Brun et al., 1992). With the model based on snow type and density (Domine et al., 2007), SSA was overestimated in surface snow, but this was mainly because Crocus underestimated density, as this model does not take into account the upward water vapor flux induced by the large temperature gradient in the subarctic snowpack (Taillandier et al., 2006); however, a generally good agreement between SSA simulations and measurements (methane adsorption) was observed when the SSA was calculated based on prognostic equations using snow age (Taillandier et al., 2007). Flanner and Zender (2006) developed a physically-based model to predict the evolution of dry snow SSA. The model considers the snow temperature, temperature gradient and snow density and uses two adjustable parameters for the distribution of crystal sizes and for the irregularity in particle spacing. A weakness of most of these previous approaches is that the wet snow metamorphism is not taken into account, whereas water within the snowpack leads to a drastic decrease of SSA (wet snow metamorphism) due to rapid rounding and an increase in the size of snow grains (Brun, 1989). However, Flanner et al. (2007) implemented wet snow metamorphism following Brun (1989) in the model of Flanner and Zender (2006). Note that wind can also have complex effect on snow grains by enhancing the rate of SSA decrease (Cabanes et al., 2003) or, on the contrary, leading to an increase in SSA (Domine et al., 2009). Morin et al. (2013) compared SSA deduced from the $R_{opt}$ values simulated by Crocus with SSA measured from SWIR reflectance (Gallet et al., 2009) in an alpine environment. They showed qualitative agreement between measured and simulated SSA and that its simulation is difficult under wet snow conditions mostly because of the difficulty in simulating adequately the vertical profile of liquid water content in the snowpack.

The main objective of this study is to evaluate an offline SSA model implemented in the one-layer CLASS snow model for different northern climate environments. More specifically, the SSA model is a multi-layer snow model driven by CLASS outputs to simulate the evolution of SSA in the different snow layers. The evolution of SSA is computed for dry snow using the model of Taillandier et al. (2007) based on snow aging, and the equation of Brun (1989) for wet snow metamorphism. The simulated SSA values are compared with measured SSA derived from SWIR reflectance (Montpetit et al., 2012; Gallet et al., 2009) for five different sites (two northern mid-latitude, arctic tundra, taiga and alpine) throughout the winter season. The model is developed in a perspective of passive microwave applications for SWE retrievals at a large scale, but could be used for other applications such as snow albedo estimates. The study also provides an additional validation of the Taillandier et al. (2007) equations using new sets of accurate in situ SSA measurements for different environments.

## 2 Method

### 2.1 CLASS-SSA model

The CLASS-SSA model operates in an "offline" mode, meaning that it uses the CLASS simulated state variables to simulate the SSA evolution, but without feedback on the snowpack evolution. The CLASS snow model is a one-layer model (a detailed description of the snow model in CLASS is given in Bartlett et al., 2006; Brown et al., 2006). Version 3.4 of the standalone driver for CLASS (Verseghy, 2009), which allows running the model using meteorological data, was used in this study. CLASS has been designed to run at a time step of 30 min or less, to ensure numerical stability of the modeled prognostic variables (Verseghy, 2009). In this study, CLASS is run at a time step of 30 min. In our case, the meteorological data used to drive the CLASS model (precipitation rate, air temperature, wind speed, air humidity, and incoming shortwave and longwave radiation) were derived from in situ measurements or from the North American Regional Reanalysis (NARR) data (Mesinger et al., 2006) (more details on driving data are provided in Sect. 2.2). The use of NARR data is motivated by the necessity to run the model at a large scale in the perspective of passive microwave space-borne applications. The thermal conductivity of snow was calculated from snow density using the empirical relationship described in Sturm et al. (1997).

The offline SSA model is a multilayer model, where layer evolution is constrained by snow density, snow depth and SWE from CLASS simulations. Figure 1 shows the flowchart of CLASS-SSA. The SSA evolution of dry snow is based on the logarithmic relationship for snow aging developed by Taillandier et al. (2007). The CLASS-SSA model adds snow layers when snowfall occurs. Consecutive precipitation

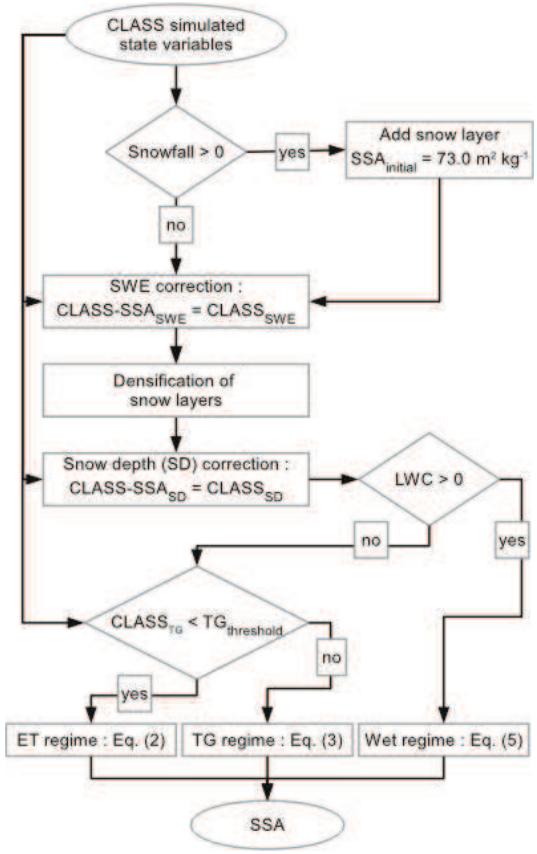


**Fig. 1.** CLASS-SSA model flow chart.

(precipitation occurring during two or more consecutive time steps) is however considered as one precipitation event and contributes to the same layer. The initial SSA ($SSA_{initial}$) was set to 73.0 $m^2 kg^{-1}$ (the mean SSA value for fresh snow measured by Domine et al., 2007; the $SSA_{initial}$ value is discussed in Sect. 4), and the density of each new snow layer was set to the fresh snow density calculated by CLASS (Hedstrom and Pomeroy, 1998). However, because we want the CLASS-SSA model to be coherent with the CLASS snow model, the snow parameters (SWE, snow depth and snow density) of the CLASS-SSA model are corrected during the snowpack evolution in order to match the corresponding values simulated by CLASS. Thus, prior to each time step, a correction factor is applied to the SWE value of every snow layer to fit the multilayer model SWE with the CLASS simulation. A densification routine is then implemented, mostly to estimate the position and thickness of each layer within the snowpack. The same densification model as the one used in CLASS (Bartlett et al., 2006) is applied to every layer. After compaction is applied to each layer, if the summed multilayer snow depth is lower than the snow depth simulated by CLASS, a correction factor is applied to the thickness of the

top snow layer so that the summed multilayer snow depth corresponds to the snow depth simulated by CLASS (Fig. 1). However, in this context, the top layer cannot be less than 100 kg m$^{-3}$. If it reaches 100 kg m$^{-3}$, densification is applied to the second layer and so on. In this case, the correction is applied only to the top layers to avoid an unrealistic thickening of the dense bottom layers. On the other hand, if the sum of the snow depths for all the layers is higher than the snow depth simulated by CLASS, a correction is applied to all the layers, but the density of any layer cannot exceed the maximum snow density estimated by CLASS. Thus, when the snowpack melts, the density of every layer increases due to the decreasing thickness, leading to wet densification.

The SSA evolution for each snow layer is then calculated considering the model of Taillandier et al. (2007) (Fig. 1). The model parameterizations for SSA evolution are based on snow age and snow temperature ($T_{\mathrm{snow}}$). Two algorithms are available, depending on the temperature gradient regime: one for equi-temperature (ET) metamorphism,

$$\begin{aligned}\mathrm{SSA}(t) = {} & [0.629 \cdot \mathrm{SSA}_{\mathrm{initial}} - 15.0 \cdot (T_{\mathrm{snow}} - 11.2)] \\ & - [0.076 \cdot \mathrm{SSA}_{\mathrm{initial}} - 1.76 \cdot (T_{\mathrm{snow}} - 2.96)] \\ & \cdot \ln\left\{ t + e^{\frac{-0.371 \cdot \mathrm{SSA}_{\mathrm{initial}} - 15.0 \cdot (T_{\mathrm{snow}} - 11.2)}{0.076 \cdot \mathrm{SSA}_{\mathrm{initial}} - 1.76 \cdot (T_{\mathrm{snow}} s - 2.96)}} \right\};\end{aligned} \tag{2}$$

and the other for strong temperature gradient (TG) metamorphism,

$$\begin{aligned}\mathrm{SSA}(t) = {} & [0.659 \cdot \mathrm{SSA}_{\mathrm{initial}} - 27.2 \cdot (T_{\mathrm{snow}} - 2.03)] \\ & - [0.0961 \cdot \mathrm{SSA}_{\mathrm{initial}} - 3.44 \cdot (T_{\mathrm{snow}} + 1.90)] \\ & \cdot \ln\{ t + e^{\frac{-0.341 \cdot \mathrm{SSA}_{\mathrm{initial}} - 27.2 \cdot (T_{\mathrm{snow}} - 2.03)}{0.0961 \cdot \mathrm{SSA}_{\mathrm{initial}} - 3.44 \cdot (T_{\mathrm{snow}} + 1.900)}} \}';\end{aligned} \tag{3}$$

where $t$ is the age of the snow layer in hours. Note that in Eqs. (2) and (3), SSA is in cm$^2$ g$^{-1}$. $T_{\mathrm{snow}}$ is the snow layer temperature (°C) calculated by linearly interpolating the air temperature and the CLASS simulated snow–soil interface temperature. Air temperature appears more accurate and representative than the surface (skin) temperature for estimating the snowpack temperature gradient. Figure 2 shows a rapid decrease in the SSA over the first few days, which is related to destructive metamorphism when snow crystals lose most of their complicated shape and break up into smaller grains with less total surface area (Sommerfeld and Lachapelle, 1970). This metamorphic process is faster in warmer snow (higher $T_{\mathrm{snow}}$) (Colbeck, 1983). After a few days, the decrease in SSA slows down earlier in the ET regime when compared with the TG regime. The process of constructive metamorphism is dominant when the temperature gradient induces water vapor transport from warm to cold temperatures, causing rapid grain growth from vapor deposition at the bottom of the snow grains (Colbeck, 1983). Hence, in the absence of that mechanism in ET conditions, the decrease in SSA slows and SSA rapidly reaches its minimum value.

According to Eqs. (2) and (3), the rate of SSA decrease for a given time step (ΔSSA) depends on snow age, snow temperature, temperature gradient and $\mathrm{SSA}_{\mathrm{initial}}$. Based on

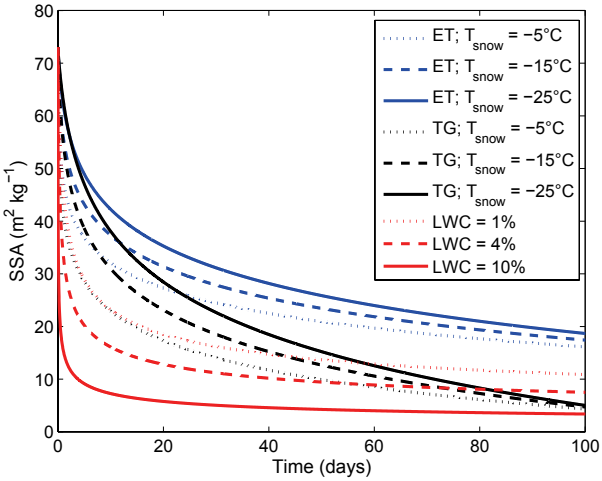


**Fig. 2.** SSA evolution as a function of the temperature gradient regime (ET or TG with LWC = 0) and snow temperature ($T_{\mathrm{snow}}$) from Eqs. (2) and (3), as well as a function of liquid water content (LWC) from Eq. (5).

Jacobi et al. (2010), we calculate the ΔSSA from Eqs. (2) and (3) according to the following:

$$\Delta\mathrm{SSA} = \mathrm{SSA}(t + \Delta t) - \mathrm{SSA}(t) \tag{4}$$

where $\Delta t$ corresponds to the time step (0.5 h). The ΔSSA is then subtracted from the model's previous SSA value. Jacobi et al. (2010) used a temperature gradient threshold ($\mathrm{TG}_{\mathrm{threshold}}$) of 15 K m$^{-1}$ to distinguish between ET and TG conditions, which will be evaluated in this study. Taillandier et al. (2007) also suggested a minimum value for SSA, because the logarithmic equation for SSA can lead to unrealistic low values. The minimal SSA value is set to 8.0 m$^2$ kg$^{-1}$, as proposed by Taillandier et al. (2007).

Nevertheless, the parameterization reported by Taillandier et al. (2007) does not take into account metamorphism during wet snow conditions. The equation of Brun (1989), derived from experimental measurements, provides a way to simulate the evolution of snow grain volume under wet snow conditions with respect to the liquid water content of the snowpack. The equation of Brun (1989) can be expressed with optical radius growth ($\Delta R_{\mathrm{opt}}$):

$$\Delta R_{\mathrm{opt}} = \frac{C_1 + C_2 \mathrm{LWC}^3}{R_{\mathrm{opt}}^2 \cdot 4\pi}, \tag{5}$$

where $C_1$ and $C_2$ are empirical coefficients ($C_1 = 1.1 \times 10^{-3}$ mm day$^{-1}$, $C_2 = 3.7 \times 10^{-5}$ mm day$^{-1}$) and LWC is the liquid water content in mass percentage. Note that in the experiment of Brun (1989), the empirical relationship was based on the volume equivalent sphere deduced from the measured mean convex snow grain radius, which is a definition closely related to the SSA. Figure 2 shows that the

SSA decrease is more pronounced when LWC increases in the snowpack. In this study, when the CLASS liquid water content is greater than zero, the model-derived SSA value is converted into its equivalent $R_{opt}$ using Eq. (1) in order to apply Eq. (5), and then reconverted to SSA. Furthermore, because the LWC distribution is not homogeneous within the snowpack, even though CLASS uses a single LWC value for the whole snowpack, here the LWC is first distributed in the top 10 cm. If the LWC in the top 10 cm is greater than 10 % in mass, the excess water is distributed to the rest of the snowpack. The 10 % limit can thus be considered as the water retention capacity. This value was chosen because 10 % in mass is the value where, in the experiment of Brun (1989), LWC reaches the irreducible water content and percolation occurs, leading to a saturation of grain growth rate increase for high LWC. However, the liquid water retention capacity of CLASS for the whole snowpack was kept at 4 %.

### 2.2 Sites and data

Snowpit measurements were conducted at five sites. Measurements were taken during the winter of 2010–2011 at the first two sites, which were located in an open mid-latitude northern environment. The sites were at the Site interdisciplinaire de recherche en environnement extérieur (SIRENE) experimental station at the Université de Sherbrooke (45.37° N, 71.92° W) and at St-Romain (45.45° N, 71.02° W; 80 km northeast of Sherbrooke) in Québec, Canada. Mean January temperature at Sherbrooke is −11.9 °C and the cumulated precipitation is 294.3 cm of snowfall, generally from November to April (National Climate Data, Environment Canada). Temperatures are generally slightly colder at St-Romain and cumulated snowfall higher because of the higher altitude (≈ 150 m over Sherbrooke). Two other sites were located close to the Churchill Northern Study Centre (58.73° N, 93.81° W) in Manitoba, Canada: one in an arctic dry fen (tundra) and the other in a taiga environment (black spruce forest). Churchill has a subarctic climate with a mean January temperature of −26.7 °C and accumulated snowfall of 191 cm, generally from October to May (National Climate Data, Environment Canada). The data were collected at these two sites during the Canadian CoReH20 Snow and Ice (CAN-CSI) campaign in the winter of 2010, which included four periods of intensive field sampling (January, February, March, and April). Further details of the campaign are provided in Derksen et al. (2012). The fifth and final site is the meteorological research station Col de Porte (CDP; 45.17° N, 5.46° E), near Grenoble, France, in the French Alps at an elevation of 1325 m. The daily average mean temperature for January is −1.63 °C and the mean total cumulated snowfall from December to April is 557 cm. Measurements for this last site were carried out during the winter of 2009–2010 (see Morin et al., 2013, 2012 for more details).

At the first four sites, SSA profiles were taken at a vertical resolution of 5 cm. The SSA was measured with the shortwave InfraRed Integrating Sphere (IRIS) system (Montpetit et al., 2012), based on the principle described by Gallet et al. (2009), which exploits the relationship between the SWIR snow reflectance and the SSA (Kokhanovsky and Zege, 2004). The density was measured with a 185 $cm^3$ density cutter, and the samples were weighed with a 100 g Pesola light series scale with an accuracy of 1 g. The temperature was measured with a Traceable 2000 digital temperature probe. Liquid water content of snow was also measured with the Snow Fork (Toikka Engineering Ltd., Espoo, Finland) at the Churchill arctic fen site during wet conditions on 13 and 16 April 2010. At the Col de Porte site (the fifth site), 16 SSA profiles were taken using the Dual Frequency Integrating Sphere for Snow SSA instrument (DUFISSS: Gallet et al., 2009), also based on the relationship between the SWIR reflectance and the SSA. Note that from late February onwards, warm conditions led to several snowmelt events, which caused a significant decrease in the snow SSA values. Hence, a distinction was made between dry snow conditions at Col de Porte (7 sets of data from 6 January to 16 February) and wet snow conditions (9 sets of data from 25 February to 20 April). The total snow depth and snow density profiles were also measured (Morin et al., 2013) and ultrasonic snow depth observations were acquired at SIRENE and Col de Porte.

NARR data (Mesinger et al., 2006) (2 m air temperature and air humidity, precipitation, 10 m wind speed, surface shortwave and longwave radiation) were used to force the CLASS model at the first four sites. Langlois et al. (2009) show that the NARR product delivers reliable input data for snowpack modeling. Forcing data from the NARR nearest neighbor pixel of each site was employed. As NARR provide data on a three-hour time step, the variables were interpolated to a 30 min time step, except for precipitation, which maintained a three-hour interval. To initialize the starting conditions, the CLASS model was run starting the year prior to the winter in this study: from 1 October 2009 to 1 June 2011 at SIRENE and St-Romain; from 1 October 2008 to 1 June 2010 at the two Churchill sites. At the Col de Porte site, meteorological variables (air temperature, humidity, windspeed, precipitation and incoming shortwave and longwave radiation) recorded with an hourly time resolution throughout the snow season of 2009–2010 (from 20 September 2009 to 10 May 2010) were interpolated to a 30 min time-step and used to drive the CLASS model (see Morin et al., 2012 for more details on the Col de Porte meteorological data).

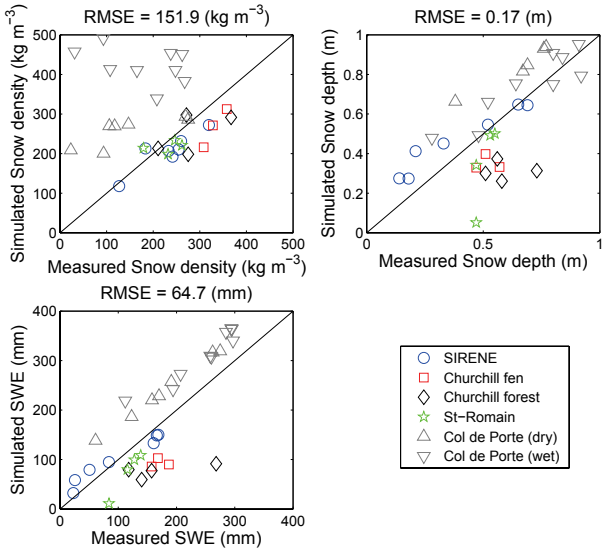


**Fig. 3.** Comparison of CLASS simulated snow properties with field measurements at different sites. Dry and wet sites at Col de Porte are separately indicated (see legend).

## 3 Results

### 3.1 CLASS snow parameter evaluation

First, an analysis of the one-layer CLASS snow model simulations was conducted. Simulated snow density, total snow depth and SWE were compared with all measurements taken in snow pits where SSA profiles were measured. Figure 3 shows that the simulation accuracy varies from one site to another. Snow density is generally accurate except at Col de Porte, where the density was overestimated. The overestimation is probably due to the high densification of snow under wet conditions with CLASS. For snow depth, there is an underestimation for the Churchill sites. Since there were underestimates at both forest and fen sites, NARR precipitation is probably the main cause. In fact, the cumulated NARR precipitation from the beginning of the snow season to the first snowpit measurement in February at the dry fen is lower (97.1 mm) than the snowpit measured SWE (157.3 mm). However, other phenomena such as blowing snow and interception by vegetation could lead to differences between the simulated and measured SWE (consequently snow depth as well). Comparisons between continuous ultrasonic snow depth observations at SIRENE and Col de Porte also show that errors in diagnosing precipitation phase at the beginning of the snow season lead to an offset of snow depth (overestimation at SIRENE) (Fig. 4a). This sensitivity to precipitation phase in CLASS is also demonstrated in Langlois et al. (2013). Figure 4b shows that underestimation of melt events at the beginning of the season also lead to positive offset in the snow depth. However, the snow depth RMSE is

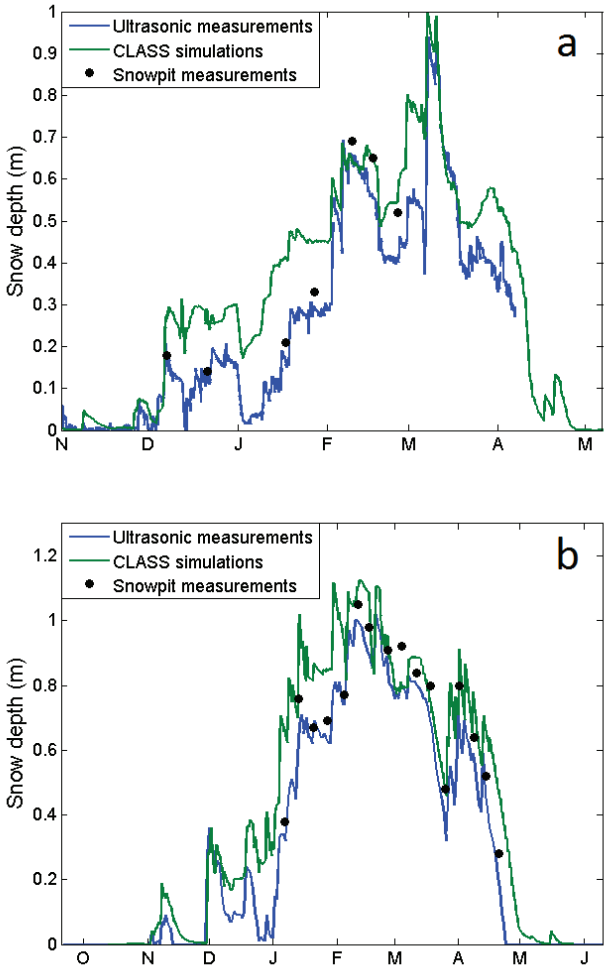


**Fig. 4.** CLASS snow depth simulations compared with Ultrasonic measurements at **(a)** SIRENE and **(b)** Col de Porte. Black dots are the snow depths from snowpit measurements.

comparable to what was found with CLASS 3.1 in the Snow Model Intercomparison Project (Brown et al., 2006). The overall SWE RMSE is 64.7 mm, which is close to what was found in Langlois et al. (2013) between modeled (CRCM) and observed SWE values for northern Québec. There is a good correlation between the measured and simulated SWE for the SIRENE and Col de Porte sites, where there is, however, a consistent overestimation. However, the SWE is underestimated at St-Romain and both Churchill sites.

### 3.2 CLASS-SSA model evaluation and validation

In this study, SSA is considered for the evaluation and validation because measurements of shortwave infrared reflectance of snow are related to SSA (see Sect. 2.2). To evaluate the CLASS-SSA simulations, an analysis of the $TG_{threshold}$ was first conducted. However, differences between the simulated

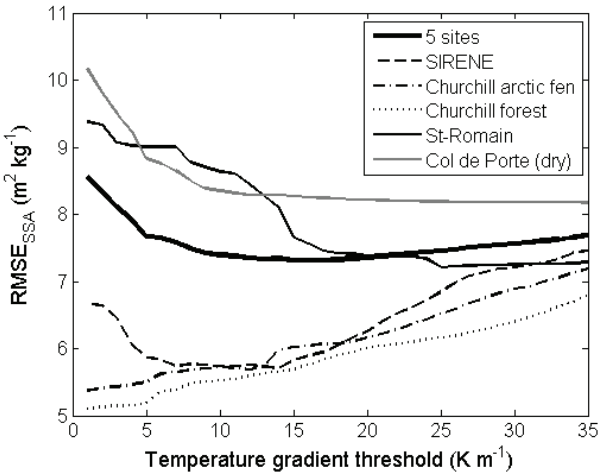


**Fig. 5.** RMSE$_{SSA}$ between the measured SSA and the simulated SSA using CLASS-SSA as a function of the temperature gradient threshold (TG$_{treshold}$).

and measured snow depths (Figs. 3 and 4), caused problems when relating measured SSA to its corresponding simulated SSA for a given snow depth in the snowpack. A correction was applied to the measured snow depth in order to match the simulated snow depth; this caused the measured profiles to be stretched or compressed. The root mean square error values between the simulated and measured SSA (RMSE$_{SSA}$) were calculated at the first four sites for different TG$_{threshold}$ values. The Col de Porte site where wet snow metamorphism dominated was excluded because wet metamorphism has a strong influence on SSA evolution that is not related to the TG$_{threshold}$. Figure 5 shows that, for TG$_{threshold}$ values between 10 K m$^{-1}$ and 20 K m$^{-1}$, the RMSE$_{SSA}$ for the 5 sites is relatively constant. The minimum RMSE$_{SSA}$ value (7.3 m$^2$ kg$^{-1}$) for the 5 sites is TG$_{threshold}$ = 16 K m$^{-1}$, which is close to the 15 K m$^{-1}$ value used by Jacobi et al. (2010). This value is also consistent with Taillandier et al. (2007), who proposed that the TG$_{threshold}$ should be between 9 K m$^{-1}$ and 20 K m$^{-1}$. The SIRENE site reached a minimum RMSE at TG$_{threshold}$ = 14 K m$^{-1}$, whereas the RMSE at both Churchill sites slightly increased with TG$_{threshold}$. The RMSE at the St-Romain site and the dry snow condition data for the Col de Porte site slightly decreased from 10 K m$^{-1}$ to 25 K m$^{-1}$ before reaching a constant value (Fig. 5).

The minimum RMSE was at TG$_{threshold}$ = 16 K m$^{-1}$and was thus used to simulate SSA with CLASS-SSA at the 5 sites (Fig. 6). Previous studies have generally defined the TG threshold for depth hoar formation between 10 K m$^{-1}$ and 20 K m$^{-1}$(Taillandier et al., 2007; Colbeck, 1983; Marbouty, 1980). However, it should be noted that the formation of faceted snow crystals has been observed at low growth rates under low gradient thresholds (Domine et al., 2003; Flin and Brzoska, 2008). Pinzer and Schneebeli (2009) proposed that alternating temperature gradients also leads to formation of rounded grains, similar to those observed in ET metamorphism. However, overall comparisons show good agreement between simulated and measured SSA (Fig. 6). More specifically, the SIRENE and St-Romain results show similar patterns with a gradient from low SSA at the bottom to higher SSA coming from fresh precipitation at the top. Nevertheless, there is a low SSA layer that appeared in mid-December 2010 caused by a melt event. This layer was observed as a melt ice-crust layer of 3 cm with low SSA (measured with a SWIR camera: Montpetit et al., 2012) during the snowpit measurements, but SSA was not measured with IRIS because it is difficult to extract this kind of snow (i.e., crusts) with the IRIS instrument. For the Churchill sites, both measured and simulated SSA are low near the bottom ($\approx$ 25 cm), which is related to the formation of depth hoar in the presence of a high temperature gradient. However, the simulated SSA values in the top layers are generally higher than the measurements. This may be due to the underestimation of the snow depth at the beginning of the season causing an underestimation of the relative thickness of the bottom layers with low SSA within the snowpack, which leads to an overestimation of the top layer thickness (Fig. 6c and d). Underestimation of the April 2010 measurements at both sites should, however, be attributed to an underestimation of snow LWC by CLASS during the spring melt, which limited the decrease of simulated SSA by wet metamorphism. In fact, LWC as measured with the Snow Fork instrument on 13 and 16 April at the Churchill arctic fen site suggests a strong underestimation by CLASS (0.2 % vs. 3.8 % on 13 April and 1.0 % vs. 15.5 % on 16 April, for CLASS and the Snow Fork, respectively). The issue with LWC is discussed in Sect. 4. The Col de Porte site illustrates the difference between the first seven dry sets of data showing good agreement, and the second period, starting on 25 February, when wet snow becomes predominant in the snowpack, giving a systematic overestimation of the SSA.

The comparison of the simulated SSA values to their corresponding measurements gives a RMSE of 8.0 m$^2$ kg$^{-1}$, which represents an error of 42.3 % (Fig. 7). Part of the error could be attributed to the fact that we did not necessarily compare the same snow layers due to different positions between the simulated and measured points. The correction applied to the simulated snow depth profile might be a factor, but the high variability within a SSA profile might also be a source of error. The simulated SSA variations are also strong within the snowpack, mainly for high SSA, where the evolution is faster (see Fig. 2). Considering the mean depth-averaged SSA weighted by the snow layer thickness, the RMSE decreases significantly to 5.1 m$^2$ kg$^{-1}$, representing an error of 25.7 %. Furthermore, the coefficient of determination ($R^2$) increases from 0.60 to 0.84. As mentioned previously, another major source of error corresponds to the influence of wet conditions, as observed at the Col de Porte site

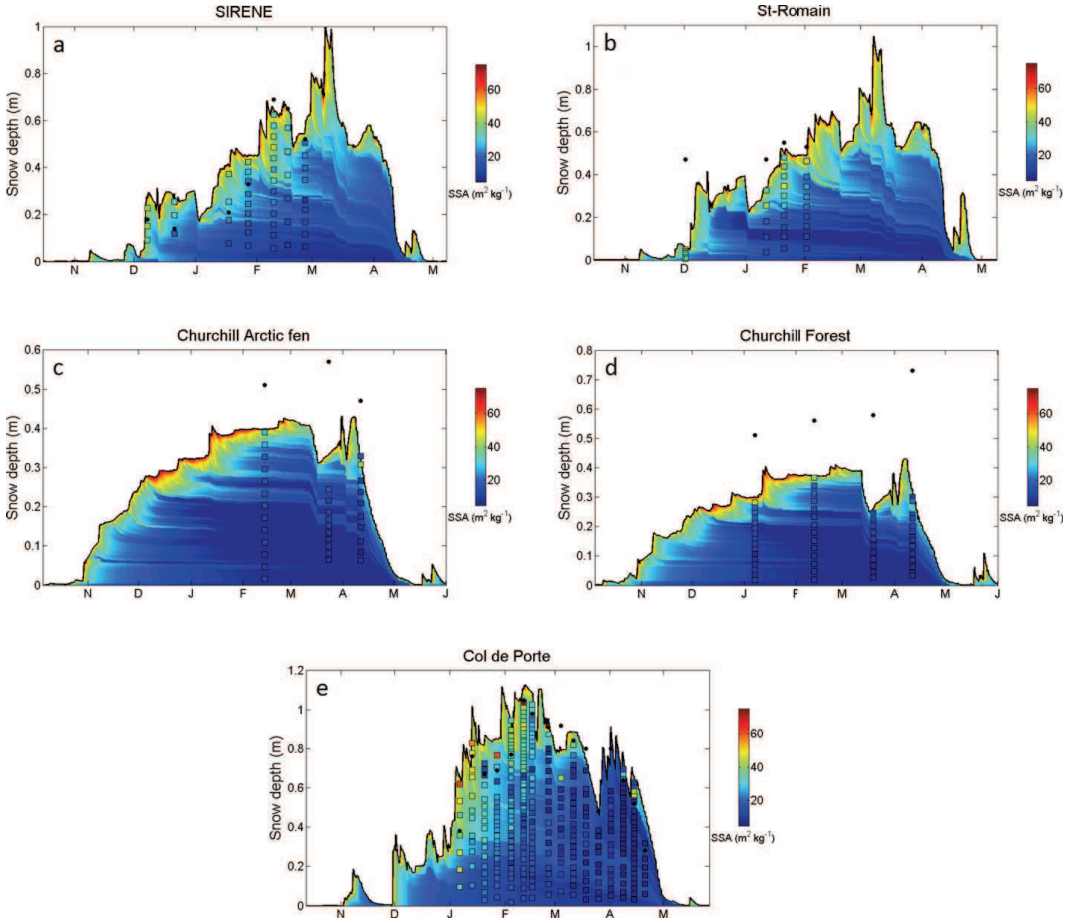


**Fig. 6.** Seasonal profile of simulated SSA at the five sites, **(a)** SIRENE, **(b)** St-Romain, **(c)** Churchill Arctic fen, **(d)** Churchill Forest, and **(e)** Col de Porte), compared to SSA measurements (squares: where the measured SSA profiles were adjusted to the simulated snow depth, see text). The measured profiles are stretched or compressed to fit with simulated snow depth. Black dots correspond to the measured snow depths.

after the mid-season. In fact, by removing data for this wet period, the depth-averaged RMSE decreases to 4.1 $m^2 kg^{-1}$ (17.5 %). As mentioned in Morin et al. (2013), even with a multi-layer model, limitations on the precision of LWC simulations exacerbate the difficulty of modeling snow grain evolution under wet conditions. The weakness of the model under wet snow conditions will be analyzed below in the Discussion (Sect. 4). The SSA at St-Romain and at Col de Porte (dry snow period) are underestimated by the model, while at the Churchill sites SSA is slightly overestimated due to the high simulated SSA in the top layers (Fig. 6c and d).

## 4 Discussion

The simulation of a stratified phenomenon such as SSA using a one-layer snow model such as CLASS requires certain assumptions and simplifications of the physics within the snowpack. These assumptions may induce errors in estimates of the SSA evolution. Here, we discuss the different elements that may impact the precision of the model and how they may influence the estimates. It is thus possible to identify the conditions under which CLASS-SSA is more limited and propose possible improvements. We then consider the proposed model's application, mainly in the context of passive microwave simulations.

### 4.1 Sources of errors

An assumption made in the CLASS-SSA approach is that the temperature profile of the snowpack is linear. In general, the temperature variations will be larger in the top layers that are responding to the variations in air temperature, while the bottom layers are less affected as the air temperature fluctuations do not reach these layers because of the low snow thermal conductivity

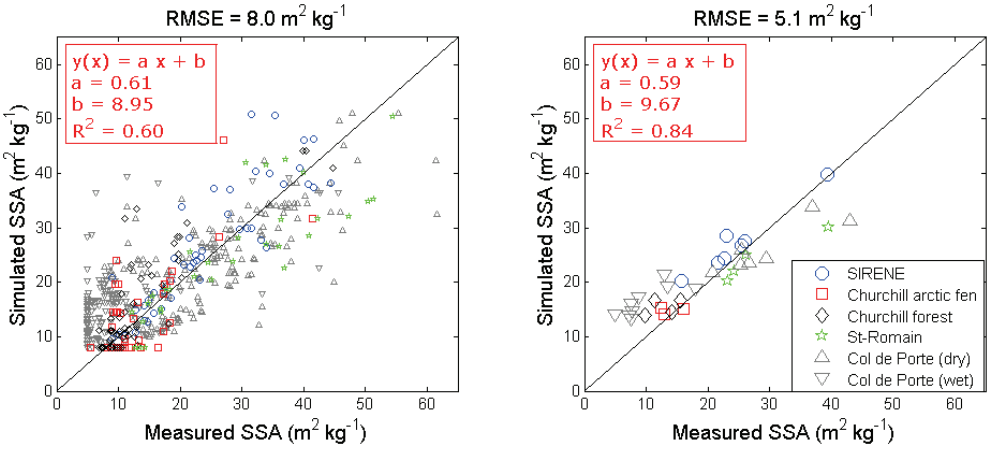


**Fig. 7.** Measured vs. simulated SSA comparison (left panel shows all points; right panel shows the one-layer average). The RMSE in averaged SSA (right panel) without the wet points is 4.1 $m^2 kg^{-1}$.

(Armstrong and Brun, 2008; Vionnet et al., 2012). Hence, in cold weather like in Churchill, the linearity of the temperature profiles is likely to induce underestimated snow layer temperatures. This phenomenon could also partly explain why the SSA of top layers at both Churchill sites is overestimated, considering that the SSA decrease is more pronounced with higher snow temperatures. Furthermore, the linearity of the temperature gradient would generally underestimate the local temperature gradient in the top layers and overestimate the local temperature gradient in the bottom layers. However, in the north during winter, this diurnal temperature cycle is generally in most cases less pronounced than over temperate or mountainous regions (Leathers et al., 1998). Thus, using a linear gradient throughout a dry and relatively shallow snowpack (below about 1 to 1.5 m depth) appears as a satisfactorily hypothesis in most cases over northern areas. Kondo and Yamazaki (1990) demonstrated that a linear temperature profile can be successfully employed in a snowmelt model.

As shown through the wet metamorphism simulation, CLASS-SSA is limited by the modeling of snow parameters in CLASS. Hence, the use of a one-layer model giving a LWC for the entire snowpack becomes a limitation. Furthermore, there might be an underestimation of LWC by CLASS. Measurements of LWC with the Snow Fork instrument at the Churchill arctic fen site suggests a strong underestimation by CLASS. Moreover, raising the limit of the simulated snowpack water retention capacity from 4 % to 10 % did not improve the simulated LWC and the SSA calculation under wet conditions in Col de Porte because the CLASS LWC rarely reaches the retention capacity. Part of the problem was, however, resolved by distributing the LWC mostly in the top layers, but the SSA evolution under wet conditions remains a weakness. Table 1 shows that the bias is significantly reduced when wet metamorphism is modeled with

**Table 1.** SSA bias and RMSE for Col de Porte wet snow condition data for different configurations of CLASS-SSA wet metamorphism.

| Model Configurations | RMSE ($m^2 kg^{-1}$) | Bias ($m^2 kg^{-1}$) |
|---|---|---|
| No wet metamorphism | 15.9 | 13.4 |
| Uniform LWC (CLASS) | 12.6 | 10.1 |
| LWC distributed in the top 10 cm (CLASS-SSA configuration) | 9.4 | 6.8 |
| Drastic increase of LWC (if LWC > 0 then LWC = 10 %) | 6.7 | −2.6 |

snowpack liquid water distributed in the top 10 cm at the Col de Porte wet sites compared to a wet metamorphism considering a uniform LWC or compared to no wet metamorphism. We also tested simulations by drastically increasing the total LWC artificially in CLASS (if LWC > 0 then LWC = 10 %); such conditions significantly reduced the simulated SSA, as expected, with a bias of $-2.6\,m^2 kg^{-1}$ for Col de Porte wet snow condition data (Table 1). This last case confirms that the problem comes from an underestimation of LWC in CLASS under warm conditions.

Snow depth errors from CLASS might also impact CLASS-SSA simulations. In fact, as shown for both Churchill sites (Fig. 6c and d), a bias in snow precipitation can impact the representation of the thickness of a given snow layer. Thus, in this study, part of the SSA error could be related to uncertainties in the NARR precipitation data (Langlois et al., 2009).

Other phenomena not parameterized in the CLASS snow model, such as blowing snow, could influence the simulated snow depth (Liston and Hiemstra, 2011). In open areas (four of our five sites), strong wind shear stress could have exceeded the snow particle resistance to dislocation (Li and Pomeroy, 1997). Hence, a less cohesive top snow layer with lower SSA could be removed almost completely in an open

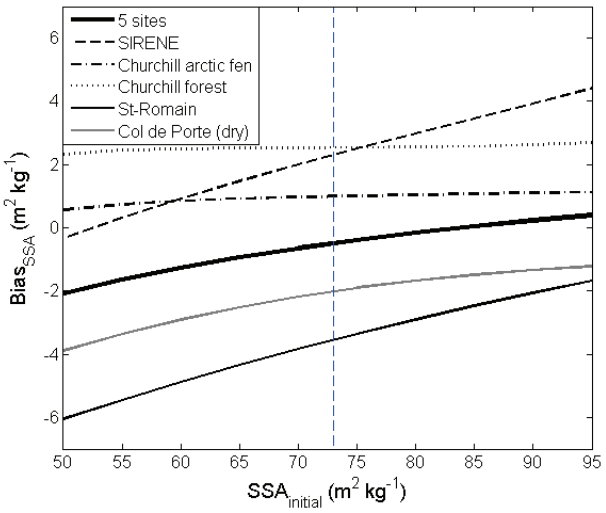


**Fig. 8.** Bias between the measured SSA and the simulated SSA using CLASS-SSA as a function $SSA_{initial}$ (the vertical dotted blue line represents the $SSA_{initial}$ set in CLASS-SSA at $73.0\,m^2\,kg^{-1}$).

arctic region like Churchill (Baggaley and Hanesiak, 2005). Furthermore, the snow thermal conductivity strongly varies between the tundra, where the snowpack has a high conductivity due to hard wind slabs, compared to taiga and forest snowpacks, which have three to four times lower thermal conductivity due to lower wind compaction and depth hoar development (see Gouttevin et al., 2012). These differences impact the snow temperature and temperature gradient but are not represented in CLASS-SSA.

In the CLASS-SSA model, the $SSA_{initial}$ value is fixed at $73.0\,m^2\,kg^{-1}$. This value was chosen based on freshly fallen snow SSA measurements (sampled maximum 24 h after snowfall) from methane adsorption by Domine et al. (2007). However, this study shows a range of 33.1 to $155.8\,m^2\,kg^{-1}$ with a standard deviation of $\pm 26.2\,m^2\,kg^{-1}$ based on 63 samples. Freshly fallen snow SSA is rarely modeled as it depends on the type of solid precipitation, which depends on the meteorological conditions (air temperature, wind, type of clouds, atmospheric stratification) when the snowflake is formed. Domine et al. (2007), however, proposed freshly fallen snow SSA values based on four types of fresh snow that can be related to density. As CLASS calculates the fresh snow density from the air temperature using the equation from Hedstrom and Pomeroy (1998), we implemented $SSA_{initial}$ values based on the Domine et al. (2007) relationship. However, this implementation did not change the results significantly: a slight increase in RMSE from 8.0 to $8.3\,m^2\,kg^{-1}$ was found. Figure 8 shows that $SSA_{initial}$ has a relatively low impact on simulations. The sensitivity to $SSA_{initial}$ values appears to be more important for the snowpack where measurements were taken mostly at the beginning of the season (SIRENE and St-Romain). A precise dynamic parameterization of freshly fallen SSA could probably improve the results, mostly for snow with high SSA at the beginning of the snow season.

### 4.2 Comparison with other models

Despite the above simplifications, the CLASS-SSA model simulates SSA with a reasonable accuracy for a wide range of snow types. Our RMSE of $8.1\,m^2\,kg^{-1}$ (Fig. 7) is comparable to the result obtained at Col de Porte by Morin et al. (2013) from internal computation of the optical radius in Crocus ($6.37\,m^2\,kg^{-1}$) and the method of Domine et al. (2007) based on the density and snow type ($8.08\,m^2\,kg^{-1}$). Snow data from the 2010 winter season at Col de Porte provide a unique and very accurate time series of SSA measurements (Morin et al., 2013). Figure 9 shows a comparison of temporal snowpack averaged SSA values at Col de Porte for CLASS-SSA, the Crocus model (Morin et al., 2013), and the measurements. When the snowpack is dry, both models underestimate the SSA. On 25 February and after, when wet conditions occurred, CLASS-SSA overestimates the SSA due an underestimation of the snowpack LWC, while Crocus still underestimates the SSA. For this dataset, CLASS-SSA simulations seem comparable to or better than Crocus in dry conditions. However, in wet conditions, Crocus better simulates the decrease in SSA as LWC increases (Fig. 9). Hence, Crocus seems to better capture the dynamics of the SSA evolution. Note that Jacobi et al. (2010) obtained, from 162 snow SSA measurements at a taiga site, an RMSE of $8.6\,m^2\,kg^{-1}$ with the implementation of the Taillandier et al. (2007) approach within Crocus, whereas the implementation of Domine et al. (2007) resulted in a RMSE of $16.2\,m^2\,kg^{-1}$ (the results were highly affected by the underestimation of snow density by Crocus).

### 4.3 $R_{opt}$ analysis for MESM

In the context of using the simulated SSA to assimilate microwave brightness temperatures ($T_B$), we now examine the impact of errors generated by the proposed approach in terms of $T_B$ error. As mentioned in Sect. 1, the DMRT MESM calculates $T_B$ from $R_{opt}$ derived from SSA. Figure 10 shows the comparison between $R_{opt}$ derived from measured SSA and $R_{opt}$ derived from simulated SSA. As the relationship between SSA and $R_{opt}$ is not linear (Eq. 1), we see that for individual points (Fig. 10, left panel), the differences between simulated and measured $R_{opt}$ are more important for larger grains. This is caused by the fact that for low SSA, a given variation of SSA leads to a larger change in the simulated $R_{opt}$ (a change of SSA from 10 to $8\,m^2\,kg^{-1}$ leads to a change in $R_{opt}$ from 0.327 to 0.409 mm). $R_{opt}$ is then much more sensitive to error in SSA for larger grains. This also partly explains why the error for wet snow condition data in Col de Porte is large. For mean $R_{opt}$ values over the snowpack, there is a RMSE of 0.043 mm and $R^2$ of 0.84, comparable to SSA results, if the wet snowpacks are excluded. There is,

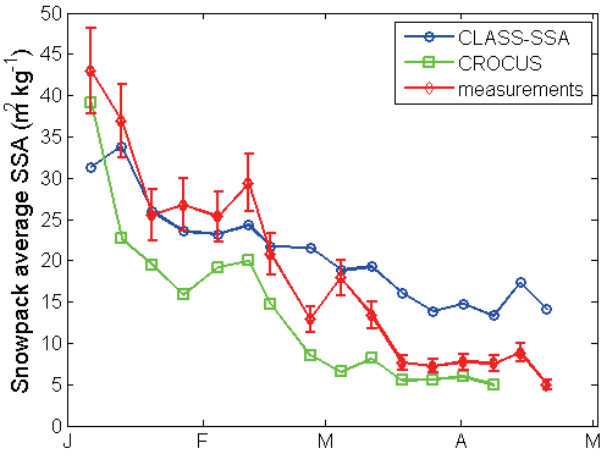


**Fig. 9.** Snowpack-averaged SSA evolution with time at Col de Porte for CLASS-SSA, Crocus (Morin et al., 2013) and the measurements. The last Crocus value was excluded because the simulations give no snow on ground. Error bars on measurements are the measurements accuracy (12 %: Gallet et al., 2009).

however, a small positive bias of 0.034 mm, mainly caused by the strong influence of large grains in the averaging.

Moreover, the density stratification is another parameter that should be considered when modeling the radiative transfer within the snowpack (e.g., Picard et al., 2012). In our case, the densification routine in CLASS-SSA is only used to calculate the depth and the position of every snow layer, and not necessarily to calculate a precise density. The simulated densities might differ from real densities. An example is the decrease of densification at the bottom snow layer when depth hoar formation occurs that is not taken into account in the SSA offline model. The correction of densities in the top layers (see Sect. 2.1) might also lead to low densities in the top layers. Here, to attenuate the effects of these simplifications in the $T_B$ simulations, we consider a bulk snowpack characterized by an effective snow grain effective radius $R_{eff}$ calculated from the averaged $R_{opt}$ following the form suggested by Kontu and Pulliainen (2010):

$$R_{eff} = a[1 - \exp(-bR_{opt})] \quad (6)$$

where $a = 1.3$ and $b = 4.7$. These empirical parameters were fitted from simulations using averaged $R_{opt}$ derived from measured SSA compared to ground-based radiometric measurements, except for the bulk snowpack (see Roy et al., 2013).

Simulations with the DMRT-ML (Picard et al., 2013) were conducted to analyze the effect of the $R_{opt}$ error on $T_B$ simulations. The $T_B$ simulations were conducted employing single-layer averaged $R_{eff}$ values (Eq. 6) $\pm$ the derived RMSE of $R_{opt}$ ($\pm$0.043 mm). Considering a snowpack of 0.5 m with a bulk density of 250 kg m$^{-3}$, an error of 0.043 mm in $R_{opt}$ leads to maximum variations of $T_B$ of the order of $\pm$23.3 K at 36.5 GHz and $\pm$2.7 K at 18.7 GHz. We thus see the high sensitivity of 36.5 GHz to grain size, given an error that could be significant in some cases (high depth hoar layer), while the proposed simple approach can be applied for $T_B$ simulations at 18.7 GHz with acceptable accuracy. Such a sensitivity analysis would benefit from further development as many combinations of snowpack parameters and conditions could occur.

### 4.4 Model applications

The simulation of snowpack parameters, such as SWE, at individual sites using an operational land-surface scheme designed for use in large-scale climate models could include large errors, as illustrated in Fig. 3. These errors could result from uncertainties in the meteorological forcing data, model parameters, as well as the nonlinearity and scaling effects of the processes modeled (e.g., Andreadis et al., 2008). The proposed model opens opportunities to couple CLASS with MESM for improving SWE estimates. Data assimilation offers the potential to merge information on snow variables from satellite observations and land-surface model simulations. CLASS-SSA was developed mainly for passive microwave $T_B$ assimilation in CLASS to improve estimates of snow parameters. The model employed in this study provides a good estimate or "first guess" of the snow grain size and a description of the snow type at a given time during the snow season. Inversion approaches, where parameters (snow depth, snow density) are retrieved by minimizing the differences between simulated and measured brightness temperatures (Langlois et al., 2012; Vachon et al., 2010; Pardé et al, 2007) will benefit from SSA simulations by taking into account the important effect of snow metamorphism on the microwave signal. This "first guess" methodology could also be used as a state initial condition in more complex data assimilation system approaches (Toure et al., 2011; Durand et al., 2009; Reichle, 2008) because the grain-size parameterization is no longer the dominant source of uncertainty. Grain size could still be considered as one of many sources of uncertainty, but with known likely error or variation. Hence, the CLASS-SSA model could be applied to improve SWE estimates at large scales from satellite-borne passive microwave information. From this perspective, as mentioned previously (Sect. 4.3), attention needs to be paid to the effect of the conversion of SSA to $R_{opt}$ on the uncertainty related to the grain size simulation that depends on the type of grains. In fact, considering Eq. (1), errors in SSA with large grains (low SSA, such as depth hoar) will lead to higher variation of $R_{opt}$ than for smaller grains (high SSA) (see Morin et al., 2013).

The proposed methodology could also be implemented for a hydrology land-surface scheme (HLSS), such as the one developed within the framework of Environment Canada's community environmental modeling system, MESH. MESH evolved from the WATCLASS model that links a hydrological routing model (WATFLOOD) (Pietroniro et al., 2006) to

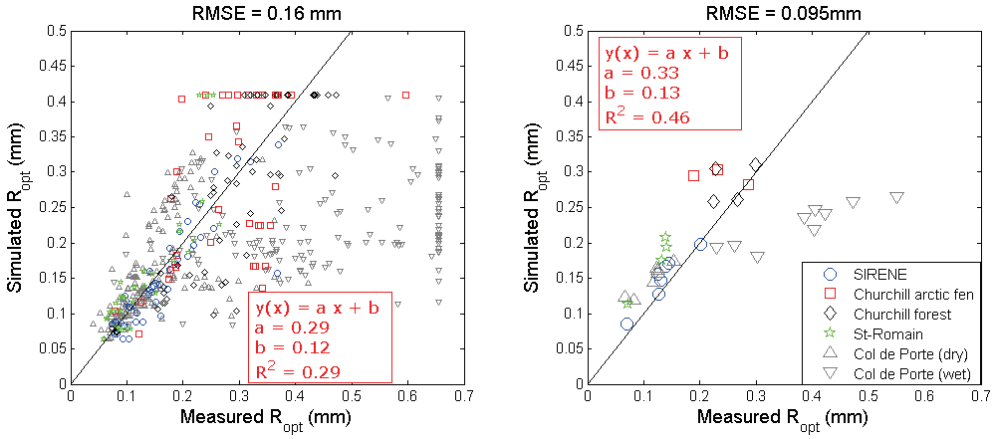


**Fig. 10.** Measured vs. simulated $R_{opt}$ derived from SSA (Eq. 1) comparison (left panel shows all points; right panel shows the one-layer average). The RMSE in averaged $R_{opt}$ (right panel) without the wet points is 0.043 mm.

the Canadian LAnd Surface Scheme (CLASS) discussed in this paper. It is used as a basis for coupling horizontal surface hydrology (river routing) with both weather and climate atmospheric models (see discussion by Teutschbein and Seibert, 2010).

Furthermore, snow surface albedo (mostly in the infrared) is driven by snow grain size. Hence, the use of SSA estimated with CLASS-SSA could lead to improved estimates of snowpack albedo, which are derived from a physically-based model. Pure snow albedo (no impurities) could be related to the SSA using a simple optical equation model suggested by Kokhanovsky and Zege (2004). Based on the simple radiative transfer model of Gardner and Sharp (2010), an error of $8.0\,m^2\,kg^{-1}$ in SSA leads to an uncertainty in the broadband albedo calculation of around $\pm 3\,\%$ for small grains ($30\,m^2\,kg^{-1}$) to around 6 % for large grains ($10\,m^2\,kg^{-1}$). It should be noted that the grains at the top of the snowpack that drive the broadband surface albedo are generally smaller (mostly in dry conditions) and thus less affected by grain uncertainty.

## 5 Conclusions

This study analyzes the coupling of a SSA evolution model with a one-layer snow model from the Canadian LAnd Surface Scheme (CLASS). The simulated SSA values were compared with a unique SSA database for five different sites, representing four different climatic environments, including a wide range of snow types. Based on the SSA decrease due to snow aging in snow layers (Taillandier et al., 2007), the CLASS-SSA model is an offline multi-layer parameterization driven by CLASS single-layer snow model outputs. The CLASS-SSA model also considers wet metamorphism, using the equation of Brun (1989) based on the liquid water content of snow.

Despite the limits of a simple one-layer snow model, it provides a SSA estimate with an overall RMSE of $8.0\,m^2\ kg^{-1}$ for individual layers, and a depth-averaged RMSE of $5.1\,m^2\ kg^{-1}$ for the snowpack SSA. The model, however, shows weaknesses in the wet snow metamorphism regime, which is mostly due to a low bias in the snow model simulations of LWC within the snowpack.

The proposed implementation of the SSA model in an offline mode and driven by a one-layer snow model offers a simple, computationally efficient and versatile approach. It would not be difficult to implement for other models as it only needs six basic inputs that are normally available from snow models (snow depth, SWE, snow density, LWC, soil–snow interface temperature, and air temperature). This approach is thus applicable for other one-layer snow models (Turcotte et al., 2007; Bélair et al., 2003), and also for multilayer models where SSA is not explicitly modeled, such as the Snow–Atmosphere–Soil Transfer (SAST) energy balance snow physics model (Sun et al., 1999).

Future work will evaluate the use of these SSA simulations for satellite passive microwave brightness temperature assimilations and surface snow albedo calculations.

*Acknowledgements.* The authors would like to thank the National Sciences and Engineering Research Council of Canada (NSERC) and Environment Canada for their financial support. All of our colleagues who helped us during the field campaigns in France and Canada are also gratefully acknowledged. We thank Samuel Morin, (Météo-France – CNRS, CNRM-GAME/Centre d'Études de la Neige), for providing the Col de Porte dataset and valuable suggestions on the manuscript. We thank Diana Verseghy (Climate Processes Section, Environment Canada) for providing the CLASS model code.

We also thank Ghislain Picard and Florent Domine for their helpful comments and the two reviewers who helped to improve the quality of the manuscript.

Edited by: F. Dominé

## References

Adams, E. and Sato, A.: Model for effective thermal conductivity of a dry snow cover composed of uniform ice spheres, Ann. Glaciol., 18, 300–304, 1993.

Andreadis, K. M., Liang, D., Tsang, L., Lettenmaier, D. P., and Josberger, E. G.: Characterization of errors in a coupled snow hydrology microwave emission model, J. Hydrometeorol., 9, 149–164, 2008.

Aoki, T., Kuchiki, K., Niwano, M., Kodama, Y., Hosaka, M., and Tanaka, T.: Physically based snow albedo model for calculating broadband albedos and the solar heating profile in snowpack for general circulation models, J. Geophys. Res., 116, D11114, doi:10.1029/2010JD015507, 2011.

Armstrong, R. and Brun, E.: Snow and climate: physical processes, surface energy exchange and modeling, Cambridge University Press, Cambridge, 2008.

Arnaud, L., Picard, G., Champollion, N., Domine, F., Gallet, J. C., Lefebvre, E., Fily, M., and Barnola, J. M.: Measurement of vertical profiles of snow specific surface area with a 1 cm resolution using infrared reflectance: instrument description and validation, J. Glaciol., 57, 17–29, 2011.

Baggaley, D. G. and Hanesiak, J. M.: An empirical blowing snow forecast technique for the Canadian arctic and the Prairie provinces, Weather Forecast., 20, 51–62, 2005.

Bartelt, P. and Lehning, M.: A physical SNOWPACK model for the Swiss avalanche warning, Part I: Numerical model, Cold region Science and Technology, 35, 123–145, 2002.

Bartlett, P. A., MacKay, M. D., and Verseghy, D. L.: Modified snow algorithms in the Canadian land surface scheme: model runs and sensitivity analysis at three boreal forest stands, Atmos. Ocean, 44, 207–222, 2006.

Belair, S., Brown, R., Mailhot, J., Bilodeau, B., and Crevier, L.: Operational implementation of the ISBA land surface scheme in the Canadian regional weather forecast model. Part II: Cold season results, J. Hydrometeorol., 4, 371–386, 2003.

Bougamont, M., Bamber, J. L., and Greuell, W.: A surface mass balance model for the Greenland ice sheet, 110, 2003–2012, 2005.

Brown, R., Bartlett, P., MacKay, M., and Verseghy, D.: Evaluation of snow cover in CLASS for SnowMIP, Atmos. Ocean, 44, 223–238, 2006.

Brucker, L., Picard, G., Arnaud, L., Barnola, J.-M., Schneebeli, M., Brunjail, H., Lefebvre, E., and Fily, M.: Modelling time series of microwave brightness temperature at Dome C, Antarctica, using vertically resolved snow temperature and microstructure measurements, J. Glaciol., 57, 171–182, 2011.

Brun, E.: Investigation on wet-snow metamorphism in respect of liquid-water content, Ann. Glaciol., 13, 22–26, 1989.

Brun, E., David, P., Suduland, M., and Brunot, G.: A numerical model simulate snow-cover stratigraphy for operational avalanche forecasting, J. Glaciol., 38, 14–22, 1992.

Cabanes, A., Legagneux, L., and Domine, F.: Rate of evolution of the specific surface area of surface snow layers, Environ. Sci. Technol., 37, 661–666, 2003.

Caya, D. and Laprise, R.: A semi-implicit semi-Lagrangian regional climate model: the Canadian RCM, Mon. Weather Rev., 127, 341–362, 1999.

Chen, S. and Baker, I.: Evolution of individual snowflakes during metamorphism, J. Geophys. Res., 115, D21114, doi:10.1029/2010JD014132, 2010.

Colbeck, S.: Theory of metamorphism of dry snow, J. Geophys. Res., 88, 5475–5482, 1983.

Derksen, C., Toose, P., Lemmetyinen, J., Pulliainen, J., Langlois, A., Rutter, N., and Fuller, M.: Evaluation of passive microwave brightness temperature simulations and snow water equivalent retrievals through a winter season, Remote Sens. Environ., 117, 236–248, 2012.

Domine, F., Cabanes, A., Taillandier, A., and Legagneux, L.: Specific surface area of snow samples determined by $CH_4$ adsorption at 77 K and estimated by optical microscopy and scanning electron microscopy, Environ. Sci. Technol., 35, 771–780, 2001.

Domine, F., Lauzier, T., Cabanes, A., Legagneux, L., Kuhs, W., Techmer, K., and Heinrichs, T.: Snow metamorphism as revealed by scanning electron microscopy, Microsc. Res. Techniq., 62, 33–48, 2003.

Domine, F., Taillandier, A.-S., and Simpson, W. R.: A parameterization of the specific surface area of seasonal snow for field use and for models of snowpack evolution, J. Geophys. Res., 112, F02031, doi:10.1029/2006JF000512, 2007.

Domine, F., Albert, M., Huthwelker, T., Jacobi, H.-W., Kokhanovsky, A. A., Lehning, M., Picard, G., and Simpson, W. R.: Snow physics as relevant to snow photochemistry, Atmos. Chem. Phys., 8, 171–208, doi:10.5194/acp-8-171-2008, 2008.

Domine, F., Taillandier, A.-S., Cabanes, A., Douglas, T. A., and Sturm, M.: Three examples where the specific surface area of snow increased over time, The Cryosphere, 3, 31–39, doi:10.5194/tc-3-31-2009, 2009.

Durand, M. and Liu, D.: The need for prior information in characterizing snow water equivalent from microwave brightness temperatures, Remote Sens. Environ., 126, 248–257, 2012.

Durand, M., Kim, E. C., and Margulis, S.: Quantifying uncertainty in modeling snow microwave radiance for a mountain snowpack at the point-scale, including stratigraphic effects, IEEE T. Geosci. Remote, 46, 1753–1767, 2008.

Durand, M., Kim, E., and Margulis, S.: Radiance assimilation shows promise for snowpack characterization, Geophys. Res. Lett., 36, L02503, doi:10.1029/2008GL035214, 2009.

Ettema, J., van den Broeke, M. R., van Meijgaard, E., van de Berg, W., Bamber, J. L., Box, J. E., and Bales, R. C.: Higher surface mass balance of the Greenland ice sheet revealed by high-resolution climate modeling, Geophys. Res. Lett., 36, L12501, doi:10.1029/2009GL038110, 2009.

Flanner, M. and Zender, C.: Linking snowpack microphysics and albedo evolution, J. Geophys. Res., 111, D12208, doi:10.1029/2005JD006834, 2006.

Flanner, M., Zender, C., Randerson, J., and Rasch, P.: Present-day climate forcing and response from black carbon in snow, J. Geophys. Res., 112, D11202, doi:10.1029/2006JD008003, 2007.

Flin, F. and Brzoska, J.: The temperature-gradient metamorphism of snow: vapour diffusion model and application to tomographic images, Ann. Glaciol., 49, 17–21, 2008.

Flin, F., Brzoska, J., Lesaffre, B., Coléou, C., and Pieritz, R.: Three-dimensional geometric measurements of snow microstructural evolution under isothermal conditions, Ann. Glaciol., 38, 39–44, 2004.

Franz, K., Butcher, P., and Ajami, N.: Addressing snow model uncertainty for hydrologic prediction, Adv. Water Resour., 33, 820–832, 2010.

Gallet, J.-C., Domine, F., Zender, C. S., and Picard, G.: Measurement of the specific surface area of snow using infrared reflectance in an integrating sphere at 1310 and 1550 nm, The Cryosphere, 3, 167–182, doi:10.5194/tc-3-167-2009, 2009.

Gardner, A. and Sharp, M.: A review of snow and ice albedo and the development of a new physically based broadband albedo parameterization, J. Geophys. Res., 115, F01009, doi:10.1029/2009JF001444, 2010.

Gouttevin, I., Menegoz, M., Domine, F., Krinner, G., Koven, C., Ciais, P., Tarnocai, C., and Boike, J.: How the insulating properties of snow affect soil carbon distribution in the continental pan-arctic area, J. Geophys. Res., 117, G02020, doi:10.1029/2011JG001916, 2012.

Grody, N.: Relationship between snow parameters and microwave satellite measurements: theory compared with Advanced Microwave Sounding Unit observations from 23 to 150 GHz, J. Geophys. Res., 113, D22108, doi:10.1029/2007JD009685, 2008.

Hedstrom, N. and Pomeroy, J.: Measurements and modelling of snow interception in the boreal forest, Hydrol. Process., 12, 1611–1625, 1998.

Huang, C., Margulis, S., Durand, M., and Musselman, K.: Assessment of Snow Grain-Size Model and Stratigraphy Representation Impacts on Snow Radiance Assimilation: Forward Modeling Evaluation, IEEE T. Geosci. Remote, 50, 4551–4564, 2012.

Jacobi, H.-W., Domine, F., Simpson, W. R., Douglas, T. A., and Sturm, M.: Simulation of the specific surface area of snow using a one-dimensional physical snowpack model: implementation and evaluation for subarctic snow in Alaska, The Cryosphere, 4, 35–51, doi:10.5194/tc-4-35-2010, 2010.

Jin, Z., Charlock, T. P., Yang, P., Xie, Y., and Miller, W.: Snow optical properties for different particle shapes with application to snow grain size retrieval and MODIS/CERES radiance comparison over Antarctica, Remote Sens. Environ., 112, 3563–3581, 2008.

Kaempfer, T. and Schneebeli, M.: Observation of isothermal metamorphism of new snow and interpretation as a sintering process, J. Geophys. Res., 112, D24101, doi:10.1029/2007JD009047, 2007.

Kokhanovsky, A. A. and Zege, E. P.: Scattering optics of snow, Appl. Optics, 43, 1589–1602, 2004.

Kondo, J. and Yamazaki, T.: A prediction model for snowmelt, snow surface temperature and freezing depth using a heat balance method, J. Appl. Meteorol., 29, 375–384, 1990.

Kontu, A. and Pulliainen, J.: Simulation of spaceborne microwave radiometer measurements of snow cover using in situ data and brightness temperature modeling, IEEE T. Geosci. Remote, 48, 1031–1044, 2010.

Langlois, A., Brucker, L., Kohn, J., Royer, A., Derksen, C., Cliche, P., Picard, G., Willemet, J. M., and Fily, M.: Simulation of snow water equivalent (SWE) using thermodynamic snow models in Québec, Canada, J. Hydrometeorol., 10, 1447–1463, 2009.

Langlois, A., Royer, A., Derksen, C., Montpetit, B., Dupont, F., and Goïta, K.: Coupling the snow thermodynamic model SNOWPACK with the microwave emission model of layered snowpacks for subarctic and arctic snow water equivalent retrievals, Water Ressour. Res., 48, W12524, doi:10.1029/2012WR012133, 2012.

Langlois, A., Bergeron, J., Brown, R., Royer, A., Harvey, R., Roy, A., Wang, L., and Thériault, N.: Evaluation of CLASS 2.7 and 3.5 simulations of snow cover from the Canadian Climate model (CRCM4) over Québec, Canada, J. Hydrometeorol., submitted (AMSJHM-S-13-00073), 2013.

Leathers, D. J., Palecki, M. A., Robinson, D. A., and Dewey, K. F.: Climatology of the daily temperature range annual cycle in the United States, Clim. Res., 9, 197–211, 1998.

Legagneux, L., Lauzier, T., Domine, F., Kuhs, W., Heinrichs, T., and Techmer, K.: Rate of decay of specific surface area of snow during isothermal experiments and morphological changes studied by scanning electron microscopy, Can. J. Phys., 81, 459–468, 2003.

Li, L. and Pomeroy, J.: Estimates of threshold wind speeds for snow transport using meteorological data, J. Appl. Meteorol., 36, 205–213, 1997.

Liston, G. and Hiemstra, C.: The changing cryosphere: Pan-Arctic snow trends (1979–2009), J. Climate, 24, 5691–5712, 2011.

Lyapustin, A., Tedesco, M., Wang, Y., Aoki, T., Horif, M., and Kokhanovsky, A. A.: Retrieval of snow grain size over Greenland from MODIS, Remote Sens. Environ., 113, 1976–1987, 2009.

Marbouty, D.: An experimental study of temperature gradient metamorphism, J. Glaciol., 26, 303–312, 1980.

Mesinger, F., DiMego, G., Kalnay, E., Mitchell, K., Shafran, P., Ebisuzaki, W., Jovic, D., Woollen, J., Rogers, E., and Berbery, E.: North American regional reanalysis, B. Am. Meteorol. Soc., 87, 343–360, 2006.

Montpetit, B., Royer, A., Langlois, A., Cliche, P., Roy, A., Champollion, N., Picard, G., Domine, F., and Obbard, R.: New shortwave infrared albedo measurements for snow specific surface area retrieval, J. Glaciol., 58, 941, doi:10.1016/j.coldregions.2010.01.004, 2012.

Montpetit, B., Royer, A., Roy, A., Langlois, L., and Derksen, D.: Snow microwave emission modeling of ice lenses within a snowpack using the microwave emission model for layered snowpacks, IEEE T. Geosci. Remote, available online, doi:10.1109/TGRS.2013.2250509, 2013.

Morin, S., Lejeune, Y., Lesaffre, B., Panel, J.-M., Poncet, D., David, P., and Sudul, M.: An 18-yr long (1993–2011) snow and meteorological dataset from a mid-altitude mountain site (Col de Porte, France, 1325 m alt.) for driving and evaluating snowpack models, Earth Syst. Sci. Data, 4, 13–21, doi:10.5194/essd-4-13-2012, 2012.

Morin, S., Domine, F., Dufour, A., Lejeune, Y., Lesaffre, B., Willemet, J., Carmagnola, C., and Jacobi, H.: Measurements and modeling of the vertical profile of specific surface area of an alpine snowpack, Adv. Water Resour., 55, 111–120, doi:10.1016/j.advwatres.2012.01.010, 2013.

Music, B. and Caya, D.: Evaluation of the hydrological cycle over the Mississippi River basin as simulated by the Canadian Regional Climate Model (CRCM), J. Hydrometeorol., 8, 969–988, 2007.

Niwano, M., Aoki, T., Kuchiki, K., Hosaka, M., and Kodama, Y.: Snow metamorphism and albedo process (SMAP) model for cli-

mate studies: Model validation using meteorological and snow impurity data measured at Sapporo, Japan, J. Geophys. Res., 117, F03008, doi:10.1029/2011JF002239, 2012.

Pardé, M., Goïta, K., and Royer, A.: Inversion of a passive microwave snow emission model for water equivalent estimation using airborne and satellite data, Remote Sens. Environ., 111, 346–356, 2007.

Picard, G., Brucker, L., Roy, A., Dupont, F., Fily, M., and Royer, A.: Simulation of the microwave emission of multi-layered snowpacks using the dense media radiative transfer theory: the DMRT-ML model, Geosci. Model Dev. Discuss., 5, 3647–3694, doi:10.5194/gmdd-5-3647-2012, 2012.

Pietroniro, A., Leconte, R., Toth, B., Peters, D. L., Kouwen, N., Conley, F. M., and Prowse, T.: Modelling climate change impacts in the Peace and Athabasca catchment and delta III – integrated model assessment, Hydrol. Process., 20, 4231–4235, 2006.

Pinzer, B. and Schneebeli, M.: Snow metamorphism under alternating temperature gradients: morphology and recrystallization in surface snow, Geophys. Res. Lett., 36, L23503, doi:10.1029/2009GL039618, 2009.

Reichle, R.: Data assimilation methods in the Earth sciences, Adv. Water Resour., 31, 1411–1418, 2008.

Roy, V., Goïta, K., Royer, A., Walker, A., and Goodison, B.: Snow water equivalent retrieval in a Canadian boreal environment from microwave measurements using the HUT snow emission model, IEEE T. Geosci. Remote, 42, 1850–1859, 2004.

Roy, A., Picard, G., Royer, A., Montpetit, B., Dupont, F., Langlois, A., Derksen, C., and Champollion, N.: Brightness temperature simulations of the Canadian seasonal snowpack driven by measurements of the snow specific surface area, IEEE T. Geosci. Remote, available online, doi:10.1109/TGRS.2012.2235842, 2013.

Rutter, N., Essery, R., Pomeroy, J., Altimir, N., Andreadis, K., Baker, I., Barr, A., Bartlett, P., Boone, A., Deng, H., Douville, H., Dutra, E., Elder, K., Ellis, C., Feng, X., Gelfan, A., Goodbody, A., Gusev, Y., Gustafsson, D., Hellström, R., Hirabayashi, Y., Hirota, T., Jonas, T., Koren, V., Kuragina, A., Lettenmaier, D., Li, W., Luce, C., Martin, E., Nasonova, O., Pumpanen, J., Pyles, R. D., Samuelsson, P., Sandells, M.,Schädler, G., Shmakin, A., Smirnova, T. G., Stähli, M., Stöckli, R., Strasser, U., Su, H., Suzuki, K., Takata, K., Tanaka, K., Thompson, E., Vesala, T., Viterbo, P., Wiltshire, A., Xia, K., Xue, Y., and Yamazaki, T.: Evaluation of forest snow processes models (SnowMIP2), J. Geophys. Res., 114, D06111, doi:10.1029/2008JD011063, 2009.

Scinocca, J. F., McFarlane, N. A., Lazare, M., Li, J., and Plummer, D.: Technical Note: The CCCma third generation AGCM and its extension into the middle atmosphere, Atmos. Chem. Phys., 8, 7055–7074, doi:10.5194/acp-8-7055-2008, 2008.

Sommerfeld, R. and LaChapelle, E.: The classification of snow metamorphism, J. Glaciol., 9, 3–17, 1970.

Sturm, M., Holmgren, J., König, M., and Morris, K.: The thermal conductivity of seasonal snow, J. Glaciol., 43, 26–41, 1997.

Sun, S., Jin, J., and Xue, Y.: A simple snow-atmosphere-soil transfer model, J. Geophys. Res., 104, 19587–19597, 1999.

Taillandier, A.-S., Domine, F., Simpson, W. R., Sturm, M., Douglas, T. A., and Severin, K.: Evolution of the snow area index of the subarctic snowpack in central Alaska over a whole season, consequences for the air to snow transfer of pollutants, Environ. Sci. Technol., 40, 7521–7527, 2006.

Taillandier, A.-S., Domine, F., Simpson, W. R., Sturm, M., and Douglas, T. A.: Rate of decrease of the specific surface area of dry snow: Isothermal and temperature gradient conditions, J. Geophys. Res., 112, F03003, doi:10.1029/2006JF000514, 2007.

Teutschbein, C. and Seibert, J.: Regional climate models for hydrological impact studies at the catchment scale: a review of recent modeling strategies, Geography Compass, 4, 834–860, 2010.

Toure, A., Goïta, K., Royer, A., Kim, E., Durand, M., Margulis, S., and Lu, H.: A Case study of using a multilayered thermodynamical snow model for radiance assimilation, IEEE T. Geosci. Remote, 9, 2828–2837, 2011.

Turcotte, R., Fortin, L.-G., Fortin, V., Fortin, J.-P., and Villeneuve, J.-P.: Operational analysis of the spatial distribution and the temporal evolution of the snowpack water equivalent in southern Québec, Canada, Nord. Hydrol., 38, 211–234, 2007.

Vachon, F., Goïta, K., De Sève, D., and Royer, A.: Inversion of a snow emision model calibrated with in situ data for snow water equivalent monitoring, IEEE T. Geosci. Remote, 48, 59–71, 2010.

Verseghy, D.: CLASS-A Canadian land surface scheme for GCMs, I. Soil model, Int. J. Climateol., 11, 111–133, 1991.

Verseghy, D.: CLASS – The Canadian Land Surface Scheme (Version 3.4): Technical Documentation (Version 1.1), 2009.

Verseghy, D., McFarlane, N., and Lazare, M.: CLASS-A Canadian land surface scheme for GCMs, II. Vegetation model and coupled runs, Int. J. Climateol., 13, 347–370, 1993.

Vionnet, V., Brun, E., Morin, S., Boone, A., Faroux, S., Le Moigne, P., Martin, E., and Willemet, J.-M.: The detailed snowpack scheme Crocus and its implementation in SURFEX v7.2, Geosci. Model Dev., 5, 773–791, doi:10.5194/gmd-5-773-2012, 2012.

Wiscombe, W. and Warren, S.: A model for the spectral albedo of snow, I: Pure snow, J. Atmos. Sci., 37, 2712–2733, 1980.

## B.4 Article : Snow Stratigraphic heterogeneity within ground-based passive microwave radiometer footprints : Implications for emission modeling

En 2014, le professeur Nick Rutter du Northumbria College au Royaume-Uni a publié un ouvrage sur les effets de l'hétérogénéité de la stratigrapie de la neige à l'intérieur d'un empreinte d'un radiomètre MOP. Ce travail cadre bien avec les travaux de la thèse puisqu'il tente de caractériser la variabilité spatiale locale des propriétés du couvert nival qui affectent le signal MOP émis par le couvert nival. Pour ce travail, l'acquisition et le traitement des données de SSA ainsi que la révision de l'article par des échanges entre les co-auteurs ont été faites dans le cadre de cette thèse.

AGU PUBLICATIONS

JGR

Journal of Geophysical Research: Earth Surface

RESEARCH ARTICLE
10.1002/2013JF003017

**Key Points:**
- Simulated brightness temperature biases minimized by grain scaling factors
- Sub-Arctic stratigraphic variability required distributions of simulations
- Three-layer stratigraphic representation reduced bias to about 50% of one-layer

**Correspondence to:**
N. Rutter,
nick.rutter@northumbria.ac.uk

**Citation:**
Rutter, N., M. Sandells, C. Derksen, P. Toose, A. Royer, B. Montpetit, A. Langlois, J. Lemmetyinen, and J. Pulliainen (2014), Snow stratigraphic heterogeneity within ground-based passive microwave radiometer footprints: Implications for emission modeling, *J. Geophys. Res. Earth Surf.*, *119*, 550–565, doi:10.1002/2013JF003017.

Received 22 OCT 2013
Accepted 7 FEB 2014
Accepted article online 12 FEB 2014
Published online 13 MAR 2014

This is an open access article under the terms of the Creative Commons Attribution-NonCommercial-NoDerivs License, which permits use and distribution in any medium, provided the original work is properly cited, the use is non-commercial and no modifications or adaptations are made.

# Snow stratigraphic heterogeneity within ground-based passive microwave radiometer footprints: Implications for emission modeling

**Nick Rutter[1], Mel Sandells[2], Chris Derksen[3], Peter Toose[3], Alain Royer[4], Benoit Montpetit[4], Alex Langlois[4], Juha Lemmetyinen[5], and Jouni Pulliainen[5]**

[1]Department of Geography, Northumbria University, Newcastle upon Tyne, UK, [2]NCEO, University of Reading, Reading, UK, [3]Environment Canada, Toronto, Ontario, Canada, [4]Centre d'Applications et de Recherches en Télédétection, Université de Sherbrooke, Sherbrooke, Quebec, Canada, [5]Finnish Meteorological Institute, Helsinki, Finland

**Abstract** Two-dimensional measurements of snowpack properties (stratigraphic layering, density, grain size, and temperature) were used as inputs to the multilayer Helsinki University of Technology (HUT) microwave emission model at a centimeter-scale horizontal resolution, across a 4.5 m transect of ground-based passive microwave radiometer footprints near Churchill, Manitoba, Canada. Snowpack stratigraphy was complex (between six and eight layers) with only three layers extending continuously throughout the length of the transect. Distributions of one-dimensional simulations, accurately representing complex stratigraphic layering, were evaluated using measured brightness temperatures. Large biases (36 to 68 K) between simulated and measured brightness temperatures were minimized (−0.5 to 0.6 K), within measurement accuracy, through application of grain scaling factors (2.6 to 5.3) at different combinations of frequencies, polarizations, and model extinction coefficients. Grain scaling factors compensated for uncertainty relating optical specific surface area to HUT effective grain size inputs and quantified relative differences in scattering and absorption properties of various extinction coefficients. The HUT model required accurate representation of ice lenses, particularly at horizontal polarization, and large grain scaling factors highlighted the need to consider microstructure beyond the size of individual grains. As variability of extinction coefficients was strongly influenced by the proportion of large (hoar) grains in a vertical profile, it is important to consider simulations from distributions of one-dimensional profiles rather than single profiles, especially in sub-Arctic snowpacks where stratigraphic variability can be high. Model sensitivity experiments suggested that the level of error in field measurements and the new methodological framework used to apply them in a snow emission model were satisfactory. Layer amalgamation showed that a three-layer representation of snowpack stratigraphy reduced the bias of a one-layer representation by about 50%.

## 1. Introduction

Reliable estimates of snow water equivalent (SWE) are crucial to our understanding of the energy and water balance from global to catchment scales. In particular, knowledge of the magnitude and variability in snow mass and snow cover has important hydrological implications for global water movement and direct impact on human activities, both in terms of maximization of a resource, e.g., irrigation [*Barnett et al.*, 2005] and mitigation of flooding risks [*Payne et al.*, 2004]. However, direct measurements of SWE are sparse [*Brown*, 2000; *Brown and Braaten*, 1998], especially with increasing latitude and decreasing proximity to populated areas. Attempts to simulate SWE spatially often suffer from a similar sparseness of meteorological stations, relying instead on remotely sensed measurements to constrain simulations [*Cline et al.*, 1998; *Fletcher et al.*, 2012; *Homan et al.*, 2011; *Molotch and Margulis*, 2008]. Differences in instrumentation that provide model driving data, e.g., measurement of precipitation [*Yang et al.*, 1999], also introduce uncertainty in simulations. Errors resulting from interpolation of SWE between such sparse point networks [*Takala et al.*, 2011] means that in many seasonally snow-covered areas of the world, remote sensing is the most practical method for near-real-time monitoring of snow mass distribution.

Current operational satellite data products of snow water equivalent (SWE) are produced from passive microwave measurements with a 25 × 25 km resolution [*Kelly*, 2009; *Tedesco et al.*, 2004]. Such data products are derived from native satellite footprints described in *Kelly* [2009] as having instantaneous fields of view at 19 GHz of 28 × 16 km (AMSR-E) or 69 × 43 km (SMM/I), and at 37 GHz of 14 × 8 km (AMSR-E) or 37 × 29 km


©2014. The Authors.

(SMM/I). Within these horizontal extents, footprints integrate a huge amount of complexity in land cover (nonvegetated land, lakes, and forests) and snowpack properties such as SWE, grain size, ice lenses, and crusts [*Derksen et al*., 2005; *Kurvonen and Hallikainen*, 1997; *Lemmetyinen et al*., 2009]. Differentiating the influence of subfoot print land cover types (e.g., different forest types and clearings) to account for their characteristic emission and scattering properties is possible by considering the fractional subgrid land cover fractions [*Derksen et al*., 2003]. However, it is much harder to differentiate physical properties of snow at the subsatellite footprint scale. This is particularly problematic for empirical algorithms because errors are amplified when snow properties deviate from "typical" conditions [e.g., *Chang et al*., 1987; *Kelly et al*., 2003]. Forward radiative transfer models used to estimate snow mass from brightness temperatures [e.g., *Pulliainen et al*., 1999; *Wiesmann and Matzler*, 1999] are also highly sensitive to variability in snow properties, especially grain size and layering [*Durand et al*., 2008; *Grody*, 2008; *Harlow and Essery*, 2012; *Kontu and Pulliainen*, 2010; *Tedesco et al*., 2006].

Acquiring enough in situ measurements of snowpack properties to capture the spatial variability of snow within a satellite footprint sufficiently is challenging. Very few experimental campaigns [e.g., *Elder et al*., 2009] have collected sufficient, simultaneous snow pit measurements across a wide enough spatial extent to allow direct comparison with satellite brightness temperatures. However, even in high-quality data sets such as those presented by *Elder et al*. [2009], measurements tend to be proximate to road or trail networks creating a spatially uneven distribution of measurements throughout the satellite pixel [*Davenport et al*., 2012]. Consequently, uncertainty still exists whether or not snow pit measurements adequately captured the variability of snowpack properties throughout the footprint.

Even if snow pits are numerous and well-distributed, further uncertainties are introduced through the measurement of grain size, a proxy for microstructure, and the use of this measurement at optical wavelengths in microwave emission models. While standard field techniques exist for measurement of grain size of snow by placing snow samples on a millimeter-graded grid [*Fierz et al*., 2009], manual measurements of this kind are prone to subjectivity, especially between observers, which can lead to unsatisfying comparability of results [*Derksen et al*., 2012]. More objective in situ methods of measuring snow grain size (also referred to as texture or microstructure) in optical wavelengths [*Grenfell and Warren*, 1999] can be obtained using near-infrared and shortwave infrared photography [*Langlois et al*., 2010; *Matzl and Schneebeli*, 2006; *Montpetit et al*., 2012], integrating lasers [*Gallet et al*., 2009; *Picard et al*., 2009], methane adsorption [*Domine et al*., 2001], and contact spectroscopy [*Painter et al*., 2007]. Measurement of correlation length [*Mätzler*, 2002], another metric describing snow microstructure, can be made either directly using X-ray tomography [*Freitag et al*., 2004; *Schneebeli*, 2004] or indirectly using either a micropenetrometer [*Proksch et al*., 2012] or near-infrared photography [*Toure et al*., 2008] using established relationships [*Debye et al*., 1957; *Mätzler*, 2002]. As a result, measurements exist of snow microstructure as a visual grain size, specific surface area, optical grain radius, or correlation length. Not all of these measurements are easy to obtain and not all microwave emission models can use each measurement directly. The optimal choice of measurement results from appropriate trade-offs between resolution and practicality, allowing a sensible match between scales of measurement and simulation.

As variability in snow properties is so difficult to capture at the satellite scale, it seems reasonable to look at the much smaller scale of suborbital or ground-based sensors to test microwave models, where the potential exists to characterize snow properties more thoroughly. The use of ground-based passive microwave measurements to evaluate forward radiative transfer models, which use in situ snowpack properties, has been undertaken before [*Brogioni et al*., 2009; *Durand et al*., 2008; *Kim and England*, 2003; *Mätzler and Wiesmann*, 1999; *Montpetit et al*., 2013; *Rees et al*., 2010; *Roy et al*., 2013; *Tedesco et al*., 2005]. However, measured snowpack properties are commonly limited to a single vertical profile, often in snow pits excavated outside of the sensor footprint because of the need to maintain a consistently undisturbed measurement area. Ideally, for thorough evaluation, measurements of snowpack properties should be made throughout the horizontal extent of sensor footprints, and at a vertical resolution which at least matches the scale at which the snowpack properties interact with the passive microwave radiation (19 and 37 GHz approximately equate to wavelengths of 15 and 8 mm). Consequently, the aim of this study is to understand the impact of subfootprint spatial variability in snowpack properties on measured and simulated brightness temperatures at the plot scale. Resulting objectives are the following to: (1) present a new methodological framework that allows centimeter-scale simulations of brightness temperatures from two-dimensional (2-D) measurements of snowpack properties within footprints of ground-based passive microwave radiometers, (2) evaluate the


©2014. The Authors.

minimization of simulation bias with grain scaling factors and three different emission model extinction coefficients in relation to measurement of snowpack properties, (3) identify sensitivity of simulated brightness temperatures to the following: (i) uncertainties in field measurements, (ii) translation of 1-D profiles to 2-D stratigraphy, and (iii) experimental amalgamation of stratigraphic layering.

## 2. Methods

Measurements of snowpack properties were made at a sub-Arctic site (58.73°N, 93.82°W) near Churchill, Manitoba, Canada, as part of an experiment on the emission and backscattering properties of seasonal snow cover [*Derksen et al*., 2012]. Measured brightness temperatures from ground-based microwave radiometers were compared with brightness temperatures from a multilayer snow emission model, which was initialized with high horizontal and vertical resolution measurements of snowpack properties across an approximately 4.5 m trench. The field measurements taken, the methods to translate snow properties across the trench, and the simulations of the microwave brightness temperature are all described in the following sections.

### 2.1. Field Measurements

Passive microwave radiometers at 19 and 37 GHz (dual polarized) were mounted side-by-side on a moveable sled, approximately 1.55 m above the snow surface at an incidence angle of 53°. The radiometer design has a 3 dB half-power beamwidth of 6°. The ground footprints of the sled-mounted radiometers were elliptical with a far width of 0.29 m and a depth of 0.45 m. Uncertainty in measured brightness temperatures was $< 2$ K at each frequency and polarization, based on sequential calibrations using cold (liquid nitrogen) and warm (microwave-absorbing material) targets [*Derksen et al*., 2012].

On 12 April 2010 brightness temperature measurements (five at 19 GHz, four at 37 GHz) were made at nine positions along a linear transect so that the overlapping footprints covered a 3.8 m horizontal extent. At each position, brightness temperatures were averaged from between 200 and 400 individual measurements with a 1 s integration time. The standard deviation at each measurement position and each frequency was $< 0.3$ K. Five vertical profiles of snow temperatures were recorded within the radiometer footprints along the transect; each profile measured temperatures at the snow-ground interface and at 4 cm increments upward through the snowpack. In addition, brightness temperature measurements were made at this site on nine occasions throughout the winter, beginning 25 November 2009, which provided a seasonal context to the measurements on 12 April 2012.

Directly after radiometer measurements were made on 12 April, a 4.5 m trench was excavated through the center points of the radiometer footprints. Following protocols in *Tape et al*. [2010], the trench face was prepared for near-infrared (NIR) photographs (850 nm center wavelength) to be taken along its length. A centimeter-scale Crain measuring staff was positioned horizontally above the trench to allow georeferencing of NIR imagery along the trench face.

At three positions (75, 185, and 355 cm) along the trench, vertical profiles of snowpack stratigraphy, density and specific surface area per mass of ice ($SSA_m$) were measured. Density measurements, using a 183 $cm^3$ triangular cutter (3 cm high), were made within coherent stratigraphic layers that were identified in the field. Measurements of specific surface area ($SSA_m$) were made using a 1310 nm laser mounted with an integrating sphere [*Montpetit et al*., 2012]. Snow samples for $SSA_m$ measurements were taken using a 226 $cm^3$ cylindrical cutter (4 cm diameter) inserted vertically through the snowpack. Between five and seven samples at successively increasing depths were made per vertical profile, typically one per snow layer within the profile. The effective diameter ($d_{\mathrm{eff}}$) of the sample grain size [*Grenfell and Warren*, 1999] was determined from the $SSA_m$ following *Gallet et al*. [2009] and *Montpetit et al*. [2012]:

$$d_{\mathrm{eff}} = \frac{6}{\rho_i \cdot \mathrm{SSA}_m} \tag{1}$$

where $\rho_i$ is the density of ice (916 kg $m^{-3}$ for $SSA_m$ given in $m^2$ $kg^{-1}$).

NIR images of adjacent sections of the trench were visually stitched together using positions along the measuring staff as control points. A single-stitched image of the entire trench was then visually examined and layer boundaries were identified at a 1 cm horizontal resolution (Figure 1). A leveled string, suspended horizontally above the trench and visible in all images, allowed the positions of snowpack layer boundaries to


©2014. The Authors.

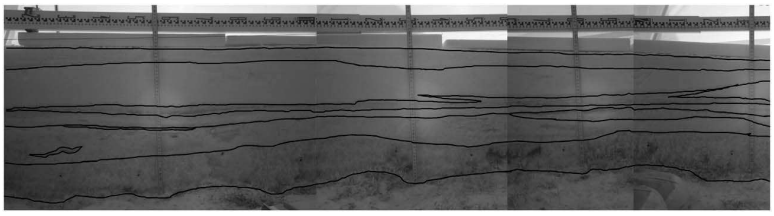

**Figure 1.** Example of layer boundary identification (black lines) on a 2.5 m section of the stitched trench image.

be adjusted with reference to a level surface. Consequently, a georectified 2-D array of internal snowpack layering was produced allowing discrete layers to be identified along the trench (Figure 2). As a guide for others, the time taken for the entire field procedure (radiometer measurements, trench excavation, and snow property characterization) was approximately 3 h.

### 2.2. Translating 1-D Profile Measurements to 2-D Stratigraphy

A complete 2-D array of snowpack properties (density, grain size, and temperature) was created from one-dimensional (1-D) profiles. Relating the measurements of snowpack properties from vertical profiles measured in the field, to stratigraphy derived from NIR images, was not straightforward. First, layers identified in the field from visual identification and hardness testing (herein collectively termed "manual inspection") did not necessarily match layers that were identified from NIR photos. Second, as temperatures were point measurements at spacing of 4 cm in the vertical, and SSA and density measurements corresponded to layers identifiable in the field, not all layers identified from NIR images coincided with measurements. Consequently, some subjectivity was introduced by translating snowpack measurements from layers identified by manual inspection to layers identified using NIR.

Manual inspection of the snowpack was carried out at three locations along the trench: at 75 cm, 185 cm, and 355 cm. To translate the snow properties across the trench, the NIR-derived stratigraphy was extracted at these locations. Densities of layers 1 to 9 and 12 were taken directly from the measurements, as shown in Figure 3a. Effective grain sizes for these layers were also taken directly from measurements, as shown in Figure 3b. Where more than one measurement was available for a particular layer, the mean of the measurements was used.

As layer 10 was not present in the three manually inspected profiles, estimates of the density and grain size were obtained by averaging the respective properties of layers 5, 8, and 9, of which layer 10 was assumed to be a continuation. As layer 11 was also not present in manual profiles, the density and grain size was assumed

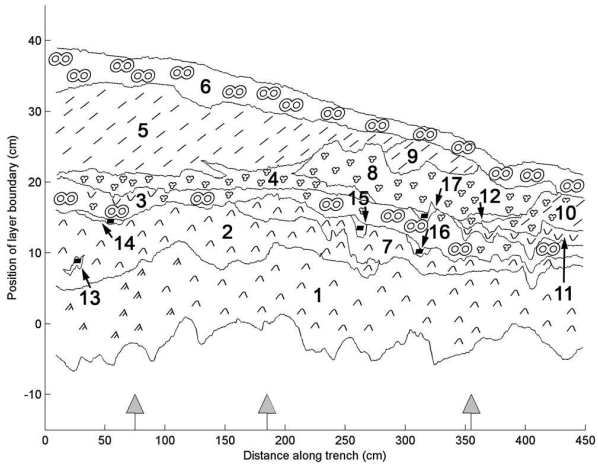


**Figure 2.** Snowpack layering (shaded and numbered) from NIR imagery, upward arrows (grey-filled arrowheads) indicate locations of manual profiles. Symbols describe snow type following the classification of *Fierz et al.* [2009]. Numbering relates layers to measurements in Table 1.


©2014. The Authors.

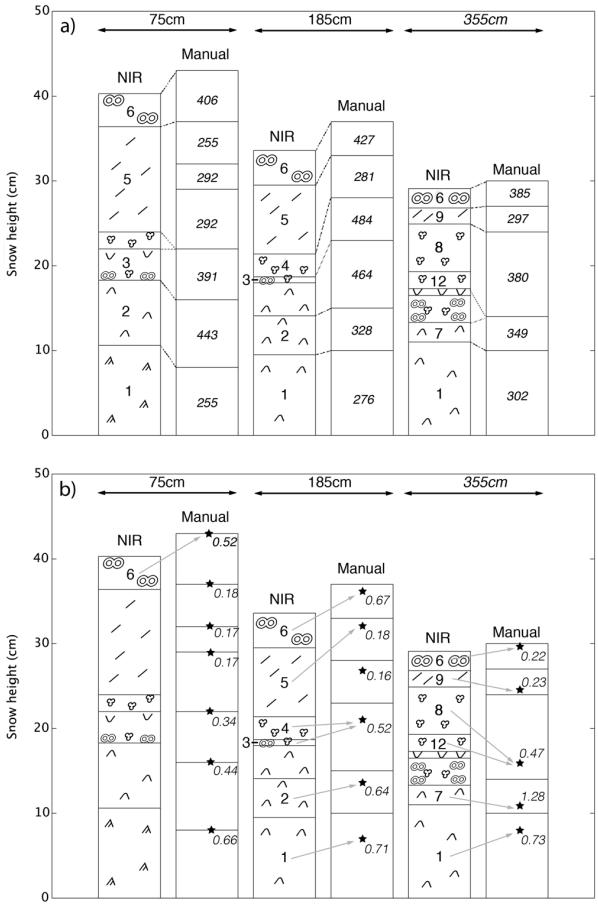


**Figure 3.** (a) Translating densities (in kg m$^{-3}$) from manual vertical profiles to NIR layers, (b) translating effective grain diameters (in millimeters) from manual vertical profiles to NIR layers, and stars represent the location of measurements within the profiles. Symbols describe snow type following the classification of *Fierz et al.* [2009].

to be the same as for layer 7 due to the similarity of their appearances in NIR images. Layers 13 to 17 were classified as ice lenses from NIR images and are treated as such in the microwave emission model.

In order to derive unique physical temperatures for each layer, a mean temperature profile was first derived from the five vertical profile measurements. Secondly, a histogram of layer heights was calculated from the NIR stratigraphy and the mean height occupied by each layer was determined. The temperature of each layer was assumed to be the temperature at the same height from the mean observed temperature profile. The soil temperature was derived from an average of the five basal temperatures and was found to be −2.9°C with a standard deviation of 0.1°C.

### 2.3. Snow Emission Model Experiments

As a result of translating measured densities (ice lenses were assumed a constant density of 916 kg m$^{-3}$), grain sizes ($d_{\text{eff}}$ derived from the SSA) and temperatures throughout the trench, each NIR layer had a single value describing each of the three snowpack properties (Table 1). These properties were applied to the 2-D array of snowpack layering and joined to a single subnivean layer describing the soil properties at the ground-snow interface. The soil was considered as a homogeneous, quasi-infinite layer with constant values of roughness, permittivity, and temperature across the trench. The mean of the temperature measurements at the soil-snow interface was used for the soil temperature. Soil roughness was calculated from the root mean square of the snow-soil interface height, relative to a 50 cm running mean (considered to be the footprint of the radiometer), and was calculated to be 10.77 mm. The permittivity of the frozen soil was


©2014. The Authors.

**Table 1.** Snowpack Layer Properties Throughout the Trench[a]

| Layer | Density (kg m$^{-3}$) | Effective Grain Diameter (mm) | Temperature (°C) |
|---|---|---|---|
| 1 | 278 | 0.72 | −3.0 |
| 2 | 386 | 0.64 | −3.4 |
| 3 | 391 | 0.52 | −3.6 |
| 4 | 484 | 0.52 | −4.0 |
| 5 | 280 | 0.18 | −4.8 |
| 6 | 406 | 0.47 | −5.0 |
| 7 | 349 | 1.28 | −3.4 |
| 8 | 380 | 0.47 | −4.1 |
| 9 | 297 | 0.23 | −4.5 |
| 10 | 319 | 0.30 | −3.6 |
| 11 | 349 | 1.28 | −3.4 |
| 12 | 380 | 0.47 | −3.5 |
| 13 | 916 | NA | −3.4 |
| 14 | 916 | NA | −3.7 |
| 15 | 916 | NA | −3.5 |
| 16 | 916 | NA | −3.3 |
| 17 | 916 | NA | −3.6 |
| Mean | 358[b] | 0.59 | −3.8 |
| Min | 278[b] | 0.18 | −5.0 |
| Max | 484[b] | 1.28 | −3.0 |

[a]NA, not applicable.
[b]This denotes excluding ice lens densities.

assumed to be 6-j, according to previous work [*Pulliainen et al.*, 1999] and based on measurements taken by *Hallikainen et al.* [1985].

Vertical profiles of snow and soil information were then extracted from this array at each centimeter along the trench as inputs to the multilayer Helsinki University of Technology (HUT) snow emission model [*Lemmetyinen et al.*, 2010]. The HUT model is a semiempirical radiative transfer model that uses parameters describing snowpack properties, such as density, grain size, and temperature, to estimate both scattering and absorption of microwave energy. The definition of total extinction of microwave energy in snow is based on an empirical relation, obtained using measurements of snow samples in laboratory conditions, representing a range of naturally formed snow in southern Finland; *Hallikainen et al.* [1987] give a relationship between the extinction of microwaves in snow, frequency (ranging between 18 and 60 GHz) and particle diameter (<1.6 mm) so that

$$\kappa_e = 0.0018 f^{2.8} d^{2.0} \tag{2}$$

where $\kappa_e$ is the extinction coefficient (dB/m), $f$ is the frequency (GHz), and $d$ is the snow grain diameter (mm). Here it is important to note that $d$ in the snow slab samples, used to derive equation (2), were quantified following the technique defined by *Fierz et al.* [2009]. Therefore, the compatibility of the HUT model to any other measures of snow microstructure, including optical-equivalent grain size, requires scaling of the measure to $d$. *Mätzler* [2002] notes that the optical-equivalent grain size is typically smaller than $d$, with the exception of perfectly round grains not present in nature.

*Kontu and Pulliainen* [2010] reported a similar formulation

$$\kappa_e = 0.08 f^{1.75} d^{1.8} \tag{3}$$

which was optimized for deeper and denser snow with larger grain sizes than taiga snow. In the experimental data used by *Hallikainen et al.* [1987], the maximum diameter of snow grains was 1.6 mm thus giving an approximate range of validity for equation (2). To account for overestimation of extinction in the presence of large grains, *Roy et al.* [2004] proposed an alternate formulation using two empirically determined constants to account for multiple scattering by densely packed ice particles. Following *Roy et al.* [2004]

$$\kappa_e = \gamma\left(f^4 d^6\right)^{\delta} \tag{4}$$

where $\gamma$ and $\delta$ are $2 \pm 1$ and $0.20 \pm 0.04$, respectively. *Roy et al.* [2004] applied a model inversion scheme to derive $\gamma$ and $\delta$ from model simulations compared with airborne observations. The observed (and measured) snow conditions thus represent average conditions over a natural snowpack, whereas *Hallikainen et al.* [1987] measured slab samples of relatively homogeneous snow. The formulation by *Roy et al.* [2004] thus includes effects inherent to natural snow such as layering. For clarity in interpretation of HUT model outputs, an optional component of HUT [*Kontu and Pulliainen*, 2010] that converted grain diameter from manual inspection ($d_{\mathrm{obs}}$) to an effective microwave grain size ($d_{\mathrm{eff}}$)

$$d_{\mathrm{eff}} = 1.5 \cdot \left(1 - e^{-1.5 \cdot d_{\mathrm{obs}}}\right) \tag{5}$$


©2014. The Authors.

**Table 2.** Summary of Model Sensitivity Experiments

| Experiment Purpose | Experiment Name | Experimental Method | Random Variation Applied |
|---|---|---|---|
| Testing measurement uncertainty | Density | Change measured densities | ±50 kg m$^{-3}$ in each snow layer |
| | Grain size | Change measured grain sizes | ±10% in each snow layer |
| | Layer boundary | Change layer boundary positions | ±1 cm to each boundary point |
| | Ice lens identification | Extend, add, or exclude ice lenses | Up to six ice lens extensions (thickness 0.1–0.5 mm) |
| Testing translation uncertainty (1-D to 2-D) | Unmeasured layers | Apply density and grain sizes measured throughout trench to unmeasured layers | Density for each layer between 278 and 484 kg m$^{-3}$. Grain diameter for each layer between 0.18 and 1.28 mm |
| | Ice lens or crusts | Simulate crusts where ice lenses were originally identified | Crust density between 500 and 916 kg m$^{-3}$ |

was not used in this study because SSA was measured rather than estimating grain size from crystal card analysis. Consequently, any relation between the model parameter and SSA-derived grain diameter is likely to be different to the relation between the model parameter and crystal card grain diameter (equation (5)).

Twelve brightness temperatures were simulated at each horizontal position, dependent on frequency (19 or 37 GHz), polarization (horizontal or vertical), and specified extinction coefficient model. The resulting spatial variability across the trench of simulated brightness temperatures and bias between measured and simulated brightness temperatures were calculated. Scaling factors, from 1.5 to 6.0 in increments of 0.1 as per *Langlois et al*. [2012], were applied to grain sizes of all layers in order to minimize the bias between measured and simulated brightness temperatures. Then, subsequent to this optimization, sensitivity experiments (Table 2) were performed to test the impact on simulated brightness temperatures of uncertainties in field measurements and translation of physical properties from 1-D profiles to 2-D layers.

Ensembles of 100 simulations of brightness temperatures across the trench were generated at each configuration of frequency, polarization, and extinction coefficient for all sensitivity experiments. Mean values of the ensembles were then compared to different frequencies and polarizations of measured brightness temperatures. A random measurement error was applied in turn to layer densities (up to ± 50 kg m$^{-3}$), effective grain diameters (up to ± 10%), or layer boundary heights (up to ± 1 cm) in each of the ensembles.

To test uncertainties in ice lens identification, the NIR stratigraphy was reexamined and the maximum potential ice lens extent was identified, compared to ice extents identified through manual inspection. As a result, six possible extensions to ice lenses in Figure 2 were identified from the NIR image: (1) Layer 14 (on top of layer 2) extended between 0.25 and 0.8 m, (2) layer 15 (on top of layer 7) extended between 1.6 m and original position, (3) additional ice lens (on top of layer 3) between 2.0 and 2.85 m, (4) additional ice lens (on top of layer 7) between 2.75 and 2.85 m, (5) layer 17 (on top of layers 3 and 11) extended between 3.05 and 4.5 m, and (6) layer 16 (on top of layer 7) extended between 3.05 and 4.5 m.

Each of the six possible ice lens additions were randomly applied or excluded in each of the 100 trench simulations, so an individual simulation may have no extensions, all extensions, or a few extensions applied. A single thickness of between 0.1 and 0.5 cm was randomly applied to each extended or additional lens.

To test the impact of deriving snow properties for layers that were not measured directly, random densities and grain sizes between the field-measured maximum and minimum throughout the trench were applied to layers 3, 4, 7, 8, 10, 11, and 12, in each of the 100 simulations. In the last sensitivity experiment, to simulate layers 13–17 as snow crusts rather than ice lenses, a single density between 500 and 916 kg m$^{-3}$ was randomly assigned to all crusts in each of the 100 simulations. As these layers were treated as high-density snow layers rather than ice, a snow grain size was required, which was assumed to be the same as the layer adjacent or surrounding the ice crust.

Finally, to test the impact of layer amalgamation on optimized simulated brightness temperatures, vertical profiles of snowpack layering were represented in four different configurations (Figure 4) of increasing complexity: (1) one layer, vertically weighted integration of all layers; (2) two layers, top layer contained layer 6; bottom layer comprised the rest of snowpack; (3) three layers, top layer contained layer 6; middle layer comprised layers 3, 4, 5, 8, 9, 10, 11, 12, and 17; bottom layer comprised layers 1, 2, 7, 13, 14, 15, and 16; and (4) *n* layer, original stratigraphy.


©2014. The Authors.

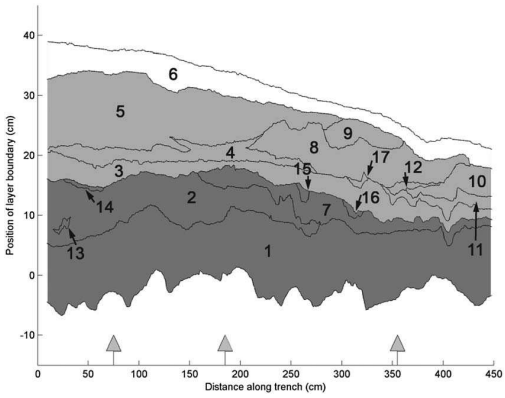


**Figure 4.** Visualization of the representation of snowpack stratigraphy in the layer amalgamation experiment. One layer: white and grey areas all combined into one layer; Two layers: white is upper layer, grey combined is lower layer; Three layers: white is upper layer, light grey is middle layer, dark grey is lower layer; *n* layer: individual layers denoted by black boundary lines.

In each layer configuration: (1) the total thickness and SWE of the vertical profiles were kept constant at each position along the trench; consequently, density was allowed to vary by horizontal position, (2) grain size was calculated as a thickness-weighted average of snow layers, and (3) temperature was calculated as a thickness-weighted average of snow and ice layers.

## 3. Results

### 3.1. Two-Dimensional Snowpack Properties

Snowpack stratigraphy across the 450 cm trench was complex (Figure 2). The number of layers in any single vertical profile ranged between six and eight, and out of 17 horizontally identifiable layers only three were continuous throughout the length of the trench. Layers were more often discontinuous than continuous even over the short trench distance.

Variability of the base layer thickness, consisting of depth hoar (layer 1 in Figure 2), was heavily influenced by the undulating hummocky ground surface layer, while the much less variable surface layer (layer 6) thickness was a function of the compaction and redistribution of recent snowfall by wind. However, between these two layers, the shape, thickness, and extent of internal layers were relict features of past meteorological events (including wind redistribution) and metamorphic activity (both kinetic grain growth and melt/refreeze). For example, layer 4, which was the densest layer consisting of an amalgam of wind-packed snow, numerous fine crusts, and very large grains trapped between the series of crusts. Between 130 and 224 cm, this layer had a distinct anvil shape most likely the result of a relict surface crust that was excavated along lines of structural weakness by wind scour and in-filled by a subsequent snowfall event. Variability of other internal discontinuous layers resulted from localized hardening of the surface layer (e.g., sun crusts and wind packing) providing resistance to wind erosion. The spatial incoherence of this resistance and the relative susceptibility of the layer beneath the surface, in part a function of metamorphism, caused the discontinuous layering pattern evident in Figure 2. Ice lenses within the trench resulted from recent surface melt percolating through the snowpack and collecting and refreezing at impermeable layer boundaries. Consequently, irregularly spaced ice lenses, which were relatively short in extent, increased the horizontal variability of snowpack properties. As a result, snow layer density and effective grain size ranged considerably (range of 206 kg m$^{-3}$ and 1.10 mm,

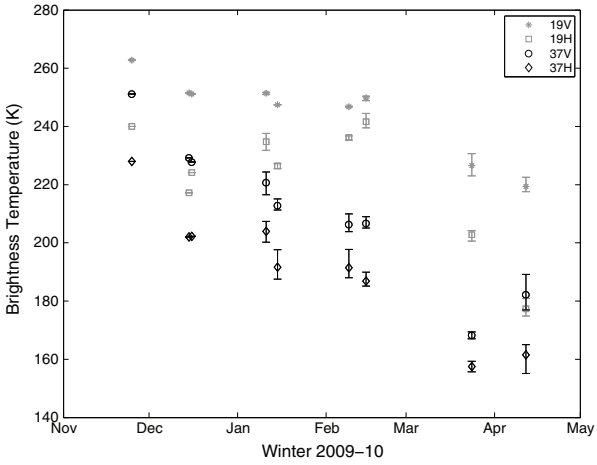


**Figure 5.** Seasonal decline in mean measured brightness temperatures at the trench site. Error bars indicate range of brightness temperatures: measurements were made at one location along the trench in November and December, at three locations in January to March, and at five locations in April.


©2014. The Authors.

**Table 3.** Bias Between Mean HUT and Mean Measured Brightness Temperatures (K), Positive Values Indicate Simulations Overestimate Measured Brightness Temperatures, Range of Bias Across Extinction Coefficients in Parentheses

| | Bias Before Grain Scaling Factors | Bias After Grain Scaling Factors |
|---|---|---|
| 19H | 51 (7) | 0.2 (1.1) |
| 19 V | 36 (8) | 0.6 (0.3) |
| 37H | 64 (2) | −0.4 (3.5) |
| 37 V | 68 (2) | −0.5 (2.2) |

respectively), although physical temperatures were more conservative, with a range of 2.0°C around a mean of −3.8°C (Table 1).

### 3.2. Bias and Optimization of Simulated Brightness Temperatures

Repeated measurements of brightness temperatures at the trench site throughout the winter showed a seasonal decline (Figure 5), which accelerated after February as a result of increased snow crystal size and slight increases in mass. Brightness temperatures at this site were similar to measurements at surrounding forest, and open fen sites [*Derksen et al*., 2012] suggesting they were typical of a broad range of sub-Arctic snowpack types. Simulated brightness temperatures, using original stratigraphy and measured SSA-derived grain diameters, were greater than measurements at all positions along the trench. Resulting mean biases of 36 to 68 K, depending on frequency and polarization (Table 3), were in part due to the low measured brightness temperatures in April. These mean biases were at least 13 K smaller at 19 GHz than 37 GHz, although the range in mean biases depending on the extinction coefficient used were larger at the lower frequency. As measurements of soil type and moisture were not taken, we could not completely discount the soil as a source of bias in simulated brightness temperature. However, soil surface temperatures were measured and were shown to be frozen (−2.9°C). *Zhang et al*. [2003] showed that soil type was of little importance for frozen soil and that the permittivity should be approximately 6-j, as applied in this study. Although it was possible that unfrozen soil beneath the frozen surface layer had an effect, the moisture-sensing depth of microwave radiation ranges from ~0.1 to 1 wavelengths [*Marshall et al*., 2008]. Consequently, for wavelengths between 0.8 mm to 1.6 cm used in this study, it was unlikely that parameterization of the soil was the main cause of the difference between measured and simulated brightness temperatures.

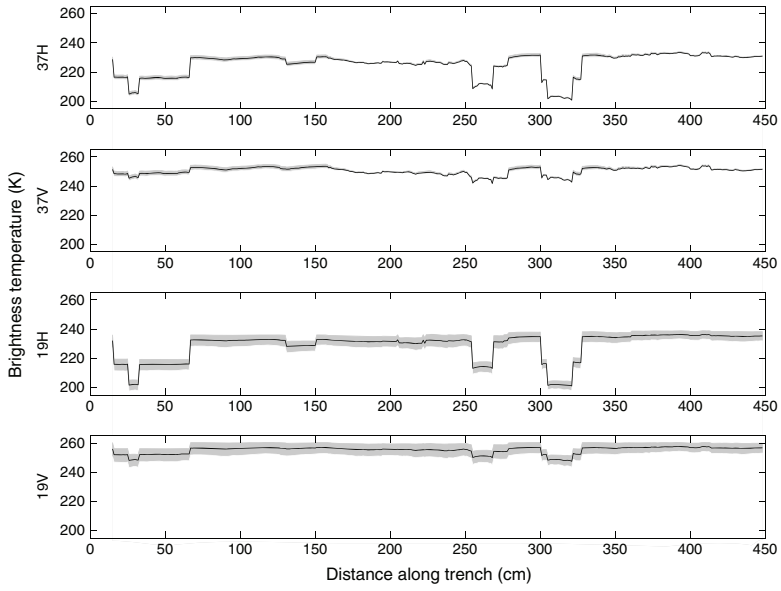


**Figure 6.** HUT brightness temperature simulations, before application of grain scaling factors, using all extinction coefficients models (mean = black line; range = shaded grey area).


©2014. The Authors.

**Table 4.** Optimal Simulated Grain Scaling Factor to Relate the Mean Simulated and Measured Brightness Temperatures for Each Combination of Frequency, Polarization, and Extinction Coefficient

| | Extinction Coefficient | | |
|---|---|---|---|
| Frequency/polarization | *Hallikainen et al.* [1987] | *Roy et al.* [2004] | *Kontu and Pulliainen* [2010] |
| 19 V | 4.2 | 3.3 | 3.2 |
| 19H | 5.3 | 4.9 | 4.2 |
| 37 V | 2.6 | 4.4 | 2.8 |
| 37H | 2.7 | 4.6 | 2.8 |

The changes in simulated brightness temperatures throughout the trench were rapid and stepped rather than slow and incremental (Figure 6). At all these frequency-polarization combinations, step changes were greater in magnitude than the small spread in simulated brightness temperatures caused by the three different extinction coefficients, which varied only slightly within individual frequency-polarization combinations throughout the trench (Figure 6). The positions of the step changes were coincident with the positions of ice lenses, which showed a greater decrease in brightness temperatures (reducing bias by bringing simulated brightness temperatures closer to measured values) at H-pol than V-pol irrespective of frequency. Where a second ice lens appeared above another along the trench, a second step change occurred in the simulated brightness temperatures, leading to a greater drop in brightness temperature than for one ice lens alone.

Application of scaling factors to measured or simulated grain size, in order to improve simulated estimates of brightness temperatures, is becoming increasingly common [*Langlois et al.*, 2012; *Montpetit et al.*, 2013; *Roy et al.*, 2013]. In the current study, the optimal grain scaling factor was the scaling factor (to the nearest 0.1) which produced the best agreement between the mean measurements and the mean simulations for each combination of frequency, polarization, and extinction coefficient. Grain scaling factors varied between 2.6 and 5.3 (Table 4). At 19 GHz, the scaling factors for all extinction coefficients were greater at H-pol than V-pol, with the *Hallikainen et al.* [1987] coefficient requiring the largest optimal scaling factors at both polarizations. Conversely, at 37 GHz, there was little difference in scaling factors between polarizations, with the coefficient of *Roy et al.* [2004] requiring the largest optimal scaling factor. The resulting biases between mean measured and mean optimized brightness temperatures (Table 3) were very low ($<$0.6 K), with an increased range in biases across the three extinction coefficients at 37 GHz than at 19 GHz. Mean simulated brightness temperatures after application of scaling factors (Figure 7) showed greater variability along the trench than simulations without scaling factors

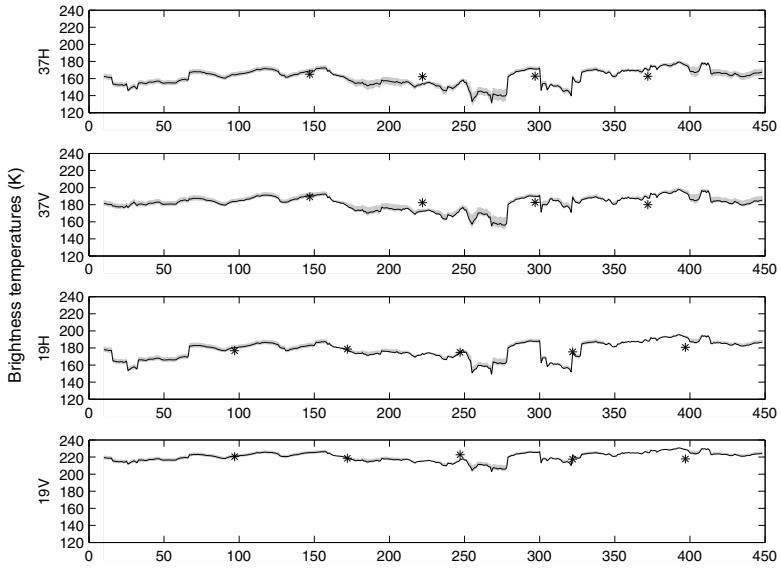


**Figure 7.** HUT brightness temperature simulations, after application of grain scaling factors, using all extinction coefficients models (mean = black line; range = shaded grey area) and measured brightness temperatures (asterisks).


©2014. The Authors.

**Table 5.** Bias of Simulated and Measured Brightness Temperatures (K) Throughout the Trench for Each Modeling Experiment

| | Bias (Mean HUT After Grain Scaling Factors − Mean Measured) | | | |
|---|---|---|---|---|
| Experiment | 19 V | 19H | 37 V | 37H |
| Density | −0.3 | −1.5 | −1.9 | −2.1 |
| Grain size | 0.3 | −0.2 | −1.1 | −0.9 |
| Layer boundary | 2.5 | 3.5 | 2.8 | 3.4 |
| Ice lens identification | −1.1 | −6.6 | −1.5 | −5.5 |
| Unmeasured layers | −3.2 | −4.5 | −7.5 | −6.8 |
| Ice lens or crusts | 0.5 | 1.1 | −1.3 | −0.2 |

(Figure 6) because less radiation is transmitted through the snowpack. In addition, decreases in brightness temperatures coincident with the position of ice lenses were still evident but were less well defined than before application of scaling factors, and the range of the three extinction coefficients was lower throughout the 19 GHz simulations and greater in sections of 37 GHz simulations than before grain scaling factors were applied.

### 3.3. Model Sensitivity and Stratigraphic Representations

Bias as a result of model sensitivity experiments ranged between 3.5 and −7.5 K (Table 5). Application of snow properties to unmeasured layers produced biases across all combinations of frequency and polarization (−3.2 to −7.5 K), which were larger at H-pol than V-pol. The identification and extension of ice lenses also increased bias at H-pol (−5.5 to −6.6 K), but not at V-pol (−1.1 to −1.5 K). Identification of layer boundary positions was the only sensitivity experiment to consistently produce positive biases (simulation overestimation) between 2.5 and 3.5 K. The remaining experiments applying measurement uncertainty to densities and grain size, as well as simulation of ice lenses as crusts, had low biases all within 2.1 K of mean measured brightness temperatures.

Bias resulting from layer representation experiments ranged between −0.5 and 14.6 K (Table 6). The bias of the one-layer stratigraphic representation of the snowpack was the largest across all combinations of frequency and polarization (4.9–14.6 K); biases decreased as stratigraphic layer representations became increasingly realistic, except for changes at V-pol from one- to two-layer representations where there was no decrease in bias or change was negligible (0.2 K). For stratigraphic representations of one to three layers, biases at H-pol were always greater than V-pol at both frequencies and biases at 19 GHz were always greater than at 37 GHz for respective polarizations.

## 4. Discussion

### 4.1. Stratigraphic Variability

Wintertime hydrometeorological processes controlling snow deposition, redistribution, scour, temperature gradient metamorphism, and melt-refreeze produced an April snowpack in Churchill which had high two-dimensional stratigraphic variability (a maximum of eight layers in any one-dimensional profile). Such stratigraphic variability is characteristic of sub-Arctic snowpacks that cover vast areas of nonboreal land in the Northern Hemisphere around the timing of peak seasonal SWE; *Derksen et al.* [2009] showed that vertical profiles at 45 locations across a 2000 km transect had an average of six layers (and as many as nine), while *Sturm and Benson* [2004] showed similar complexity, in two dimensions, in Arctic snowpacks. Consequently, it is vitally important that this stratigraphic reality is adequately represented in 1-D by multilayer emission models, and measured brightness temperatures (integrated throughout three-dimensional (3-D) volumes of snow) are evaluated using distributions of simulated brightness temperatures within sensor footprints. The

**Table 6.** Bias of Simulated and Measured Brightness Temperatures (K) Throughout the Trench for Four Different Representations of Stratigraphic Layering

| | Bias (Mean HUT After Grain Scaling Factors − Mean Measured) | | | |
|---|---|---|---|---|
| Layer Representation | 19 V | 19H | 37 V | 37H |
| One layer | 5.8 | 14.6 | 4.9 | 11.5 |
| Two layers | 5.6 | 10.9 | 4.9 | 8.4 |
| Three layers | 3.4 | 8.0 | 2.5 | 6.0 |
| *n* layer | 0.6 | 0.2 | −0.5 | −0.4 |


©2014. The Authors.

new methodological framework presented here, which assigned measured physical snow properties (density, effective grain size, and temperature) to stratigraphic layering identified using NIR photos [*Tape et al.*, 2010] in a multilayer snow emission model (HUT), has enabled this for the first time.

Conceptually, 3-D measurements of snow properties would be ideal inputs to emission models, particularly as our theoretical understanding of 3-D multiple scattering of microwaves by densely packed ice grains improves [*Tsang et al.*, 2013]. However, our current ability to accurately measure 3-D variability in snow microstructure, e.g., X-ray tomography [*Heggli et al.*, 2011], over spatial extents large enough to adequately resolve variability within the footprints of remote-sensing instruments (even of ground-based sensors) is not yet practical. Consequently, measurement of 2-D variability in this manner provides an appropriate trade-off between measurement resolution and practicality, capturing horizontal variability in the vertical gradients of grain size and density that result from the meteorological and metamorphic processes which control snowpack microstructure.

### 4.2. Bias and Scaling Factors

The horizontal variability across the trench of measured brightness temperatures in any particular combination of frequency and polarization was low (Figure 7). Across the trench, from left to right, the increase in mean grain size of vertical profiles (0.48 to 0.66 mm from linear trendline analysis) and the increased number of layer boundaries will cause increased scattering. Increased scattering will partially compensate for the decrease in SWE from left to right across the trench. In addition, reduced horizontal variability of measured brightness temperatures may be caused by the following: (1) averaging of the integrated signal received at the antenna from overlapping measurements of the main beam between adjacent radiometer footprints, (2) approximately 50% of the power integrated by the radiometer antenna coming from outside the 3 dB field of view, and (3) possible 3-D attenuation of the variability in snowpack properties exhibited by 2-D slices across footprints (e.g., discontinuous ice lenses). Simulated brightness temperatures were higher in magnitude than measurements, with a larger horizontal variability mainly influenced by the location of ice lenses. The resulting large biases required application of scaling factors to grain size in order to provide a better fit between simulated and measured brightness temperatures, thereby compensating for the uncertainty relating optical SSA to microwave model grain size input. Previous studies have applied scaling factors to optical grain size radius in DMRT-ML [*Brucker et al.*, 2011], to correlation length derived from simulated grain size in Microwave Emission Model of Layered Snowpacks (MEMLS) [*Langlois et al.*, 2012], and to correlation length from SSA in MEMLS [*Montpetit et al.*, 2013]. Scaling factors of between 0.1 and 2.85 have resulted. Only *Roy et al.* [2013] has previously attempted this for HUT, using SSA measurements of grain size. Using an optimal grain scaling factor of 3.7, *Roy et al.* [2013] concluded optical measurement of SSA will underestimate the maximum diameter from manual inspection ($D_{max}$) as the relationship between SSA and $D_{max}$ is nonlinear [*Langlois et al.*, 2010]. In the current study we extend previous work, quantifying the impact of three empirical formulations for the snow extinction coefficient. Although the mean of all scaling factors across combinations of frequency, polarization and extinction coefficient is similar (3.8) to that reported by *Roy et al.* [2013], the spread of optimal scaling factors for individual combinations, 2.6 to 5.3 (Table 4), quantifies relative differences in the ability of extinction coefficient formulations to compensate for the underestimation of extinction properties by the HUT model.

Grain scaling factors tentatively link an effective grain size derived from optical measurements to an effective grain size required for scattering and emission at microwave frequencies. Grain scaling factors reported in this study would equate to layers with effective grain diameters of between 0.5 and 6.8 mm, requiring consideration of microstructure beyond the size of individual grains [*Löwe et al.*, 2011], such as conglomerates. In addition to scatter and emission by grains, the increased sensitivity of H-pol to ice lenses, previously reported in HUT [*Rees et al.*, 2010] and MEMLS [*Durand et al.*, 2008; *Montpetit et al.*, 2013], could be a factor causing the larger scaling factors in H-pol than V-pol at both frequencies, especially at 19 GHz. Ice lenses, which were discontinuous throughout the trench, cause greater scatter at H-pol than is estimated by the HUT model, indicating that scaling factors at individual polarizations reflect more than just volume scattering by grains within layers.

The variability of extinction coefficients with frequency is strongly grain size dependent; Figure 8 helps to explain differences between optimal scaling factors for different extinction coefficients (Table 4). When grain size is small, there is little difference between the impact of the different coefficients, independent of frequency. However, as grain size increases, at 19 GHz, the extinction coefficients of *Roy et al.* [2004] are


©2014. The Authors.

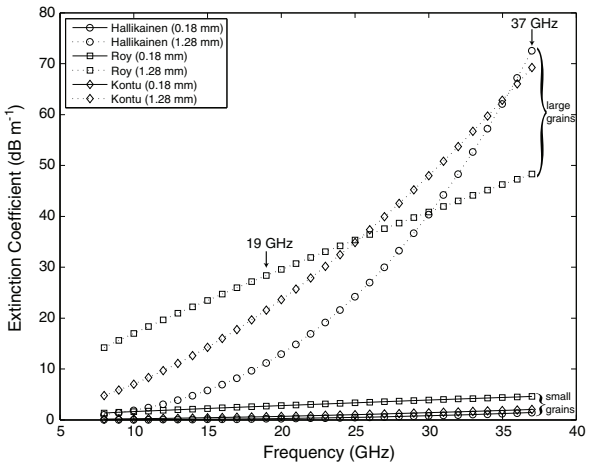


**Figure 8.** Extinction coefficients as a function of frequency at maximum and minimum measured effective grain diameters.

greater than *Kontu and Pulliainen* [2010], which are in turn greater than *Hallikainen et al.* [1987]. At 37 GHz, this order reverses. Scaling factors compensate for the differences in extinction coefficient values at each frequency, so that by using scaled grain sizes, the different extinction models equate to the same extinction coefficient. Table 4 shows *Hallikainen et al.* [1987] and *Kontu and Pulliainen* [2010] coefficients required lower compensation by scaling factors at 37 GHz than *Roy et al.* [2004], whereas at 19 GHz V-pol (excluding H-pol due to the previously discussed influence of ice lenses), the coefficients of *Kontu and Pulliainen* [2010] and *Roy et al.* [2004] required lower compensation than *Hallikainen et al.* [1987]. Used in this manner, the scaling factor has increasing physical basis as a proxy for the influence of large grains on scattering and absorption. As stratigraphic variability can be high in sub-Arctic snowpacks, due to hydrometeorological and metamorphic processes interacting with subnivean vegetation and ground roughness, it is important when modeling brightness temperatures to consider the proportions of large (hoar) and small (wind slab) grains in distributions of 1-D profiles rather than a single profile alone.

### 4.3. Sensitivity to Model Inputs and Layer Amalgamation

After experimentally adding measurement uncertainties to layer boundary positions, densities, and grain size, the impact of these uncertainties on simulated brightness temperatures was shown to be low (all within 3.5 K of mean measured brightness temperatures). This suggests that the level of error in field measurements of these variables and the framework for translating them into a snow emission model were sufficient for the purpose of model evaluation. The simulation of crusts where lenses were identified showed similar low levels of bias. However, rather than suggest that the distinction between lenses and crusts are unimportant for scattering, this may be a limitation of the simplicity in which the HUT model could be experimentally forced to replicate real crusts. Field observations revealed thin crusts resulting from insolation or wind hardening, with large grains adhering to the underside of the crusts (e.g., intermittently present throughout layer 4). The large grains most likely resulted from metamorphism where upward vapor transport was limited by impermeable crusts. Large gradients in dielectric properties and grain size, which were present between discontinuities in ice crusts and snow, have important scattering and reflective properties [*Kim*, 2006; *Mätzler*, 1996]. Such discontinuities were only partially accounted for by experimental changes in density as, for these simulations of crusts, grain size was made constant with that of adjoining layers. However, as the air content in ice lenses can decrease the density by more than half [*Mätzler and Wiesmann*, 1999] and density of ice lenses influences scattering potential [*Durand et al.*, 2008], it is important that density of ice lenses and crusts are more accurately reflected by HUT and more reliable field measurements are obtained.

The importance of correctly identifying the spatial extent of discontinuous ice lenses at H-pol agreed with *Rees et al.* [2010] who showed the influence of continuous ice lenses was not adequately represented by the implementation of two-layer HUT. Simulated brightness temperatures were much less sensitive at V-pol.


©2014. The Authors.

Where measurements of grain sizes and densities in individual layers were not available, assigning layers random values within the range of measured values shown in Figure 3 only created a maximum absolute bias of 7.5 K. This test, of potentially the weakest part of the methodological framework, suggested that the methods translating 1-D profiles to 2-D stratigraphy were appropriate.

The biases associated with layer amalgamation have implications for the wider application of HUT over regional to global scales, for example, in data assimilation products such as GlobSnow, where realistic vertical complexity in snowpacks cannot be characterized from near-real-time snow observations at climate stations [*Takala et al*., 2011]. The increase in bias from the original stratigraphy to a one-layer representation was more pronounced (more than double) at H-pol than V-pol at both frequencies, most likely highlighting sensitivity of H-pol to ice lenses and the necessity to include their scattering capability in large-scale applications. For the purpose of high resolution, distributed, physical snow modeling at the regional scale, a three-layer snowpack representation approaches current computational limitations, e.g., SNODAS [*Rutter et al*., 2008]. Consequently, improvements in accuracy provided by a three-layer approach to emission modeling will be of interest to future assimilation schemes that combine physical and emission models. In this study, bias of the three-layer representation was between 51 and 58% of the bias at one-layer representation. To achieve a further decrease of a similar percentage magnitude would require the original stratigraphy.

## 5. Conclusions

Two-dimensional stratigraphic layering was highly variable (up to eight layers in any one-dimensional profile) throughout a 4.5 m trench in a snowpack at Churchill, Manitoba, Canada, in April 2010. The variability of stratigraphic layering in the trench was highly representative of sub-Arctic and Arctic snowpacks.

Large biases (36 to 68 K) between simulated and measured brightness temperatures were minimized (−0.5 to 0.6 K) by the application of scaling factors to grain size. Grain scaling factors (2.6 to 5.3) compensated for the uncertainty relating optical SSA to HUT model grain size inputs and quantified relative differences in the ability of extinction coefficients to compensate for underestimation of extinction and absorption properties by the HUT model. Such large grain scaling factors suggest that the HUT model requires consideration of microstructure beyond the size of individual grains (e.g., conglomerates) and accurate representation of ice lenses, particularly for simulations at horizontal polarizations.

The variability of extinction coefficients with frequency is strongly grain size dependent. When grain size was small, independent of frequency, there was little difference between the impact of the different extinction coefficients. However, with increasing grain size, differences between coefficients at different frequencies became increasingly variable.

Consequently, when modeling brightness temperatures, it is important to consider the proportions of large (hoar) and small (wind slab) grains in distributions of 1-D profiles rather than a single profile alone, especially in sub-Arctic snowpacks where stratigraphic variability can be high.

Experiments to assess model sensitivity to measurement uncertainty and uncertainty in translating 1-D profiles to 2-D stratigraphy suggested that the level of error in field measurements and the methodological framework used to apply them in a snow emission model were satisfactory. The importance of correctly identifying the spatial extent of discontinuous ice lenses at H-pol was also demonstrated. In the layer amalgamation experiment, this study showed that a three-layer representation of the snowpack reduced the bias (across combinations of frequency, polarization, and extinction coefficients) to between 51 and 58% of the bias in a one-layer representation.

**Acknowledgments**
We would like to thank Bryn Hubbard, Martin Schneebeli, and four anonymous reviewers for their insightful and constructive comments that greatly improved this manuscript. Funding for the field measurements used in this study was provided by Environment Canada and the Canadian Space Agency. Logistical support in the field was provided by the Churchill Northern Studies Centre (thanks to LeeAnn Fishback, Carley Basler, and Clifford Paddock). Sandells acknowledges support from the Natural Environment Research Council (NERC) and the National Centre for Earth Observation (NCEO).

## References

Barnett, T. P., J. C. Adam, and D. P. Lettenmaier (2005), Potential impact of a warming climate on water availability in snow-dominated regions, *Nature*, *438*, 303–309.

Brogioni, M., G. Macelloni, E. Palchetti, S. Paloscia, P. Pampaloni, S. Pettinato, E. Santi, A. Cagnati, and A. Crepaz (2009), Monitoring snow characteristics with ground-based multifrequency microwave radiometry, *IEEE Trans. Geosci. Remote Sens.*, *47*(11), 3643–3655.

Brown, R. D. (2000), Northern hemisphere snow cover variability and change, 1915–97, *J. Clim.*, *13*(13), 2339–2355.

Brown, R. D., and R. O. Braaten (1998), Spatial and temporal variability of Canadian monthly snow depths, 1946–1995, *Atmosphere-Ocean*, *36*(1), 37–54.

Brucker, L., G. Picard, L. Arnaud, J.-M. Barnola, M. Schneebeli, H. Brunjail, E. Lefebvre, and M. Fily (2011), Modeling time series of microwave brightness temperature at Dome C, Antarctica, using vertically resolved snow temperature and microstructure measurements, *J. Glaciol.*, *57*(201).


©2014. The Authors.

Chang, A., J. Foster, and D. Hall (1987), NIMBUS-7 SMMR derived global snow cover parameters, *Ann. Glaciol.*, *9*, 39–44.
Cline, D., K. Elder, and R. Bales (1998), Scale effects in a distributed snow water equivalence and snowmelt model for mountain basins, *Hydrol. Processes*, *12*, 1527–1536.
Davenport, I. J., M. J. Sandells, and R. J. Gurney (2012), The effects of variation in snow properties on passive microwave snow mass estimation, *Remote Sens. Environ.*, *118*, 168–175.
Debye, P., H. R. Anderson, and H. Brumberger (1957), Scattering by an inhomogenous solid. II. The correlation function and its application, *J. Appl. Phys.*, *28*(679), 679–683.
Derksen, C., A. Walker, and B. Goodison (2003), A comparison of 18 winter seasons of in situ and passive microwave-derived snow water equivalent estimates in Western Canada, *Remote Sens. Environ.*, *88*, 271–282.
Derksen, C., A. E. Walker, B. E. Goodison, and J. W. Strapp (2005), Integrating in situ and multiscale passive microwave data for estimation of subgrid scale snow water equivalent distribution and variability, *IEEE Trans. Geosci. Remote Sens.*, *43*(5), 960–972.
Derksen, C., A. Silis, M. Sturm, J. Holmgren, G. E. Liston, H. Huntington, and D. Solie (2009), Northwest Territories and Nunavut snow characteristics from a sub-Arctic traverse: Implications for passive microwave remote sensing, *J. Hydrometeorol.*, *10*(2), 448–463.
Derksen, C., P. Toosea, J. Lemmetyinenb, J. Pulliainenb, A. Langloisc, N. Rutterd, and M. C. Fuller (2012), Evaluation of passive microwave brightness temperature simulations and snow water equivalent retrievals through a winter season, *Remote Sens. Environ.*, *117*, 236–248.
Domine, F., A. Cabanes, A.-S. Taillandier, and L. Legagneux (2001), Specific surface area of snow samples determined by CH4 adsorption at 77 K, and estimated by optical microscopy and scanning electron microscopy, *Environ. Sci. Technol.*, *35*, 771–780.
Durand, M., E. J. Kim, and S. A. Margulis (2008), Quantifying uncertainty in modeling snow microwave radiance for a mountain snowpack at the point-scale, including stratigraphic effects, *IEEE Trans. Geosci. Remote Sens.*, *46*(6), 1753–1767.
Elder, K., D. Cline, G. E. Liston, and R. Armstrong (2009), NASA Cold Land Processes Experiment (CLPX 2002/03): Field measurements of snowpack properties and soil moisture, *J. Hydrometeorol.*, *10*(1), 320–329.
Fierz, C., R. L. Armstrong, Y. Durand, P. Etchevers, E. Greene, D. M. McClung, K. Nishimura, P. K. Satyawali, and S. A. Sokratov (2009), The International Classification for Seasonal Snow on the Ground. IHP-VII Technical Documents in Hydrology No.83, IACS Contribution No.1, UNESCO-IHP, Paris.
Fletcher, S. J., G. E. Liston, C. A. Hiemstra, and S. D. Miller (2012), Assimilating MODIS and AMSR-E snow observations in a snow evolution model, *J. Hydrometeorol.*, *13*, 1475–149.
Freitag, J., F. Wilhelms, and S. Kipfstuhl (2004), Microstructure-dependent densification of polar firn derived from X-ray microtomography, *J. Glaciol.*, *50*(169), 243–250.
Gallet, J. C., F. Domine, C. S. Zender, and G. Picard (2009), Measurement of the specific surface area of snow using infrared reflectance in an integrating sphere at 1310 and 1550 nm, *The Cryosphere*, *3*(2), 167–182.
Grenfell, T. C., and S. G. Warren (1999), Representation of a nonspherical ice particle by a collection of independent spheres for scattering and absorption of radiation, *J. Geophys. Res.*, *104*(D24), 31,697–31,709.
Grody, N. (2008), Relationship between snow parameters and microwave satellite measurements: Theory compared with Advanced Microwave Sounding Unit observations from 23 to 150 GHz, *J. Geophys. Res.*, *113*, D22108, doi:10.1029/2007JD009685.
Hallikainen, M. T., F. T. Ulaby, M. Dobson, M. El-Rayes, and L.-K. Wu (1985), Microwave dielectric behavior of wet soil–Part I: Empirical models and experimental observations, *IEEE Trans. Geosci. Remote Sens.*, *GE-23*(1), 25–34.
Hallikainen, M., F. Ulaby, and T. Deventer (1987), Extinction behavior of dry snow in the 18- to 90-GHz range, *IEEE Trans. Geosci. Remote Sens.*, *GE-25*(6), 737–745.
Harlow, C., and R. Essery (2012), Tundra snow emissivities at MHS frequencies: MEMLS validation using airborne microwave data measured during CLPX-II, *IEEE Trans. Geosci. Remote Sens.*, *50*(11), 4262–4278.
Heggli, M., B. Köchle, M. Matzl, B. R. Pinzer, F. Riche, S. Steiner, D. Steinfeld, and M. Schneebel (2011), Measuring snow in 3-D using X-ray tomography: Assessment of visualization techniques, *Ann. Glaciol.*, *52*(58), 231–236.
Homan, J. W., C. H. Luce, J. P. McNamara, and N. F. Glenn (2011), Improvement of distributed snowmelt energy balance modeling with MODIS-based NDSI-derived fractional snow-covered area data, *Hydrol. Processes*, *25*, 650–660.
Kelly, R. (2009), The AMSR-E snow depth algorithm: Description and initial results, *J. Remote Sens. Soc. Jpn.*, *29*, 307–317.
Kelly, R., A. Chang, L. Tsang, and J. Foster (2003), A prototype AMSR-E global snow area snow depth algorithm, *IEEE Trans. Geosci. Remote Sens.*, *41*(2), 230–242.
Kim, M. J. (2006), Single scattering parameters of randomly oriented snow particles at microwave frequencies, *J. Geophys. Res.*, *111*, D14201, doi:10.1029/2005JD006892.
Kim, E. J., and A. W. England (2003), A yearlong comparison of plot-scale and satellite footprint-scale 19 and 37 GHz brightness of the Alaskan North Slope, *J. Geophys. Res.*, *108*(D13), 4388, doi:10.1029/2002JD002393.
Kontu, A., and J. Pulliainen (2010), Simulation of spaceborne microwave radiometer measurements of snow cover using in situ data and brightness temperature modeling, *IEEE Trans. Geosci. Remote Sens.*, *48*(3), 1031–1044.
Kurvonen, L., and M. Hallikainen (1997), Influence of land-cover category on brightness temperature of snow, *IEEE Trans. Geosci. Remote Sens.*, *35*(2), 367–377.
Langlois, A., A. Royer, B. Montpetit, G. Picard, L. Brucker, L. Arnaud, P. Harvey-Collard, M. Fily, and K. Goïta (2010), On the relationship between snow grain morphology and in-situ near infrared calibrated reflectance photographs, *Cold Reg. Sci. Technol.*, *61*(1), 34–42.
Langlois, A., A. Royer, C. Derksen, B. Montpetit, F. Dupont, and K. Goïta (2012), Coupling the snow thermodynamic model SNOWPACK with the microwave emission model of layered snowpacks for subarctic and arctic snow water equivalent retrievals, *Water Resour. Res.*, *48*, W12524, doi:10.1029/2012WR012133.
Lemmetyinen, J., C. Derksen, J. Pulliainen, W. Strapp, P. Toose, A. Walker, S. Tauriainen, J. Pihlflyckt, J. Kärnä, and M. T. Hallikainen (2009), A comparison of airborne microwave brightness temperatures and snowpack properties across the boreal forests of Finland and Western Canada, *IEEE Trans. Geosci. Remote Sens.*, *47*(3), 965–978.
Lemmetyinen, J., J. Pulliainen, A. Rees, A. Kontu, Q. Yubao, and C. Derksen (2010), Multiple-layer adaptation of HUT snow emission model: Comparison with experimental data, *IEEE Trans. Geosci. Remote Sens.*, *48*(7), 2781–2794.
Löwe, H., J. Spiegel, and M. Schneebeli (2011), Interfacial and structural relaxations of snow under isothermal conditions, *J. Glaciol.*, *57*(203), 499–510.
Marshall, H. P., G. Koh, and M. Sturm (2008), Ultra-broadband portable microwave FMCW radars for measuring snow depth, snow water equivalent, and stratigraphy: Practical considerations. Proceedings of the XXIXth International Union of Radio Science (URSI) General Assembly.
Matzl, M., and M. Schneebeli (2006), Measuring specific surface area of snow by near-infrared photography, *J. Glaciol.*, *52*(179), 558–564.
Mätzler, C. (1996), Microwave permittivity of dry snow, *IEEE Trans. Geosci. Remote Sens.*, *34*(2), 573–581.
Mätzler, C. (2002), Relation between grain-size and correlation length of snow, *J. Glaciol.*, *48*(162), 461–466.


©2014. The Authors.

Mätzler, C., and A. Wiesmann (1999), Extension of the microwave emission model of layered snowpacks to coarse-grained snow, *Remote Sens. Environ.*, *70*(3), 317–325.
Molotch, N. P., and S. A. Margulis (2008), Estimating the distribution of snow water equivalent using remotely sensed snow cover data and a spatially distributed snowmelt model: A multi-resolution, multi-sensor comparison, *Adv. Water Resour.*, *31*, 1503–1514.
Montpetit, B., A. Royer, A. Langlois, P. Cliche, A. Roy, N. Champollion, G. Picard, F. Domine, and R. Obbard (2012), New shortwave infrared albedo measurements for snow specific surface area retrieval, *J. Glaciol.*, *58*(11), 941–952.
Montpetit, B., A. Royer, A. Roy, A. Langlois, and C. Derksen (2013), Snow microwave emission modeling of ice lenses within a snowpack using the Microwave Emission Model for Layered Snowpacks, *IEEE Trans. Geosci. Remote Sens.*, *51*(9), 4705–4717.
Painter, T. H., N. P. Molotch, M. Cassidy, M. Flanner, and K. Steffen (2007), Contact spectroscopy for determination of stratigraphy of snow optical grain size, *J. Glaciol.*, *53*(180), 121–127.
Payne, J. T., A. W. Wood, A. F. Hamlet, R. N. Palmer, and D. P. Lettenmaier (2004), Mitigating the effects of climate change on the water resources of the Columbia River Basin, *Clim. Change*, *62*(1-3), 233–256.
Picard, G., L. Arnaud, F. Domine, and M. Fily (2009), Determining snow specific surface area from near-infrared reflectance measurements: Numerical study of the influence of grain shape, *Cold Reg. Sci. Technol.*, *56*(1), 10–17.
Proksch, M., H. Löwe, and M. Schneebeli (2012), Statistical model for the correlation length of snow derived from Snow-Micro-Pen measurements, *Geophys. Res.*, Abstr. 14 EGU2012: 14125.
Pulliainen, J. T., J. Grandell, and M. T. Hallikainen (1999), HUT snow emission model and its applicability to snow water equivalent retrieval, *IEEE Trans. Geosci. Remote Sens.*, *37*(3), 1378–1390.
Rees, A., J. Lemmetyinen, C. Derksen, J. Pulliainen, and M. English (2010), Observed and modelled effects of ice lens formation on passive microwave brightness temperatures over snow covered tundra, *Remote Sens. Environ.*, *114*(1), 116–126.
Roy, V., K. Goïta, A. Royer, A. E. Walker, and B. E. Goodison (2004), Snow water equivalent retrieval in a Canadian boreal environment from microwave measurements using the HUT snow emission model, *IEEE Trans. Geosci. Remote Sens.*, *42*(9), 1850–1859.
Roy, A., G. Picard, A. Royer, B. Montpetit, F. Dupont, A. Langlois, C. Derksen, and N. Champollion (2013), Brightness temperature simulations of the Canadian seasonal snowpack driven by measurements of the snow specific surface area, *IEEE Trans. Geosci. Remote Sens.*, *99*, 1–13.
Rutter, N., D. Cline, and L. Li (2008), Evaluation of the NOHRSC snow model (NSM) in a one-dimensional mode, *J. Hydrometeorol.*, *9*(4), 695–711.
Schneebeli, M. (2004), Numerical simulation of elastic stress in the microstructure of snow, *Ann. Glaciol.*, *38*, 339–342.
Sturm, M., and C. Benson (2004), Scales of spatial heterogeneity for perennial and seasonal snow layers, *Ann. Glaciol.*, *38*, 253–260.
Takala, M., K. Luojus, J. Pulliainen, C. Derksen, J. Lemmetyinen, J.-P. Kärnä, J. Koskinen, and B. Bojkov (2011), Estimating northern hemisphere snow water equivalent for climate research through assimilation of space-borne radiometer data and ground-based measurements, *Remote Sens. Environ.*, *115*(12), 3517–3529.
Tape, K. D., N. Rutter, H. P. Marshall, R. Essery, and M. Sturm (2010), Recording microscale variations in snowpack layering using near-infrared photography, *J. Glaciol.*, *56*(195), 75–80.
Tedesco, M., R. E. J. Kelly, J. L. Foster, and A. T. C. Chang (2004), *AMSR-E/Aqua Daily L3 Global Snow Water Equivalent EASE-Grids V002*, National Snow and Ice Data Center: Digital media, Boulder, Colo.
Tedesco, M., E. J. Kim, A. Gasiewski, M. Klein, and B. Stankov (2005), Analysis of multiscale radiometric data collected during the Cold Land Processes Experiment-1 (CLPX-1), *Geophys. Res. Lett.*, *32*, L18501, doi:10.1029/2005GL023006.
Tedesco, M., E. J. Kim, D. Cline, T. Graf, T. Koike, R. Armstrong, M. J. Brodzik, and J. Hardy (2006), Comparison of local scale measured and modelled brightness temperatures and snow parameters from the CLPX 2003 by means of a dense medium radiative transfer theory model, *Hydrol. Processes*, *20*(4), 657–672.
Toure, A. M., K. Goïta, A. Royer, C. Mätzler, and M. Schneebeli (2008), Near-infrared digital photography to estimate snow correlation length for microwave emission modeling, *Appl. Opt.*, *47*(36), 6723–6733.
Tsang, L., K.-H. Ding, S. Huang, and X. Xu (2013), Electromagnetic computation in scattering of electromagnetic waves by random rough surface and dense media in microwave remote sensing of land surfaces, *Proc. IEEE*, *101*(2), 255–279.
Wiesmann, A., and C. Matzler (1999), Microwave emission model of layered snowpacks, *Remote Sens. Environ.*, *70*(3), 307–316.
Yang, D. Q., et al. (1999), Quantification of precipitation measurement discontinuity induced by wind shields on national gauges, *Water Resour. Res.*, *35*(2), 491–508.
Zhang, L., J. Shi, Z. Zhang, and K. Zhao (2003), The estimation of dielectric constant of frozen soil-water mixture at microwave bands, *IEEE Int. Geosci. Remote Sens. Symp.*, *4*, 2903–2905.


©2014. The Authors.

## B.5 Article : Creation of a Lambertian Microwave Surface for Retrieving the Downwelling Contribution in Ground-Based Radiometric Measurements

Bruno Courtemanche a publié un article publié en 2015 sur la création d'une surface lambertienne dans les MOP qui permet de mesurée la contribution descendante de l'environnement. Ce travail s'inscrit dans le cadre de cette thèse puisqu'il tente de développer des instruments pour isoler les différentes composantes qui contribuent au signal MOP mesuré à la surface du couvert nival. Pour ce travail, l'élaboration et la conception de la plaque lambertienne ont été réalisées dans le cadre de cette thèse. La prise de mesures et la révision de l'article ont aussi été faite dans les travaux de cette thèse.

# Creation of a Lambertian Microwave Surface for Retrieving the Downwelling Contribution in Ground-Based Radiometric Measurements

Bruno Courtemanche, Benoit Montpetit, Alain Royer, and Alexandre Roy

***Abstract*—Downwelling radiative fluxes from inhomogeneous environments are not easy to quantify from the total measured signal contribution. We propose the use of a Lambertian reflector to assess this issue. Using ray tracing to extrapolate the bidirectional reflectance distribution function of a surface with high reflectivity in the microwave spectrum, we characterized a surface that acts as a near-Lambertian reflector at 37 GHz. After implementing such a plate using molded aluminum and getting its emissivity, we validated its Lambertian reflectance properties based on microwave surface-based radiometer measurements. This analysis also gives guidelines on how to make a Lambertian surface for different wavelengths in the microwave spectrum. Field experiments show the usefulness of such a Lambertian plate to estimate the downwelling contribution in ground-based radiometric measurements.**

***Index Terms*—Downwelling brightness temperature, Lambertian reflector, passive microwave, ray tracing.**

## I. Introduction

RADIOMETRIC measurements are primarily dependent on the radiative physical properties of a specific target, e.g., its emissivity $(\epsilon)$ (or reflectivity). These measurements also depend on the properties of the sensor used, e.g., its frequency (wavelength) and incidence angle. For accurate radiometric measurements of a nonblackbody target $(\epsilon \neq 1)$, it is necessary to isolate and quantify the contribution of the downwelling radiative fluxes emitted by the surrounding environment of the target reflected toward the radiometer. Field measurements are often made in complex environments where the contributions of the different emission sources surrounding the target are difficult to estimate.

Regardless of the observation angles, studies using passive microwave brightness temperatures $(Tb)$ have to consider both sources of the measured Tb $(\mathrm{Tb}_{\mathrm{measured}})$, i.e., the emission by the surface itself $(T_{\mathrm{target}} * \epsilon_{\mathrm{target}})$ and the portion of the downwelling radiative fluxes emitted by the surrounding environment $(\mathrm{Tb}_{\downarrow})$ of the target reflected $((1 - \epsilon_{\mathrm{target}}))$ toward the radiometer. Thus

$$\mathrm{Tb}_{\mathrm{measured}} = \epsilon_{\mathrm{target}} T_{\mathrm{target}} + (1 - \epsilon_{\mathrm{target}})\mathrm{Tb}_{\downarrow}. \quad (1)$$

Manuscript received November 14, 2013; revised March 24, 2014 and June 29, 2014; accepted July 8, 2014. This work was supported by the Natural Sciences and Engineering Research Council of Canada.

The authors are with the Centre d'Applications et de Recherches en Télédétection, Université de Sherbrooke, Sherbrooke, QC J1K 2R1, Canada (e-mail: bruno.courtemanche@usherbrooke.ca; benoit.montpetit2@usherbrooke.ca).

Color versions of one or more of the figures in this paper are available online at http://ieeexplore.ieee.org.

Digital Object Identifier 10.1109/LGRS.2014.2346138

Measurements from surface-based radiometers (SBRs) are one of the cases where additional tools are needed to isolate the signal emitted by the target from all of the other sources in the integrated measurement of the sensor. For example, in the case of snow microwave emission studies, in which the snow emissivity allows the snow properties to be remotely characterized [1]–[3], the downwelling radiation from the sky [4] or the forest canopy above the snow surface [5], [6], reflected on the snow, significantly alters the retrieval if it is not corrected as the snow reflectance can be important. For example, assuming a typical snow emissivity ranging from 0.75 to 0.95 at 37 GHz [10] and a downwelling $T_a$ ranging from 30 K (for a clear sky) to 150 K (for the surrounding area), the error generated by neglecting $T_a$ could vary from 1.5 K to up to 40 K, which is significant.

To isolate and quantify the downwelling radiative fluxes from the environment of the target, a Lambertian surface $(LS)$ with a low emissivity (highest reflectivity) would be an ideal tool to discriminate the contribution of the environment from the contribution of the target. A radiometer is first used to measure a target Tb. Then, a Lambertian plate is placed over the target, and the Tb measurement of the Lambertian plate allows the retrieval of the integrated $\mathrm{Tb}_{\downarrow}$ [using (1) by replacing subscript target by LS]. In order to use the integrated $\mathrm{Tb}_{\downarrow}$ obtained by the LS, target reflection or scattering must primarily have a Lambertian rather than a specular pattern. However, even if this is not the case, the integrated $\mathrm{Tb}_{\downarrow}$ obtained by the LS will still be a good approximation in an inhomogeneous environment (as demonstrated in Section IV).

We propose a Lambertian microwave surface in the form of an aluminum plate with a structure generating multiple reflections, i.e., a surface where the incident radiation will be reflected a great number of times, spreading the initial radiation in all directions. To help determine the appropriate surface to use, the following were done: 1) ray-tracing simulations were conducted to determine the surface properties needed; 2) a plate was created and characterized; and 3) field measurements were conducted on a reference bare soil surface measured under different surrounding environments to validate the use of such a Lambertian plate to retrieve the downwelling Tb.

## II. Ray Tracing Modeling

A ray-tracing model has been implemented for this study to select the geometric surface pattern that acts as a near-Lambertian reflector. A hemispherical grid was created from the duplication of icosahedron cells. This hemispherical grid,

1545-598X © 2014 IEEE. Personal use is permitted, but republication/redistribution requires IEEE permission.
See http://www.ieee.org/publications_standards/publications/rights/index.html for more information.

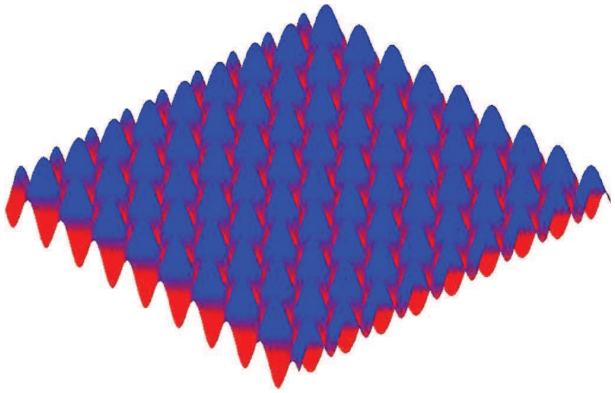

Fig. 1. Representation of the modeled surface of interest described by (2) with parameters $a = 3.4$ and $b = 3.5$.

which is composed of 2528 cells, was placed over the modeled surface and used to integrate the contribution by all reflected rays. Each triangular cell being identical to one another, the number of integrated rays in each cell is equivalent to a measured radiance. Twelve emission sources were used to characterize the reflection by the surface.

The proposed surface pattern, as shown in Fig. 1, can be defined by

$$z = \frac{a}{2}\left(\sin\frac{2\pi x}{b} + \cos\frac{2\pi y}{b}\right) \tag{2}$$

where the constant $a$ defines the amplitude of the peaks, and $b$ defines the distance between them. The ray-tracing approach was used to define the optimal ratio of $(a : b)$ giving an isotropic distribution of reflections. It appears that, from a great number of simulations using a large range of $(a : b)$ values, the ratio $a : b \approx 1$ seems to act as a near-Lambertian reflector.

The results in Fig. 2 show, apart from a backscattering area and very large angles, a near-Lambertian reflection pattern when the $a : b$ ratio is $(a = 3.5 : b = 3.5)$. We also show arbitrarily tested ratios such as $(a = 7.0 : b = 3.5)$ and $(a = 3.5 : b = 7.0)$. It is interesting to note that, when $a$ is larger than $b$, the dispersion of the reflected radiation is greater at low incident angles. On the contrary, when the gap is larger than the amplitude height, specular reflections occur, and it generates a pattern of reflected radiation mainly oriented toward the source. That backscatter response from the LS can be avoided when using the LS by choosing an azimuthal configuration where the backscatter contribution is negligible.

Fig. 3 highlights a key characteristic of the plate showing that the contribution to the radiation at angles close to nadir mainly comes from rays that have undergone multiple reflections, allowing a more evenly spread radiation in all directions. Verification of multiple reflections has helped to better characterize the surface when the ratio approached the optimal $a : b \approx 1$ ratio.

## III. *In Situ* Validation

Afterward, an aluminum plate was created by duplication of a mold $(a = 3.4 : b = 3.5)$ using a standard industrial wet

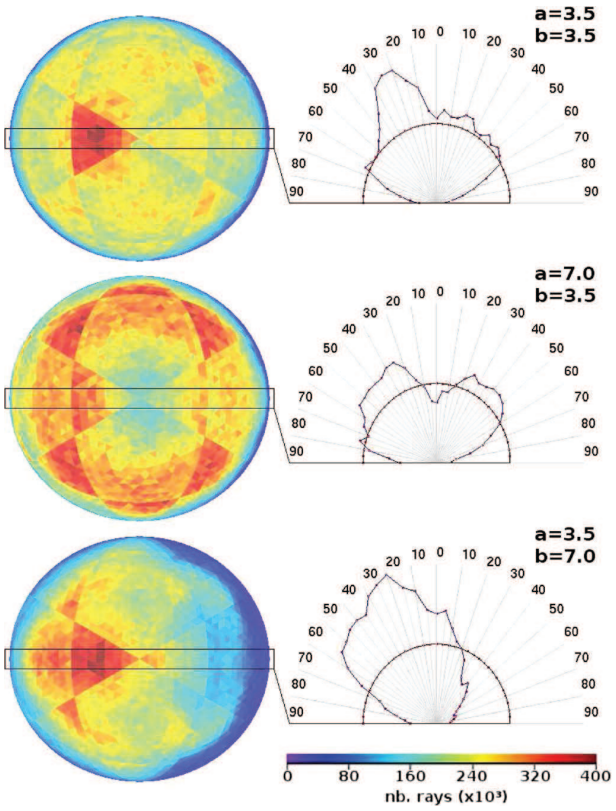


Fig. 2. Ray tracing results for the surface of interest (shown in Fig. 1) for different amplitude ($a$) to gap ($b$) ratios [see (2)]. View projection from (left) nadir observation perspective and from a (right) planar cut through transect identified by the rectangle. The semicircle shows a perfect Lambertian contribution. An isotropic source was placed at 5 cm west of the reflective surface. The size of the source is 125 × 30 cm, and it was placed at the same level as the reflective surface.

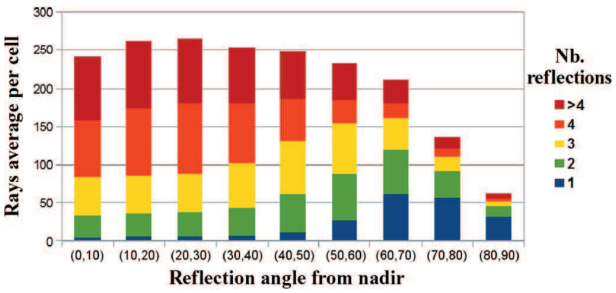


Fig. 3. Radiation contribution by the number of successive reflections of the incident radiation depending on the angle from nadir with $a = 3.4$ and $b = 3.5$ parameters.

sand molding technique. Special attention was paid to the smoothness of the geometric surface pattern. The plate is 50 cm wide by 60 cm long. The size of the aluminium plate was carefully chosen to ensure that the measurement footprint with respect to the antenna beamwidth and the distance of the antenna from the plate would always be inside the plate with good tolerances.

We thus conducted a series of field measurements to determine the emissivity of this plate and to validate its Lambertian properties. These measurements took place in the middle of

TABLE I
MODELED AND MEASURED TB FROM DIFFERENT SOURCES

| Source | 19 GHz H-Pol | 19 GHz V-Pol | 37 GHz H-Pol | 37 GHz V-Pol |
|---|---|---|---|---|
| Sky $0^o$ NARR | 7.0 K | | 14.8 K | |
| Sky $0^o$ Measured | 9.4 K | 8.9 K | 15.6 K | 15.9 K |
| Total $Tb_{\downarrow}$ NARR | 11.0 K | | 25.3 K | |
| Sky $55^o$ measured | 15.4 K | 14.4 K | 25.9 K | 26.3 K |
| $Tb_{Plate}$ $60^o$ | 41.9 K | 43.6 K | 47.7 K | 46.6 K |

frozen Magog Lake, Quebec, Canada (45.325° N; 72.037° W), 750 m from the shore on February 7, 2013, in clear-sky conditions during the afternoon. Measurements were performed using PR-1900 and PR-3700 radiometers (Radiometrics Corporation) with a beamwidth of 6° for 19 GHz and 5° for 37 GHz. Tb measurements were previously calibrated using a microwave absorber (Ecosorb) target at ambient temperature and at low temperature using liquid nitrogen [7], [8]. Absolute error for the calibration target temperature was assessed at 2 K, and overall precision was assessed at 2 K for 19 GHz and $<1$ K for 37 GHz, based on a 3-db width of the main beam.

To characterize the plate emissivity $(\epsilon_{\text{plate}})$ from the measured Tb $(\text{Tb}_{\text{measured}})$ and its temperature $(T_{\text{plate}})$, the same relationship as (1) was used.

The temperature of the plate was measured using a thermocouple throughout the experiment, giving variations ranging from $-2\,^{\circ}\text{C}$ to $0\,^{\circ}\text{C}$ for the area facing the sun and to $-6.5\,^{\circ}\text{C}$ for the opposite face. The downwelling radiation $(\text{Tb}_{\downarrow})$ was modeled using the atmospheric model implemented in the Helsinki University of Technology snow emission model [9] driven with the atmospheric profile conditions derived from the North American Regional Reanalysis (NARR) data. Tb measurements of the sky at 0° (SBR at zenith) and 55° from zenith, the latter approximately corresponding to the total downwelling radiation [11], were also taken. The distance from both antennas to the center of the plate was 1.9 m, resulting in a footprint less than 20 cm for 19 GHz and 17 cm for 37 GHz. A laser mounted on the radiometer was used to ensure proper positioning of the plate. Table I compares these modeled and measured Tb.

The differences between the modeled NARR and measured sky nadir and hemispheric Tb are negligible at 37 GHz. These differences are slightly larger at 19 GHz. Using both NARR and measured hemispheric Tb, the minimum and maximum emissivity values were calculated [see (1)]. The air temperature was stable at 262.2 K during the experiment. From (1), retrieved emissivity values for the plate are between 0.107 and 0.131 at 19 GHz and 0.086 and 0.095 at 37 GHz.

To validate the Lambertian nature of the plate, an experiment was set up consisting of positioning an emission source, a 72 cm $\times$ 130 cm $\times$ 10 cm wood panel at two azimuth angles, i.e., 90° and 180°, as illustrated in Fig. 4. Radiometers were oriented to measure toward the east. The orientation of the sensor was chosen in order to have a similar solar irradiation for both measurement setups. In addition to the two azimuthal configurations, the wood panel is first vertically placed and then tilted at 60° and 30° outward. These changes in the panel orientation modify the contribution of the emission source from different directions, testing the Lambertian nature of the plate. The viewing angle of the radiometer was set at 30° and 60°.

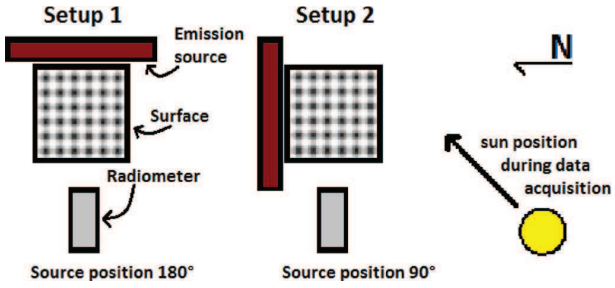


Fig. 4. Diagram of the Lambertian properties validation setup experiment.

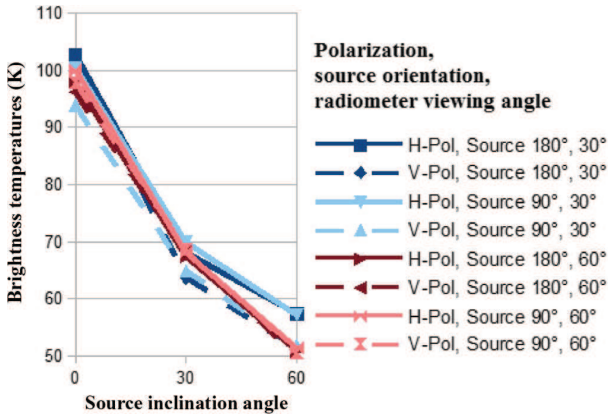


Fig. 5. Lambertian validation results at 37-GHz vertical and horizontal polarizations.

Fig. 5 shows the measured plate Tb for the different experimental configurations at 37 GHz in both vertical (V-Pol) and horizontal (H-Pol) polarizations.

For both observation configurations at 37 GHz, there is a slight variation of Tb (see Fig. 5), except for the Tb measured at V-Pol at an incident angle of 30° and the emission source at an azimuth angle of 90°. A difference of less than 3 K is measured for a 30° viewing angle, whereas this difference increases to about 4 K for measurements at 60°. Changing the angle of the source (see Fig. 5) shows some interesting results. The specular reflective area should have a lower Tb for a configuration where the emission source is at a 90° azimuth angle (see dark-colored lines in Fig. 5) compared with a 180° azimuth angle (see light-colored lines in Fig. 5). Instead, a Lambertian pattern was observed. A Tb slightly below was witnessed for the measurements collected in V-Pol (see dashed lines in Fig. 5). Fig. 6 gives the results at 19 GHz in both polarizations for a viewing angle of 60°.

The observations made at 19 GHz (see Fig. 6) show that the reflection by the plate seems more specular than Lambertian since measurements with the source configuration at 180° (dark-colored lines) have higher Tb than those taken with the source configuration at 90° (light-colored lines). This can be explained by the fact that the wavelength (1.58 cm) is higher than the minimum distances inside a gap for $b = 3.5$. A plate with properties similar to the one presented here is thus unable to reproduce a Lambertian reflection pattern at 19 GHz. Phenomena of surface roughness could also increase the specular nature of the plate.

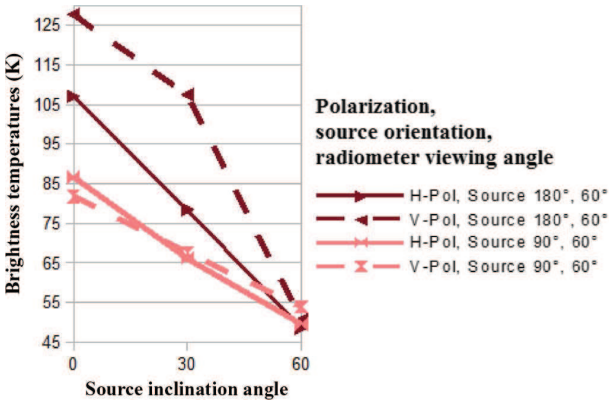


Fig. 6. Lambertian validation results at 19 GHz for vertical and horizontal polarizations.

We propose a simple approach to define the geometry of the plate depending on the wavelength ($\lambda$) to obtain a Lambertian pattern. To select the adequate $a, b$ parameters, the minimum distance in a gap must be similar or slightly higher in size to the wavelength to allow a more homogeneous distribution of the incident radiation. This minimum distance in a gap can be expressed in a planar cut through the plate into the maximum peaks transect [see (3)] and another one in the maximum and minimum peaks transect [see (4)] when $\Delta y_1$ and $\Delta y_2$ tend to 0. Thus

$$\Delta y_1 = a - a\cos\frac{\pi\lambda}{b} - \lambda \tag{3}$$

$$\Delta y_2 = 2a - 2a\cos\frac{\pi\lambda}{\sqrt{2}b} - \lambda. \tag{4}$$

For example, $a = 3.4$ and $b = 3.5$ have a minimum distance in a gap lower than the wavelength in less than 2% of the vertical axis using $(\Delta y_1 + \Delta y_2)/2a$. To reproduce the Lambertian pattern observed at 37 GHz for 19-GHz measurements, the ratio should be closer to $a = b \geq 6.9$ cm.

## IV. Surface Emissivity Retrieval

To demonstrate the efficiency of the proposed Lambertian plate, an experiment was set up to retrieve the emissivity of a dry homogeneous soil sample (Portland cement ASTM C150-Type 1, nonhydrated) at 37 GHz, 55° incident angle, for different downwelling radiative fluxes. To perform the experiment, the radiometer, the soil sample, and the Lambertian plate were installed on a flatbed trailer to ensure that measurements were taken at the same angle and identical geometric conditions. In addition, four humidity and temperature sensors were placed in the soil sample, and a temperature sensor was used to keep track of the temperature of the plate before and after each radiometric measurement. These measurements show that the temperature and humidity of the soil sample remained constant during the experiment, which means that the emissivity of the soil remained constant for every site. At the Université de Sherbrooke campus, eight sites were chosen, four under low downwelling radiative fluxes (open space sites, S1 to S4 in Table II) and four under high downwelling radiative fluxes corresponding to coniferous and deciduous forest sites (S5 to S8 in Table II). These measurements were made on October 21, 2013, during the night under covered-sky conditions.

TABLE II
Tb Measurements and Derived Soil Sample Emissivity for Different Sites

| Site | Tb H-Pol (K) | | Tb V-Pol (K) | | T (K) | | Soil $\epsilon$ | |
|---|---|---|---|---|---|---|---|---|
| | Plate | Soil | Plate | Soil | Plate | Soil | H-Pol | V-Pol |
| S1 | 47.9 | 230.3 | 47.4 | 265.2 | 286.0 | 287.1 | 0.785 | 0.917 |
| S2 | 52.9 | 233.3 | 50.4 | 265.4 | 286.0 | 287.4 | 0.791 | 0.916 |
| S3 | 54.9 | 236.2 | 50.9 | 265.7 | 286.8 | 287.4 | 0.801 | 0.917 |
| S4 | 64.2 | 234.9 | 66.4 | 266.7 | 286.3 | 287.7 | 0.786 | 0.914 |
| S5 | 107.7 | 237.9 | 112.3 | 269.7 | 285.7 | 287.2 | 0.751 | 0.910 |
| S6 | 135.7 | 243.4 | 139.8 | 272.1 | 287.2 | 287.9 | 0.735 | 0.904 |
| S7 | 178.7 | 270.4 | 173.0 | 277.6 | 287.0 | 287.8 | 0.856 | 0.919 |
| S8 | 205.1 | 264.5 | 205.3 | 279.1 | 287.7 | 287.8 | 0.745 | 0.905 |

The soil emissivities in Table II were calculated using (1) with an emissivity of 0.095 for the Lambertian plate as defined by the *in situ* validation. Mean soil emissivity, supposed to remain constant even under different environments, is 0.781 with a standard deviation of 0.038 in horizontal polarization and 0.913 in vertical polarization with a standard deviation of 0.006. In vertical polarization, the use of the Lambertian plate allowed the characterization of the soil emissivity with very small variation margin by quantifying and removing the contribution of the surrounding environment, regardless of the downwelling contribution sources. In horizontal polarization, the soil emissivity can be estimated, but a 0.121 variation in the emissivity is present, mainly in the forested sites. This variation could be caused by specular reflections of the downwelling emissions on the soil surface, which is not measured by the Lambertian aluminum plate.

Horizontal polarization measurements indicate that it might be more useful to measure both integrated $\mathrm{Tb}_{\downarrow}$ and specular $\mathrm{Tb}_{\downarrow}$ to access if the surface has a Lambertian or a specular reflection pattern. Regarding only the specular contribution, even measurements of a small footprint with a small beamwidth antenna come from a much larger environment footprint. To get that exact footprint contribution, the antenna should be directly pointed at the environment footprint, upside down from the previous measurement, placing it underground. A smaller footprint could be measured by pointing at the specular angle. The problem with this technique is the enormous variations in measured Tb by slightly moving the antenna while keeping the same inclination and orientation (we refer to this problem as case P). A worst case P scenario would be the following: doing measurements in a forest where trees could conceal their own contribution or measurements of normally concealed trees while moving the antenna, thus rendering an inadequate integration of the radiative fluxes. Regarding the footprint, surfaces are rarely perfectly plane. Contributions from different angles other than the specular angle from the antenna make the use of a Lambertian reflector more adequate than a specular reflector. Measurements using a specular reflector also return to the case P problem because of the environment complexity, except for flat specularly reflecting targets where the LS is not helpful. Taking into consideration that the surface reflectance distribution is not only specular, using a Lambertian reflector to retrieve

contribution $Tb_{\downarrow}$ from an inhomogeneous environment seems to be a better way to approximate the downwelling contribution to the signal. The target reflection characteristics depend on the electromagnetic frequency used for the measurements. It is important to choose an LS with the adequate geometry and to determine the target reflection characteristics when selecting whether to use the LS with or without a specular reflector.

## V. Conclusion

This study has demonstrated that it is possible to determine a plate pattern that acts as a near-Lambertian surface. A protocol was also suggested to implement such plates for different wavelengths in the microwave spectrum. A plate was created with an available mold, and its Lambertian properties were validated at 37 GHz with *in situ* experiments. This experiment showed that regardless of the surrounding environment, radiometric measurements of the created plate were able to measure the integrated hemispherical downwelling contribution of the area. Such a tool will greatly improve the accuracy of ground-based microwave radiometric measurements in complex environments such as in the Canadian boreal forest.

## Acknowledgment

The computing time for the ray tracing modeling was provided through the Compute Canada national HPC platform. The authors would like to thank D. Lascelle and P. Cliche for their help during field measurements.

## References

[1] C. Mätzler, "Applications of the interaction of microwaves with the natural snow cover," *Remote Sens. Rev.*, vol. 2, no. 2, pp. 259–392, 1987.
[2] R. E. Kelly, T. Chang, L. Tsang, and J. L. Foster, "A prototype AMSR-E global snow area and snow depth algorithm," *IEEE Trans. Geosci. Remote Sens.*, vol. 41, no. 2, pp. 234–242, Feb. 2003.
[3] A. Frei *et al.*, "A review of global satellite-derived snow products," *Adv. Space Res.*, vol. 50, no. 8, pp. 1007–1029, Oct. 2012.
[4] E. G. Choudhury, B. T. Pampaloni, P. Kerr, and Y. H. Njoku, *Passive Microwave Remote Sensing of Land-Atmosphere Interactions*. Boca Raton, FL, USA: CRC Press, 1995.
[5] A. Roy *et al.*, "A simple parameterization for a boreal forest radiative transfer model at microwave frequencies," *Remote Sens. Environ.*, vol. 124, pp. 371–383, 2012.
[6] P. Pampaloni, "Microwave radiometry of forests," *Waves Random Media*, vol. 14, no. 2, pp. S275–S298, 2004.
[7] K. W. Asmus and C. Grant, "Surface based radiometer (SBR) data acquisition system," *Int. J. Remote Sens.*, vol. 20, no. 15/16, pp. 3125–3129, 1999.
[8] F. Solheim, "Use of pointed water vapor radiometers to improve GPS surveying accuracy," M.S. thesis, Univ. Colorado, Boulder, 1993.
[9] J. T. Pulliainen, J. Grandell, and M. T. Hallikainen, "HUT snow emission model and its applicability to snow water equivalent retrieval," *IEEE Trans. Geosci. Remote Sens.*, vol. 37, no. 3, pp. 1378–1390, May 1999.
[10] A. Wiesmann and C. Mätzler, "Microwave emission model of layered snowpacks," *Remote Sens. Environ.*, vol. 70, no. 3, pp. 307–316, Dec. 1999.
[11] C. Mätzler and P. Rosenkranz, "Dependence of microwave brightness temperature on bistatic surface scattering: Model functions and application to AMSU-A," *IEEE Trans. Geosci. Remote Sens.*, vol. 45, no. 7, pp. 2130–2138, Jul. 2007.

# C Annexe : Liste des présentations et affiches de congrès

Royer, A., Roy, A., **Montpetit, B.**, et Langlois, A. 2014. Coupling the Canadian Land Surface Scheme to a microwave model to simulate the snow microwave brightness temperature under boreal forest. Présentation orale à Microsnow, Reading, UK, 3-7 août 2014.

Dolant, C., Langlois, A., Todorovic, V., **Montpetit, B.**, Roy, A., and Royer, A. 2014. Detection of a rain-on-snow event (ROS) using an empirical algorithm using passive microwave radiometry. Présentation orale à l'Eastern Snow Conference, Boone, NC, US, 3-5 juin 2014.

**Montpetit, B.**, Royer A., Roy A. 2013. Detecting ice lenses and melt-refreeze crusts using satellite passive microwaves. Invited Speaker. 2013 AGU fall meeting, San Francisco, USA, December 9-13th 2013.

Langlois, A., Royer, A., **Montpetit, B.** 2013. Seasonal measurements of snow physical and radiometric properties during rain-on-snow events (ROS) over eastern Canada. International Geoscience and Remote Sensing Symposium (IGARSS), Melbourne, Australia, July 21st-26th, 2013.

**Montpetit, B.**, Royer, A., Langlois, A., Cliche, P., Marchand, N., Thériault, N., Roy, A., Lefebvre, E. and Lesaffre, B. 2013. Improvement of snow passive microwave modeling using in-situ temporal snow and radiometric measurements in James Bay area, Québec. 70th Eastern Snow Conference, Huntsville (Ontario), Canada, June 4th-6th 2013.

**Montpetit, B.**, Royer, A., Langlois, A., Chum, M., Cliche, P., Roy, A., Champollion, N., Picard, G. and Obbard, R. 2011. New short wave infrared albedo measurements for snow specific surface area retrievals. Invited Speaker. Snow Grain Size Workshop, Grenoble, France, April 2nd-5th, 2013.

**Montpetit, B.**, Royer, A., Roy, A., Langlois, A. and Derksen, C. 2012. Snow microwave emission modeling of ice lenses within a snowpack using the Microwave Emission Model of Layered Snowpacks (MEMLS), 69th Eastern Snow Conference, Claryville, New York, USA, June 5-7th 2012.

Roy, A., Royer, A., Picard, G., Langlois, A., Morin, S., **Montpetit, B.** and Cliche, P. 2012. Snow specific surface area simulation using one-layer snow model for SWE retrieval from passive microwave brightness temperature, 69th Eastern Snow Conference, Claryville, New York, USA, June 5-7th 2012.

**Montpetit, B.**, Royer, A., Langlois, A., Roy, A., Cliche, P., Champollion, N., Picard, G., Domine,

F. and Obbard, R. 2012. New short wave infrared albedo measurements for snow specific surface area retrievals, GEC3 Student's day, Montreal (Quebec), Canada, April 2012.

Roy, A., Picard, G., Royer, A., Dupont, F., Langlois, A., **Montpetit, B.** and Derksen, C. 2012. Snow radiative transfer model parameterization with snow microstructure measurements, 12th Special Meeting on Microwave Radiometry and Remote Sensing of Environment MicroRad, Rome, Italy, March 5-9th 2012.

**Montpetit, B.**, Royer, A., Langlois, A., Chum, M., Cliche, P., Roy, A., Champollion, N., Picard, G. and Obbard, R. 2011. In-situ measurements for snow grain size and shape characterization using optical method, 68th Eastern Snow Conference, Montreal (Quebec), Canada, June 14-16th 2011.

Roy, A., Royer, A., Langlois, A., Morin, S., **Montpetit, B.** and Cliche, P. 2011. Snow specific surface area simulations using the one-layer CLASS model, 68th Eastern Snow Conference, Montreal (Quebec), Canada, June 14-16th 2011.

Langlois, A., Brucker, L., **Montpetit, B.**, Roy, A. and Derksen, C. 2011. Simulations of snow passive microwave brightness temperature using couple snow thermodynamic and emission models, Canadian Symposium on Remote Sensing, Sherbrooke (Quebec), Canada, June 13-16th 2011.

Langlois, A., Royer, A., **Montpetit, B.**, Roy, A., and Derksen, C. 2010. Measurements of snow radiometric and microstructure properties over a transect of plot-scale field observations : Application to snow thermodynamic and passive microwave emission models, American Geophysical Union (AGU) Fall meeting, San Francisco, CA, USA, December 15-18th 2010.

Roy, A., Langlois, A., Royer, A., **Montpetit, B.**, Champollion, N., Picard, G., Domine, F., and Fily, M. 2010. Field measurements of snow grain specific surface area (SSA) using near infrared photography and laser reflectometry in Northern Canadian tundra, American Geophysical Union (AGU) Fall meeting, San Francisco, CA, USA, December 15-18th 2010.

Royer, A., Langlois, A., Roy, A., **Montpetit, B.**, Goïta, K., Derksen, C., Dupont, F., Champollion, N., Picard, G., and Fily, M. 2010. Snow properties retrieval un subarctic regions using passive microwave remote sensing and modeling, ArcticNet 7th Scientific Meeting, Ottawa, QC, December 14th - 17th 2010.

M. Fily, L. Arnaud, C. Carmagnola, N. Champollion, P. Cliche, F. Domine, F. Dupont,J.-C., Gallet ,A. Langlois, **B. Montpetit**, S. Morin, G. Picard, A. Roy, and A. Royer. 2010. A set of devices to acquire vertical profiles of snow specific surface area, ArcticNet 7th Scientific Meeting, Ottawa,

QC, December 14th - 17th 2010.

Langlois, A., Royer, A., Dupont, F., Goïta, K., Cliche, P., Fily, M., Picard, G., Brucker, L., **Montpetit, B.**, and Derksen, C. 2010. Improvement of passive microwave vegetation correction using airborne radiometer measurements for Snow Water Equivalent (SWE) retrieval, Eastern Snow Conference, Hancock, MA, USA, June 9-10 2010.

Langlois, A., Royer, A., **Montpetit, B.**, Picard, G., Brucker, L., Arnaud, L., Goïta, K., and Fily, M. 2010. Relationship between snow grain morphology and in-situ near infrared calibrated reflectance photographs. IGARSS Annual Scientific Meeting, Cape Town, South Africa, July 13th - 17th 2009.